universität wien

DISSERTATION / DOCTORAL THESIS

Titel der Dissertation / Title of the Doctoral Thesis

„Mathematical modelling and simulation of epithelial-to-mesenchymal transitions leading to cell migration“

verfasst von / submitted by

Steffen Plunder, M.Sc.

angestrebter akademischer Grad / in partial fulfilment of the requirements for the degree of

Doktor der Naturwissenschaften (Dr.rer.nat.)

Wien, 2022 / Vienna, 2022

Studienkennzahl lt. Studienblatt / degree programme code as it appears on the student record sheet:	UA 796 605 405
Dissertationsgebiet lt. Studienblatt / field of study as it appears on the student record sheet:	Mathematik
Betreut von / Supervisor:	Assoz. Prof. Sara Merino Aceituno, PhD

Abstract

The thesis consists of three parts, as described next.

Part I: Many agent-based models are subject to inequality constraints, e.g. non-overlapping conditions, which make them hard to analyse and simulate. Here we explore the well-posedness of these models and propose a new numerical method. In particular, we first show the well-posedness of these models thanks to the theory of differential inclusions. Second, adapt a method that appears in the literature of computer graphics called position based dynamics (PBD) to solve first-order differential inclusions.

Part II: The primary project of this PhD thesis is the study of epithelial-to-mesenchymal Transitions (EMT), which are complex cellular processes that play a crucial role in neural tube formation and also occur in wound healing, fibrosis and the initial stage of metastasis. EMT is a crucial biological process that can lead to cells migrating the tissue in which they reside. In this part of the thesis, we develop an EMT model, extending an existing model for growing epithelium. Since the model is an agent-based model with constraints, using the PBD method exposed in part I, we can simulate millions of different epithelial-to-mesenchymal transitions and perform a statistical ranking to identify the key factors leading to cellular migration. Our findings led to new biological hypotheses, which the group of biologists led by Eric Theveneau (CNRS, Toulouse) tested experimentally.

Part III: We show the mean-field limit for a particle system with constraints. This particle system is inspired by models for muscle contraction.

Kurzzusammenfassung

Diese Doktorarbeit besteht aus drei Teilen, wie im Folgenden beschrieben.

Teil I: Viele Agenten-basierte Modelle enthalten Ungleichheitsnebenbedingungen, z.B. um Überlappungen von Objekten zu vermeiden. Wir untersuchen die Wohlgestelltheit solcher Modelle und schlagen eine neue numerische Methode vor. Zuerst zeigen wir Existenz und Eindeutigkeit mithilfe der Theorie von differentiellen Inklusionen. Danach passen wir die Position-based Dynamics (PBD) Methode aus der Computer Grafik Literatur an um differentielle Inklusionen erster Ordnung zu lösen.

Teil II: Das Hauptprojekt dieser Doktorarbeit ist die Untersuchung von Epithelial-mesenchymale Transitionen (EMT). Dies ist ein komplexer Zellprozesss welcher eine entscheidende Rolle spielt in der Entwicklung der Neuralröhre, aber auch in der Wundheilung, Fibrose und Anfangsstadien von Metastase. EMT führt zur Zellmigration aus dem Gewebe heraus. In diesen Teil der Arbeit erweitern wir ein existierendes Modell für wachesendes um EMT zu modellieren. Die PBD Methode (aus Teil I) wurde speziell für dieses Modell angepasst und ermöglicht es Millionen von EMT Szenarien zu simulieren. Durch eine statistische Auswertung können wir so die Schlüsselfaktoren identifizieren, welche zur Zellmigration führen. Unsere Ergebnisse haben zu neuen biologischen Hypothesen geführt welche von der Gruppe von Eric Theveneau (CNRS, Toulouse) ausgewertet wurden.

Teil III: In diesen Teil untersuchen wir ein Partikelmodell mit algebraischen Nebenbedingungen, welche inspiriert sind von Muskelmodellen. Wir beweisen Konvergenz der Durchschnittsfeld-Näherung (mean-field limit).

Contents

Prologue

'The only interesting thing about vertebrates is the neural crest.'

This (somewhat facetious) quote, attributed to Thorogood (1989) [GG00], might come as a surprise to those mathematicians who don't know what *neural crest cells* are. It is, however, still alive in the thoughts of nowadays biologists, as the following tweet shows [ZT22].

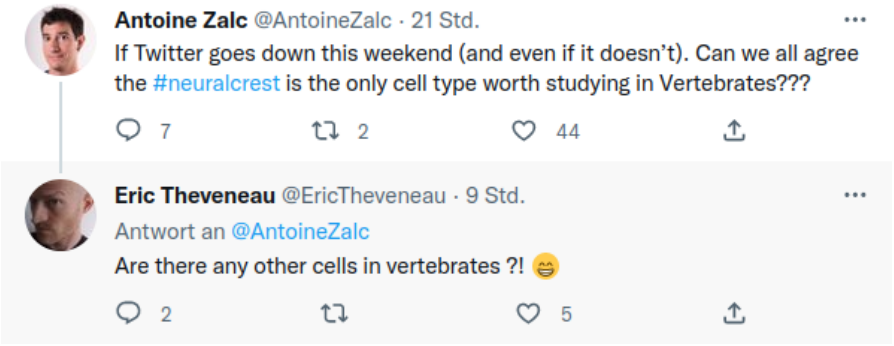

Neural crest cells play an important role in the early development of animal embryo. Indeed, almost every part of our body (from head to toe) contain some former neural crest cells. This large distribution of neural crest cells is possible because of their ability to migrate far distances and due to their genetic flexibility, which allows these cells to fulfil many different roles.

One of the key properties of neural crest cells is that they perform the epithelial-to-mesenchymal transition, which is a process during which these cells change their cell type allowing them to migrate. This thesis is at its core about the mathematical exploration of the epithelial-to-mesenchymal transition.

Introduction

This thesis is primarily about models explaining how neural crest cells initiate migration. More broadly, we are interested in the underlying process known as the epithelial-to-mesenchymal transition. During this transition, cells change their characteristic traits and gain migratory functions.

We used agent-based modelling to help experimentalists with difficult-to-test questions about epithelial-to-mesenchymal transitions. Our results lead the biologists to rethink assumptions about this process and to conduct experiments with provided new biological results.

After finding the right model and fitting mathematical framework, the main challenge became to make simulations fast enough for extensive ensemble simulations. We found that a new method from NVIDIA, called position-based dynamics (PBD), made our computations 300 times faster.

In the following, we outline the structure of this thesis in more detail.

Overview

This thesis consists of three parts. In the first part, we develop the mathematical theory of differential inclusions and present the position-based dynamics method. These foundations are applied in the second part, where we model and analyse epithelial cells with agent-based models. Our main application is a model for transitions between epithelial and mesenchymal cells. In the third part, we prove mean-field convergence for a system with constrained particles. This last part is independent of the other projects, but it has in common that we investigate an ODE system with constraints.

Part I: Theory of differential equations with inequality constraints and position-based dynamics

Many agent-based models contain objects which should not overlap. Mathematically, this leads to differential equations with inequality constraints. Crucially, such inequalities give rise to non-smooth behaviour at the transitions between unconstrained motion and sliding cases, see Figure 1. For example, when an object hits the ground, it will change its velocity discontinuously. One approach to deal with such behaviour are differential inclusions.

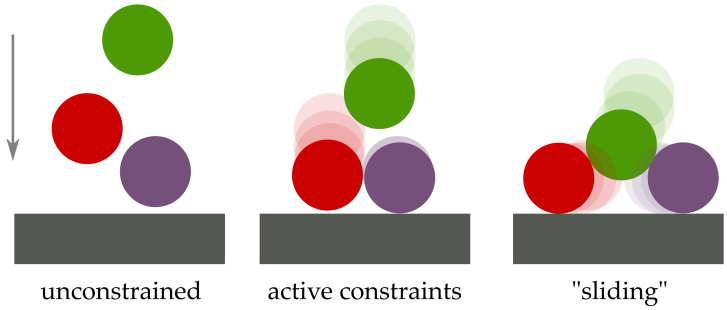

Figure 1. Illustrative example of typical interaction between particles with volume.

Chapter 1 introduces the formalism of differential inclusions to prove the well-posedness of first-order differential equations with inequality constraints. The study of differential inclusions relies on tools from convex analysis, such as normal cones or subderivatives. However, most non-overlap conditions do not result in convex sets, which makes classical theorems inapplicable. To solve this, one can use the extension of convex analysis on uniformly prox-regular sets. A set is prox-regular if the orthogonal projection onto the set is unique for points close enough to the set. The results from [BV10] show the well-posedness of differential inclusions on prox-regular sets.

The theory in Chapter 1 applies, in particular, to the agent-based models in the second part of this thesis. These agent-based models are first-order ODEs with inequality constraints which fulfil the assumptions needed for well-posedness of the corresponding differential inclusions.

In Chapter 2, we analyse a method called *position based dynamics* (PBD), which was developed by NVIDIA [Mül+06] for fast and stable simulation of physical systems with contacts. We can adapt the PBD method for first-order differential inclusions with only minor changes. The method shows surprisingly good properties, such as numerical stability at large time steps and a fast runtime. Moreover, the PBD method converges in numerical tests to the exact solutions. However, a full proof of convergence is still not available.

While the mathematical foundations are yet to be established, we think that PBD is a useful tool for modelling, since it is likely the easiest method to deal with constraints.

It only requires one simple operation per overlap, but neither Lagrangian multipliers nor artificial numerical parameters. This lowers the complexity of implementations and could accelerate the development of new models.

Part II: Modeling of the epithelia-to-mesenchymal transition

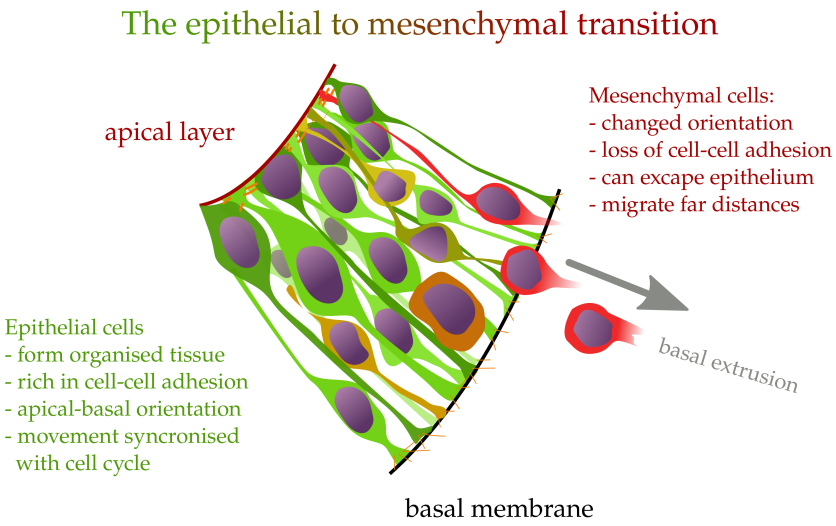

Figure 2. Sketch of an epithelial tissue with cells transforming from epithelial to mesenchymal cell type. Mesenchymal cells can escape the tissue basally which is an important process in developmental biology.

The primary project of this PhD thesis is the study of epithelial-to-mesenchymal transitions (EMT), which are complex cellular processes which play a crucial role in neural tube formation and also occur in wound healing, fibrosis and the initial stage of cancer development. After EMT, cells typically have gained some or all functions of mesenchymal cells and start to migrate by leaving the epithelium basally, see Figure 2.

In Chapter 3, we introduce an agent-based model of growing epithelium based on [Fer+19]. An epithelium is a skin-like tissue in which cells arrange themselves in a dense structure. The model fits experimental data from Theveneau's lab (CNRS, Toulouse), where the chick embryo neural tube serves as a model organism. In the model, we represent cells with simple mechanical components, such as linear springs, repulsive forces and non-overlapping constraints. The components model the cytoskeleton, the adhesion between cells and the cell's nucleus. As a collective, the cells of the model form a tissue-like layer which shares characteristics with the experimental data of Theveneau's lab. The model from [Fer+19] also features cell cycle-dependent changes of the cytoskeleton dynamics, which lead to realistic growth behaviour.

Our contribution is a modification of the model from [Fer+19] to improve its runtime and numerical stability. All modifications are such that our model remains consistent with the simulations in [Fer+19] to avoid duplicated work. The simulations in [Fer+19] use the

damped Arrow Hurwicz method to solve non-convex constrained energy minimisation problems in each time step. We initially tried different minimisation methods but found that these led to different local minima and, thus, to a completely different model. Our main observation is that the damped Arrow Hurwicz method can introduce damping between time steps, which explains the discrepancy with other solvers. As a consequence, the actual simulations in [Fer+19] correspond to an overdamped Newton equation instead. Therefore, we consider the overdamped Newton equations to gain access to new numerical methods, which are generally more straightforward than non-convex optimisation schemes. This change makes it possible to use the position based dynamics method. Thanks to that, we can simulate over 300 times faster with equivalent simulation outcomes. The new simulation is also numerically more stable, allowing us to explore a more extensive range of parameters.

Chapter 4 contains the main results of our interdisciplinary project. Here we extend the model for growing epithelium from Chapter 3 to allow specific epithelial cells to gain traits of mesenchymal cell types. Opposite to epithelial cells, mesenchymal cells can detach from the epithelium and start migrating. In addition, they exhibit different cytoskeleton dynamics and a different sense of direction.

As sketched in Figure 2, those cells undergoing the epithelial-to-mesenchymal transition (EMT) can leave the epithelium on the basal side. Such basal extrusion is the start of collective cell migration of mesenchymal cells, therefore, it is natural to ask which mesenchymal characteristics contribute the most to basal extrusion.

EMT is not a switch between epithelial and mesenchymal cell types but a collection of many non-compulsory transformations. This leads to heterogeneity of possible cell types within the epithelial-to-mesenchymal spectrum. Our model is as minimal as possible, with only four parameters determining if and when certain transformations occur. Nevertheless, all these different parameter combinations plus groups of cells with different parameters give thousands of possible EMT scenarios.

Using the PBD method, we can simulate millions of different EMT scenarios and perform a statistical ranking to identify the key factors leading to basal extrusion. We compare not only different timings for the individual EMT steps, but also the impact of group sizes and the difference between homogeneous and heterogeneous groups of EMT cells.

We identify three main features which explain most cases of basal extrusion in silico (i.e. in our simulations).

- First, it is no surprise that cells showing protrusive activities (i.e. a mechanism to extend in specific directions and pull themselves forward) are much more efficient at exiting basally than cells replying on passive forces to reach the basal side. Even more, cells without protrusive activities are at risk of exiting on the wrong side, the apical side. This aspect is challenging since apical extrusion does only occur in experiments where certain cells functions are inhibited, but not in normal control settings. However, we realise that protrusive activities are

key to explaining experimental results, since, other EMT factors cannot explain alone the high rate of basal extrusion that is observed experimentally.
- Second, the simulations show that cells without protrusions only have a high chance of successful basal exit if they are already in a favourable position close to the basal side at the onset of EMT.
- Finally, we did not find any relevant correlation between the timing of EMT transition events and the resulting extrusion rates. This indicates that the order in which the transition takes place is irrelevant.

The simulation results challenged some experimental views on the nature of EMT and led to new hypotheses to resolve the dichotomy between the simulations and experimental beliefs. Some of these experiments are still ongoing. In particular,

- the first *in silico* observation fits to published *in vivo* experiments [Kil+98] where cells without the ability to form protrusions are exiting the epithelium apically. This indicates that protrusions play already a key role in the initial stage of EMT, since they are necessary to explain why (under physiological conditions) all cells escape basally.
- For the second in silico observation, Theveneau's lab found supporting experimental evidence. The experiments showed that cells undergoing EMT will already position themselves at the basal side before the EMT programs start. This 'preparation' underlines that the position could be a crucial favouring factor for basal extrusion.
- Finally, the observation that the timing of EMT transformation events is irrelevant is hard to test experimentally. Overall, the simulations let us conclude that there might be many more important factors than timing.

Part III: Mean-field convergence for a particle system with constraints.

The last part of this thesis is independent of the former two. The project is a follow-up to my master's thesis, where I studied mathematical aspects of models for muscle contraction.

Our motivation from the modelling side is a particular aspect of muscle contraction. In non-specialists' terms, a muscle contracts because billions of tiny filaments inside the muscle are pulling simultaneously, see Figure 3. If we consider the whole muscle together with the billions of tiny filaments as a coupled mathematical system, then the question occurs how the whole muscle and the filaments interact. Clearly, the contraction force is the sum of the billion individual pulling forces. On the other hand, also the filaments will extend according to the deformation of the whole muscle. Typically one neglects this second direction of interaction, as it contributes little to the overall dynamics since the filaments often detach or break. However, in this more mathematically driven part of the thesis, we will prove which system arises in the mean-field limit if one considers both directions of this coupling.

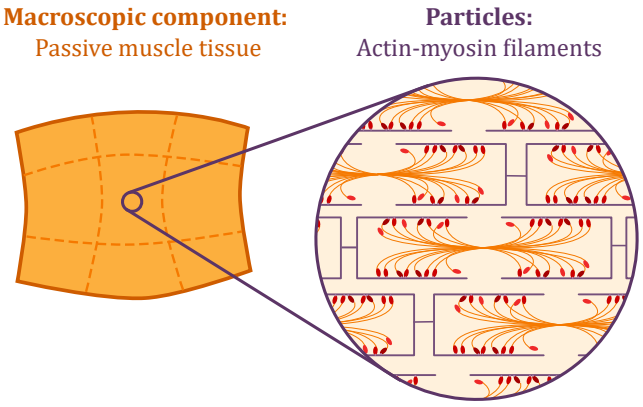

Figure 3. Sketch of the relation between a whole muscle tissue and the tiny filaments (actin-myosin filaments) which can make the muscle contract.

On the mathematical side, the question is how the classical mean-field limit theory works out if the particles are all subject to a particular set of constraints. Interestingly, there are many theorems about mean-field convergences and coarse-graining, which all have the common assumption of a flat geometry, i.e. unconstrained particles. Due to a lack of a suitable theorem, we prove the mean-field limit following the classical approach as in [Gol16]. On the way, we also obtain Dobrushin's stability estimate for this particular type of coupled system.

One aspect that sets our constrained particle systems apart from other mean-field limits is the occurrence of a *mean-field mass*. The mean-field mass relates to the inertia of particles which have to move when the overall system moves. The mean-field mass can even be non-constant if the constrained particles have to move at different speeds to keep up with the constraint.

Chronological overview of this PhD thesis

Marina A. Fereirra's PhD

Agent-based model
for healthy pseudo-stratified epithlium

My master's thesis

Simulation and Lagrangian modelling
of skeleton muscle tissue

Start of my PhD

Chapter 3

Q: What are the key factors of the epithelial-to-mesenchymal transtion leading to basal extrusion?

Added rules for
epithelial-to-mesenchymal transition (EMT)
to an existing model for growing epithelium.

Realise existing model is actually solving
overdamped Newton equations
with inequality constraints.
→ gives access to faster numerical methods!

Chapter 4

EMT is very heterogeneous!
To compare many different scenarios,
use thousands of simulations
and statistical ranking.

Modelling leads to biological hypotheses:
1. Cells position themself already basally
   before onset of EMT!
2. Does apical extruion occur in
   the absense of cell protrusions?

Experimental validation:
1. is tested with experiments.
2. currently ongoing but relates to published data.

Chapter 5

Q: Our muscles contract due to the accumulated force of billions of cross-bridges. How can kinetic theory be applied to such a mechanical system?

Mean-field limit for particle systems
with uniform, full-rank constraints.

Chapter 1

Q: Which theory is applicable to ODEs with non-convex inequality constraints?

Use existing mathematical framework:
Well-posedness theory for
differential inclusions on prox-regular sets.

Theory applies to the EMT model and
the cell migration model.

Chapter 2

Q: How can we simulate overdamped Newton equations with inequality constraints in the fastest possible way?

Adapt a popular method from computer graphics,
position-based dynamics, to first-order systems.

→ ×300 speed up for our model!

Notation

Within this thesis, we will use the following notation.

For vector valued variables or functions, we mostly use boldface font such as $\boldsymbol{x} \in \mathbb{R}^d$. Since we often deal with particle systems, we will write $\boldsymbol{\mathcal{X}} = (\boldsymbol{X}_1, \dots, \boldsymbol{X}_N) \in \mathbb{R}^{2N}$ where we use $\boldsymbol{X}_i \in \mathbb{R}^2$ to refer to the coordinates of the ith particle.

Upper indices might refer to the current time-step, e.g. $\boldsymbol{\mathcal{X}}^k = (\boldsymbol{X}_1^k, \dots, \boldsymbol{X}_N^k)$.

We use ∂ as the notation for the differential, e.g. for a function $\boldsymbol{F} : \mathbb{R}^d \to \mathbb{R}^n$ we write $\partial \boldsymbol{F}(\boldsymbol{x}) : \mathbb{R}^d \to \mathbb{R}^n$ for the derivative at a point $\boldsymbol{x} \in \mathbb{R}^d$. For a (tangent) vector $\boldsymbol{v} \in \mathbb{R}^d$, we write $\partial \boldsymbol{F}(\boldsymbol{x})[\boldsymbol{v}] \in \mathbb{R}^n$ if we want to emphasise the linearity. Otherwise, we simply use the common association $\partial \boldsymbol{F}(\boldsymbol{x}) \in \mathbb{R}^{n \times d}$ and write $\partial \boldsymbol{F}(\boldsymbol{x})\boldsymbol{v}$ instead. Higher order derivatives are notated as $\partial^2 \boldsymbol{F}(\boldsymbol{x}) : \mathbb{R}^d \times \mathbb{R}^d \to \mathbb{R}^n$ where we might write $\partial^2 \boldsymbol{F}(\boldsymbol{x})[\boldsymbol{v}, \boldsymbol{w}] \in \mathbb{R}^n$ for two tangent vector $\boldsymbol{v}, \boldsymbol{w} \in \mathbb{R}^d$.

In this thesis, we will always use the standard Euclidean scalar product $\boldsymbol{v} \cdot \boldsymbol{w} \coloneqq \sum_{i=1}^n v_i w_i$ for finite dimensional vectors and $\|\boldsymbol{v}\| = \sqrt{\boldsymbol{v} \cdot \boldsymbol{v}}$ denotes the Euclidean norm. The nabla operator denotes the transposed of the gradient, i.e., for a function $g : \mathbb{R}^d \to \mathbb{R}$ we define $\nabla g(\boldsymbol{x}) \coloneqq (\partial g(\boldsymbol{x}))^T \in \mathbb{R}^d$.

For a function $\boldsymbol{x} : [0, T] \to \mathbb{R}^d$ where $[0, T]$ denotes a time interval, we will use dots to denote time derivatives, i.e. $\dot{\boldsymbol{x}} = \frac{\mathrm{d}\boldsymbol{x}}{\mathrm{d}t}$ and $\ddot{\boldsymbol{x}} = \frac{\mathrm{d}^2\boldsymbol{x}}{\mathrm{d}t^2}$.

Moreover, we denote the sup norm as

$$\|\boldsymbol{x}\|_\infty \coloneqq \sup_{t \in [0,T]} \|\boldsymbol{x}(t)\|.$$

Finally, we will introduce some notation from convex analysis in Chapter 1. Most notable, we denote the distance between a point $\boldsymbol{x} \in \mathbb{R}^d$ and a set $S \subset \mathbb{R}^d$ as $\operatorname{dist}(\boldsymbol{x}, S)$ and the orthogonal projection onto the set S is denoted as P_S. Finally, we denote the normal cone of a closed set S at a point $\boldsymbol{x} \in \mathbb{R}^d$ as $N(S, \boldsymbol{x})$ (as defined in Definition 1.23).

Chapter 1

Differential equations with inequalities: well-posedness via differential inclusions

This chapter sets up the mathematical framework that will be applied in Chapters 2 to 4. We introduce the theory of first-order differential inclusions, which arise when we solve differential equations subject to inequality constraints.

In physical contexts, non-overlap conditions between objects are a common source of inequality constraints. One would typically differentiate between plastic and elastic contact for objects in touch. Let's consider an (infinitely stiff) rubber ball which falls on the ground. We will observe very non-smooth behaviour at its impact: The velocity

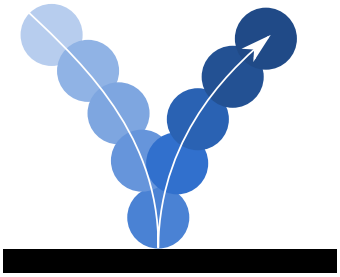

Figure 1. Example for the non-smooth dynamics of a bouncing ball. For second-order dynamics, such as $m\ddot{\boldsymbol{x}} = \boldsymbol{F} - \mu\dot{\boldsymbol{x}}$, the forces cannot be regular functions, but are instead distributions.

will change discontinuously, and even worse: the forces at contact are only generalised

functions (e.g. distributions or measures), see Figure 1. It is not surprising that analysing such *non-smooth mechanical systems* is very difficult.

Fortunately, we do not have to deal with such complicated and potentially ill-posed systems in this thesis. We only need first-order systems such as the *overdamped limit of Newton's equations*. An approximative example of overdamped dynamics would be a rubber ball inside water. Due to friction, the rubber ball would have essentially no acceleration and at contact with the ground, it would not jump up again but instead just stop (or slide), see Figure 2.

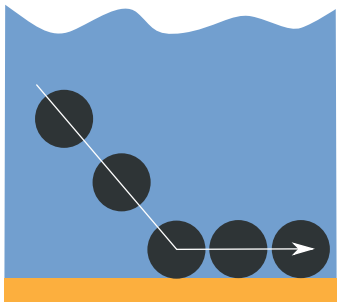

Figure 2. Example for overdamped dynamics, such as $\mu\dot{\boldsymbol{x}} = \boldsymbol{F}$, where collisions lead to a different behaviour which is mathematically less challenging that the second-order counterpart.

Our actual application is not that far from this idealised scenario since we will deal with cells in our body which are primarily embedded in water (and a heterogeneous environment). Therefore, we choose to use *overdamped Newton equations* to formulate our models. More specifically, we will use *agent-based models* with non-overlap conditions.

The theory of differential inclusions allows us to provide well-posedness results for our agent-based models and serves as a foundation for the numerical analysis in Chapter 2. As a first example, we could consider the idealised rubber ball inside water again. We could model the system with an energy W such as

$$W(x) = \begin{cases} mgx & \text{if } x \geq 0, \\ \infty & \text{if } x < 0. \end{cases}$$

where m denotes the mass, g the gravity constant and x the rubber ball's height above the ground. With a bit of non-smooth analysis, one can define the subderivative of such a function as

$$\partial W(x) = \begin{cases} \{mg\} & \text{if } x \geq 0, \\ (-\infty, 0] & \text{if } x = 0, \\ \emptyset & \text{if } x < 0. \end{cases}$$

If we then try to write down the overdamped Newton equation, we will notice that the right-hand sides are suddenly set-valued. This leads to a *differential inclusion*

$$\mu\dot{x} \in -\partial W(x)$$

with damping coefficient μ.

The primary aim of this chapter is to provide show well-posedness for such differential inclusions. The theory of differential inclusions is very diverse and still an active area of research. The used views have not yet converged to one all-containing approach, and there are many different ways to formulate the same systems. We will focus first on the most elementary cases which require some convexity assumptions. However, since our agent-based models do not satisfy the convexity requirements, we will also present results from [BV10] which apply to so-called *prox-regular* sets. Replacing the convexity requirements with prox-regularity still yields a useful well-posedness theory that applies to our models and serves as a foundation for the numerical analysis in Chapter 2.

In this chapter, we first recall the overdamped Newton equation in Section 1 and show how we can use overdamped Newton equations with inequalities for agent-based modelling. We then introduce the classical theory of first-order differential inclusions in Section 2. Section 3 present classical well-posedness results for the convex case. Finally, we consider in Section 4 the non-convex case and present well-posedness results which make the theory applicable to our agent-based models.

My contribution

All content from this chapter is well-known. The use of prox-regularity for agent-based models was proposed in [BV10].

1. Agent-based modelling with inequalities

Agent-based modelling is an umbrella term for many different approaches to model systems with many identical parts ('agents') which follow specific rules which are specified by agent-agent interactions and agent-environment interactions. The underlying idea is that simple individual rules for agents and their interaction might lead to emergent behaviour for a crowd of agents. Typical examples are pedestrian dynamics [BCD18; App+14] or traffic models [MKT18], but also within biology, the use of such models is prevalent.

In this thesis, we restrict ourselves to off-lattice models, meaning that the agents' positions are in continuous space (rather than fixed onto a lattice).

Alternatives to agent-based modelling are often continuity equations. Such models have the advantage that they are computationally more efficient when there are numerous agents. However, it is often difficult to derive the correct continuity equations for complicated interaction rules. Therefore, agents-based models are typically used when complex interaction rules might be essential for the observed behaviour. For a

comparison between different modelling methodologies in the context of cell migration, we refer to [FO22; BE20].

Our agent-based models are also physical systems in the form of the overdamped Newton equation. Therefore we will first recall the basics of overdamped mechanics and then define a toy model which serves as the primary example for developing the mathematical theory in this chapter.

1.1. Overdamped Newton equations in biology

First, we want to discuss how first-order equations arise in biological models. Most physical models rely on Newton's second law. For example, in this form

$$m\ddot{\boldsymbol{x}} = \boldsymbol{F} - \mu\dot{\boldsymbol{x}} = -\nabla_{\boldsymbol{x}} W - \mu\dot{\boldsymbol{x}}, \tag{1.1}$$

where $\boldsymbol{x} \in \mathbb{R}^d$ denotes the position, m is the mass, μ the damping coefficient and $\boldsymbol{F}$ denotes the forces which are the negative gradient of the potential energy W, Especially in biological models, the damping term deserves some attention. In cell biology, almost everything swims essentially in water and is surrounded by many other objects. Therefore, much kinetic energy dissipates into the environment, leading to cells' damped motion (i.e., there are no inertial effects).

We can easily estimate the time scale for which the system is overdamped. For simplicity, we consider a constant force $\boldsymbol{F}$ in (1.1) and we denote the velocity as $\boldsymbol{v} \coloneqq \dot{\boldsymbol{x}}$ which yields

$$\dot{\boldsymbol{v}} = \frac{\boldsymbol{F}}{m} - \frac{\mu}{m}\boldsymbol{v} \quad \Rightarrow \quad \boldsymbol{v}(t) = \left(\boldsymbol{v}^{\text{init}} - \frac{\boldsymbol{F}}{\mu}\right) e^{-\frac{\mu}{m}t} + \frac{\boldsymbol{F}}{\mu}$$

for the initial condition $\boldsymbol{v}(0) = \boldsymbol{v}^{\text{init}}$.

We see that

$$\boldsymbol{v} \to \frac{\boldsymbol{F}}{\mu} \quad \text{as } t \to \infty,$$

where the relevant time scale for the convergence is $\tau = \frac{m}{\mu}$.

Therefore, if we consider simulations on a time interval $[0, T]$ where $\frac{m}{\mu} \ll T$, then we obtain good approximations by solving the *overdamped Newton equation*

$$\mu\dot{\boldsymbol{x}} = \boldsymbol{F} = -\nabla_{\boldsymbol{x}} W.$$

Example 1.1 (Linear drag in biological fluids)**.** Within this thesis, we will deal with cells of radius around $R = 5\,\mu\text{m}$. Following the example from [Cle16, Sec. 6.7.1], we can estimate the amount of drag force using Stokes law. If we assume that cells are nearly-spherical objects with radius R, then the drag force is

$$\boldsymbol{F}^{\text{drag}} = 6\pi R\eta\boldsymbol{v},$$

where η is the macroscopic viscosity of the fluid. In the case of cytoplasm (which is the fluid surrounding cells), we might approximate the viscosity as $\eta = 10^{-1}\,\text{kg}\,\text{m}^{-1}\,\text{s}^{-1}$ which is 100 times larger than that of water [Cle16].

Taking the drag as the source for damping in the system, we obtain the damping parameters

$$\mu \approx 6\pi R\eta = 9.42 \times 10^{-3}\,\mathrm{g\,s^{-1}}.$$

To see how close this is to an overdamped motion, we use the estimate that typically, cells have a density of $1.05\,\mathrm{g\,L^{-1}}$, which is 1.05 times the density of water. This yields a mass approximation

$$m \approx 1.05\,\mathrm{g\,L^{-1}} \cdot \frac{4}{3}\pi R^3 = 0.55 \times 10^{-12}\,\mathrm{g}$$

Finally, the typical time scale is at least a few minutes up to a couple of days. Comparing the numbers, we get

$$\frac{m}{\mu} = 5.833 \times 10^{-11}\,\mathrm{s}.$$

This indicates that the motion of cells is in the overdamped regime and essentially without inertia. In terms of fluid dynamics, this shows that we deal with a very small Reynolds number.

In other terms, a cell which moves by self-propulsion will immediately stop once the self-propulsion stops. There is no free-swimming of cells at this scale.

This thesis mainly uses the overdamped Newtonian equation as our underlying physical law for all models.

1.2. Main example: Non-overlapping disk

We will now define an agent-based model that captures the models' mathematical difficulty in Chapters 3 and 4 but without their biological complexity. This model serves as our toy example in this chapter. The following example is inspired by [MV11].

Model 1.2 (Non-overlapping disks as a complementary problem)**.** We consider N disks with centers at the positions $\boldsymbol{\mathcal{X}} = (\boldsymbol{X}_1, \dots, \boldsymbol{X}_N) \in \mathbb{R}^{2N}$ and with radius $R > 0$. We will write $\boldsymbol{X}_i$ to refer to the ith position vector of $\boldsymbol{\mathcal{X}}$.

The disks are not allowed to overlap, which leads to the conditions

$$\delta_{ij}(\boldsymbol{\mathcal{X}}) \coloneqq \|\boldsymbol{X}_i - \boldsymbol{X}_j\| \geq 2R \quad \text{for } 1 \leq i < j \leq N \tag{1.2}$$

where $\delta_{ij}(\boldsymbol{\mathcal{X}})$ denotes the distance between the centers of the ith and the jth disk.

We will use a linear index to refer to all constraints for notational ease. Let us define $g_1, \dots, g_M : \mathbb{R}^{2N} \to \mathbb{R}$ for $M = \binom{N}{2}$ as

$$(g_1, \dots, g_M) \coloneqq (\delta_{12} - 2R, \delta_{13} - 2R, \dots, \delta_{(N-1),N} - 2R).$$

With this notation, (1.2) is equivalent to

$$g_k(\boldsymbol{\mathcal{X}}) \geq 0 \quad \text{for } 1 \leq k \leq M. \tag{1.3}$$

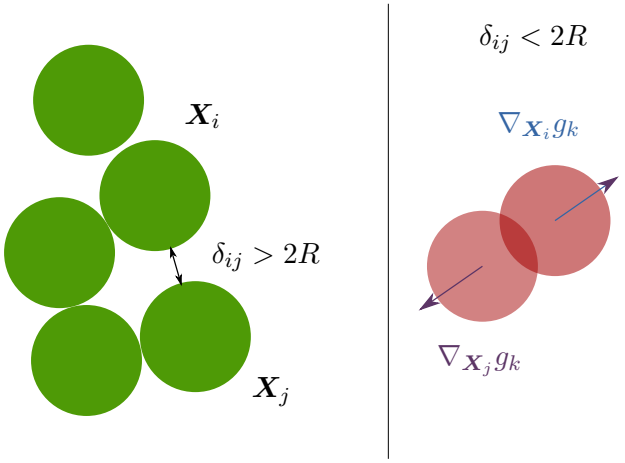

Figure 3. Sketch of the disk model and the distance functions. The right plot shows an infeasible configuration as the corresponding gradients.

The governing equations for our model are

$$\dot{\boldsymbol{X}}_i = \boldsymbol{F}_i(\boldsymbol{\mathcal{X}}) + \sum_{k=1}^{M} \lambda_k \nabla_{\boldsymbol{X}_i} g_k(\boldsymbol{\mathcal{X}}) \tag{1.4}$$

$$g_k(\boldsymbol{\mathcal{X}}) \geq 0, \quad \lambda_k \geq 0 \quad \text{and} \quad \lambda_k g_k(\boldsymbol{\mathcal{X}}) = 0 \tag{1.5}$$

for $1 \leq i \leq N$ and $1 \leq k \leq M$. The values $(\lambda_1(t), \ldots, \lambda_M(t))$ are the Lagrangian multipliers which from together with $\boldsymbol{\mathcal{X}}$ the unknowns of this differential equation.

The first equation (1.4) is the overdamped Newton law (with damping coefficient $\mu = 1$) and the second equation (1.5) are called the *complementary conditions* or Signorini conditions [LN04] which ensure that the disks are pushed into overlapping free conditions whenever two disks are in contact.

We will refer to (1.4) and (1.5) as the *non-overlapping disks model as a differential complementarity problem*.

The presented formulation is very common in contact mechanics and related fields. Lagrangian multipliers are a helpful starting point for many numerical methods, for example, to develop *augemented Lagrangian methods* [Wri06] where iterative methods compute the multipliers in each time-step.

1.3. Non-overlapping disks as differential inclusions

To motivate how differential inclusions occur, we can use subdifferentials to rephrase (1.4) and (1.5) as a gradient flow problem. In Section 2, we will provide precise definitions for the following informal derivation.

Let us consider we are given a set $S \subset \mathbb{R}^d$ and a function $\boldsymbol{F} : \mathbb{R}^d \to \mathbb{R}^d$ and we would like to find an equation of the type

$$\dot{\boldsymbol{x}} = \boldsymbol{F}(\boldsymbol{x}) + \text{'something to ensure } \boldsymbol{x} \in S\text{'}. \tag{1.6}$$

The question is how to define the extra terms which force $\boldsymbol{x}$ to stay in the feasible set.

One idea is to use the distance function between points to sets, which is

$$\operatorname{dist}(\boldsymbol{x}, S) := \inf_{\boldsymbol{y} \in S} \|\boldsymbol{x} - \boldsymbol{y}\|.$$

Using this function, we could define a potential energy which is zero inside S and increases very fast if $\boldsymbol{x}$ is far away from S, e.g.

$$W_n(\boldsymbol{x}) := n \operatorname{dist}(\boldsymbol{x}, S) \tag{1.7}$$

for any $n \geq 0$.

Our candidate equation would then be

$$\dot{\boldsymbol{x}} = \boldsymbol{F}(\boldsymbol{x}) - \nabla_{\boldsymbol{x}} W_n(\boldsymbol{x}) \tag{1.8}$$

which is probably already quite satisfying, but if $\boldsymbol{F}$ is large enough, it could push $\boldsymbol{x}$ into the unfeasible region.

To cure this, we could take the limit $n \to \infty$ which converges to the indicator function

$$W(\boldsymbol{x}) := \limsup_{n \to \infty} W_n(\boldsymbol{x}) = I_S(\boldsymbol{x}) = \begin{cases} \infty & \text{if } \boldsymbol{x} \notin S \\ 0 & \text{if } \boldsymbol{x} \in S. \end{cases}$$

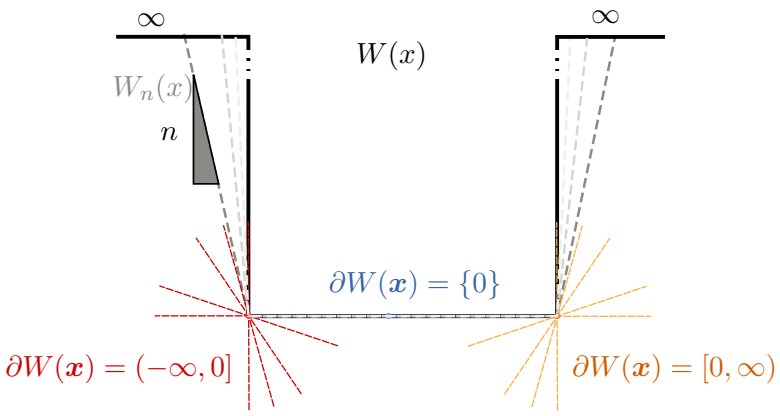

Figure 4. Sketch of the indicator function for an interval and the corresponding subdifferentials. We can identify elements of the subdifferentials as lines (or hyperplanes) fitting below the graph of the function W.

Taking the classical gradient of W is impossible, but we could compute the *subdifferential* of $W : \mathbb{R}^d \to \mathbb{R} \cup \infty$. At a point $\boldsymbol{x} \in \mathbb{R}^d$, the subdifferential $\partial W(\boldsymbol{x})$ is characterised by

$$\boldsymbol{v} \in \partial W(\boldsymbol{x}) \quad \Leftrightarrow \quad W(\boldsymbol{y}) - W(\boldsymbol{x}) \geq \boldsymbol{v} \cdot (\boldsymbol{y} - \boldsymbol{x}) \quad \text{for all } \boldsymbol{y} \in \mathbb{R}^d. \tag{1.9}$$

At non-smooth points, $\partial W(\boldsymbol{x})$ might be an empty set or contain more than one element.

If we consider for example $S = [0, 1] \subset \mathbb{R}$, then we would obtain

$$\partial W(x) = \begin{cases} \{0\} & \text{if } x \in (0, 1) \\ \emptyset & \text{if } x < 0 \text{ or } x > 1 \\ (-\infty, 0] & \text{if } x = 0 \\ [0, \infty) & \text{if } x = 1. \end{cases}$$

See Figure 4 for an illustration of the subdifferentials.

Returning to our initial goal, we could now take the limit $n \to \infty$ in (1.8) and obtain

$$\dot{\boldsymbol{x}} \in \boldsymbol{F}(\boldsymbol{x}) - \partial W(\boldsymbol{x})$$

which now is a *differential inclusion* since the right-hand side is suddenly set-valued.

Surprisingly, this formulation is (under some assumptions) equivalent to a formulation as a differential complementarity system with Lagrangian multipliers [Bro+06].

The set $\partial W(\boldsymbol{x}) = \partial I_S(\boldsymbol{x})$ has also a geometric interpretation, recalling (1.7) we can intuitively see that $\partial W(\boldsymbol{x})$ is the set of all outward pointing normal vectors of S, e.g.

$$\partial W(\boldsymbol{x}) = \partial I_S(\boldsymbol{x}) = N(S, \boldsymbol{x})$$

where $N(S, \boldsymbol{x})$ denotes the normal cone of S at $\boldsymbol{x}$ (which we will define later).

With this informal derivation, we could reformulate the model of non-overlapping disks in the following form.

Model 1.3 (Non-overlapping disks as a differential inclusion)**.** In the setup of Model 1.2, we define the set of feasible points as

$$S \coloneqq \{\boldsymbol{\mathcal{X}} \in \mathbb{R}^{2N} \mid g_j(\boldsymbol{\mathcal{X}}) \geq 0 \text{ for all } 1 \leq j \leq M\}.$$

The corresponding differential inclusion reads

$$\dot{\boldsymbol{\mathcal{X}}} \in \boldsymbol{\mathcal{F}}(\boldsymbol{\mathcal{X}}) - N(S, \boldsymbol{\mathcal{X}}) \tag{1.10}$$

where $N(S, \boldsymbol{\mathcal{X}})$ denotes the normal cone of S at the point $\boldsymbol{\mathcal{X}}$.

For future reference, we will also define the sets of pairwise non-overlap as

$$S_j \coloneqq \{\boldsymbol{\mathcal{X}} \in \mathbb{R}^{2N} \mid g_j(\boldsymbol{\mathcal{X}}) \geq 0\}$$

for $1 \leq j \leq M$.

The main results from this chapter are to show well-posedness (existence, uniqueness and continuous dependency on initial data) for (1.10). Moreover, we will see that this model is equivalent to (1.4) and (1.5).

2. Differential inclusions

A differential inclusion is a differential equation where the right-hand side is set-valued. In the following we will provide an introduction to differential inclusions, however, for details we refer to [Fil88; AB08]. We use the notation of multifunctions to make this rigorous.

Definition 1.4 (Multifunction)**.** A multi-function in $\mathbb{R}^d$ is a map

$$\mathcal{F} : \mathbb{R}^d \to 2^{\mathbb{R}^d}$$

where $2^{\mathbb{R}^d}$ denotes the set of all subsets of $\mathbb{R}^d$. We denote a multifunction in $\mathbb{R}^d$ as

$$\mathcal{F} : \mathbb{R}^d \rightrightarrows \mathbb{R}^d.$$

Definition 1.5 (Differential inclusion in $\mathbb{R}^d$)**.** A differential inclusion in $\mathbb{R}^d$ is characterised by a multi-function $\mathcal{F} : \mathbb{R}^d \rightrightarrows \mathbb{R}^d$, an initial $\boldsymbol{x}^{\text{init}} \in \mathbb{R}^d$ and it is expressed as

$$\dot{\boldsymbol{x}} \in \mathcal{F}(\boldsymbol{x}), \quad \boldsymbol{x}(0) = \boldsymbol{x}^{\text{init}}. \tag{1.11}$$

Solutions of differential inclusions might fail to be differentiable, instead we will use the space of absolutely continuous functions.

Definition 1.6 (Absolute continuity)**.** A function $\boldsymbol{f} : [a, b] \to \mathbb{R}^d$ is absolutely continuous if for every $\varepsilon > 0$ there exists a $\delta > 0$ such that for any finite sequences of disjoint intervals $(x_k, y_k) \subset [a, b]$ we have

$$\text{if} \quad \sum_k |y_k - x_k| < \delta, \quad \text{then} \quad \sum_k \|\boldsymbol{f}(y_k) - \boldsymbol{f}(x_k)\| < \varepsilon.$$

We denote the space of absolutely continuous functions as $AC([a, b], \mathbb{R}^d)$.

The following lemma gives a more helpful characterisation of absolute continuity.

Lemma 1.7 (Alternative definition of absolute continuity, [Cla13])**.**
A function $\boldsymbol{f} : [a, b] \to \mathbb{R}^d$ is absolutely continuous if and only if there exists a Lebesgue integrable function $\boldsymbol{g} : [a, b] \to \mathbb{R}^d$ such that

$$\boldsymbol{f}(x) = \boldsymbol{f}(a) + \int_a^x \boldsymbol{g}(t)\,\mathrm{d}t$$

for all $x \in [a, b]$.

Lemma 1.7 implies in particular that for almost every $x \in [a, b]$ the derivative $f'(x)$ exists, which is important for the solution concept of differential inclusions.

Definition 1.8 (Solution of differential inclusions)**.** For $T > 0$ fixed, we say that that $\boldsymbol{x} \in AC([0,T], \mathbb{R}^d)$ is a solution of the differential inclusion (1.11) if it satisfies

$$\begin{cases} \dot{\boldsymbol{x}}(t) \in \mathcal{F}(\boldsymbol{x}(t)) & \text{for a.e. } t \in [0,T], \\ \boldsymbol{x}(0) = \boldsymbol{x}^{\text{init}}. \end{cases} \tag{1.12}$$

Example 1.9 (Step multi-function)**.** Differential inclusions also arise as a way to integrate discontinuous differential equations. For example, we could consider the ODE

$$\dot{x} = -\text{sign}(x)$$

where sign is the sign function with the convention $\text{sign}(0) = 0$. This equation has no classical solutions. However, we could consider the following differential inclusion instead

$$\dot{x} \in \begin{cases} -1 & \text{if } x > 0 \\ [-1,1] & \text{if } x = 0 \\ 1 & \text{if } x < 0 \end{cases} \tag{1.13}$$

with $x(0) = c > 0$

It turns out that the unique solution is $x(t) = \max(c - t, 0)$.

This solution fails to be in $C^1([0,T], \mathbb{R})$ since the derivative does not exist at $t = c$. However, the derivative exists almost everywhere, and for $t \neq c$ is equal to

$$\dot{x}(t) = -\mathbb{1}_{\{t<c\}}(t)$$

where $\mathbb{1}_A$ denotes the indicator function which is 1 over A and zero otherwise. The existence of an almost everywhere defined derivative proves that x is absolutely continuous by Lemma 1.7.

2.1. Well-posedness

There are several ways to show well-posedness for differential inclusions. With well-posedness, we refer to existence, uniqueness and continuous dependency on initial data.

The following continuity concept for multi-functions is needed to state the existence theorem.

Definition 1.10 (Upper semicontinuity of multi-functions)**.** A multi-function $\mathcal{F} : \mathbb{R}^d \rightrightarrows \mathbb{R}^d$ is *upper semi continuous* in $\boldsymbol{x} \in \mathbb{R}^d$ if for all $\varepsilon > 0$ there exists a $\delta > 0$ such that

$$\text{if } \|\boldsymbol{x} - \boldsymbol{y}\| < \delta, \quad \text{then} \quad \mathcal{F}(\boldsymbol{y}) \subseteq \mathcal{F}(\boldsymbol{x}) + B_\varepsilon$$

where $B_\varepsilon \subset \mathbb{R}^d$ denotes the open ball with radius ε and the sum of sets denotes the Minkowsky addition $A + B \coloneqq \{a + b \mid a \in A, b \in B\}$.

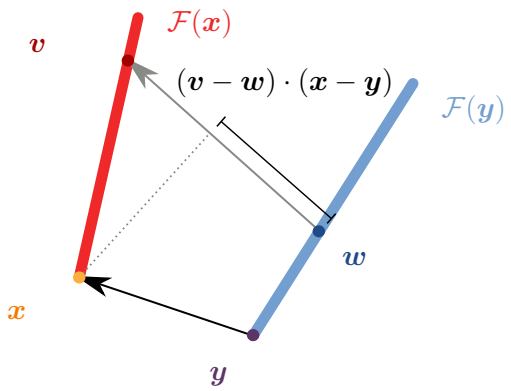

Figure 5. Sketch of the vectors involved for the definition of one-sided Lipschitz continuity. Here, the red and blue lines indicate the sets $\mathcal{F}(\boldsymbol{x})$ and $\mathcal{F}(\boldsymbol{y})$. In this example, the scalar product between $\boldsymbol{x}-\boldsymbol{y}$ and $\boldsymbol{v}-\boldsymbol{w}$ is positive, but in general, it could also be negative.

Theorem 1.11 (Existence of solutions, see [AB08, Lemma 2.13])**.** *Let $\mathcal{F}:\mathbb{R}^d \rightrightarrows \mathbb{R}^d$ be an upper semi continuous multi-function such that $\mathcal{F}(\boldsymbol{x}_0)$ is non-empty, closed and convex for all $\boldsymbol{x}_0 \in \mathbb{R}^d$ and let $\mathcal{F}$ be of at most linear growth, i.e. for some constant $M_{\mathcal{F}} > 0$ we have*

$$\|\boldsymbol{y}\| \leq M_{\mathcal{F}}(1+\|\boldsymbol{x}_0\|) \quad \text{for all } \boldsymbol{x}_0 \in \mathbb{R}^d, \boldsymbol{y} \in \mathcal{F}(\boldsymbol{x}_0).$$

Then, for each $\boldsymbol{x}^{\text{init}} \in \mathbb{R}^d$ there exists a solution $\boldsymbol{x} \in AC([0,T],\mathbb{R}^d)$ which solves the differential inclusion

$$\dot{\boldsymbol{x}} \in \mathcal{F}(\boldsymbol{x}), \quad \boldsymbol{x}(0) = \boldsymbol{x}^{\text{init}}.$$

The previous theorem does not assert uniqueness. One general property which ensures uniqueness is *one-sided Lipschitz continuity*.

Definition 1.12 (One-sided Lipschitz continuity)**.** A multi-function $\mathcal{F}:\mathbb{R}^d \rightrightarrows \mathbb{R}^d$ is called *one-sided L-Lipschitz continuous* if there exists a constant $L \in \mathbb{R}$ such that for all $\boldsymbol{x},\boldsymbol{y} \in \mathbb{R}^d$

$$(\boldsymbol{v}-\boldsymbol{w})\cdot(\boldsymbol{x}-\boldsymbol{y}) \leq L\|\boldsymbol{x}-\boldsymbol{y}\|^2 \quad \text{for all } \boldsymbol{v} \in \mathcal{F}(\boldsymbol{x}), \boldsymbol{w} \in \mathcal{F}(\boldsymbol{y}). \tag{1.14}$$

We note that negative Lipschitz constants are explicitly allowed in Definition 1.12. We will later deal with situations where negative Lipschitz constants occur.

Theorem 1.13 (Uniqueness [AB08, Lemma 2.31])**.** *Let $\mathcal{F}:\mathbb{R}^d \rightrightarrows \mathbb{R}^d$ be a one-sided L-Lipschitz continuous multi-function. Then if $\boldsymbol{x},\boldsymbol{y} \in AC([0,T],\mathbb{R}^d)$ are solutions of the differential inclusion (1.11) (with possibly different initial values), then*

$$\|\boldsymbol{x}(t)-\boldsymbol{y}(t)\| \leq \exp(Lt)\|\boldsymbol{x}(0)-\boldsymbol{y}(0)\|$$

for all $t \in [0,T]$.

In particular, if solutions exist for (1.11) then the solution is unique and depends continuously on the initial data.

Remark 1.14. If we consider the right-hand side from (1.13), which we might denote as $-\overline{\text{sign}}$ with the convention $-\overline{\text{sign}}(0) = [-1, 1]$, then we can show both upper semicontinuity and one-sided Lipschitz continuity.

As an example, we show both properties around $x = 0$:

- **Upper semicontinuity:** Follows trivial since $-\overline{\text{sign}}(y) \subseteq [-1, 1] = -\overline{\text{sign}}(0)$ holds for all $y \in \mathbb{R}$.
- **One-sided Lipschitz continuity:** For $y \in \mathbb{R}$ we consider two cases
  - If $y > 0$, let $v \in -\overline{\text{sign}}(x) = [-1, 1]$ and $w \in -\overline{\text{sign}}(y) = \{-1\}$, then we obtain
    $$(v - w)(x - y) = (v + 1)(0 - y) \leq 0 \leq 2(x - y)^2$$
    where we use $(v + 1) \geq 0$.
  - For $y < 0$ we obtain in the same way $(v - w)(x - y) \leq 0$.

Summarizing, this shows that Theorems 1.11 and 1.13 are applicable in Example 1.9.

Remark 1.15 (Monotone maps)**.** In Remark 1.14, we actually showed a stronger property for the $-\overline{\text{sign}}$ function, namely that it is a *monotone map*, which is nothing else than a one-sided L-Lipschitz continuous map with $L = 0$.

We note that $\overline{\text{sign}}$ would neither be monotone nor one-sided Lipschitz. Therefore, a multifunction $\mathcal{F} : \mathbb{R}^d \rightrightarrows \mathbb{R}^d$ might be one-sided Lipschitz continuous, but $-\mathcal{F}$ might not have the same property.

In the systems that we investigate in this thesis (e.g. Model 1.3), the multi-functions $\mathcal{F}$ considered will neither be upper semicontinuous nor one-sided Lipschitz continuous. In the next sections, we will develop the theory to show well-posedness also for systems like Model 1.3. The main theorems of this chapter (Theorem 1.31 and Lemma 1.32) generalise Theorem 1.11 and Theorem 1.13.

3. ODEs with inequality constratins: the convex case

A large class of differential inclusions are ordinary differential equations (ODEs) with inequality constraints. A famous class of such problems are Moreau's sweeping processes, where solutions have to stay within moving sets. For ODEs with inequalities, the geometry of the feasible set determines in which direction the velocities are corrected such that solutions stay feasible. Typically, the correction velocities have to be aligned with normal vectors of the feasible set.

Before we can define the differential inclusions which arise from inequality constraints, we have to define basic notations from convex analysis, such as the normal cone of a set and projections. The following definitions can be found in any textbook on convex analysis, for example [RW98; HL93; Cla13; BP12].

In the previous sections we have considered abstract multi-functions as the right hand side of differential inclusions. We will now restrict ourselves to situations where the right hand side is a of particular form.

3.1. Definition of the normal cone

In the following, we provide two different definitions for normal cones. The first definition is the classical characterisation for convex sets, after that, we define a more general notation of so-called proximal normal cones which are applicable also in non-convex setups.

We let $C \subseteq \mathbb{R}^d$ be a convex set, i.e., for each two points $\boldsymbol{x}, \boldsymbol{y} \in C$ we have

$$\lambda \boldsymbol{x} + (1-\lambda)\boldsymbol{y} \in C \quad \text{for all } \lambda \in (0,1).$$

Using the convexity, we can define the cone of all normal directions.

Definition 1.16 (Normal cone of convex sets)**.** Let C be a non-empty convex set. We define the normal cone as

$$N_C(\boldsymbol{x}) \coloneqq \{\boldsymbol{v} \in \mathbb{R}^d \mid \boldsymbol{v} \cdot (\boldsymbol{y} - \boldsymbol{x}) \leq 0 \text{ for all } \boldsymbol{y} \in C\}.$$

See Figure 6 for a sketch of normal cones in the convex case. We note that normal cones are in particular convex cones, which means that they are closed under vector addition and multiplication with positive scalars, i.e. for $\boldsymbol{v}, \boldsymbol{w} \in N_C(\boldsymbol{x})$ we also have $\alpha \boldsymbol{v} + \boldsymbol{w} \in N_C(\boldsymbol{x})$ for all $\alpha > 0$.

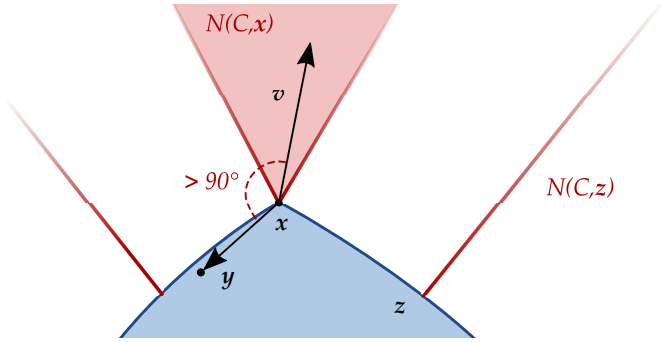

Figure 6. Example for normal cones of a convex set.

We note the following three cases which typically occur for normal cones of closed, convex sets C:

- If $\boldsymbol{x} \in C \setminus \partial C$ then the normal cone is a singleton $N_C(\boldsymbol{x}) = \{\boldsymbol{0}\}$.
- If $\boldsymbol{x} \notin C$ then $N_C(\boldsymbol{x}) = \emptyset$.
- For boundary points $\boldsymbol{x} \in \partial C$ the normal cone contains all outward pointing normal vectors.

Let us consider an ODE such as

$$\dot{\boldsymbol{x}} = \boldsymbol{F}(\boldsymbol{x})$$

where $\boldsymbol{F} : \mathbb{R}^d \to \mathbb{R}^d$ is a (single-valued) function. Normal cones are the canonical choice to extend ODEs with feasiblity conditions such as

$$\boldsymbol{x}(t) \in C \quad \text{for all } t > 0$$

where C is a closed, non-empty and convex set.

As motivated in Section 1.3, we could consider

$$\dot{\boldsymbol{x}}(t) \in \boldsymbol{F}(\boldsymbol{x}) - N_C(\boldsymbol{x}) \tag{1.15}$$

which is a differential inclusion with right hand side

$$\mathcal{F}(\boldsymbol{x}) \coloneqq \boldsymbol{F}(\boldsymbol{x}) - N_C(\boldsymbol{x}).$$

One property of convex sets is that the normal cones are monotone multi-functions. Definition 1.16 directly implies that for $\boldsymbol{x}, \boldsymbol{y} \in C$ we have

$$(\boldsymbol{v} - \boldsymbol{w}) \cdot (\boldsymbol{x} - \boldsymbol{y}) \leq 0 \quad \text{for all } \boldsymbol{v} \in N_C(\boldsymbol{x}), \boldsymbol{w} \in N_C(\boldsymbol{y}).$$

Therefore, in the case $\boldsymbol{F} = 0$, Theorem 1.13 implies uniqueness of solutions of (1.15).

With normal cones of convex sets we can already define a large class of systems which formed the development of differential inclusions.

Example 1.17 (Moreau's sweeping process)**.** The sweeping process was introduced by J. Moreau to model problems in plasticity theory [Mor77]. Nowadays it still provides an important class of differential inclusions.

The name is rather intuitive, imagine a moving convex set, i.e. $C : [0, T] \rightrightarrows \mathbb{R}^d$ such that $C(t) \subset \mathbb{R}^d$ such that $C(t)$ is closed, bounded and convex for each $t \in [0, T]$.

The aim of Moreau's sweeping process is to ensure that the position $\boldsymbol{x}(t)$ remains within $C(t)$. This can be realised with the differential inclusion

$$\dot{\boldsymbol{x}}(t) \in -N_{C(t)}(\boldsymbol{x}(t)) \quad \text{for a.e. } t \in [0, T], \tag{1.16}$$

$$\boldsymbol{x}(0) \in C(0). \tag{1.17}$$

We remark that one could consider this system as a non-smooth gradient flow problem such that

$$\boldsymbol{x}(t) \in -\partial I_{C(t)}$$

where ∂ denotes the subderivative of the indicator function

$$I_{C(t)} = \begin{cases} 0 & \text{if } \boldsymbol{x} \in C(t), \\ \infty & \text{if } \boldsymbol{x} \notin C(t). \end{cases}$$

Intuitively, the sweeping process is the minimal movement requires such that $\boldsymbol{x}$ stays within the moving set, e.g. $\boldsymbol{x}(t) \in C(t)$.

Moreau's sweeping process is well-posed, provided the dependency $t \mapsto C(t)$ is regular enough. First, we define the Hausdorff distance d_H between two sets $A, B \subseteq \mathbb{R}^d$ as

$$d_H(A,B) \coloneqq \max\{\sup_{\boldsymbol{a}\in A} \operatorname{dist}(\boldsymbol{a},B), \sup_{\boldsymbol{b}\in B} \operatorname{dist}(\boldsymbol{b},A)\}.$$

We say a map $t \mapsto C(t)$ is L-Lipschitz continuous with respect to the Hausdorff distance d_H, if

$$d_H(C(t),C(s)) \leq L|t-s| \quad \text{for all } t,s \in [0,T]. \tag{1.18}$$

With this notation, we can state the follow existence and uniqueness theorem.

Theorem 1.18 (Well-posedness of Moreau's sweeping process [AB08, Theorem 2.37])**.** *Let $T > 0$ and suppose $t \mapsto C(t)$ is L-Lipschitz continuous with respect to the Hausdorff distance and that $C(t)$ is non-empty, closed and convex for every $t \in [0,T]$. Then there is an unique solution $\boldsymbol{x} \in AC([0,T],\mathbb{R}^d)$ solving (1.16) and (1.17). Moreover, for almost every $t \in [0,T]$ we have $\|\dot{\boldsymbol{x}}(t)\| \leq L$.*

4. The non-convex case: uniform prox-regular sets

The theory developed so for is not applicable to the model of non-overlapping disks (Model 1.3). The key problem is that the set of non-overlapping disks (with radius $R > 0$)

$$\{(\boldsymbol{X}_1,\dots,\boldsymbol{X}_N) \in \mathbb{R}^{2N} \mid \|\boldsymbol{X}_i - \boldsymbol{X}_j\| \geq 2R \text{ for all } 1 \leq i < j \leq N\}$$

is not convex.

However, the problem of missing convexity was solved in [ET06; BV10; MV11] where the theory of differential inclusion was extended to so-called *uniformly prox-regular* sets.

To define prox-regularity, we quickly recall the definition of (orthogonal) projections.

Definition 1.19 (Projection)**.** For a closed set $A \subseteq \mathbb{R}^d$, we define the projection

$$\mathrm{P}_A(\boldsymbol{x}) \coloneqq \operatorname*{argmin}_{\boldsymbol{y}\in A} \|\boldsymbol{x}-\boldsymbol{y}\|. \tag{1.19}$$

In general, the projection is a multi-function $\mathrm{P}_A : \mathbb{R}^d \rightrightarrows \mathbb{R}^d$. However, when the projection is single-valued we will treat it like a regular function.

Definition 1.20 (Distance)**.** For any non-empty set $A \subseteq \mathbb{R}^d$ we define the distance between a point and the set A as

$$\operatorname{dist}(\boldsymbol{x},A) \coloneqq \inf_{\boldsymbol{y}\in A} \|\boldsymbol{x}-\boldsymbol{y}\|. \tag{1.20}$$

It is well-known that the projection onto convex, closed, non-empty sets C is unique, i.e. P_C is single valued. This property motivates the following definition of prox-regular sets, which share this property of convex sets at least in a local sense.

Definition 1.21 (Uniform prox-regularity)**.** A set $S \subset \mathbb{R}^d$ is uniformly prox-regular if there exists $\eta > 0$ such that on

$$S_\eta \coloneqq \{\boldsymbol{x} \in \mathbb{R}^d \mid \operatorname{dist}(\boldsymbol{x}, S) < \eta\} \tag{1.21}$$

the projection P_S is unique.

We will call S a η-prox-regular if it is uniformly prox-regular with constant η.

Intuitively, η-prox-regular sets are such that one can roll a sphere with radius η along the entire boundary without ever touching two points. An example for prox-regularity is shown in Figure 7.

For properties of prox-regular sets, we refer to [Wei+17b; ANT17] or the upcoming book [Thi22].

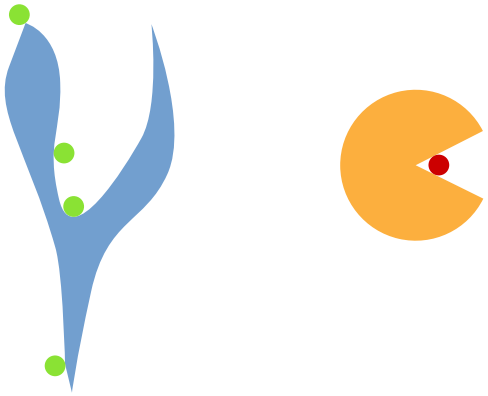

uniformly prox-regular not prox-regular

Figure 7. Left: Example for a non-convex but uniformly prox-regular set. Here the rolling ball condition is visualised with the green disks. **Right:** The Pacman-like set is not uniformly prox-regular since for points in the middle of the mouth (like the center of the red disk) the projection is not unique.

The following result ensures that the set of non-overlapping disks is indeed uniformly prox-regular.

Proposition 1.22 ([Ven11, Prop. 4.5])**.** *For $R > 0$ and $d, N \in \mathbb{N}$, the set*

$$S = \{(\boldsymbol{X}_1, \dots, \boldsymbol{X}_N) \in \mathbb{R}^{dN} \mid \|\boldsymbol{X}_i - \boldsymbol{X}_j\| \geq 2R \quad \textit{for all } 1 \leq i < j \leq N\}$$

is η-proxy-regular with constant

$$\eta = \frac{R}{6N}\left(\frac{1}{3}\sin\left(\frac{2\pi}{N}\right)\right)^d.$$

We note that the proof of Proposition 1.22 is not trivial, since it relies on complicated case distinctions between different ways how spheres can overlap.

4.1. Proximal normal cones

The definition of normal vectors for convex sets does not apply for prox-regular sets. Instead, we use the notation of proximal normal vectors.

Definition 1.23 (Proximal normal cone)**.** Let $A \subset \mathbb{R}^d$ be a closed set. A vector $\boldsymbol{n} \in \mathbb{R}^d$ is called a proximal normal vector of A at $\boldsymbol{x}$ if for some $\alpha > 0$ we have

$$\boldsymbol{x} \in \mathrm{P}_A(\boldsymbol{x} + \alpha \boldsymbol{n}) \tag{1.22}$$

We define the set of proximal normal vectors as

$$N(A, \boldsymbol{x}) := \{\boldsymbol{n} \in \mathbb{R}^d \mid \boldsymbol{x} \in \mathrm{P}_S(\boldsymbol{x} + \alpha \boldsymbol{n}) \text{ for some } \alpha > 0\}.$$

We note that for closed, convex sets C, both definitions of normal vectors are equivalent, i.e. we have $N_C(\boldsymbol{x}) = N(C, \boldsymbol{x})$ for all $\boldsymbol{x} \in \mathbb{R}^d$. However, Figure 8 shows an example of a proximal normal vector which is not a normal vector in the sense of the convex definition for normal cones (Definition 1.16).

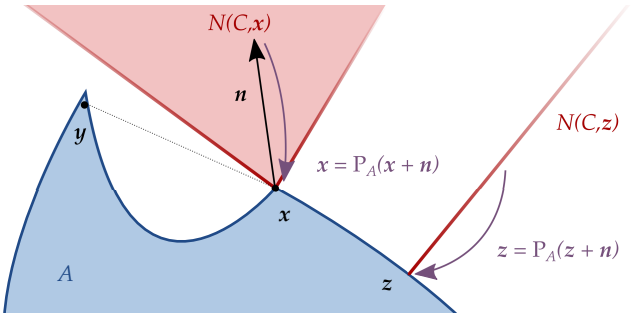

Figure 8. Example of proximal normal cones for a non-convex set. Notice that $\boldsymbol{n}$ would not be a normal vector according to Definition 1.16 since $\boldsymbol{n} \cdot (\boldsymbol{y} - \boldsymbol{x}) > 0$. However, Definition 1.23 ensures that $N(A, \boldsymbol{x})$ depends only on the local shape of the set A around $\boldsymbol{x}$.

In the following, we will sometimes deal with points $\boldsymbol{x}, \boldsymbol{y} \in \mathbb{R}^d$ such that the difference $\boldsymbol{y} - \boldsymbol{x}$ is a normal vector. For such cases, the Definition 1.23 implies:

$$\boldsymbol{x} = \mathrm{P}_S(\boldsymbol{y}) \quad \Leftrightarrow \quad \mathrm{P}_S(\boldsymbol{x} + (\boldsymbol{y} - \boldsymbol{x})) = \boldsymbol{x} \quad \Rightarrow \quad \boldsymbol{y} - \boldsymbol{x} \in N(S, \boldsymbol{x}). \tag{1.23}$$

With the notation of proximal normal cones, we can generalise (1.15) to prox-regular sets. This leads to the following differential inclusion

$$\dot{\boldsymbol{x}} \in \boldsymbol{F}(\boldsymbol{x}) - N(S, \boldsymbol{x}), \tag{1.24}$$

$$\boldsymbol{x}(0) = \boldsymbol{x}^{\mathrm{init}}, \tag{1.25}$$

where $S \subset \mathbb{R}^d$ is uniformly prox-regular, $\boldsymbol{F} : \mathbb{R}^d \to \mathbb{R}^d$ is a function and $\boldsymbol{x}^{\mathrm{init}} \in S$ is the initial state.

4.2. Relation to nonlinear differential complementarity problems

For modelling and numerics, it is more common to use complementarity problems to add inequality constraints to differential equations.

If the feasible sets is described by inequality constraint functions $\boldsymbol{g} = (g_1, \dots, g_M)$ such that

$$\boldsymbol{x} \in S \quad \Leftrightarrow \quad g_\ell(\boldsymbol{x}) \geq 0 \quad \text{for all } 1 \leq l \leq M,$$

then the corresponding differential complementarity problem reads

$$\dot{\boldsymbol{x}} = \boldsymbol{F}(\boldsymbol{x}) + \sum_{j=1}^{M} \lambda_j \nabla_{\boldsymbol{x}} g_j(\boldsymbol{x}) \tag{1.26}$$

$$g_\ell(\boldsymbol{x}) \geq 0, \quad \lambda_\ell \geq 0, \quad \lambda_\ell g_\ell(\boldsymbol{x}) = 0 \quad \text{for all } 1 \leq \ell \leq M, \tag{1.27}$$

where $\lambda_1, \dots, \lambda_M$ are the Lagrangian multipliers.

For the equivalence between differential inclusions and complementarity systems we need that the terms $\sum_j \lambda_j \, \nabla_{\boldsymbol{x}} \, g_j(\boldsymbol{x})$ are equivalent to all proximal normals.

Definition 1.24 (Linear normal cone)**.** For continuously differentiable constraint functions $g_1, \dots, g_M : \mathbb{R}^d \to \mathbb{R}$, we define for $\boldsymbol{x} \in \mathbb{R}^d$ the linearised normal cone as

$$N^{\boldsymbol{g}}(\boldsymbol{x}) \coloneqq \left\{ -\sum_{j=1}^{M} \lambda_j \nabla_{\boldsymbol{x}} g_j(\boldsymbol{x}) \mid g_j(\boldsymbol{x}) \geq 0, \quad \lambda_j \geq 0, \quad \lambda_j g_j(\boldsymbol{x}) = 0 \quad \text{for all } 1 \leq j \leq M \right\}.$$

In our context, the *basic constraint qualification condition* [HL93, Chapter VII, Section 2.2] is the equivalence of the normal cones, i.e., $N(S, \boldsymbol{x}) = N^{\boldsymbol{g}}(\boldsymbol{x})$. The constraint qualification is essential to show the equivalence between (1.24) and (1.25) and (1.26) and (1.27).

In the case of the model for non-overlapping disks Model 1.2, the following result ensures the constraint qualification condition.

Theorem 1.25 ([Ven11, Proposition 2.8])**.** *For S as defined in Model 1.3 and $\boldsymbol{g} = (g_1, \dots, g_M)$ as defined in Model 1.2, we have*

$$N(S, \boldsymbol{x}) = N^{\boldsymbol{g}}(\boldsymbol{x}) \quad \textit{for all } \boldsymbol{x} \in \mathbb{R}^{2N}.$$

Moreover, if we define

$$S_j \coloneqq \{\boldsymbol{\mathcal{X}} \in \mathbb{R}^{2N} \mid g_j(\boldsymbol{\mathcal{X}}) \geq 0\},$$

then we obtain

$$N(S, \boldsymbol{x}) = \sum_{j=1}^{M} N(S_j, \boldsymbol{x}) \quad \textit{for all } \boldsymbol{x} \in \mathbb{R}^{2N}.$$

For general results on the equivalence between differential inclusions and complementarity systems, we refer to [Bro+06]. The equivalence in the uniformly prox-regular case is shown in [ANT17, Section 9.2].

4.3. Hypomonotonicity

We saw in Theorem 1.13 that solutions of $\dot{\boldsymbol{x}} \in \mathcal{F}(\boldsymbol{x})$ are unique, if $\mathcal{F}$ is one-sided semicontinuous. Unfortunately, the map $\boldsymbol{x} \mapsto \boldsymbol{F}(\boldsymbol{x}) - N(S, \boldsymbol{x})$ is not one-sided semicontinuous, however, we obtain a related property for proximal normal cones.

Let us first consider the case $\boldsymbol{F} = 0$. A key property of normal cones of η-prox-regular sets is that the map

$$\boldsymbol{x} \mapsto -N(S, \boldsymbol{x})$$

is *hypomonotone*, i.e.

$$-(\boldsymbol{v} - \boldsymbol{w}) \cdot (\boldsymbol{x} - \boldsymbol{y}) \leq \frac{\|\boldsymbol{v}\| + \|\boldsymbol{w}\|}{2\eta} \|\boldsymbol{x} - \boldsymbol{y}\|^2 \tag{1.28}$$

for all $\boldsymbol{x}, \boldsymbol{y} \in S$ and for all $\boldsymbol{v} \in N(S, \boldsymbol{x})$, $\boldsymbol{w} \in N(S, \boldsymbol{y})$, see [PRT00, Proposition 2.8 and Corollary 2.6.].

Hypomonotonicity is related to one-sided Lipschitz continuity in the following sense. Denoting the unit ball as $B_1(\mathbf{0}) \subset \mathbb{R}^d$, then hypomonotonicity implies that

$$\boldsymbol{x} \mapsto -N(S, \boldsymbol{x}) \cap B_1(\mathbf{0})$$

is one-sided Lipschitz with constant $\frac{1}{\eta}$. In Lemma 1.32, we will see that hypomonotonicity is indeed sufficient to ensure uniqueness of solutions for (1.24) and (1.25).

4.4. Scalarly upper semicontinuity

Next, we generalise upper semicontinuity, which was the essential property in Theorem 1.11 to ensure existence of solutions.

In the following we will use support functions.

Definition 1.26 (Support function [RW98, Section 8.E])**.** For a set $A \subseteq \mathbb{R}^d$ we define the support function $\sigma(A, \cdot) : \mathbb{R}^d \to \mathbb{R} \cup \{\pm\infty\}$ as

$$\sigma(A, \boldsymbol{w}) \coloneqq \sup_{\boldsymbol{v} \in A} \boldsymbol{v} \cdot \boldsymbol{w}. \tag{1.29}$$

The support function characterises the closed half-spaces containing A [RW98], i.e. we have for any $\alpha > 0$ the relation

$$A \subseteq \{\boldsymbol{v} \mid \boldsymbol{v} \cdot \boldsymbol{w} \leq \alpha\} \quad \Leftrightarrow \quad \sigma(A, \boldsymbol{w}) \leq \alpha.$$

This is sketched in Figure 9.

Since taking a supremum over a larger set will always increase the value, we obtain

$$A \subseteq B \quad \Leftrightarrow \quad \sigma(A, \boldsymbol{v}) \leq \sigma(B, \boldsymbol{v}) \quad \text{for all } \boldsymbol{v} \in \mathbb{R}^d. \tag{1.30}$$

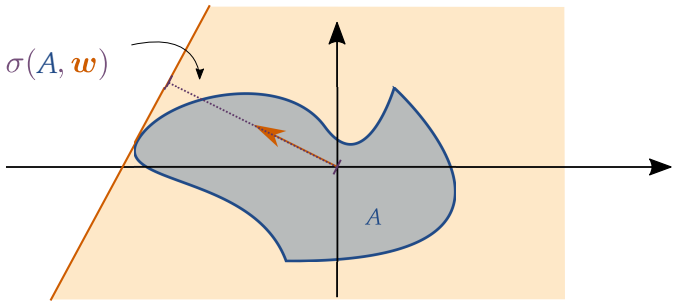

Figure 9. Sketch of the support function and the relation to half-spaces containing A.

Moreover, for any closed sets $A, B \subset \mathbb{R}^d$ we have [RW98, Theorem 8.24]

$$\sigma\left(A + B, \boldsymbol{v}\right) = \sigma\left(A, \boldsymbol{v}\right) + \sigma\left(B, \boldsymbol{v}\right) \quad \text{for all } \boldsymbol{v} \in \mathbb{R}^d. \tag{1.31}$$

Using the support function, we can define the following property for multi-functions.

Definition 1.27 (Scalarly upper semicontinuity, cp. [ET06, Sec. 2.1])**.** A multi-function $\mathcal{F} : \mathbb{R}^d \rightrightarrows \mathbb{R}^d$ is *scalarly upper semicontinuous* if for any $\boldsymbol{v} \in \mathbb{R}^d$,

$$\boldsymbol{x} \mapsto \sigma\left(\mathcal{F}(\boldsymbol{x}), \boldsymbol{v}\right) \tag{1.32}$$

is upper semicontinuous. Explicitly, we require that

$$\limsup_{\boldsymbol{y} \to \boldsymbol{x}} \sigma(\mathcal{F}(\boldsymbol{y}), \boldsymbol{v}) \leq \sigma(\mathcal{F}(\boldsymbol{x}), \boldsymbol{v}) \tag{1.33}$$

holds for all $\boldsymbol{x} \in \mathbb{R}^d$ and all $\boldsymbol{v} \in \mathbb{R}^d$.

We recall that a (single-valued) function $f : \mathbb{R}^d \to \mathbb{R} \cup \{\pm\infty\}$ is upper semicontinuous at $\boldsymbol{x}_0$ if it satisfies Definition 1.10, which simplifies in the single-valued case to the condition

$$\limsup_{\boldsymbol{x} \to \boldsymbol{x}_0} f(\boldsymbol{x}) \leq f(\boldsymbol{x}_0)$$

which yields (1.33) in the context of Definition 1.27.

The following proposition shows that for uniformly prox-regular sets S the map $\boldsymbol{x} \mapsto -N(S, \boldsymbol{x}) \cap B_1(\mathbf{0})$ is scalarly upper semicontinuous.

Proposition 1.28 ([ANT17, Proposition 3.4 (ii)])**.** *Let S be η-prox-regular and $\boldsymbol{x} \in S$, then*

$$\limsup_{\boldsymbol{x}_n \to \boldsymbol{x}} \sigma\left(-N(S, \boldsymbol{x}_n) \cap B_1(\mathbf{0}), \boldsymbol{w}\right) \leq \sigma\left(-N(S, \boldsymbol{x}) \cap B_1(\mathbf{0}), \boldsymbol{w}\right) \tag{1.34}$$

for all $\boldsymbol{w} \in \mathbb{R}^d$. In particular, $\boldsymbol{x} \mapsto -N(S, \boldsymbol{x}) \cap B_1(\mathbf{0})$ is scalarly upper semicontinuous.

Remark 1.29 (Relation to subdifferentials)**.** We note that for uniformly prox-regular sets S one has the relation

$$N(S, \boldsymbol{x}) \cap B_1(\mathbf{0}) = \partial \mathrm{dist}(\boldsymbol{x}, S)$$

where ∂ denotes the proximal subdifferential with respect to $\boldsymbol{x}$. Moreover, different notations of subdifferentials coincide, such as the Clark subdifferential or the Mordukhovich limiting subdifferential, see [ANT17, Proposition 2.3].

The following corollary will be useful in Chapter 2, Section 3.

Corollary 1.30. *Let $S_1, \dots, S_k$ and $S = \bigcap_j S_j$ be defined as in Theorem 1.25.*

Then for sequences $(\boldsymbol{p}_j^{(n)})_{n\in\mathbb{N}}$ with $\boldsymbol{p}_j^{(n)} \in S_j$ and $\boldsymbol{p}_j^{(n)} \to \boldsymbol{x}$ as $n \to \infty$, we get

$$\limsup_{n\to\infty} \sigma\left(-\sum_j N(S_j, \boldsymbol{p}_j^{(n)}) \cap B_1(\mathbf{0}), \boldsymbol{w}\right) \leq \sigma\left(-N(S, \boldsymbol{x}) \cap B_1(\mathbf{0}), \boldsymbol{w}\right) \tag{1.35}$$

for all $\boldsymbol{w} \in \mathbb{R}^d$.

Proof. First we apply Proposition 1.28 for each $1 \leq j \leq M$, which yields

$$\limsup_{n\to\infty} \sigma(-N(S_j, \boldsymbol{p}_j^{(n)}) \cap B_1(\mathbf{0}), \boldsymbol{w}) \leq \sigma(-N(S_j, \boldsymbol{x}) \cap B_1(\mathbf{0}), \boldsymbol{w}).$$

Since $A \mapsto \sigma(A, \boldsymbol{w})$ is Minkowsky additive (1.31) and $\limsup$ is subadditiv we get

$$\begin{aligned}
&\limsup_n \sigma(-\sum_{j=1}^M N(S_j, \boldsymbol{p}_j^{(n)}) \cap B_1(\mathbf{0}), \boldsymbol{w}) \\
&\quad = \limsup_n \sum_{j=1}^M \sigma(-N(S_j, \boldsymbol{p}_j^{(n)}) \cap B_1(\mathbf{0}), \boldsymbol{w}) \\
&\quad \leq \sum_{j=1}^M \sigma(-N(S_j, \boldsymbol{x}) \cap B_1(\mathbf{0}), \boldsymbol{w}) \\
&\quad = \sigma(-\sum_{j=1}^M N(S_j, \boldsymbol{x}) \cap B_1(\mathbf{0}), \boldsymbol{w}).
\end{aligned}$$

Finally, Theorem 1.25 implies

$$-\sum_{j=1}^M N(S_j, \boldsymbol{x}) = -N(S, \boldsymbol{x}) \tag{1.36}$$

which yields the claim. □

4.5. Well-posedness on uniformly prox-regular sets

In this section we will present the proofs for existence and uniqueness of the differential inclusion

$$\dot{\boldsymbol{x}} - \boldsymbol{F}(\boldsymbol{x}) \in -N(S, \boldsymbol{x}), \tag{1.37}$$

$$\boldsymbol{x}(0) = \boldsymbol{x}^{\text{init}}. \tag{1.38}$$

Before we can state the well-posedness result, we have to collect a few assumptions.

- $S \subset \mathbb{R}^d$ is non-empty, closed and η-prox-regular.
- The forces $\boldsymbol{F} : \mathbb{R}^d \to \mathbb{R}^d$ are Lipschitz continuous, i.e., there exists a constant L_F such that for all $\boldsymbol{x}, \boldsymbol{y} \in \mathbb{R}^d$

$$\|\boldsymbol{F}(\boldsymbol{x}) - \boldsymbol{F}(\boldsymbol{y})\| \leq L_F \|\boldsymbol{x} - \boldsymbol{y}\|. \tag{A1}$$

- The forces grow at most linearly, i.e., there exists a constant M_F such that for all $\boldsymbol{x} \in \mathbb{R}^d$

$$\|\boldsymbol{F}(\boldsymbol{x})\| \leq M_F(1 + \|\boldsymbol{x}\|). \tag{A2}$$

  We note that Lipschitz continuity implies that the function grows at most linearly.

To prove existence of solutions, we show convergence of an iterative scheme. We use Moreau's catch-up scheme, which is defined (for $h > 0$) as

$$\boldsymbol{x}_{k+1} = P_S(\boldsymbol{x}_k + h\boldsymbol{F}(\boldsymbol{x}_k)). \tag{1.39}$$

See Figure 10 for a visualisation of the catch-up scheme. The catch-up scheme is the equivalent of the explicit Euler method for differential inclusion. Recalling (1.23), we see that (1.39) implies

$$\boldsymbol{x}_k - \boldsymbol{x}_{k+1} + h\boldsymbol{F}(\boldsymbol{x}_k) \in N(S, \boldsymbol{x}_{k+1})$$

which is a discrete variation of (1.37).

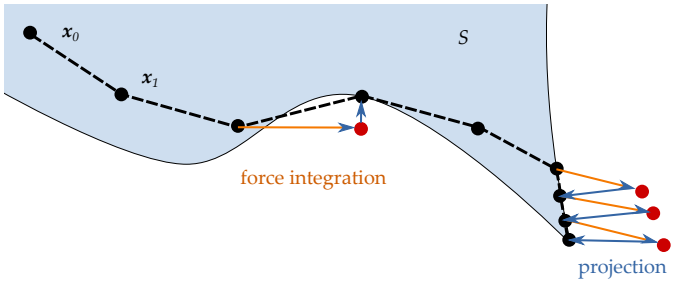

Figure 10. Example for Moreau's catch-up scheme. As long as the solution remains inside the set S, the method is equivalent to the explicit Euler method. However, each time the Euler method leaves the feasible set S, a projection onto P_S resolves the infeasibility.

Theorem 1.31 ([BV10, Theorem 1.2]). *Let $\boldsymbol{F} : \mathbb{R}^d \to \mathbb{R}^d$ be a Lipschitz function (A1) admitting at most a linear growth (A2) and $\eta > 0$ be a fixed real. Let S be nonempty, closed and η-prox-regular subset of $\mathbb{R}^d$. Then for all $\boldsymbol{x}^{\text{init}} \in S$ and any $T > 0$, the system*

$$\begin{cases} \dot{\boldsymbol{x}}(t) & \in \boldsymbol{F}(\boldsymbol{x}(t)) - N(S, \boldsymbol{x}(t)) \quad \text{for a.e. } t \in [0,T], \\ \boldsymbol{x}(0) & = \boldsymbol{x}^{\text{init}} \end{cases} \tag{1.40}$$

has an absolutely continuous solution $\boldsymbol{x} : [0,T] \to \mathbb{R}^d$.

Hypomonotonicity implies uniqueness of solutions.

Lemma 1.32 (cp. [BV10, Prop. 3.4]). *In the same setup as Theorem 1.31, assume that $\boldsymbol{x}, \boldsymbol{y} \in \mathrm{AC}([0,T], \mathbb{R}^d)$ are two solutions of (1.37) for initial conditions $\boldsymbol{x}(0) = \boldsymbol{x}^{\text{init}}$ and $\boldsymbol{y}(0) = \boldsymbol{y}^{\text{init}}$. Then, there exists a constant $a > 0$ such that for all $t \in [0,T]$*

$$\|\boldsymbol{x}(t) - \boldsymbol{y}(t)\| \leq a \|\boldsymbol{x}^{\text{init}} - \boldsymbol{y}^{\text{init}}\|. \tag{1.41}$$

Thanks to Proposition 1.22, the well-posedness theorems are directly applicable to the model of non-overlapping disks (Model 1.3).

Corollary 1.33. *Let S be defined as in Model 1.3 and assume $\boldsymbol{F} : \mathbb{R}^{2N} \to \mathbb{R}^{2N}$ is Lipschitz continuous. Then for all $\boldsymbol{\mathcal{X}}^{\text{init}} \in \mathbb{R}^{2N}$ and any $T > 0$, the system*

$$\begin{cases} \dot{\boldsymbol{\mathcal{X}}}(t) & \in \boldsymbol{F}(\boldsymbol{\mathcal{X}}(t)) - N(S, \boldsymbol{\mathcal{X}}(t)) \quad \text{for a.e. } t \in [0,T], \\ \boldsymbol{\mathcal{X}}(0) & = \boldsymbol{\mathcal{X}}^{\text{init}} \end{cases} \tag{1.42}$$

as a unique, absolutely continuous solution $\boldsymbol{\mathcal{X}} : [0,T] \to \mathbb{R}^{2N}$ which depends continuously on the initial data.

4.6. Proof of well-posedness

In this section we show the proof from [Ven11] with the only adaptation that we use the scalarly upper semicontinuity as in the main proofs in [ET06; ANT17]. We remark, that in the references the more general case of time-dependent feasible sets $S(t)$ is considered, since we only need the result for time-independent sets, the following proof is simpler.

4.6.1. Basic tools from functional analysis. For the existence proof, we need some tools from functional analysis, which we recall in the next section. For a general reference we refer to [Bre11; Cla13].

We denote the Lebesgue spaces as $L^p([0,T], \mathbb{R}^d)$ for $1 \leq p \leq \infty$ and we denote the corresponding norms as

$$\|\boldsymbol{x}\|_p \coloneqq \left(\int_0^T \|\boldsymbol{x}(s)\|^p \, \mathrm{d}s \right)^{\frac{1}{p}}$$

for $1 \leq p < \infty$ and $\boldsymbol{x} : [0,T] \to \mathbb{R}^d$. In the case $p = \infty$ we, have

$$\|\boldsymbol{x}\|_\infty \coloneqq \inf\{C \geq 0 \mid \|\boldsymbol{x}(t)\| \leq C \text{ for a.e. } t \in [0,T]\}.$$

We recall that for $1 \leq p \leq \infty$, the Lebesgue spaces $L^p([0,T],\mathbb{R}^d)$ are Banach spaces.

We denote the Sobolev spaces of m times differentiable functions as $W^{m,p}([0,T],\mathbb{R}^d)$ where p denotes the underlying Lebesgue space.

For a general (real) Banach space X with dual space X' and dual pairing $\langle\cdot,\cdot\rangle : X' \times X \to \mathbb{R}$, a sequence $(x_n)_{n\in\mathbb{N}} \subset X$ is weakly convergent to $x \in X$ if

$$\langle x', x_n\rangle \to \langle x', x\rangle \quad \text{for all } x' \in X'.$$

We then write $x_n \rightharpoonup x$ in X as $n \to \infty$.

A sequence $(x'_n)_{n\in\mathbb{N}} \subset X'$ is weak* convergent to $x' \in X'$, if

$$\langle x'_n, x\rangle \to \langle x', x\rangle \quad \text{for all } x \in X.$$

We denote weak* convergence as $x'_n \rightharpoonup^* x'$ in X' as $n \to \infty$.

In the existence proof, we will use that the dual space of $L^1([0,T],\mathbb{R}^d)$ is $L^\infty([0,T],\mathbb{R}^d)$ and that there exists an isometry $L^\infty([0,T],\mathbb{R}^d) \to L^1([0,T],\mathbb{R}^d)$.

Moreover, we need the following theorem which allows to construct a strongly convergence sequence as convex combinations of elements of a weakly convergence sequence.

Lemma 1.34 (Mazur's Lemma [Bre11, Corollary 3.8])**.** *Let $\boldsymbol{x}^{(n)} \rightharpoonup \boldsymbol{x}$ be a weakly convergent sequence in a Banach space X. Then, there exists a sequence $\boldsymbol{z}^{(n)}$ of convex combinations*

$$\boldsymbol{z}^{(n)} = \sum_{\ell=n}^{\infty} \lambda_\ell^{(n)} \boldsymbol{y}^{(\ell)} \quad \text{with } \lambda_\ell^{(n)} \in [0,1] \text{ and } \sum_{\ell=n}^{\infty} \lambda_\ell^{(n)} = 1$$

such that

$$\boldsymbol{z}^{(n)} \to \boldsymbol{x} \quad \text{in } X.$$

We also need the following Lemma which follows from the Banach-Alaoglu theorem.

Lemma 1.35 ([Bre11, Excersice 8.2])**.** *Let $(\boldsymbol{x}^{(n)})_n$ be a bounded sequence in $W^{1,\infty}([0,T],\mathbb{R}^d)$. Then there exists a subsequence $(\boldsymbol{x}^{(n_k)})_k$ and some $\boldsymbol{x} \in L^\infty([0,T],\mathbb{R}^d)$ such that*

$$\boldsymbol{x}^{(n_k)} \to \boldsymbol{x} \quad \text{in } L^\infty([0,T],\mathbb{R}^d)$$

and

$$\dot{\boldsymbol{x}}^{(n_k)} \rightharpoonup^* \dot{\boldsymbol{x}} \quad \text{in } L^\infty([0,T],\mathbb{R}^d).$$

Finally, we will use the following discrete variant of the Gronwall inequality.

Theorem 1.36 (Discrete Gronwall lemma for forward differences)**.** *Given a fixed integer $n > 0$, a sequence $(a_k)_{k\in 1,\dots,n}$ with $a_k \in \mathbb{R}^d$ and constants $A, B, T > 0$ such that*

$$\|a_{k+1} - a_k\| \leq \frac{T}{n}(A + B\|a_k\|) \quad \text{for all } 1 \leq k \leq n, \tag{1.43}$$

then,

$$a_k \leq \left(1 + B\frac{T}{n}\right)^n + \frac{1}{B}\left(\left(1 + B\frac{T}{n}\right)^n - 1\right) A \tag{1.44}$$

$$\leq \exp(BT) + A\frac{\exp(BT) - 1}{B} \tag{1.45}$$

for all integers $0 \leq k \leq n$.

4.6.2. The existence proof.

Proof of Theorem 1.31.

Step 1.

For a fixed time interval $[0, T]$, we define $h = \frac{T}{n}$ for some $n \geq 1$ and define the sequence $(\boldsymbol{x}_k)_{k\in\mathbb{N}}$ iteratively via

$$\boldsymbol{x}_{k+1} \in P_S(\boldsymbol{x}_k + h\boldsymbol{F}(\boldsymbol{x}_k)), \tag{1.46}$$

$$\boldsymbol{x}_0 = \boldsymbol{x}^{\text{init}}. \tag{1.47}$$

For cases with non-unique projection, we pick $\boldsymbol{x}_{k+1}$ randomly inside the set. We will see that for sufficiently large n all projections will be unique.

Now, we consider discrete time-steps are $t_k = kh$ and define the linear interpolation function $x^{(n)} \in C([0, T], \mathbb{R}^d)$ as

$$x^{(n)}(t) = \boldsymbol{x}_k + \frac{(t - t_k)}{h}(\boldsymbol{x}_{k+1} - \boldsymbol{x}_k) \quad \text{for } t \in [t_k, t_{k+1}). \tag{1.48}$$

Finally, we define the piecewise constant mapping $\boldsymbol{F}^{(n)} : [0, T] \to \mathbb{R}^d$ via

$$\boldsymbol{F}^{(n)}(t) = \boldsymbol{F}(\boldsymbol{x}_k) = \boldsymbol{F}(x^{(n)}(t_k)) \quad \text{for } t \in [t_k, t_{k+1}), 1 \leq k \leq n. \tag{1.49}$$

Step 2. Our next goal is to show that $\boldsymbol{x}^{(n)}$ and $\dot{\boldsymbol{x}}^{(n)}$ are bounded. First, we show that $\|\boldsymbol{x}^{(n)}\|_\infty < \infty$.

By definition, each $\boldsymbol{x}_k \in S$ since it is the projection onto this set and $\boldsymbol{x}^{\text{init}} \in S$ by assumption.

With $\boldsymbol{x}_{k+1} \in \mathrm{P}_S(\boldsymbol{x}_k)$, we get

$$\begin{aligned} \|\boldsymbol{x}_{k+1} - (\boldsymbol{x}_k + h\boldsymbol{F}(\boldsymbol{x}_k))\| &= \operatorname{dist}(\boldsymbol{x}_k + h\boldsymbol{F}(\boldsymbol{x}_k), S) \\ &\leq \operatorname{dist}(\boldsymbol{x}_k, S) + h\|\boldsymbol{F}(\boldsymbol{x}_k)\| \\ &\leq hM_F(1 + \|\boldsymbol{x}_k\|), \end{aligned} \tag{1.50}$$

where the last inequality follows from $\boldsymbol{x}_k \in S$ and M_F is the linear growth constant for $\boldsymbol{F}$ from (A2).

Hence,

$$\begin{aligned}\|\boldsymbol{x}_{k+1}-\boldsymbol{x}_k\| &\le \|\boldsymbol{x}_{k+1}-\boldsymbol{x}_k-h\boldsymbol{F}(\boldsymbol{x}_k)\|+\|h\boldsymbol{F}(\boldsymbol{x}_k)\|\\ &\le hM_F(1+\|\boldsymbol{x}_k\|)+\|h\boldsymbol{F}(\boldsymbol{x}_k))\|\\ &\le hM_F(1+\|\boldsymbol{x}_k\|)+hM_F(1+\|\boldsymbol{x}_k\|)\\ &\le 2hM_F(\|\boldsymbol{x}_k\|+1) \qquad (1.51)\end{aligned}$$

where we use

Applying the discrete Grownwall inequality (Theorem 1.36) yields

$$\|\boldsymbol{x}_k\| \le C_1 < \infty \quad \text{for all } 0 \le k \le n, \qquad (1.52)$$

for a constant C_1 which only depends on T and M_F.

Moreover, we obtain

$$\frac{\|\boldsymbol{x}_{k+1}-\boldsymbol{x}_k\|}{h} \le 2M_F(1+C_1) =: C_2 < \infty. \qquad (1.53)$$

This implies for the piecewise linear interpolant $\boldsymbol{x}^{(n)}$ that

$$\|\boldsymbol{x}^{(n)}\|_\infty \le C_1 \quad \text{and} \quad \|\dot{\boldsymbol{x}}^{(\mathrm{n})}\|_\infty \le C_2. \qquad (1.54)$$

We note that as a result, for sufficiently large n we get

$$\operatorname{dist}(\boldsymbol{x}_k+h\boldsymbol{F}(\boldsymbol{x}_k),S) \le hM_F(1+\|\boldsymbol{x}_k\|) \le hM_F(1+C_1) < \eta. \qquad (1.55)$$

Since the set S is η-prox-regular, this implies that the projections in (1.39) are unique for sufficiently large n.

Step 3. We notice that $\boldsymbol{x}^{(n)}$ satisfies the requirements of Lemma 1.35, which implies existence a function $\boldsymbol{x} \in L^\infty([0,T],\mathbb{R}^d)$ such that a subsequence of $(\boldsymbol{x}^{(n)})_n$ (which we denote without relabeling) satisfies

$$\dot{\boldsymbol{x}}(n) \rightharpoonup^* \dot{\boldsymbol{x}} \quad \text{in } L^\infty([0,T],\mathbb{R}^d), \qquad (1.56)$$

$$\boldsymbol{x}^{(n)} \to \boldsymbol{x} \quad \text{in } L^\infty([0,T],\mathbb{R}^d). \qquad (1.57)$$

As the uniform limit of continuous functions on a compact interval, we even obtain that the limit is continuous, i.e., $\boldsymbol{x} \in C([0,T],\mathbb{R}^d)$. Moreover, from the embedding $L^\infty([0,T],\mathbb{R}^d) \subseteq L^1([0,T],\mathbb{R}^d)$, we obtain that weak* convergence in L^∞ implies weak convergence in L^1, i.e.,

$$\dot{\boldsymbol{x}}^{(n)} \rightharpoonup \dot{\boldsymbol{x}} \quad \text{in } L^1([0,T],\mathbb{R}^d). \qquad (1.58)$$

Using the Lipschitz continuity of $\boldsymbol{F}$, one can show (see [Ven11, Lemma 3.6]) that

$$\boldsymbol{F}^{(n)} \rightharpoonup \boldsymbol{F}(\boldsymbol{x}(\cdot)) \quad \text{in } L^1([0,T],\mathbb{R}^d).$$

We now want to show that the limit $\boldsymbol{x}$ is a solution of the differential inclusion, i.e.,

$$\dot{\boldsymbol{x}} - \boldsymbol{F}(\boldsymbol{x}) \in -N(S,\boldsymbol{x}). \qquad (1.59)$$

Step 4. By Mazur's Lemma, there exists a sequence $\boldsymbol{z}^{(n)} \in L^1([0,T],\mathbb{R}^d)$ such that

$$\boldsymbol{z}^{(n)} \in \left\{ \sum_{\ell=n}^{\infty} \lambda_\ell \left(\dot{\boldsymbol{x}}^{(\ell)} - \boldsymbol{F}^{(\ell)} \right) \;|\; \lambda_\ell \in [0,1] \text{ s.t. } \sum_{\ell=n}^{\infty} \lambda_\ell = 1 \right\}, \tag{1.60}$$

and with

$$\boldsymbol{z}^{(n)} \to \dot{\boldsymbol{x}} - \boldsymbol{F}(\boldsymbol{x}(\cdot)) \quad \text{in } L^1([0,T],\mathbb{R}^d) \quad \text{as } n \to \infty. \tag{1.61}$$

We denote the limit as $\boldsymbol{z} \coloneqq \dot{\boldsymbol{x}} - \boldsymbol{F}(\boldsymbol{x}(\cdot))$.

By taking a subsequence (again, we skip relabeling), we obtain for a dense set $\mathcal{T} \subseteq [0,T]$ the pointwise convergence

$$\boldsymbol{z}^{(n)}(t) \to z(t) = \dot{\boldsymbol{x}}(t) - \boldsymbol{F}(\boldsymbol{x}(t)) \quad \text{for all } t \in \mathcal{T} \quad \text{as } n \to \infty. \tag{1.62}$$

Step 5. The next step is to analyse the normal cones which are related to the projection in each time step of the catch-up scheme. We assume that n is large enough such that all projections are unique.

In this case,

$$\boldsymbol{x}_{k+1} = P_S(\boldsymbol{x}_k + h\boldsymbol{F}(\boldsymbol{x}_k)) \tag{1.63}$$

with (1.23) we get the following inclusion

$$(\boldsymbol{x}_k + h\boldsymbol{F}(\boldsymbol{x}_k)) - \boldsymbol{x}_{k+1} \in N(S, \boldsymbol{x}_{k+1}). \tag{1.64}$$

which leads to

$$(\boldsymbol{x}_{k+1} - \boldsymbol{x}_k) - h\boldsymbol{F}(\boldsymbol{x}_k) \in -N(S, \boldsymbol{x}_{k+1}). \tag{1.65}$$

Dividing by h yields

$$\dot{\boldsymbol{x}}^{(n)}(t) - \boldsymbol{F}^{(n)}(t) \in -N(S, \boldsymbol{x}_{k+1}) \quad \text{for } t \in (t_k, t_{k+1}). \tag{1.66}$$

Let us denote the position of the normal cones as

$$\boldsymbol{p}^{(n)}(t) \coloneqq \boldsymbol{x}_{k+1} = \boldsymbol{x}^{(n)}(t_{k+1}) \quad \text{for } t \in [t_k, t_{k+1}),$$

which allows us to state (1.66) as

$$\dot{\boldsymbol{x}}^{(n)}(t) - \boldsymbol{F}^{(n)}(t) \in -N(S, \boldsymbol{p}^{(n)}) \quad \text{for } t \in [0,T].$$

Moreover, (A2) and (1.54) give

$$\|\dot{\boldsymbol{x}}^{(\mathrm{n})}(t) - \boldsymbol{F}^{(n)}(t)\| \leq C_3,$$

with $C_3 \coloneqq C_2 + M_F(1 + C_1)$. Therefore, we have

$$\dot{\boldsymbol{x}}^{(n)}(t) - \boldsymbol{F}^{(n)}(t) \in -N(S, \boldsymbol{p}^{(n)}) \cap B_{C_3}(\boldsymbol{0}) \quad \text{for } t \in [0,T]. \tag{1.67}$$

Step 6. We now use scalarly lower semicontinuity of $\boldsymbol{x} \mapsto -N(S,\boldsymbol{x}) \cap B_{C_3}(\boldsymbol{0})$ to obtain convergence of the right hand side of (1.67). Let us fix a value $t \in \mathcal{T}$ and we pick an

arbitrary test direction $\boldsymbol{w} \in \mathbb{R}^d$. Since $\boldsymbol{z}^{(n)}$ is a convex combination of $\boldsymbol{x}^{(n)} - \boldsymbol{F}^{(n)}$ we obtain

$$\boldsymbol{w} \cdot \boldsymbol{z}(t) \leq \limsup_n \boldsymbol{w} \cdot \boldsymbol{z}^{(n)}(t) \tag{1.68}$$

$$\leq \limsup_n \boldsymbol{w} \cdot (\boldsymbol{x}^{(n)}(t) - \boldsymbol{F}^{(n)}(t)) \tag{1.69}$$

$$\leq \limsup_n \sigma(-N(S, \boldsymbol{p}^{(n)}(t)) \cap B_{C_3}(\boldsymbol{0}), \boldsymbol{w}) \tag{1.70}$$

where σ denotes the support function (see Definition 1.26). The strong convergence of $\boldsymbol{x}^{(n)}$ in (1.57) implies $\boldsymbol{p}^{(n)}(t) \to \boldsymbol{x}(t)$. Thanks to Proposition 1.28, we conclude that

$$\limsup_n \sigma(-N(S, \boldsymbol{p}^{(n)}(t)) \cap B_{C_3}(\boldsymbol{0}), \boldsymbol{w}) \leq \sigma(-N(S, \boldsymbol{x}(t)) \cap B_{C_3}(\boldsymbol{0}), \boldsymbol{w}). \tag{1.71}$$

Finally, taking the supremum over all $\boldsymbol{w} \in \mathbb{R}^d$ we get

$$\sigma(\{\boldsymbol{z}(t)\}, \cdot) \leq \sigma(-N(S, \boldsymbol{x}(t)) \cap B_{C_3}(\boldsymbol{0}), \cdot) \tag{1.72}$$

which implies (see (1.30))

$$\boldsymbol{z}(t) \in -N(S, \boldsymbol{x}(t)). \tag{1.73}$$

Therefore, the limit function $\boldsymbol{x}$ satisfies

$$\dot{\boldsymbol{x}}(t) - \boldsymbol{F}(\boldsymbol{x}(t)) \in -N(S, \boldsymbol{x}(t)) \tag{1.74}$$

for a.e. $t \in [0, T]$. Which concludes the proof. □

4.6.3. Proof of uniqueness of solutions. In the following proof we see the role of hypomonotonicity as a tool to prove uniqueness of solutions. We note, that we skip in the end one technical step, as we are mainly interested in demonstrating the role of hypomonotonicity.

Proof of Lemma 1.32. Let $\boldsymbol{x}, \boldsymbol{y}$ be two solutions of the differential inclusion. Since the functions are absolutely continuous, there exists $\dot{\boldsymbol{x}}, \dot{\boldsymbol{y}}$ defined almost everywhere such that

$$\boldsymbol{x}(t) = \boldsymbol{x}(0) + \int_0^t \dot{\boldsymbol{x}}(s)\,\mathrm{d}s$$

$$\boldsymbol{y}(t) = \boldsymbol{y}(0) + \int_0^t (\dot{\boldsymbol{y}}(s) - \boldsymbol{F}(\boldsymbol{y}(s))) + \boldsymbol{F}(\boldsymbol{y}(s))\,\mathrm{d}s.$$

Moreover, if we denote

$$\boldsymbol{v}(t) \coloneqq \dot{\boldsymbol{x}}(t) - \boldsymbol{F}(\boldsymbol{x}(t)) \in -N_S(\boldsymbol{x}(t)) \tag{1.75}$$

$$\boldsymbol{w}(t) \coloneqq \dot{\boldsymbol{y}}(t) - \boldsymbol{F}(\boldsymbol{y}(t)) \in -N_S(\boldsymbol{y}(t)). \tag{1.76}$$

Next, we use the hypomonotonicity of the normal cones to compute

$$\begin{aligned}\frac{1}{2}\frac{\mathrm{d}}{\mathrm{d}t}\|\boldsymbol{x}(t)-\boldsymbol{y}(t)\|^2 &\leq (\dot{\boldsymbol{x}}(t)-\dot{\boldsymbol{y}}(t))\cdot(\boldsymbol{x}(t)-\boldsymbol{y}(t))\\ &\leq -(\boldsymbol{v}(t)-\boldsymbol{w}(t))\cdot(\boldsymbol{x}(t)-\boldsymbol{y}(t))+(\boldsymbol{F}(\boldsymbol{x}(t))-\boldsymbol{F}(\boldsymbol{y}(t)))\cdot(\boldsymbol{x}(t)-\boldsymbol{y}(t))\\ &\leq \frac{\|\boldsymbol{v}(t)\|+\|\boldsymbol{w}(t)\|}{2\eta}\|\boldsymbol{x}(t)-\boldsymbol{y}(t)\|^2+L_F\|\boldsymbol{x}(t)-\boldsymbol{y}(t)\|^2\end{aligned}$$

Then, Grownwall's lemma implies

$$\|\boldsymbol{x}(t)-\boldsymbol{y}(t)\| \leq \|\boldsymbol{x}^{\mathrm{init}}-\boldsymbol{y}^{\mathrm{init}}\|\int_0^t\left(L_F+\frac{\|\boldsymbol{v}(t)\|+\|\boldsymbol{w}(t)\|}{2\eta}\right)\mathrm{d}s. \tag{1.77}$$

For $t\in[0,T]$, one can show (see [ET05, Proof of Proposition 1]) that this integral is bounded which implies the claim. □

5. Conclusion

We have shown that the existing theory of differential inclusions applies to a large class of differential equations which are constrained to uniformly prox-regular sets. This covers, in particular, the model of non-overlapping disks (Model 1.2) and the presented theorems also cover our applications in Chapters 3 and 4.

There are many extensions of the theory presented here. Even on uniformly prox-regular sets, one can consider measure differential inclusions [ANT17], stochastic differential inclusions [BV11] or second-order differential inclusions [BV12]. Besides that, there are many equivalent reformulations which all have their own merits, as for example the recent survey [BT20] shows.

Chapter 2

First-order position based dynamics: a simple and fast method.

In this chapter, we introduce a variation of the *position based dynamics* (PBD) method [Mül+06]. The PBD method is popular in computer graphics since it is fast, simple and stable. It can solve contact problems in an authentic-looking way. However, it is not a jack of all trades, since it does not converge to exact solutions of the underlying second-order contact problems.

Position based dynamics sets itself apart from other numerical methods, by neither computing the contact forces (force based) nor the post-collision velocities (velocity based). Using a position based approach is a major relaxation of the precise contact rules but it simplifies the numerics as it improves the stability of simulations.

Until 2019, the method was often dismissed as not physically correct. But the most recent improvements showed that by fusing the projections with the force integration, one can simulate very stiff and typically challenging problems [Mac+19]. The authors of PBD even challenge everyone[1] to find a method which is can beat PBD in one of the following categories:

- accuracy,
- stability,
- speed or
- simplicity.

[1] See `https://matthias-research.github.io/pages/challenges/challenges.html`.

Especially for simulations with limited computational budget, the PBD method is an attractive choice.

While PBD is very popular in computer graphics, it seems that PBD has not yet arrived in the math community. This is no surprise since the method is not very rigorous at resolving elastic collisions (i.e. second-order contact mechanics), however, the PBD method is a good candidate to solve first-order differential inclusions, such as inequality constrained gradient flows or overdamped Newton equations.

In our application in Chapters 3 and 4, we will see that the PBD method leads to several magnitudes of runtime improvement and increases the stability of the simulations compared to the previously used method.

In this chapter, we will first give an overview of general numerical methods for differential inclusion, see Section 1. Then, Section 2 introduces the PBD method in its different variants. We then show consistency of the PBD method in Section 3 and provide numerical evidence for the convergence of the method in Section 4.

My contribution

The position based dynamics method was proposed for second-order systems [Mül+06] and refined in [Mac+19]. I adapted position based dynamics to first-order problems and performed numerical convergence tests. The analysis of theoretical aspects in Section 3 is new, but relies on ideas from [Ven11] and [ET06].

1. Numerical methods for differential inclusions

First, we will outline a few numerical methods for differential inclusions. However, this section is not aiming to give a complete overview, especially since many methods are very domain specific. For a recent overview of numerical methods for differential inclusions, we refer to [KS22].

There are three main classes of numerical methods for differential inclusions. Especially for systems with contact and collisions, a rigorous but also complex choice are *event-driven* methods. These methods compute the time of the next collision, solve the system till then and finally resolve the collisions one-by-one. For details on even-drive methods we refer to [LN04; AB08].

The second type are *time-stepping* methods, which allow several collisions to happen during one time step and try to resolve all collisions at once by solving linear complementary problems. A typical challenge for time-stepping methods is that objects do overlap in between calculations and if the unwanted overlap is too large it can lead to stability issues, forcing very small time-steps in many applications. Time-stepping methods are discussed in [Wri06; AB08; LN04; KS22]

Finally, one can use *smooth approximations* of the non-smooth dynamics. An example is the penalty method, where the overlap of colliding objects is allowed but penalised with a repulsive force. For strong enough penalty, the solutions converge to solutions of the

non-smooth system. For other examples of smoothing approaches, we refer to [LN04; VCK99].

Each of these three strategies has its own advantages and disadvantages. The particular application is often essential for the choice of the right numerical method. The most rigorous methods are typically event-driven methods, however, these methods are very complicated to implement and less performant for large systems.

1.1. Reference methods for first-order differential inclusions

In this section, we will introduce three methods for first-order differential inclusions. We will later compare the PBD method against these reference methods to test the convergence of PBD.

We aim to solve the following differential-inclusion

$$\dot{\boldsymbol{x}} \in \boldsymbol{F}(\boldsymbol{x}) - N(S, \boldsymbol{x}) \tag{2.1}$$

where $\boldsymbol{x} \in \mathbb{R}^d$ are the positions, $\boldsymbol{F} : \mathbb{R}^d \to \mathbb{R}^d$ are the forces and $N(S, \boldsymbol{x})$ is the (proximal) normal cone of $S \subset \mathbb{R}^d$ at $\boldsymbol{x}$. We notice that we neglect the damping coefficient μ here, e.g. the physically correct equation is $\mu\dot{\boldsymbol{x}} \in \boldsymbol{F}(\boldsymbol{x}) - N(S, \boldsymbol{x})$ but for the development of the numerical methods we set $\mu = 1$ in the following.

We assume that the assumptions of Theorem 1.31 are satisfied. In particular, we assume that S is a closed, non-empty and η-prox-regular set. This implies that the projection operator $\mathrm{P}_S : \mathbb{R}^d \to S$ is well-defined and single valued for all $\boldsymbol{x}$ with $\mathrm{dist}(\boldsymbol{x}, S) < \eta$.

In the following sections we use $\Delta t > 0$ to denote size of the numerical time steps.

1.1.1. Moreau's catch-up scheme. We have seen Moreau's catch-up scheme [Mor99] already in the proof of Theorem 1.31. The method is defined by

$$\boldsymbol{x}_{k+1} = \mathrm{P}_S\left(\boldsymbol{x}_k + \Delta t \boldsymbol{F}(\boldsymbol{x}_k)\right).$$

The proof of Theorem 1.31 is in fact a proof of the convergence for this numerical method.

However, Moreau's catch-up scheme is mostly of theoretical interest. In many practical applications it is not possible to compute P_S fast enough.

1.1.2. Inner convex approximation. The key to obtain applicable methods is to find efficient ways to approximate the projection onto the feasible set.

The method proposed in [Ven11] uses the so-called inner convex approximation of a speed-up to the projection onto S.

Let us assume S is given by M constraints functions $g_\ell : \mathbb{R}^d \to \mathbb{R}$, such that

$$\boldsymbol{x} \in S \quad \Leftrightarrow \quad g_\ell(\boldsymbol{x}) \geq 0 \quad \text{for all } 1 \leq \ell \leq M.$$

The convex inner approximation at $\boldsymbol{x}$ is defined as

$$\tilde{S}(\boldsymbol{x}) \coloneqq \{\boldsymbol{y} \in \mathbb{R}^d \mid g_\ell(\boldsymbol{x}) + \nabla_{\boldsymbol{x}} g_\ell(\boldsymbol{x}) \cdot (\boldsymbol{y} - \boldsymbol{x}) \geq 0\}.$$

This set forms a convex polytope which allows fast numerical approximation of the projection operator $\mathrm{P}_{\tilde{S}(\boldsymbol{x})}$. An example of the convex inner approximation is shown in Figure 1.

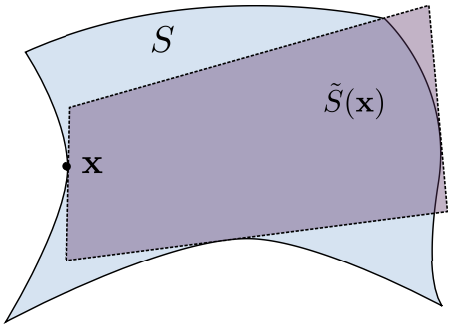

Figure 1. Example of the convex inner approximation for a set S. Notice that the approximation depends on the point $\boldsymbol{x}$.

The results in [Ven11; BV13] show that one can replace S with $\tilde{S}(\boldsymbol{x})$ in the catch-up scheme without loss of convergence. This motivates the following numerical method

$$\boldsymbol{x}_{k+1} = \mathrm{P}_{\tilde{S}(\boldsymbol{x}_k)} \left(\boldsymbol{x}_k + \Delta t \boldsymbol{F}(\boldsymbol{x}_k)\right).$$

1.1.3. Penalty method. Both of the previous methods were non-smooth time-stepping methods. We will now given an example for the *smoothening approach*, namely the penalty method.

As in Section 1.1.2, we assume that S is given by constraint functions g_ℓ for $1 \leq \ell \leq M$. We define the penalty forces as

$$\boldsymbol{F}_\ell^{\text{penalty}}(\boldsymbol{x}) \coloneqq \begin{cases} \nabla g_\ell(\boldsymbol{x}) & \text{if } g_\ell(\boldsymbol{x}) < 0, \\ \mathbf{0} & \text{else.} \end{cases}$$

Instead of solving (2.1), we consider now the following ordinary differential equation (ODE)

$$\dot{\boldsymbol{x}} = \boldsymbol{F}(\boldsymbol{x}) + \varepsilon \sum_{\ell=1}^{M} \boldsymbol{F}_\ell^{\text{penalty}}(\boldsymbol{x}) \tag{2.2}$$

where $\varepsilon > 0$ is the penalty parameter which determines how strong the penalty forces are. (We recall that we neglect the damping coefficient μ here, which would be required for physically correct units.)

For (2.2) one might apply any numerical scheme for ODEs which makes penalty methods very easy to implement. For $\varepsilon \to \infty$ the dynamics converge to the non-smooth behaviour.

However, the stiffness of these systems typically also increases dramatically for large penalty parameters which forces small time-steps or implicit numerical methods.

2. Position based dynamics

In the following, we will introduce the original position based dynamics (PBD) method. The PBD method was first presented in [Mül+06] and then updated in [MMC16] and [Mac+19]. We use the most recent variant from [Mac+19]. For a survey on PBD we refer to [BMM17]. In addition, the webpage `https://matthias-research.github.io/pages/challenges/challenges.html` shows impressive, interactive examples.

2.1. Requirements for the use of position based dynamics

The crucial assumptions for the application of PBD is that the feasible set $S \subset \mathbb{R}^d$ is the intersection of several uniformly prox-regular sets $S_1, \dots, S_M$ such that

$$S = \bigcap_{j=1}^{M} S_j$$

is also uniformly prox-regular (see Definition 1.21). Moreover, for the sets S_j we need that the corresponding projection map

$$\mathrm{P}_{S_j} : \mathbb{R}^n \to S_j \quad \text{is computationally fast.}$$

Typically, the sets S_j represents the overlap-free states for each pair of objects, like in Model 1.3.

2.2. The original method: second-order position based dynamics

Informally speaking, PBD approximates solutions of Newton's second law

$$m\ddot{\boldsymbol{x}} = \boldsymbol{F}(\boldsymbol{x})$$

where m is the mass, $\boldsymbol{x} \in \mathbb{R}^d$ are the positions and $\boldsymbol{F} : \mathbb{R}^d \to \mathbb{R}^d$ are the forces. In addition, one imposes constraints such as

$$\boldsymbol{x}(t) \in S \quad \text{for all } t > 0$$

where $S \subset \mathbb{R}^d$ is the feasible set.

Remark 2.1 (Well-posedness and impact laws)**.** To obtain a well-posed problem which combines Newton's second law and the constraint $\boldsymbol{x} \in S$, one would need to formulate impact laws, which determine the post-collision velocities after each collision. Such problems are discussed in contact mechanics [Wri06]. However, a precise mathematical formulation of second-order contact problems is very technical. While we could ask for absolutely continuous solutions in the first-order case (Chapter 1), the second-order case needs to allow discontinuous velocities which in turn leads to measure valued solutions and the corresponding equations are called *measure differential inclusions* [AB08].

Since we are only interested in the first-order setting, we neglect the technical aspects of the second-order case. Instead, we just present the numerical method in the following.

Method 2.2 (Second-order position based dynamics [Mac+19])**.** Given a state $\boldsymbol{x}_k \in S$ and $\boldsymbol{v}_k \in T(S, \boldsymbol{x})$, a simplified[2] variant of the PBD method with time step Δt reads

$$\tilde{\boldsymbol{v}}_{k+1} \coloneqq \boldsymbol{v}_k + \Delta t \boldsymbol{F}(\boldsymbol{x}_k, \boldsymbol{v}_k), \tag{2.3}$$

$$\tilde{\boldsymbol{x}}_{k+1} \coloneqq \boldsymbol{x}_k + \Delta t \tilde{\boldsymbol{v}}_{k+1}, \tag{2.4}$$

$$\boldsymbol{x}_{k+1} \coloneqq \mathrm{P}_{S_M} \circ \cdots \circ \mathrm{P}_{S_1}(\tilde{\boldsymbol{x}}_{k+1}) \tag{2.5}$$

$$\boldsymbol{v}_{k+1} \coloneqq \Delta t^{-1}(\boldsymbol{x}_{k+1} - \boldsymbol{x}_k). \tag{2.6}$$

The PBD has the structure of a predictor-corrector scheme: The first part (2.3) and (2.4) is the symplectic Euler method [HLW10] and the second part (2.5) and (2.6) is a correction step to fix possible violations of the constraint $\boldsymbol{x} \in S$ (2.5) and to obtain consistent velocities for the iteration.

The method is called *position based* since the projections literally shift the positions of objects in (2.5), instead of computing post-collision velocities or contact forces.

We will comment in more detail on PBD in the first-order context, which we introduce next.

2.3. First-order position based dynamics

We are interested in solving first-order equations with position based dynamics. The PBD method does not require any changes, we just remove the velocity specific steps. We note that a similar approach is presented in [Wei+17a].

For S and S_j as defined in Section 2.1, we aim at solving the following differential inclusion

$$\dot{\boldsymbol{x}} \in \boldsymbol{F}(\boldsymbol{x}) - N(S, \boldsymbol{x}) \tag{2.7}$$

for forces $\boldsymbol{F} : \mathbb{R}^d \to \mathbb{R}^d$.

Method 2.3 (First-order position based dynamics)**.** For given state $\boldsymbol{x}_k \in \mathbb{R}^d$, the time-stepping of rule the first-order PBD method reads

$$\tilde{\boldsymbol{x}}_{k+1} = \boldsymbol{x}_k + \Delta t \boldsymbol{F}(\boldsymbol{x}_k) \tag{2.8}$$

$$\boldsymbol{x}_{k+1} = \mathrm{P}_{S_M} \circ \cdots \circ \mathrm{P}_{S_1}(\tilde{\boldsymbol{x}}_{k+1}). \tag{2.9}$$

Just like the second-order variant, this method is a predictor-corrector scheme:

- The prediction uses an explicit Euler step which ignores the constraints. This can possibly lead to infeasible states, e.g. $\tilde{\boldsymbol{x}}_{k+1} \notin S$.

[2] In the original form, the projection maps P_{S_j} are not available computationally, but instead, one uses a single step of a local Gauss-Newton iteration [DR15, Section 3.3] to compute the projections P_{S_j}.

- For the correction, the intermediate state $\tilde{\boldsymbol{x}}$ is projected with an *iterative projection* onto the set $S_1, \dots, S_M$. This projection approximates P_S but it can happen that even the corrected state is not feasible, i.e $\boldsymbol{x}_{k+1} \notin S$.

Figure 2 shows an example of the PBD method.

The key feature of PBD is that the iterative projections (2.9) are very fast compared to more elaborated approximations of P_S. By using a very cheap method for the projection step, on can use smaller time steps. This trade-off between cheap but many time-steps is at the core of PBD.

Smaller time steps have many advantages and overall simplify also the projection steps themselves. For example, if we consider the distance to the feasible set P_{S_j}, then we directly obtain

$$\mathrm{dist}(\tilde{\boldsymbol{x}}_{k+1}, S) \leq \mathrm{dist}(\boldsymbol{x}_k, S) + \Delta t \|\boldsymbol{F}(\boldsymbol{x}_k)\|,$$

which shows that for smaller time-steps the added infeasibility is at most linear in Δt. As a result, the correction step has less difficult problems to solve for smaller time steps. In addition, the force integration becomes also more accurate at the same time. In [Mac+19], the authors show that the use of small time-steps leads to more accurate results compared to methods which use more accurate projections but larger time steps.

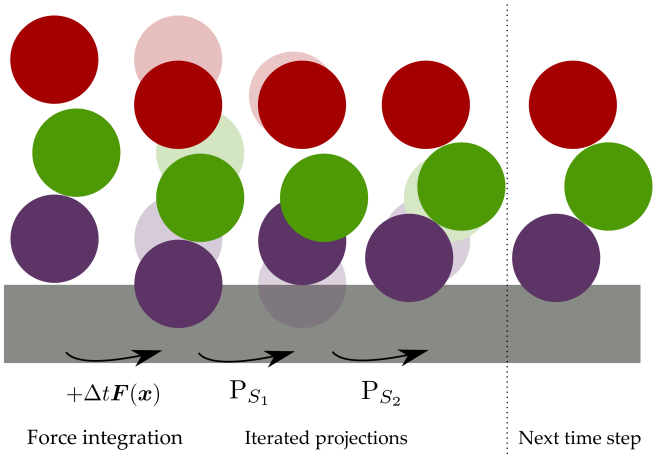

Figure 2. Example of the PBD method *with very large time steps*: During the prediction step, forces are integrated without any constraints. Then, possible constraint violations are corrected by iterative projections. The iterated projection can lead to infeasible states for the next steps. However, by choosing sufficiently small time steps the infeasibility will also decrease. Crucially, the use of large time steps does not make the simulations unstable, i.e. one does not experience stiffness problems like with penalty methods.

Remark 2.4 (Alternating projections)**.** The iterated projections in (2.9) are similar to the method of *alternating projections*. For two sets $A, B \subset \mathbb{R}^d$, the method of alternating projections finds a point in the intersection $A \cap B$ by iterating

$$\boldsymbol{x}_{k+1} = \mathrm{P}_A\left(\mathrm{P}_B\left(\boldsymbol{x}_k\right)\right).$$

Under additional assumptions, one can show local convergence of this iteration also in non-convex cases [LLM09].

If A, B are closed subspaces of a Hilbert space, then the corresponding iteration is called Von Neumann's alternating projections [Von49, Lemma 22].

2.4. Implementation of position based dynamics

We now turn our attention tothe implementation of the PBD method for Model 1.3. This implementation is very close to our actual applications in Chapters 3 and 4. Compared to most other methods, the PBD does not need to compute Lagrangian multipliers or to solve linear complementarity problems.

Example 2.5 (PBD method for non-overlapping disks)**.** We first recall that the constraints in Model 1.3 are of the form

$$S_{ij} = \{\boldsymbol{\mathcal{X}} \in \mathbb{R}^{2N} \mid \|\boldsymbol{X}_i - \boldsymbol{X}_j\| \geq 2R\}$$

where R is the disk radius and $\boldsymbol{\mathcal{X}} = (\boldsymbol{X}_1, \dots, \boldsymbol{X}_N) \in \mathbb{R}^{2N}$ are the center positions of N disks.

If two disks overlap, then the corresponding projection $\mathrm{P}_{S_{ij}}$ is given by the following computation

$$\begin{aligned}
\delta_{ij} &\coloneqq \max(2R - \|\boldsymbol{X}_i - \boldsymbol{X}_j\|, 0),\\
\tilde{\boldsymbol{X}}_i &\coloneqq \boldsymbol{X}_i - \frac{\delta_{ij}}{2}\frac{\boldsymbol{X}_j - \boldsymbol{X}_i}{\|\boldsymbol{X}_j - \boldsymbol{X}_i\|},\\
\tilde{\boldsymbol{X}}_j &\coloneqq \boldsymbol{X}_j + \frac{\delta_{ij}}{2}\frac{\boldsymbol{X}_j - \boldsymbol{X}_i}{\|\boldsymbol{X}_j - \boldsymbol{X}_i\|}.
\end{aligned}$$

In these equations, the term δ_{ij} represents the current overlap of the disks. Each disk is shifted by half of the overlap, which is exactly the projection (with respect to the Euclidean norm).

This leads to Algorithm 1, which simulates Model 1.3. We note that Algorithm 1 is remarkably simple, most methods for differential inclusions (with the exception of penalty methods) would compute Lagrangian multipliers, which requires inner iterations to solve linear complementarity problems (for example with the projected Gauss-Seidel method [ST96] or the projected Jacobi method [TBV12]).

Remark 2.6 (Efficient collision detection and parallelism)**.** The main computational effort of the PBD is the collision detection. Therefore, an efficient implementation requires similar techniques as used in molecular dynamics and particle simulations.

For the collision detection, one can use for example the linked cell method [GKZ07]. If the maximal number of contacts is locally bounded, then an efficient collision detection allows an implementation of Algorithm 1 with linear runtime $\mathcal{O}(N)$ instead of $\mathcal{O}(N^2)$.

Algorithm 1: First-order PBD method for the non-overlapping disk model

$t \leftarrow 0$
while $t < t^{\text{end}}$ **do**
  $t \leftarrow t + \Delta t$
  $(\boldsymbol{F}_1, \dots, \boldsymbol{F}_N) \leftarrow \boldsymbol{\mathcal{F}}(\boldsymbol{X}_1, \dots, \boldsymbol{X}_N)$ `/* Compute forces */`
  for $i \in \{1, \dots, N\}$ **do**
    $\boldsymbol{X}_i \leftarrow \boldsymbol{X}_i + \Delta t \boldsymbol{F}_i$ `/* Prediction step */`
  end
  for $i \in \{1, \dots, N\}$ **do**
    for $j \in \{1, \dots, i-1\}$ **do**
      $\delta_{ij} \leftarrow \|\boldsymbol{X}_i - \boldsymbol{X}_j\| - 2R$ `/* Detect overlap */`
      if $\delta_{ij} < 0$ **then**
        $\boldsymbol{X}_{ij} \leftarrow {}^{(\boldsymbol{X}_j - \boldsymbol{X}_i)}/_{(\delta_{ij}+2R)}$
        $\boldsymbol{X}_i \leftarrow \boldsymbol{X}_i - \frac{d}{2}\boldsymbol{X}_{ij}$ `/* Fix overlap */`
        $\boldsymbol{X}_j \leftarrow \boldsymbol{X}_j + \frac{d}{2}\boldsymbol{X}_{ij}$
      end
    end
  end
end

Moreover, the PBD method is suitable for parallelisation [FP15; BMM17], however parallelism is not straightforward for PBD.

3. Theoretical aspects of first-order PBD

In this section, we prove that the PBD method is a numerically consistent method. This alone does not prove convergence of the PBD method, but it shows that each limit of the PBD method would be a solution.

Let us first recall the the notation of consistency for ordinary differential equations. For a given one-step method with *numerical flow* $\boldsymbol{x}_{k+1} = \Phi_{\Delta t}(\boldsymbol{x}_k)$, we say that a method is consistent if for all $\boldsymbol{x} \in \mathbb{R}^d$

$$\frac{\Phi_{\Delta t}(\boldsymbol{x}) - \boldsymbol{x}}{\Delta t} \to \boldsymbol{F}(\boldsymbol{x}) \quad \text{for } \Delta t \to 0. \tag{2.10}$$

We note, that this property alone does not imply convergence of the numerical method. Consistency is rather the minimal condition each reasonable numerical method has to satisfy. For convergence, one would need to find additional stability bounds, to ensure that the local errors do not accumulate to a significant global error, see for example [HNW93, Theroem II.3.6].

3.1. Consistency of the first-order PBD method

In the following, we show that PBD is a consistent numerical method in a particular sense.

To generalise (2.10) for numerical approximations of $\dot{\boldsymbol{x}} \in \boldsymbol{F}(\boldsymbol{x}) - N(S, \boldsymbol{x})$, we need to choose a notation of convergence for multi-functions (or sets). Here, we will use the notation of scalarly upper semicontinuity (see Definition 1.27). This choice is inspired by the proof of Theorem 1.31.

For the PBD method, the numerical flow is given by

$$\Phi_{\Delta t}^{\mathrm{PBD}}(\boldsymbol{x}) = \mathrm{P}_{S_M} \circ \cdots \circ \mathrm{P}_{S_1}(\boldsymbol{x} + \Delta t \boldsymbol{F}(\boldsymbol{x})).$$

This map describes the update for each time step, i.e. $\boldsymbol{x}_{k+1} = \Phi_{\Delta t}^{\mathrm{PBD}}(\boldsymbol{x}_k)$ is equivalent to Method 2.3.

Definition 2.7 (Consistency, in a scalarly upper semicontinuous sense)**.** Let $\boldsymbol{F} : \mathbb{R}^d \to \mathbb{R}^d$ be a bounded function. We call a one-step method with numerical flow $\Phi_{\Delta t} : \mathbb{R}^d \to \mathbb{R}^d$ a consistent discretisation of (2.7), if there exists a constant $R > 0$ such that for all $\boldsymbol{x} \in S$ we have

$$\limsup_{\Delta t \to 0} \sigma\left(\frac{\Phi_{\Delta t}(\boldsymbol{x}) - \boldsymbol{x}}{\Delta t} - \boldsymbol{F}(\boldsymbol{x}), \boldsymbol{w}\right) \to \sigma(-N(S, \boldsymbol{x}) \cap B_R(\boldsymbol{0}), \boldsymbol{w}) \quad \text{for all } \boldsymbol{w} \in \mathbb{R}^d,$$

where $\sigma(K, \boldsymbol{w}) \coloneqq \sup_{\boldsymbol{v} \in K} \boldsymbol{v} \cdot \boldsymbol{w}$ denotes the support function (Definition 1.26).

The proof of Theorem 1.31 uses exactly this concept of consistency to show that Moreau's catch-up scheme converges to a solution of the differential equation. This motivates the definition of consistency.

Lemma 2.8 (Consistency of first-order PBD for the non-overlapping disks model)**.** *Let S be the set of non-overlapping disks and S_j be the sets of pairwise non-overlap, as defined Theorem 1.25. For $\boldsymbol{F} : \mathbb{R}^d \to \mathbb{R}^d$ bounded, i.e., $\|\boldsymbol{F}\|_\infty < \infty$, the PBD method is consistent in the sense of Definition 2.7.*

Proof. Let $\boldsymbol{x} \in S$ be an arbitrary feasible point.

We define the following intermediate points

$$\begin{aligned} \boldsymbol{p}_0 &\coloneqq \boldsymbol{x} + \Delta t \boldsymbol{F}(\boldsymbol{x}), \\ \boldsymbol{p}_j &\coloneqq \mathrm{P}_{S_j}(\boldsymbol{p}_{j-1}) \quad \text{for } 1 \le j \le M. \end{aligned} \tag{2.11}$$

With this notation, we obtain

$$\Phi_{\Delta t}^{\mathrm{PBD}}(\boldsymbol{x}) = \boldsymbol{p}_M.$$

By definition of the proximal normal cone (Definition 1.23), (2.11) is equivalent to

$$\boldsymbol{p}_{j-1} - \boldsymbol{p}_j \in N(S_j, \boldsymbol{p}_j) \quad \text{for } 1 \le j \le M.$$

This shows

$$\frac{\Phi_{\Delta t}^{\mathrm{PBD}}(\boldsymbol{x}) - \boldsymbol{x}}{\Delta t} - \boldsymbol{F}(\boldsymbol{x}) = \boldsymbol{p}_M - \boldsymbol{p}_0 \in -\sum_{j=1}^{M} N(S_j, \boldsymbol{p}_j). \tag{2.12}$$

Figure 3 visualises the relation between the numerical approximation and the corresponding normal cones.

Finally, we show that $\boldsymbol{p}_j \to \boldsymbol{x}$ as $\Delta t \to 0$. First, we notice that

$$\|\boldsymbol{p}_0 - \boldsymbol{x}\| \leq \Delta t \|\boldsymbol{F}(\boldsymbol{x})\|.$$

This shows the convergence $\boldsymbol{p}_0 \to \boldsymbol{x}$ for $\Delta t \to 0$.

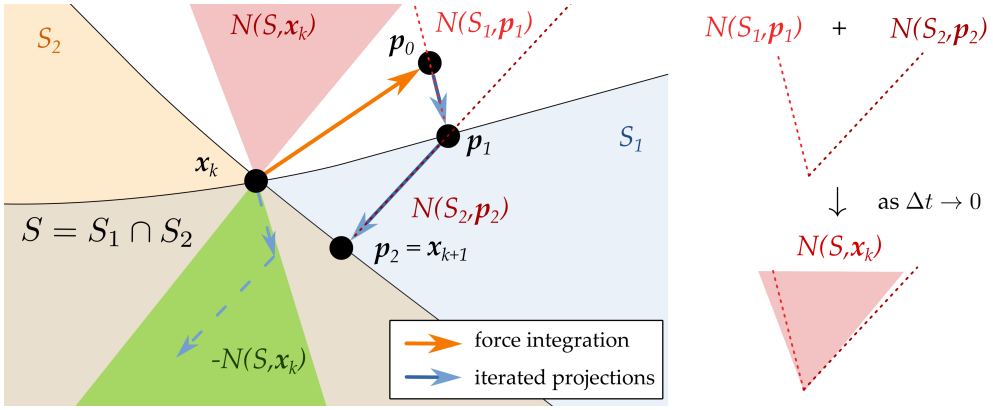

Figure 3. Left: example of the intermediate points of the PBD method ($\boldsymbol{p}_0, \boldsymbol{p}_1$ and $\boldsymbol{p}_2$). Notice how the iterated projections go into directions aligned with the corresponding normal cones, e.g $\boldsymbol{p}_1 - \boldsymbol{p}_0 \in -N(S_1, \boldsymbol{p}_1)$. **Right:** In the limit, $\boldsymbol{p}_j \to \boldsymbol{x}_k$, we obtain that the Minkowski sum of the corresponding normal cones converges. This is the geometric foundation for the proof of Lemma 2.8.

By induction, we show the convergence of the remaining intermediate points. We assume that for $j \geq 1$ the following holds

$$\|\boldsymbol{p}_{j-1} - \boldsymbol{x}\| \leq 2^{j-1} \Delta t \|\boldsymbol{F}(\boldsymbol{x})\|.$$

Since $\boldsymbol{x} \in S$, we know in particular $\boldsymbol{x} \in S_j$, which implies

$$\|\boldsymbol{p}_{j-1} - \mathrm{P}_{S_j}(\boldsymbol{p}_{j-1})\| \leq \|\boldsymbol{p}_{j-1} - \boldsymbol{x}\| \leq 2^{j-1} \Delta t \|\boldsymbol{F}(\boldsymbol{x})\|$$

which proves the induction step

$$\|\boldsymbol{p}_j - \boldsymbol{x}\| \leq \|\mathrm{P}_{S_j}(\boldsymbol{p}_{j-1}) - \boldsymbol{p}_{j-1}\| + \|\boldsymbol{p}_{j-1} - \boldsymbol{x}\| \leq 2^j \Delta t \|\boldsymbol{F}(\boldsymbol{x})\|. \tag{2.13}$$

This shows that for $1 \leq j \leq M$ we have $\boldsymbol{p}_j \to \boldsymbol{x}$ as $\Delta t \to 0$.

Moreover, (2.13) shows

$$\left\| \frac{\Phi_{\Delta t}^{\mathrm{PBD}}(\boldsymbol{x}) - \boldsymbol{x}}{\Delta t} - \boldsymbol{F}(\boldsymbol{x}) \right\| \leq (2^j + 1) \|\boldsymbol{F}\|_\infty.$$

Using $R = (2^j + 1)\|\boldsymbol{F}\|_\infty + 1$, we obtain from (2.12) that

$$\frac{\Phi_{\Delta t}^{\mathrm{PBD}}(\boldsymbol{x}) - \boldsymbol{x}}{\Delta t} - \boldsymbol{F}(\boldsymbol{x}) \in -\sum_{j=1}^{M} N(S_j, \boldsymbol{p}_j) \cap B_R(\boldsymbol{0}).$$

Finally, Corollary 1.30 proves the claim, i.e.,

$$\begin{aligned}
&\limsup_{\Delta t \to 0} \sigma\left(\frac{\Phi_{\Delta t}^{\mathrm{PBD}}(\boldsymbol{x}) - \boldsymbol{x}}{\Delta t} - \boldsymbol{F}(\boldsymbol{x}), \boldsymbol{w}\right) \\
&\qquad \leq \limsup_{\Delta t \to 0} \sigma\left(-\sum_{j=1}^{M} N(S_j, \boldsymbol{p}_j) \cap B_R(\boldsymbol{0}), \boldsymbol{w}\right) \\
&\qquad = \sigma(-N(S, \boldsymbol{x}) \cap B_R(\boldsymbol{0}), \boldsymbol{w}) \quad \text{for all } \boldsymbol{w} \in \mathbb{R}^d.
\end{aligned}$$

□

4. Numerical examples

We tested the numerical convergence of PBD with numerical experiments. In our examples, the PBD method always converges to the reference solution and we estimate that the order of convergence is 1.

4.1. Computational of a reference solution

It is in general difficult to obtain explicit solutions for first-order differential inclusions. While one can compute explicitly simple situations such as a stack of disks, in general the most challenging situations arise when multiple objects slide alongside each other. For such cases, the computation of explicit solutions is basically impossible.

Therefore, we will use Moreau's catch-up scheme (Section 1.1.1) to compute high accuracy reference solutions. We know that the method converges in our setting (as the proof of Theorem 1.31 shows) and by choosing a sufficiently small time step size we can assume that the computed solution is accurate enough to serve as a reference solution.

The numerical implementation is challenging and not runtime-efficient, as there are no ideal algorithms to compute the projection P_S for prox-regular sets S. However, we found that the open source solver `Ipopt` [Lou03] is accurate enough, provided we use very small tolerance values. (We set the relative tolerance parameter `tol` to 10^{-11} which was much larger than the errors introduced by the time-stepping). Ipopt uses an interior point algorithm which can handle general nonlinear constraints.

In addition, we also implemented the method based on inner convex approximations from Section 1.1.2. The computed solutions from this convergent method coincided with the solutions computed with Moreau's catch-up scheme.

4.2. Convergence plots

We now show convergence studies for two examples.

(1) First, we consider four disks, which are all attracted to a central point. Here, disks are sliding alongside each other until they are in a global equilibrium.
(2) Second, we consider ten disks falling into a corner with constant speed. This situation models a crowded scenario, where multiple disks will be stacked on top of each other at the end of the simulation.

The first experiment is presented in Figure 4. We found that the PBD method converges to the reference solution with order 1. Interestingly, the global error decreases at the end of the simulation, e.g. at $t = 2$, compared to times at which the disks are sliding alongside each other, e.g $t = 1$. This shows that the PBD is able to capture the correct equilibrium of this system.

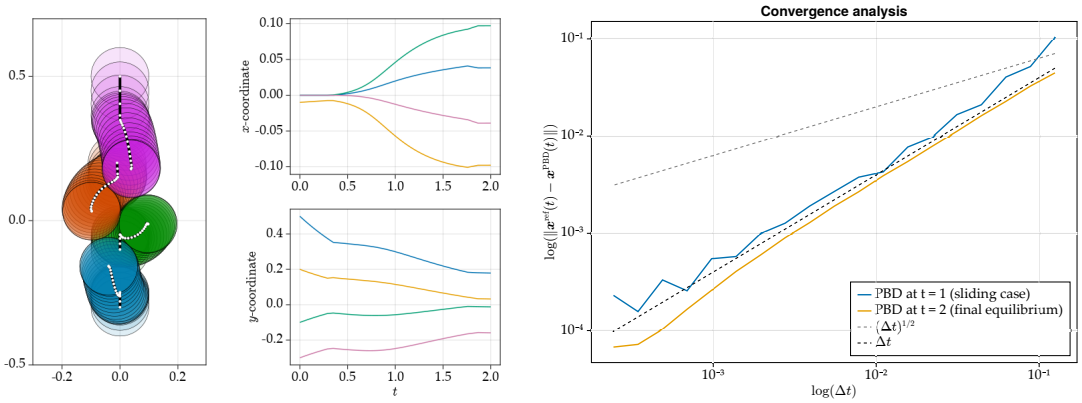

Figure 4. Left: Example simulation of four disks with non-overlapping constraints and forces $\boldsymbol{F}(\boldsymbol{x}) = -\boldsymbol{x}$. **Right:** The PBD method converges to the reference solution computed with Moreau's catch-up scheme (and Ipopt). We note that the PBD converges with order 1.

Figure 5 shows the second numerical convergence study. In this setup, ten disks are dropped to fall into a corner. At time $t = 1$ most disks are falling and possibly sliding alongside each other, at $t = 2$ some disks will already be in the corner and the incoming disks will take the free spots. Finally, at $t = 3$ most disks will be in a stationary position. This test case is representative of crowded situations, where disks are on top of each other, which leads to pressure on the lower disks.

The result is again that the PBD method again converges to the reference solution with order 1.

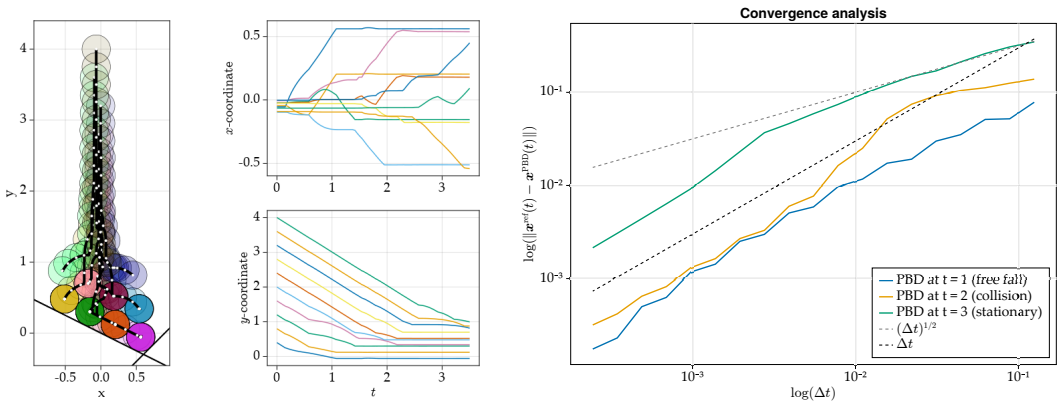

Figure 5. Left: Example simulation of ten disks with non-overlapping constraints and a downward pointing gravity force $\boldsymbol{F}_i(\boldsymbol{x}) = (0, -1)^T$. In addition, the disks cannot overlap with the two black lines forming a corner. **Right:** Also here, the the PBD converges to the reference solution with order 1.

4.3. Comparison with the penalty method

A surprising comparison arises between the penalty method and the PBD method. Both the penalty method and the PBD method are prone to produce overlap between objects due to their inexact handling of the constraints.

The application of the penalty method depends crucially on the choice of the penalty parameter ε (see Section 1.1.3). For too large penalty parameters, simulations become unstable, but for too small penalty parameters, the constraints will be violated too strongly. In general, it is difficult to find the optimal penalty parameter a priori, i.e. before the simulation.

In the following, we run the penalty method multiple times with different penalty parameters ε and compare only the penalty method with optimal choice of ε with the PBD method.

Figure 6 shows that PBD is able to outperform the penalty method by a small margin, even for optimal choice of the penalty parameter. This shows the the PBD method can be used to solve the problem of unknown optimal penalty parameters.

We will observe a similar behaviour in our actual application in Chapter 3, where the PBD is able to reproduce and outperform another method which relies on numerical parameters for which the optimal values are unknown.

5. Conclusion

In this chapter we have presented the first-order PBD method. The key features of the PBD are fast runtime, simple implementation and surprising numerical stability.

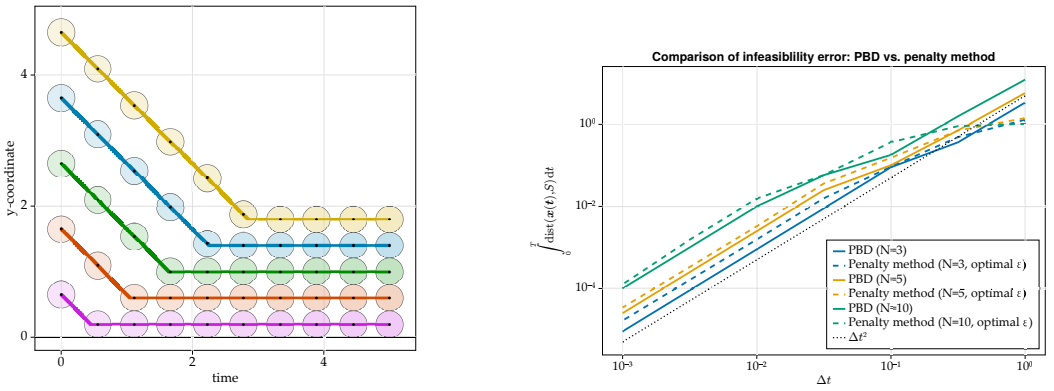

Figure 6. Comparison of the infeasibility error during simulations with PBD (solid line) and the penalty method (dashed). Note that for the penalty method on needs to determine the penalty parameter ε, typically this is not a trivial task.

Our numerical experiments show that the PBD method seems to converge (with order of convergence 1) and the proof for the consistency of PBD supports this by showing that all convergent limits of the PBD method will solve the first-order differential inclusion.

Establishing the convergence of the PBD method would be an important next step, since PBD is a powerful method for simulating agent-based models under constraints. One of the main benefits of PBD is also the simplicity, which allows effortless implementation also of complex constraints.

Chapter 3

Simulation of growing epithelial tissue with position based dynamics

A fundamental question in developmental biology how tissues and organs are formed. Put in the most simple terms, it is the question of how a single cell can grow into a chicken. Epithelial cells play an important role in the early development of embryos, where most cells are either *epithelial cells* or *mesenchymal cells*. Epithelial cells typically form tightly connected sheets or tubes whereas mesenchymal cells are unconnected and often operate individually [GG00]. This interplay between organised tissue (epithelium) and flexible cells (mesenchymal cells) makes it possible that a bunch of cells can divide and grow into organised structures like organs or even whole beings.

Our primary aim in this thesis is to study the so-called epithelial-to-mesenchymal transition (EMT) which will be the focus of Chapter 4. As the name suggest, epithelial cells can change their behaviour and become mesenchymal. This process is key to development. But before we can model EMT, we need a model for the host epithelial tissue itself.

In this chapter, we will present a model for epithelial tissue development introduced in [Fer+19]. The model describes the growth of pseudostratified epithelium, fitting to experimental data from the neural tube of chicken embryos, which are a common model organism in developmental biology, see Figure 1.

We will discuss two modifications of the existing model, which allow us to obtain the same simulation results as in [Fer+19] but at a much lower computational cost ($\sim 300\times$ faster) and with improved numerical stability:

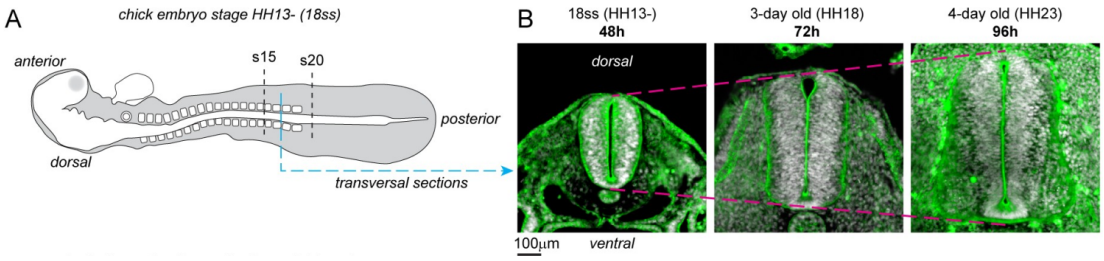

Figure 1. Snapshots of the early stages of chick embryo growth. The tube-like tissue in figure B is the *neural tube*, a (pseudostratified) epithelial tissue. *Image source: [Fer+19, Fig. 1].*

- First, we replace the quasi-steady state model from [Fer+19] with an overdamped Newton equation. This is possible since the previously used numerical method used damping internally and its solutions are close to solutions of a related overdamped Newton equation.
- Second, we use the first-order PBD method which we developed in Chapter 2 to simulate the overdamped Newton equations.

The modifications allow us to simulate parameter ranges which were previously inaccessible due to numerical instability issues of the formerly used method and the faster runtime will allow us to simulate a large number of scenarios leading to EMT.

The structure of this chapter is as follows. First, we will introduce the biological setup in Section 1. In Section 2, we will explain the mathematical model for developing epithelium from [Fer+19] and we discuss the used numerical discretisation. In Section 3, we derive the overdamped Newton equation and show that in practical applications the new approach yields equivalent results. Finally, we show simulation examples in Section 4.

My contribution

The main reference of this chapter is [Fer+19]. My contribution is the introduction of an equivalent overdamped Newton equation and the adaptation of position based dynamics for this model.

1. Biological background

Before we dive into mathematical details, we want to give a rough overview of the biological background, and the experimental model organism particularly of the chick embryo, which is where experiments are carried out by Theveneau's team (CNRS, Toulouse).

1.1. General types of epithelial tissue

Epithelial tissue is one of the four basic types of tissues in the human body, together with connective tissue, muscle tissue and nervous tissue, see Figure 2. Typically, epithelium

acts as a boundary layer (like our skin) or in the inverted case it acts like a pipe (such as the bladder) [Phi+12] and it functions as a protective, absorbing, filtering or secreting layer.

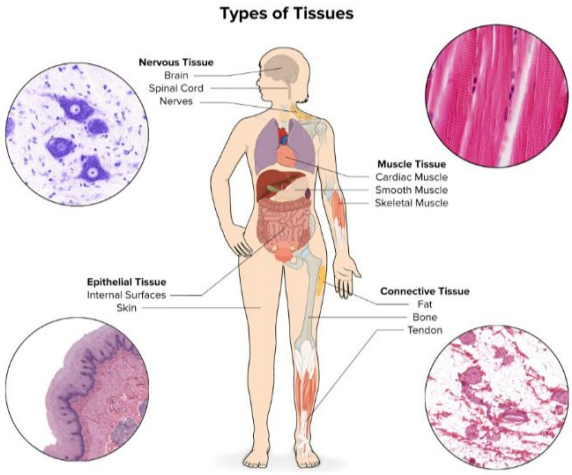

Figure 2. The four different types of basic tissue. *Image source:* `http://histologyguide.com/` *FIG 023, with kind permission from Todd Clark Brelje.*

Structurally, epithelia are densely packed and highly organised tissues in the shape of sheets or tubes. On the so-called *basal* side, the epithelium is attached to the basal membrane via cell-matrix adhesion. Here, matrix refers to the extracellular matrix which is a domain typically filled with fibers to which the epithelial cells can hold onto. The opposite side is called the *apical* side at which the tissue is unattached, forming a apical surface due to many cell-cell junctions. The high level of adhesion among the cells and between cells and the basal matrix is essential for the dense, organised structure of epithelium. An example is shown in Figure 3.

One classifies epithelia according to the number of layers and the shape of its cells, as shown in Figure 4. *Simple* epithelia have only one thin layer of cells whereas *stratified* epithelia have multiple layers of cells. The cell shapes range from *squamous* cells (very thin, flat plates) to *cuboibal* cells (round or cube-like shape) and *columnar* cells (elongated cells which are higher than wide). In addition to these classifications, there are two special types: *Pseudostratified columnar epithelium* (PSE) is technically a single layer epithelium with columnar cells, however, the nuclei of the cells arrange themself in a seemingly stratified way. The second type is *transitional epithelia* where cells change their shape in response to stretching.

Examples of epithelial tissues in the human body are the outer layer of the skin which is a stratified squamous epithelium, various types of glands, which are mostly stratified cubical epithelia, and, for example, our taste buds have simple columnar epithelial cells.

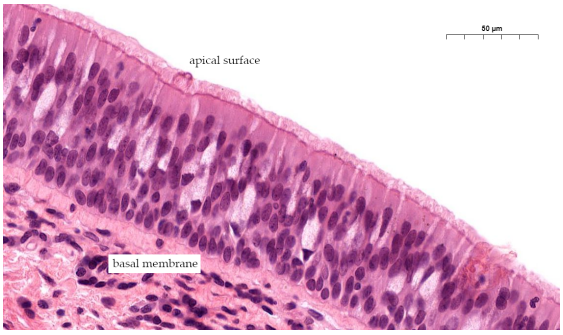

Figure 3. Microscopy image of pseudostratified epithelium in the upper fold of the larynx. The nuclei are in dark purple (basophilic) ellipses. While each cell reaches from the basal membrane to the apical surface, the nuclei are distributed on the apical-basal axis which is characteristic of pseudostratified epithelia. The basal membrane separates the epithelium from the underlying connective tissue. On the apical surface, we can see the thin, hair-like cilia. *Image source:* `http://histologyguide.com/` *MH 135 Larynx, with kind permission from Todd Clark Brelje.*

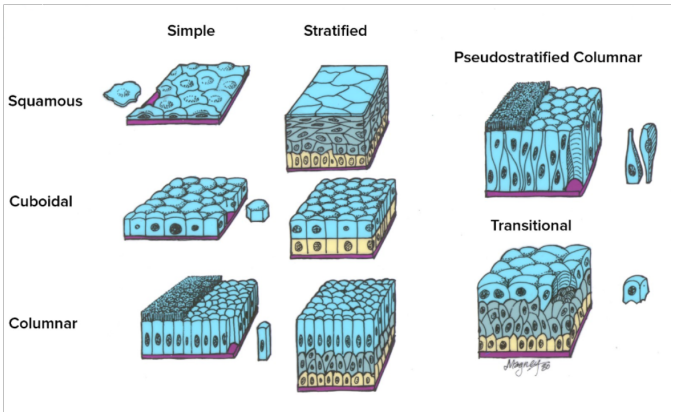

Figure 4. Examples of different types of epithelial tissue. In this thesis, we will work on models for pseudostratified columnar epithelium (PSE). *Image source:* `http://histologyguide.com/` *FIG 008, with kind permission from Todd Clark Brelje.*

1.2. Pseudostratified epithelium from the neural tube of the chick embryo

The experimental data for [Fer+19] was obtained from the *neural tube* (NT) of the chick embryo. The neural tube is a pseudo-stratified epithelium which grows rapidly in the early stages of embryo development. Figure 5 shows electro-microscopy images which zoom into a section of the neural tube.

Figure 6 show the characteristic of pseudostratified epithelium, namely the long columnar cells which span from the basal side (the exterior of the tube) to the apical side (inside of the tube). The nuclei are visible as the thicker round parts of the cell.

In the right image of Figure 6 we can also see the basal extracellular matrix, which consists of a network of fibers.

The chick neuroepithelium was picked for this project, as it is an ideal biological model to study epithelial-to-mesenchymal transitions [Yan+20]. However, for now, we will focus on the situation without EMT.

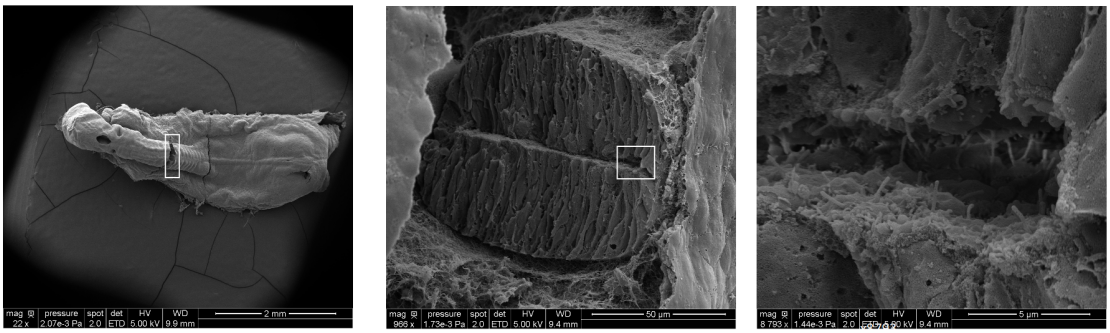

Figure 5. Electromicroscopy images of a chick embryo with a crack exposing the neural tube. **Left:** Overview image of the chick embryo, compare Figure 1. **Center:** Close-up on the neutral tube displaying the pseudostratified structure of the epithelium. Here, the inside of the tube is the apical side, whereas the outside is the basal side. **Right:** View on the apical layer of the epithelium. The small hair-like pins are primary cilia, which are part of the apical signalling. *Image source: unpublished, provided by Dr. Eric Theveneau (CNRS).*

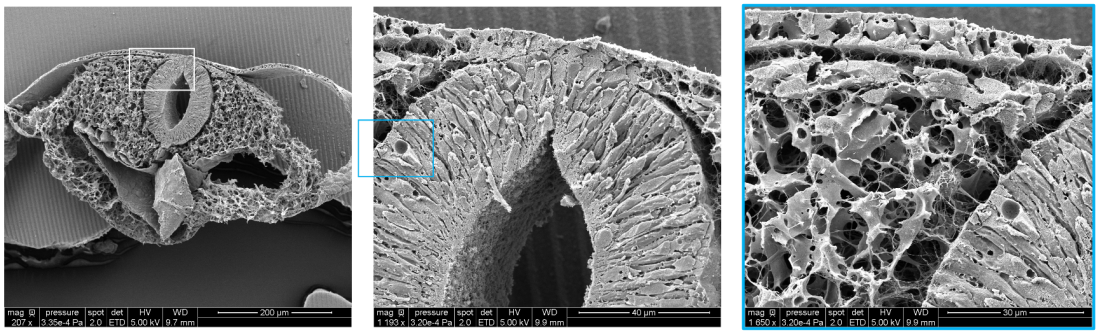

Figure 6. Electromicroscopy of the neural tube. **Left:** Overview image. **Center:** Close-up on the neutral tube displaying the pseudostratified structure of the epithelium. Note how the epithelial cells span from the basal layer up to the apical layer. The thicker part of each cell is the position of the nuclei. **Right:** Fibers of the basal matrix below the epithelium. *Image source: unpublished, provided by Dr. Eric Theveneau (CNRS).*

1.3. Interkinetic nuclear movement (INM)

A characteristic of pseudostratified epithelium (PSE) is the spread of nuclei on the apicobasal axis which form multiple layers despite their columnar cell shape. The nuclei positions within PSE are not static but depend on the cell cycle. This coordinated movement is called *interkinetic nuclear movement* (INM). It consists of an apical to basal movement during the G1 phase, the S phase and a passive part of the G2 phase. Followed

by a fast basal to apical displacement during the active part of the G2 phase and mitosis. The dynamics of INM are sketched in Figure 7.

In the neuroepithelium, the driver for the basal to apical movement are the microtubules of the cell's cytoskeleton. (But the mechanism can also be driven by cytoskeletons with actin-myosin filaments [Fer+19]).

One consequence of INM is that effectively all cell division occurs on the apical side of the tissue, which has an impact on its growth, density and shape.

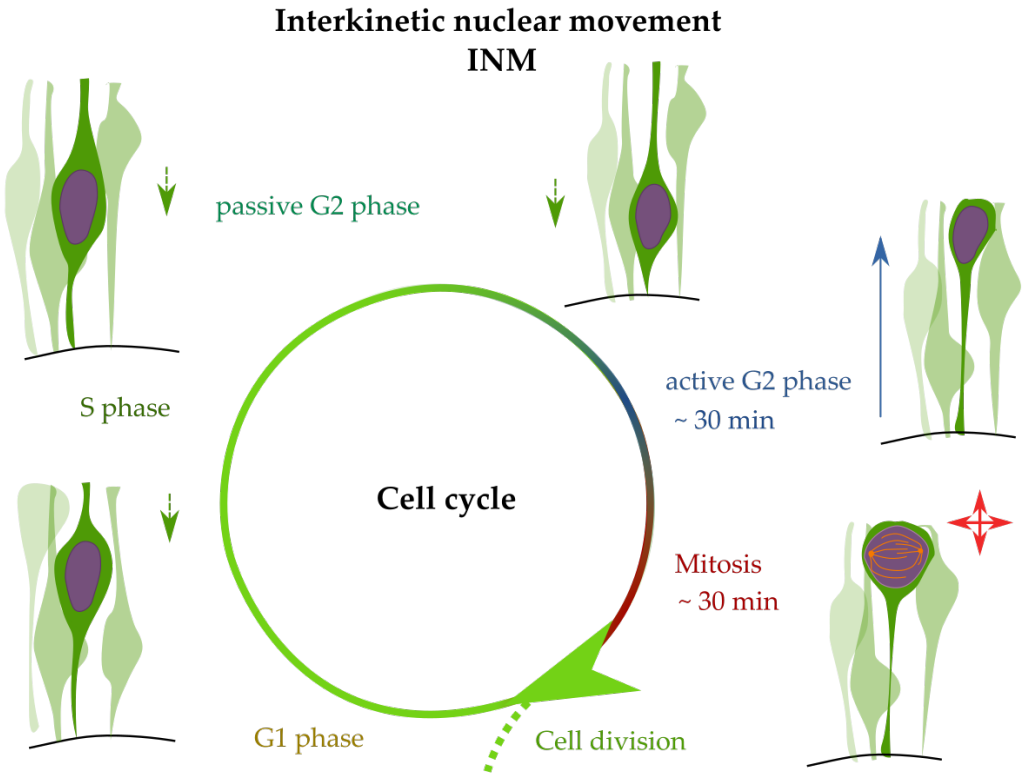

Figure 7. Sketch of interkinetic nuclei movement (INM) during the cell cycle. For most of the cell cycle, the nuclei will move slowly and irregularly to the basal side (black line). Just one hour before cell division the cytoskeleton of the cell pushed the nucleus to the apical side. During the cell division process, the nucleus gets stiffer and might take up more space.

2. Model for growing epithelium (PSE model)

We will now describe the model from [Fer+19]. We call it the PSE model, since it represents pseudostratified epithelium. First, we will outline the components of the model and then we provide the mathematical details required for the implementation of the model.

2.1. Description of the PSE model

We consider as main mechanical components the cell nucleus, the cell's cytoskeleton and the points of adhesion between cells at the apical and basal layers of the tissue. We simplify the interaction between cells by only considering contact between nuclei and ignoring possible interaction between the rest of the cell bodies as these are relatively slim compared to the nuclei.

The model is a *quasi-steady state model*: at each step a potential energy is minimised and in between steps cell parameters will be updated to the model interkinetic nuclear movement (INM) and discrete events, such as cell division.

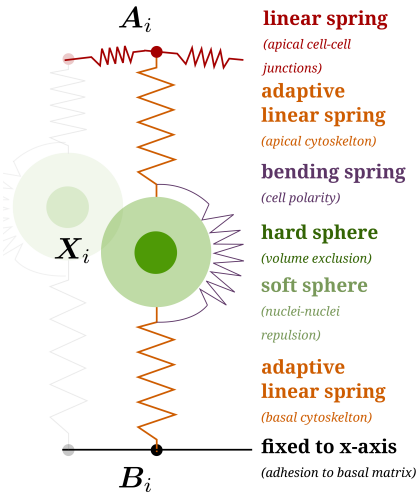

Figure 8. Overview of the model components for a single cell. The green sphere represents the cell nucleus and the adaptive springs model the cytoskeleton. The apical network consists of linear springs connecting neighbouring points. The basal network is a static line to which the basal points of the cells are constrained. Interkinetic nuclear movement is modelled by changing the rest lengths of the adaptive springs.

The model incorporates the following elements (see Figure 8):

Volume exclusion and elasticity of nuclei. The mechanical pushing between nuclei leads to the pseudostratified nature of the tissue. As such it is important to model volume exclusion. However, the nuclei are not just rigid objects, instead, they can deform, that allows them to squeeze through small spaces in crowded environments. To capture the volume exclusion and the non-rigid nature, we model each nucleus as a hard sphere with strict non-overlap conditions to other nuclei. We complement this with repulsive forces between pairs of nuclei within a called soft sphere of each cell.

Apical cell-cell junctions. The apical side of the neural tube is at the boundary to the central lumen. The apical side does not provide any organised structure for cells to grab onto. Instead, the cells themselves form the apical layer of the tissue, which consists of a

network of cell junctions with adhesive contacts. For a simple two-dimensional model of the tissue, we simplify this structure to a line of apical points which represent the cell position at the apical layer. These *apical points* are connected with linear springs to their neighbours, which models the adhesive bonds.

Basal cell-matrix adhesion. The situation is very different at the basal layer since it borders the basal extracellular matrix, which is filled with a dense network of fibers. Since the cells can form cell-matrix junctions we introduce basal points which represent the most basal part of each cell which is connected to the basal layer. Due to the dense fibers in the extracellular matrix, we model the basal membrane as a static line with the condition that basal points have to lie on the fixed basal line.

Cytoskeleton. The cytoskeleton regulates the position of the cell nuclei via microtubules. We model the cytoskeleton as two linear springs that span between the basal point and the nuclei center, and the apical point and the nuclei center. In the G1 phase, S phase and passive G2 phase of the cell cycle, the rest lengths of these springs will change in a way to match the current extension of the cytoskeleton.

Interkinetic nuclear movement (INM). During the active G2 phase and mitosis, the cells will rapidly move apically. This is modelled by changing the rest lengths of the basal-nuclei and apical-nuclei springs such that the most apical position is the equilibrium for both springs.

Proliferation. At the end of the cell cycle, cells will divide into two daughter cells. However, since we only model a 2D slice of the tissue, we have to account for the fact that in the real tissue, not all daughters end up in the same 2D slice. Therefore, only in $20\,\%$ of all cell divisions a second daughter is created within the simulated 2D slice.

Since the cell nucleus becomes more rigid during mitosis, we also increase the radius of the hard sphere during the mitosis phase.

Putting all these rules together, we obtain a model of growing epithelial tissue. The growth is created by INM, proliferation and the combination of the right stiffness coefficients for apical-apical junctions and cytoskeleton springs.

2.2. Mathematical model

In the following, we provide the mathematical definitions of the forces, constraints and cell events which implement the model described in Section 2.1.

We consider a tissue with N cells where the ith cell has the apical point at position $\boldsymbol{A}_i \in \mathbb{R}^2$, the basal point at $\boldsymbol{B}_i \in \mathbb{R}^2$ and the center of the nuclei is at $\boldsymbol{X}_i \in \mathbb{R}^2$. We collect all these positions for the whole tissue in the vectors $\boldsymbol{\mathcal{X}} = (\boldsymbol{X}_1, \dots, \boldsymbol{X}_N) \in \mathbb{R}^{2N}$, $\boldsymbol{\mathcal{A}} = (\boldsymbol{A}_1, \dots, \boldsymbol{A}_N) \in \mathbb{R}^{2N}$ and $\boldsymbol{\mathcal{B}} = (\boldsymbol{B}_1, \dots, \boldsymbol{B}_N) \in \mathbb{R}^{2N}$. Moreover, we write $\boldsymbol{\mathcal{Z}} = (\boldsymbol{\mathcal{A}}, \boldsymbol{\mathcal{B}}, \boldsymbol{\mathcal{X}}) \in \mathbb{R}^{6N}$ to denote all positions at once.

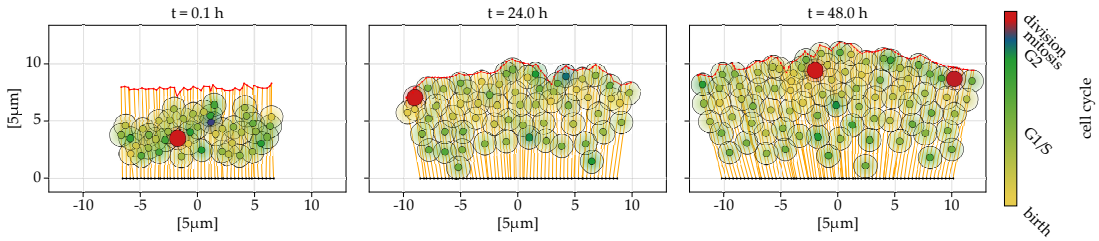

Figure 9. Example simulation of the PSE model. The spheres represent the nuclei, composed out of a transparent sphere for the soft repulsion range and a smaller sphere for the hard center. The red lines on top represent the springs of the apical layer and the back line on the bottom the basal layer. The springs modelling the cytoskeleton are orange.

The model also has dynamic cell parameters which we denote as $\boldsymbol{\mathcal{P}} \in \mathbb{R}^{3N}$, we will provide its definition later. The vector $\boldsymbol{\mathcal{P}}$ contains the radii of non-overlap and the desired rest lengths for the apical-nuclei and basal-nuclei springs.

The mechanical description of the cells is given by an potential energy

$$W : \mathbb{R}^{6N} \times \mathbb{R}^{3N} \to \mathbb{R}$$

and a set of feasible states

$$S \subset \mathbb{R}^{6N}.$$

We will define both in the next sections. The forces of the system are $-\nabla_{\boldsymbol{\mathcal{Z}}} W(\boldsymbol{\mathcal{Z}}, \boldsymbol{\mathcal{P}})$ with the additional constraint that $\boldsymbol{\mathcal{Z}} \in S$ at all times.

We describe next the different components of the model in the following order.

2.2.1: cell cycle and age of cells,
2.2.2: modelling of the cytoskeleton,
2.2.3: interkinetic nuclear movement (INM),
2.2.4: apical cell junctions,
2.2.5: cell division,
2.2.6: forces in the system (energy terms),
2.2.7: constraints.

In Section 2.2.8 we tie together all these components into a quasi-steady state model.

2.2.1. Cell cycle and age of cells. We denote the age of a cell as $t_i^{\text{age}} := t - t_i^{\text{birth}}$.

At the birth of each cell, the duration of the next cell cycle is randomly assigned as

$$t_i^{\text{cycle}} \sim \mathcal{U}(T^{\text{min-age}}, T^{\text{max-age}}), \tag{3.1}$$

where $T^{\text{min-age}} < T^{\text{max-age}}$ denote the minimal and maximal lifespan for each cell.

Cell division happens at the end of the cell cycle, i.e., when $t_i^{\text{age}} = t_i^{\text{cycle}}$. We denote the duration of the G2 phase as T^{G2} and the duration of the mitosis phase as T^{mitosis}.

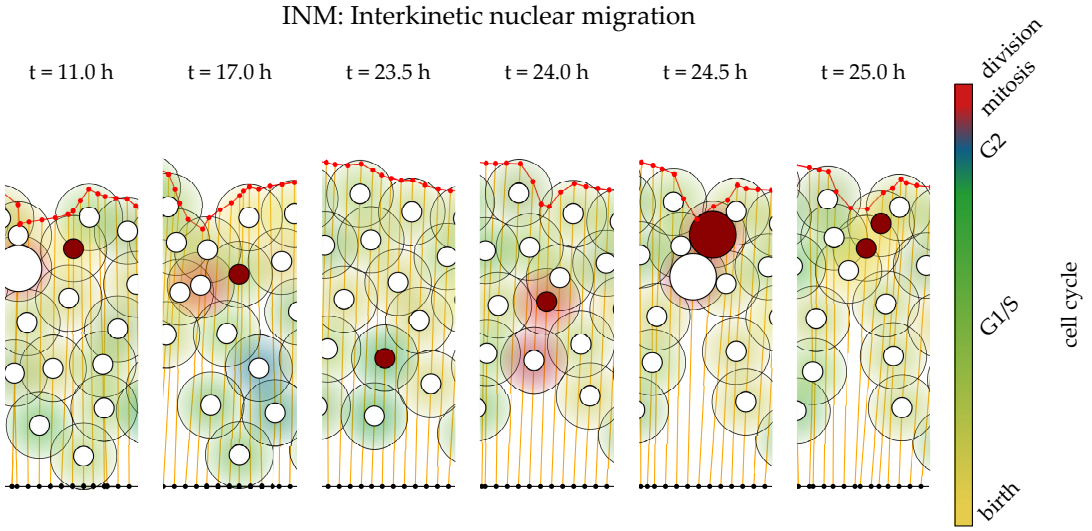

Figure 10. The coloured spheres are the soft spheres which also indicate the current cell cycle. The white (or red) sphere inside is the hard sphere with non-overlapping constraints. **Interkinetic nuclear movement:** In this example, the red cell has a $14\,\mathrm{h}$ long cell cycle which starts at $t = 11\,\mathrm{h}$. During the passive phase, it incrementally moves basally. However, in the last hour, it moves rapidly to the apical layer, increases in size and divides. **Cell division:** Finally, the cell divides into two offsprings. Since we only simulate a 2D slice, only $20\,\%$ of all division yield a second offspring to keep growth rates realistic.

Accordingly, the G2 phase of the ith cell starts when $t_i^{\mathrm{age}} = t_i^{\mathrm{G2}} := t_i^{\mathrm{cycle}} - T^{\mathrm{G2}} - T^{\mathrm{mitosis}}$ and the mitosis phase starts at $t_i^{\mathrm{age}} = t_i^{\mathrm{mitosis}} := t_i^{\mathrm{cycle}} - T^{\mathrm{mitosis}}$.

2.2.2. Adaptive rest lengths. The cytoskeleton is modelled with the apical-nuclei and basal-nuclei springs. The apical and basal springs of the ith cell have adaptive rest lengths, which we denote by $\eta_i^{\mathrm{ax}} \in \mathbb{R}$ and $\eta_i^{\mathrm{bx}} \in \mathbb{R}$. The indices ${}^{\mathrm{ax}}$, ${}^{\mathrm{bx}}$ are used to denote values related to the apical-nuclei and basal-nuclei springs.

The rest lengths of the cytoskeleton are dynamic and follow the differential equations

$$\dot{\eta}_i^{\mathrm{ax}} = -k^{\mathrm{ax}}(\eta_i^{\mathrm{ax}} - \eta_i^{\mathrm{ax}*}), \tag{3.2}$$

$$\dot{\eta}_i^{\mathrm{bx}} = -k^{\mathrm{bx}}(\eta_i^{\mathrm{bx}} - \eta_i^{\mathrm{bx}*}), \tag{3.3}$$

where the parameters $k^{\mathrm{ax}}, k^{\mathrm{bx}} > 0$ denote the speed of adaptation to new desired rest lengths $\eta_i^{\mathrm{ax}*}, \eta_i^{\mathrm{bx}*}$.

The desired rest lengths change depending on the cell phase. During the G1 and the S phase, the cytoskeleton of the cell will adapt to the current extension and, therefore, we set the desired rest lengths to the current extension of the corresponding linear springs.

We define

$$\eta_i^{\mathrm{ax}*} \coloneqq \|\boldsymbol{X}_i - \boldsymbol{A}_i\| - R^{\mathrm{soft}},$$
$$\eta_i^{\mathrm{bx}*} \coloneqq \|\boldsymbol{X}_i - \boldsymbol{B}_i\| - R^{\mathrm{soft}},$$

whenever $t_i^{\mathrm{age}} < t_i^{\mathrm{G2}}$.

2.2.3. Interkinetic nuclear movement. The nuclei movement during the cell cycle is controlled by changing the desired rest lengths of the cells' cytoskeletons.

At the onset of the active G2 phase, the apical cytoskeleton contracts and the basal cytoskeleton extends, which leads to an upward migration of the cells to prepare for cell division. Therefore, when $t_i^{\mathrm{age}} \geq t_i^{\mathrm{G2}}$, we set

$$\eta_i^{\mathrm{ax}*} \coloneqq 0\,\mu\mathrm{m},$$
$$\eta_i^{\mathrm{bx}*} \coloneqq \|\boldsymbol{A}_i - \boldsymbol{B}_i\| - 2R^{\mathrm{soft}}.$$

During the mitosis phase, the nuclei stiffen up and increase in size. We model this by setting

$$R_i^{\mathrm{hard}}(t) \coloneqq 0.7R^{\mathrm{soft}}(t), \tag{3.4}$$

when $t_i^{\mathrm{age}} \geq t_i^{\mathrm{mitosis}}$.

The resulting dynamics are shown in Figure 10.

2.2.4. Apical junctions. For apical junctions, we use linear springs with dynamic rest length, similar as for the cytoskeleton. Apical junctions exists between cells which are next to each other on the apical side of the tissue. Therefore, we define the edges of the apical layer as a set

$$\mathcal{A} \coloneqq \{(1,2),(2,3),\ldots,(N-1,N)\}. \tag{3.5}$$

Each apical junction modelled as linear spring with rest length η_{ij}^{aa} where $(i,j) \in \mathcal{A}$ are indices of apically adjacent cells.

The rest length of the apical-apical springs changes according to

$$\dot{\eta}_{ij}^{\mathrm{aa}} = -k^{\mathrm{aa}}\eta_{ij}^{\mathrm{aa}} \quad \text{for all } (i,j) \in \mathcal{A}, \tag{3.6}$$

where k^{aa} denotes the speed of adaptation.

2.2.5. Cell division. As described earlier, since we only model a 2D slice of a three-dimensional tissue, the growth of the tissue would be too fast if cells divide at a realistic rate. Instead of modifying the cell cycle, we consider that with a probability $p^{\mathrm{div}} \in (0,1)$ both daughter cells will be part of the modelled 2D slice but in the other cases the second daughter cell will be 'outside' of the simulation slice and hence no cell is added to the simulation.

Division with two offsprings.

Let t be the time of cell division and t^+ denote the time right after the cell division. We increase the number of cells $N \mapsto N+1$ and shift the position of all cells by an offset

$$\Delta \boldsymbol{X} \coloneqq 0.05\,\mu\mathrm{m} \begin{pmatrix} 1 \\ 0 \end{pmatrix}, \tag{3.7}$$

and the positions of the new cells are defined as

$$\begin{aligned} \boldsymbol{X}_i(t^+) &\coloneqq \boldsymbol{X}_i(t) - \Delta \boldsymbol{X}, & \boldsymbol{X}_{N+1}(t^+) &\coloneqq \boldsymbol{X}_i(t) + \Delta \boldsymbol{X}, \\ \boldsymbol{A}_i(t^+) &\coloneqq \boldsymbol{A}_i(t) - \Delta \boldsymbol{X}, & \boldsymbol{A}_{N+1}(t^+) &\coloneqq \boldsymbol{A}_i(t) + \Delta \boldsymbol{X}, \\ \boldsymbol{B}_i(t^+) &\coloneqq \boldsymbol{B}_i(t) - \Delta \boldsymbol{X}, & \boldsymbol{B}_{N+1}(t^+) &\coloneqq \boldsymbol{B}_i(t) + \Delta \boldsymbol{X}. \end{aligned}$$

For each offspring, a new duration for the next cell division is generated, i.e.

$$\begin{aligned} t_i^{\mathrm{birth}} = t_{N+1}^{\mathrm{birth}} &\coloneqq t, \\ t_i^{\mathrm{cycle}}, t_{N+1}^{\mathrm{cycle}} &\sim \mathcal{U}(T^{\mathrm{min-age}}, T^{\mathrm{max-age}}). \end{aligned}$$

Moreover, we revert the mitosis-related increase of the hard radius from (3.4), i.e.

$$R_i^{\mathrm{hard}}(t^+) \coloneqq R^{\mathrm{hard}} \tag{3.8}$$

where R^{hard} is the default size of the hard spheres in passive phase.

Finally, the apical network $\mathcal{A}$ will be updated, by adding the edge $(i, N+1)$ and by connecting the former right apical neighbour of the ith cell with the new $N+1$th cell. Equally, the basal network $\mathcal{B}$ will be updated (the basal network will be defined in Section 2.2.6).

Division with one offspring.

For cell division with only one offspring, the total number of cells stays the same and we only generate a new duration for the upcoming cell cycle, i.e.

$$\begin{aligned} t_i^{\mathrm{birth}} &\coloneqq t, \\ t_i^{\mathrm{cycle}} &\sim \mathcal{U}(T^{\mathrm{min-age}}, T^{\mathrm{max-age}}). \end{aligned}$$

The position vectors remain the same. But, we revert the mitosis-related change of the hard radius as in (3.8)

2.2.6. Energy terms. The potential energy of the system is composed by the two linear springs (apical and basal cytoskeleton), linear springs connecting adjacent apical points, the bending spring (cell straightness) and finally the potential for pair-wise soft-repulsion between nuclei.

We define the energy terms in their non-dimensional form as in [Fer+19].

The apical and basal linear springs have potential energy

$$W_i^{\mathrm{ax}} = \frac{\alpha^{\mathrm{ax}}}{R^{\mathrm{soft}} + \eta_i^{\mathrm{ax}}}(\|\boldsymbol{X}_i - \boldsymbol{A}_i\| - R^{\mathrm{soft}} - \eta_i^{\mathrm{ax}})^2, \tag{3.9}$$

$$W_i^{\mathrm{bx}} = \frac{\alpha^{\mathrm{bx}}}{R^{\mathrm{soft}} + \eta_i^{\mathrm{bx}}}(\|\boldsymbol{X}_i - \boldsymbol{B}_i\| - R^{\mathrm{soft}} - \eta_i^{\mathrm{bx}})^2, \tag{3.10}$$

where $\alpha^{\mathrm{ax}}, \alpha^{\mathrm{bx}}$ are the stiffness coefficients of the apical and basal springs and R_i^{soft} denotes the radius of the soft repulsion of each cell. We recall that $\eta_i^{\mathrm{ax}}, \eta_i^{\mathrm{bx}}$ are the (dynamic) rest lengths.

The apical-apical cell junctions are also linear springs

$$W_{ij}^{\mathrm{aa}} = \frac{\alpha^{\mathrm{aa}}}{2R^{\mathrm{soft}}}(\|\boldsymbol{A}_i - \boldsymbol{A}_j\| - \eta_i^{\mathrm{aa}})^2 \quad \text{for all} (i,j) \in \mathcal{A}, \tag{3.11}$$

where α^{aa} denotes the stiffness coefficient and η_i^{aa} is the rest length of the apical-apical spring.

The most complicated part is the straightness energy term which corresponds to a bending spring acting on the angle between the apical-nuclei and basal-nuclei axes. It is defined as

$$W_i^{\mathrm{axb}} = \alpha^{\mathrm{axb}} \left(\frac{(\boldsymbol{A}_i - \boldsymbol{X}_i) \cdot (\boldsymbol{B}_i - \boldsymbol{X}_i)}{\|\boldsymbol{A}_i - \boldsymbol{X}_i\| \|\boldsymbol{B}_i - \boldsymbol{X}_i\|} + 1 \right) \tag{3.12}$$

where α^{axb} is a stiffness coefficient. The equilibrium of W_i^{axb} corresponds to the case when the angle between the apical-nuclei and basal-nuclei axes is $180°$, i.e., if the center of the nucleus $\boldsymbol{X}_i$ lies on the straight line joining the apical and the basal points $(\boldsymbol{A}_i, \boldsymbol{B}_i)$. If we denote the angle as

$$\gamma := \angle(\boldsymbol{A}_i - \boldsymbol{X}_i, \boldsymbol{B}_i - \boldsymbol{X}_i),$$

then we can rewrite the energy in the following way

$$W_i^{\mathrm{axb}} = \alpha^{\mathrm{axb}}(\cos(\gamma) + 1) = \alpha^{\mathrm{axb}}(\cos(\pi) - \cos(\gamma - \pi)),$$

which shows that the equilibrium is at $\gamma = \pi = 180°$.

Finally, we define the energy of the soft-repulsion between cell nuclei. We then define the repulsive energy between two nuclei as a linear spring with a cut-off

$$W_{ij}^{\mathrm{xx}} = \begin{cases} -\frac{\alpha^{\mathrm{xx}}}{2R^{\mathrm{soft}}}(\|\boldsymbol{X}_i - \boldsymbol{X}_j\| - 2R^{\mathrm{soft}})^2 & \text{if } \|\boldsymbol{X}_i - \boldsymbol{X}_j\| \le 2R^{\mathrm{soft}}, \\ 0 & \text{else.} \end{cases} \tag{3.13}$$

Here, α^{xx} denotes the soft-repulsion stiffness between cells and we recall that R^{soft} is the soft radius which defines the disks where the repulsive forces act.

Collecting all these energy terms, we obtain the potential of the entire system

$$W := \sum_{i=1}^{N}(W_i^{\mathrm{ax}} + W_i^{\mathrm{bx}} + W_i^{\mathrm{axb}}) + \sum_{(i,j)\in\mathcal{A}} W_{ij}^{\mathrm{aa}} + \sum_{i=1}^{N}\sum_{j=1}^{i-1} W_{ij}^{\mathrm{xx}}. \tag{3.14}$$

2.2.7. Constraints. We consider four kinds of constraints. First, to model volume exclusion, which is a strict non-overlap constraint between the hard spheres of each cell, i.e.,

$$\|\boldsymbol{X}_j - \boldsymbol{X}_i\| \geq R_j^{\text{hard}} + R_i^{\text{hard}} \quad \text{for } 1 \leq i < j \leq N, \tag{C1}$$

where R_i^{hard} denotes the radius of the ith hard sphere.

The other constraints determine the shape of the basal layer. The first condition enforces a maximal distance $d^{\max-\text{basal}}$ between two consecutive basal points, i.e.

$$\|\boldsymbol{B}_j - \boldsymbol{B}_i\| \leq d^{\max-\text{basal}}, \quad (i,j) \in \mathcal{B} \tag{C2}$$

where $\mathcal{B}$ are all edges of neighbouring basal points

$$\mathcal{B} = \{(1,2),(2,3),\dots,(N-1,N)\}. \tag{3.15}$$

The second condition keeps all basal points on a fixed line which represents the basal layer. We consider the basal layer to be a static straight line. Therefore, all basal points are restricted to the static basal layer, which is exactly the x-axis, i.e.,

$$\boldsymbol{B}_i \in S^{\text{basal}-\text{layer}} := \mathbb{R} \times \{0\}. \tag{C3}$$

Additionally, all basal points have a fixed order. If we denote the x-coordinate of a basal point as $x(\boldsymbol{B}_i)$, then the condition reads:

$$x(\boldsymbol{B}_j) - x(\boldsymbol{B}_i) \geq 0, \quad \text{for all } (i,j) \in \mathcal{B}. \tag{C4}$$

Finally, we can combine all constraints (C1) to (C4) to obtain the set of feasible states as

$$S := \{(\boldsymbol{\mathcal{X}}, \boldsymbol{\mathcal{A}}, \boldsymbol{\mathcal{B}}) \in \mathbb{R}^{6N} \mid \text{such that (C1) to (C4) are satisfied}\} \tag{3.16}$$

2.2.8. The quasi-steady state model. After collecting all components of the model, we can now state the full quasi-steady state model from [Fer+19].

Notation. In the following we have to deal with discrete time-stepping schemes. We will use the following convention. *Lower indices refer to individual cells and upper indices denote the current time-step.* For example: $\boldsymbol{\mathcal{X}}^k$ is the kth time-step, $\boldsymbol{X}_i^k$ is the ith cell at the kth time-step. When the time-step is not important we just write $\boldsymbol{X}_i$ to denote the position of the ith cell.

The dynamic cell parameters of the ith cell are $\boldsymbol{P}_i = (R_i^{\text{hard}}, \eta_i^{\text{ax}*}, \eta_i^{\text{bx}*})$ which are the hard radius and the desired rest lengths of the apical-nuclei and basal-nuclei springs. We write $\boldsymbol{\mathcal{P}} = (\boldsymbol{P}_1, \dots, \boldsymbol{P}_N) \in \mathbb{R}^{3N}$ for the collection of all these parameters.

Model 3.1 (Quasi steady-state model (QSS model))**.** The model as proposed in [Fer+19] is discrete in time. The initial data consists out of the initial configuration $\boldsymbol{\mathcal{Z}}^0 \in \mathbb{R}^{6N}$ at $t_0 = 0$, initial rest lengths $\boldsymbol{\eta}^{\text{ax},0}, \boldsymbol{\eta}^{\text{bx},0}$ and $\boldsymbol{\eta}^{\text{aa},0}$ and initial cell parameters $\boldsymbol{\mathcal{P}}^0$. Let $\Delta t > 0$ be the discrete time increment. Given the state of the system at time $t_k = k\Delta t$, as $(\boldsymbol{\mathcal{Z}}^k, \boldsymbol{\mathcal{P}}^k)$, we compute the state of the system at the next time step as follows:

- Increase time step $t_{k+1} = t_k + \Delta t$.
- Perform cell division as defined in Section 2.2.5. (This step possibly updates $\boldsymbol{\mathcal{Z}}^k$ and $\boldsymbol{\mathcal{P}}^k$ and increases their dimensions if new cells are born.)
- Update dynamic cell parameters $\boldsymbol{\mathcal{P}}^k \mapsto \boldsymbol{\mathcal{P}}^{k+1}$. This step updates the hard radii R_i^{hard} (increase during mitosis), see Section 2.2.3 and it sets the desired rest lengths $\eta_i^{\mathrm{ax}*}, \eta_i^{\mathrm{bx}*}$ according to the cell cycle (see Section 2.2.3).
- Update adaptive rest lengths $\eta_i^{\mathrm{ax}}, \eta_i^{\mathrm{bx}}, \eta_i^{\mathrm{aa}}$ (see Sections 2.2.2 and 2.2.4).
- Add noise to the nuclei positions

$$\tilde{\boldsymbol{X}}_i^{k+1} - \boldsymbol{X}_i^k \sim \mathcal{N}_2(0, 2D\Delta t), \tag{3.17}$$

  where $\mathcal{N}_2(0, 2D\Delta t)$ denotes the 2 dimensional normal distribution with diagonal covariance matrix. The positions $\tilde{\boldsymbol{\mathcal{X}}} k+1 \in \mathbb{R}^{2N}$ are used in the next step as initial value for the energy minimisation.

- Find a local minimum close to the current state $(\boldsymbol{\mathcal{A}}^k, \tilde{\boldsymbol{\mathcal{X}}}^{k+1}, \boldsymbol{\mathcal{B}}^k)$ of the following constrained minimisation problem

$$\boldsymbol{\mathcal{Z}}^{k+1} \in \operatorname*{argmin}_{\boldsymbol{\mathcal{Z}} \in S} W(\boldsymbol{\mathcal{Z}}, \boldsymbol{\mathcal{P}}^{k+1}).$$

  The potential energy W incorporates the energies coming from the apical-apical, apical-nuclei, basal-nuclei springs; the soft repulsion force between nuclei; the straightness force between the apical-basal connection (Section 2.2.6). The feasible set S enforces non-overlap of the hard disks positioned inside each nuclei and constrain the basal points to the x-axis, see Section 2.2.7.

Remark 3.2 (Regularisation)**.** The local minimisation in the QSS model might not be unique in some circumstances. One might add a regularising term

$$\boldsymbol{\mathcal{Z}}^{k+1} \coloneqq \operatorname*{argmin}_{\boldsymbol{\mathcal{Z}} \in S} \Big(W(\boldsymbol{\mathcal{Z}}, \boldsymbol{\mathcal{P}}^k) + c\|\boldsymbol{\mathcal{Z}} - \boldsymbol{\mathcal{Z}}^k\| \Big)$$

where $c > 0$ is a constant.

However, we will later replace the QSS model with an overdamped Newtonian model which resolves the uniqueness issues.

2.2.9. Calibration of the model parameters. In the following we collect all the model parameters, which are exactly as in [Fer+19]. The values and units are shown in Tables 1 and 2.

For a detailed discussion of the parameter choices we also refer to [Fer+19]. We will just summarise a few key points.

- The diffusion coefficient D was measured from in vivo experimental data of individual cell trajectories.

- Timings and distances were obtained from experimental data as well, however, the real tissue is not a straigth line, therefore these values represent an idealised patch of the tissue. However, by counting the number of layers that the cells form in vivo, one can estimate values for $d^{\mathrm{init-apical}}, d^{\mathrm{max-basal}}$ depending on the number of cells.
- The soft and hard radii $R^{\mathrm{soft}}, R^{\mathrm{hard}}$ are used to model the fact that cells are deformable and can adapt ellipsoidal shapes. Here, R^{soft} represents the longest axis of the cell shape and R^{hard} the shortest axis.
- The stiffness coefficients are relative to each other (since the model is non-dimensional). The parameters were fitted such that the growth of the tissue in height and width fits to the real behaviour of the tissue.

parameter	value	description
N^{init}	60	number of cells
h^{init}	$50\,\mu\mathrm{m}$	initial tissue height
w^{init}	$40\,\mu\mathrm{m}$	initial tissue width
$d^{\mathrm{init-apical}}$	$1.66\,\mu\mathrm{m}$	initial distance between apical points
$d^{\mathrm{max-basal}}$	$0\,\mu\mathrm{m}$	maximal allowed distance between basal points
p^{div}	$20\,\%$	probability of division with single offspring
D	$2.5\,\mu\mathrm{m}^2/\mathrm{h}$	diffusion coefficient

Table 1. Default model parameters used for simulations. The cell specific parameters are given in Table 2.

2.3. Computational methods for the PSE model

In [DFM17], the authors developed a new numerical method to solve sphere packing problems which were applied (by the same authors) to the PSE model. The proposed method is called the damped Arrow-Hurwicz algorithm (DAHA) and it generalises the Arrow-Hurwicz algorithm [Vaj60].

The essential idea is to solve a minimisation problem with constraints of the form,

$$\operatorname*{argmin}_{\boldsymbol{\mathcal{Z}} \in S} W(\boldsymbol{\mathcal{Z}}) \tag{3.18}$$

using an augmented Lagrangian approach.

For the minimisation algorithm, the representation of the feasible set S is relevant. Let us assume that S is defined by inequality constraint functions, i.e.

$$\boldsymbol{\mathcal{Z}} \in S \quad \Leftrightarrow \quad g_\ell(\boldsymbol{\mathcal{Z}}) \geq 0, \quad \text{for all } 1 \leq \ell \leq M, \tag{3.19}$$

where M is the total number of constraints. For example, in the setup of Section 2.2.7 we have $M = \frac{N(N-1)}{2} + 2(N-1) + N$ constraints.

parameter	value	description
R^{soft}	$5\,\mu\text{m}$	radius of soft repulsion
R^{hard}	$1.66\,\mu\text{m}$	radius of non-overlap (during S/passive G2 phase)
$R^{\text{hard,G2}}$	$0.7R^{\text{soft}}$	radius of non-overlap (during active G2, mitosis phase)
η^{init}	$7.5\,\mu\text{m}$	initial rest length of linear springs (cytoskeleton)
T^{G2}	$30\,\text{min}$	duration of G2 phase
T^{mitsis}	$30\,\text{min}$	duration of mitosis
$T^{\text{min}-\text{cycle}}$	$10\,\text{h}$	minimal duration of full cell cycle
$T^{\text{max}-\text{cycle}}$	$21\,\text{h}$	maximal duration of full cell cycle
k^{aa}	$1\,\text{h}^{-1}$	adaption speed of apical-apical spring
k^{ax}	$5\,\text{h}^{-1}$	adaption speed of apical-nuclei spring
k^{bx}	$5\,\text{h}^{-1}$	adaption speed of basal-nuclei spring
α^{aa}	5	stiffness of apical-apical spring
α^{ax}	2	stiffness of apical-nuclei spring
α^{bx}	2	stiffness of basal-nuclei spring
α^{xx}	1	stiffness of nuclei-nuclei repulsion
α^{axb}	15	stiffness bending spring (straightness)

Table 2. Default cell parameters for neural tube cells.

parameter	value	description
Δt	$0.1\,\text{h}$	time step (between cell events)

Table 3. Numerical parameters used for simulations.

Since the convergence rates can depend on the representation, we define g_ℓ as the square of (C1) to (C4). The constraint (C3) might be implemented by eliminating the y-coordinates of $\boldsymbol{B}_i$ from the entire model.

The principle idea of the Uzawa-Arrow-Hurwicz algorithm [AHU58] is to find a related dynamic system such that solutions to the minimisation problems are hopefully attractive equilibria of the constructed dynamical system.

In the following, we will only outline the algorithms. For a more detailed exposition of the damped Arrow-Hurwicz algorithm using the Lagrangian approach, we refer to [DFM17].

The Uzawa-Arrow-Hurwicz algorithm can be derived as a nonlinear variant of the Uzawa algorithm (see Appendix 1) applied to the saddle-point problem

$$\inf_{\boldsymbol{\mathcal{Z}}\in\mathbb{R}^{6N}} \sup_{\boldsymbol{\lambda}\in\mathbb{R}^{M}} \mathcal{L}(\boldsymbol{\mathcal{Z}},\boldsymbol{\lambda}) \tag{3.20}$$

for the Lagrangian

$$\mathcal{L}(\boldsymbol{\mathcal{Z}},\boldsymbol{\lambda}) = W(\boldsymbol{\mathcal{Z}}) + \sum_{\ell=1}^{M} \lambda_\ell \min(0, g_\ell(\boldsymbol{\mathcal{Z}})).$$

Solutions of (3.20) will also be solutions of the original problem (3.18).

The key idea of the Arrow-Hurwicz algorithm is to approximate solutions of (3.20) by solving $\inf_{\boldsymbol{\mathcal{Z}}\in\mathbb{R}^{6N}} \mathcal{L}(\boldsymbol{\mathcal{Z}},\boldsymbol{\lambda}_n)$ and $\sup_{\boldsymbol{\lambda}\in\mathbb{R}^{M}} \mathcal{L}(\boldsymbol{\mathcal{Z}}_n,\boldsymbol{\lambda})$ iteratively for fixed values $\boldsymbol{\mathcal{Z}}_{n+1}, \boldsymbol{\lambda}_n$.

In the following we will use lowercase $\boldsymbol{z}\in\mathbb{R}^{6N}$ to denote the states during the iterations of the minimisation algorithms.

Method 3.3 (Arrow-Hurwicz algorithm)**.** Let α, β be fixed parameters for the step size of the gradient descent methods.

To find a local minimum around $\boldsymbol{z}_0$, we pick $\boldsymbol{\lambda}_0 \coloneqq \mathbf{0} \in \mathbb{R}^M$ and iterate the following steps until convergence for $n > 0$

- We compute $\boldsymbol{z}_{n+1}$ as

$$\boldsymbol{z}_{n+1} \coloneqq \boldsymbol{z}_n - \alpha(\nabla_{\boldsymbol{z}} W(\boldsymbol{z}_n) + \sum_{\ell=1}^{M} \lambda_\ell \nabla_{\boldsymbol{z}} g_\ell(\boldsymbol{z}_n)).$$

- Using the previously compute value for $\boldsymbol{z}_{n+1}$, we compute $\boldsymbol{\lambda}_{n+1}$ via

$$\lambda_{\ell,n+1} \coloneqq \min(0, \lambda_{\ell,n} - \beta g_\ell(\boldsymbol{z}_{n+1})).$$

  where $\lambda_{\ell,n}$ denotes the ℓth component of $\boldsymbol{\lambda}$ at the nth step.

For the analysis of the Arrow-Hurwicz method, one can consider the Arrow-Hurwicz algorithm as the semi-implicit Euler method applied to the system

$$\dot{\boldsymbol{z}} = -\alpha(\nabla_{\boldsymbol{z}} W(\boldsymbol{z}) + \sum_{\ell=1}^{M} \lambda_\ell \nabla_{\boldsymbol{z}} g_\ell(\boldsymbol{z})) \tag{3.21}$$

$$\dot{\lambda}_\ell = \begin{cases} 0 & \text{if } \lambda_\ell = 0 \text{ and } g_\ell(\boldsymbol{z}) \geq 0 \\ -\beta g_\ell(\boldsymbol{z}) & \text{otherwise.} \end{cases} \tag{3.22}$$

The dynamical system (3.21) and (3.22) has every solution of (3.18) as an equilibrium.

As observed in [DFM17], the direct application of the Arrow-Hurwicz algorithm does not always converge for the problem of non-overlapping spheres. This motivated the damped Arrow-Hurwicz algorithm (DAHA) where the dynamics from (3.21) and (3.22) are modified by considering the second-order system with damping.

Replacing (3.21) with

$$\ddot{\boldsymbol{\mathcal{Z}}} = -c\dot{\boldsymbol{\mathcal{Z}}} - \alpha\left(\nabla_{\boldsymbol{\mathcal{Z}}} W(\boldsymbol{\mathcal{Z}}) - \sum_{\ell=1}^{M} \lambda_\ell \nabla_{\boldsymbol{\mathcal{Z}}} g_\ell(\boldsymbol{\mathcal{Z}})\right) - \gamma \sum_{\ell=1}^{M} \lambda_\ell g_\ell(\boldsymbol{\mathcal{Z}}) \nabla_{\boldsymbol{\mathcal{Z}}} g_\ell(\boldsymbol{\mathcal{Z}}) \tag{3.23}$$

we obtain a different dynamical system which has also all solutions of (3.18) as equilibria. This equation was derived by taking a time derivative of the DAHA method and then replacing one term to remove oscillatory solutions.

A discretisation of (3.22) and (3.23) yields the damped Arrow-Hurwicz algorithm (DAHA).

Method 3.4 (Damped Arrow-Hurwicz algorithm)**.** Given an initial state and parameters α, β, γ, c, a local minimum of $\operatorname{argmin}_{\boldsymbol{\mathcal{Z}} \in S} W(\boldsymbol{\mathcal{Z}})$ around $\boldsymbol{z}_0 \in \mathbb{R}^{6N}$ is computed with the following steps:

- Initialise $\boldsymbol{z}_1 \coloneqq \boldsymbol{z}_0$ and $\boldsymbol{\lambda}_0 = \mathbf{0} \in \mathbb{R}^M$.
- Iterating for $n \geq 1$ the following steps until

$$\frac{1}{\Delta\tau}\|\boldsymbol{z}_{n+1} - \boldsymbol{z}_n\| \leq \varepsilon \|\boldsymbol{z}_n\|. \tag{3.24}$$

  - Compute $\boldsymbol{z}_{n+1}$ such that

$$\begin{aligned} \frac{1}{\Delta\tau^2}\Big(\boldsymbol{z}_{n+1} - 2\boldsymbol{z}_n + \boldsymbol{z}_{n-1}\Big) = &-\frac{c}{2\Delta\tau}\left(\boldsymbol{z}_{n+1} - \boldsymbol{z}_{n-1}\right) \\ &-\alpha\left(\nabla_{\boldsymbol{z}} W(\boldsymbol{z}_n) - \sum_{\ell=1}^{M} \lambda_{\ell,n} \nabla_{\boldsymbol{z}} g_\ell(\boldsymbol{z}_n)\right) \\ &-\gamma\left(\sum_{\ell=1}^{M} g_\ell(\boldsymbol{z}_n)\lambda_{\ell,n} \nabla_{\boldsymbol{z}} g_\ell(\boldsymbol{z}_n)\right) \end{aligned} \tag{3.25}$$

  - Update the Lagrangian multipliers

$$\lambda_{\ell,n+1} = \min(0, \lambda_{\ell,n} - \Delta\tau\beta g_\ell(\boldsymbol{z}_n)).$$

    where $\lambda_{\ell,n}$ represents the ℓth component of $\boldsymbol{\lambda}_n$.

Remark 3.5. One can reduce the parameters in (3.25). For example, we can choose without loss of generality $\Delta\tau = 1$.

	α	β	γ	c	$\Delta\tau$	ε
value	10^{-4}	0.25	10^{-3}	2	1	10^{-6}

Table 4. Numerical parameters for the DAHA method as used in [Fer+19].

Solving (3.25) for $\boldsymbol{z}_{n+1}$ yields,

$$\begin{aligned}\boldsymbol{z}_{n+1} = \frac{1}{1+\frac{1}{2}\Delta\tau c}\Big(&2\boldsymbol{z}_n - (1-\frac{1}{2}\Delta\tau c)\boldsymbol{z}_{n-1} \\ &- \Delta\tau^2\alpha\Big(\nabla_{\boldsymbol{z}} W(\boldsymbol{z}_n) - \sum_{\ell=1}^{M}\lambda_{\ell,n}\nabla_{\boldsymbol{z}} g_\ell(\boldsymbol{z}_n)\Big) \\ &- \Delta\tau^2\gamma\Big(\sum_{\ell=1}^{M} g_\ell(\boldsymbol{z}_n)\lambda_{\ell,n}\nabla_{\boldsymbol{z}} g_\ell(\boldsymbol{z}_n)\Big)\Big).\end{aligned}$$

We observe that for $c = \frac{2}{\Delta\tau}$ the method reduces to a one-step method.

In the numerical comparison study [DFM17], the DAHA method was shown to improve the Arrow-Hurwicz method in application to sphere packing problems. For special cases such as $N = 2$ one can show that the underlying dynamical system (3.22) and (3.23) has an attractive equilibrium which coincides with a local minimum of the constrained minimisation problem (3.18)

2.3.1. Choice of parameters for DAHA method. The choice of parameters for the DAHA method requires a balance between runtime and accuracy.

Especially the energy terms can lead to instabilities, since (3.25) is a non-stiff time stepping method applied to the potentially stiff system (3.23), depending on the energies. Such instabilities can lead to non-terminating conditions of the iteration since the numerical errors in each step might be larger than the demanded accuracy.

Increasing the damping coefficient c and the time-step size Δt can reduce the numerical instabilities, but it also directly increases the number of required iterations.

The simulations in [Fer+19] use parameters as in Table 4. We note that the damping coefficient c is relatively large compared to α and γ. For the particular choice, the update rule reads simplifies to

$$\boldsymbol{z}_{n+1} = \boldsymbol{z}_n - \alpha\nabla_{\boldsymbol{z}} W(\boldsymbol{z}_n) + \sum_{\ell=1}^{M}\left(\alpha\lambda_{\ell,n} - \gamma\lambda_{\ell,n} g_\ell(\boldsymbol{z}_n)\right)\nabla_{\boldsymbol{z}} g_\ell(\boldsymbol{z}). \tag{3.26}$$

We see in particular, that the Damped Arrow-Hurwicz Algorithm approaches the equilibrium on an overdamped trajectory.

These parameters represent a compromise between runtime, stability and accuracy, as we will see in the next section.

2.3.2. Discussion of the stopping criterium. In the following we will show an error estimate for DAHA which will later explain why DAHA prefers solutions which are close the starting point.

Remark 3.6 (Error estimate for DAHA)**.** The stopping criterium (3.24) looks very unsuspicious, but because of the added damping, its role changes compared to the classical Arrow-Hurwicz algorithm.

Let us consider the situation without constraints, e.g. $M = 0$, and with parameters as in Table 4. In this case the DAHA method reduces to a gradient decent method with fixed step size.

Given a starting point $\boldsymbol{z}_0 \in \mathbb{R}^{6N}$, let $n^* \in \mathbb{N}$ be the index at which the stopping criterium (3.24) is satisfied for the first time.

For parameters as in Table 4, the update rule for $\boldsymbol{z}_n$ is simply a gradient decent method

$$\boldsymbol{z}_{n+1} = \boldsymbol{z}_n - \alpha \nabla_{\boldsymbol{z}} W(\boldsymbol{z}_n) \tag{3.27}$$

Inserting (3.27) into the stopping criterium (3.24) yields

$$\frac{\|\nabla_{\boldsymbol{z}} W(\boldsymbol{z}_{n^*})\|}{\|\boldsymbol{z}_{n^*}\|} \leq \frac{\varepsilon}{\alpha} = \frac{10^{-6}}{10^{-4}} = 0.01.$$

This shows that the error of the minimisation is on the scale $\frac{\varepsilon}{\alpha}$. We note that this does not imply that the error of the minimisation is just $1\,\%$. The crucial point here is that not $\varepsilon = 10^{-6}$ but $\frac{\varepsilon}{\alpha} = 0.01$ determines the accuracy of the approximation.

3. Modification of the PSE model

In this section, we will present our modifications of the PSE model, which will improve the runtime and stability of simulations. The principle idea is to replace the quasi-steady state simulation by an overdamped Newton equation. Using the theory from Chapter 1 and the PBD method from Chapter 2, we obtain a well-posed model with a fast numerical discretisation.

Without noise and cell events, the mechanics of the new model is

$$\mu \dot{\boldsymbol{\mathcal{Z}}} \in -\nabla_{\boldsymbol{\mathcal{Z}}} W(\boldsymbol{\mathcal{Z}}) - N(S, \boldsymbol{\mathcal{Z}})$$

where μ denotes the damping coefficient and $N(S, \boldsymbol{\mathcal{Z}})$ the normal cone of S at $\boldsymbol{\mathcal{Z}}$. When we add noise and cell events to the model, we a PSE model related to the QSS-PSE model. We will call this new model the *first-order PSE model* (FO-PSE).

The main goal of this section is to show that this new FO-PSE model gives actually equivalent simulations results matching to simulations of the QSS-PSE model with DAHA.

The FO-PSE model yields the following improvements:

- **Runtime:** On a modern computer[1], our implementation of the PSE model with DAHA takes around $27\,\mathrm{s}$ to simulate $10\,\mathrm{h}$ of epithelial tissue growth. With the FO-PSE model and the PBD method, we can bring this down to $0.08\,\mathrm{s}$, which is over $300\times$ faster.
- **Stability:** In roughly every fourth situation, the DAHA solver has stability issues which lead to non-terminating states. Given that each simulation of the OSS-PSE model requires hunderds minimisations of non-convex problems, it is in general difficult to find a stuitable solver for this task and it is not clear if the minimisation is also sometimes ill-defined. By changing to the easier and well-posed overdamped Newton equation, we can fix these stability issues.
- **Consistency with previous results:** The fitting to experimental data is often one of the crucial bottlenecks of interdisciplinary research. Therefore, we strictly wanted to avoid any duplicated work such as re-fitting parameters to make a new model work. With the right choice of the damping coefficient, the FO-PSE model reproduces the results from [Fer+19]. This was also the main reason, why we did not simply replace DAHA with another solver.

3.1. Derivation of an equivalent overdamped model

Figure 11 shows the number of iterations which DAHA during simulation of the PSE model. For the default parameter $\varepsilon = 10^{-6}$, the number of iterations in most cases close to $n^* \approx 7500$. This allows us to rescale the dynamical system which DAHA solves. Teh rescaled system serves as the main equation in our new model, replacing the quasi-steady state approach.

Let us consider (without loss of generality) the first time step of the OSS-PSE model. We denote the starting point of the energy minimisation as $\boldsymbol{z}_0 = \boldsymbol{\mathcal{Z}}^0 \in \mathbb{R}^{6N}$.

In the following we will ignore the constraints to simplify the computation.

Taking (3.26) as a starting point, we see that the terminal state of the DAHA is the end point of the following gradient flow problem

$$\frac{\mathrm{d}\boldsymbol{z}}{\mathrm{d}\tau} = -\alpha \nabla_{\boldsymbol{z}} W(\boldsymbol{z}), \tag{3.28}$$

for $\tau \in [0, n^*]$ and where n^* denotes the iteration at which the stopping criterium is satisfied.

The next time step is therefore approximatively

$$\boldsymbol{\mathcal{Z}}^1 \approx \boldsymbol{z}(n^*). \tag{3.29}$$

[1] Intel i7-9750H CPU with six cores 2.6 GHz and sufficient RAM.

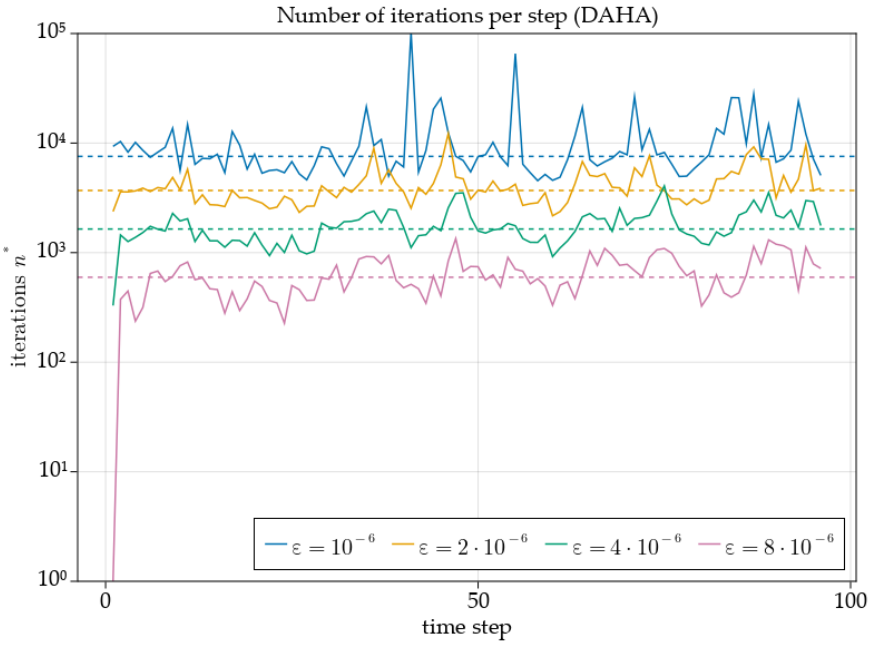

Figure 11. Number of iterations used by the DAHA method for different tolerance parameters. The dashed lines show the average number of iterations per time step.

Since $\boldsymbol{\mathcal{Z}}^1$ represents the state at time $t = \Delta t$, we can now match these two timescales (t and τ), by defining the time-scaling constant

$$\delta := \frac{\Delta t}{n^*}$$

and applying the transformation

$$t := \delta\tau, \quad \tilde{\boldsymbol{z}}(t) := \boldsymbol{z}(\tau), \quad \frac{\mathrm{d}\tilde{\boldsymbol{z}}}{\mathrm{d}t} = \frac{\mathrm{d}\boldsymbol{z}}{\mathrm{d}\tau}\frac{\mathrm{d}\tau}{\mathrm{d}t} = \delta^{-1}\frac{\mathrm{d}\boldsymbol{z}}{\mathrm{d}\tau}.$$

which yields the system

$$\delta\frac{\tilde{\boldsymbol{z}}}{\mathrm{d}t} = -\alpha\nabla_{\boldsymbol{z}}W(\tilde{\boldsymbol{z}}) \tag{3.30}$$

for $t \in [0, \Delta t]$. Figure 12 sketches this rescaling.

Therefore, we can approximate the transition between $\boldsymbol{\mathcal{Z}}^0$ and $\boldsymbol{\mathcal{Z}}^1$ with a continuous system

$$\mu\boldsymbol{\mathcal{Z}} = -\nabla_{\boldsymbol{\mathcal{Z}}}W(\boldsymbol{\mathcal{Z}}) \tag{3.31}$$

where the damping coefficient is $\mu = \frac{\delta}{\alpha}$.

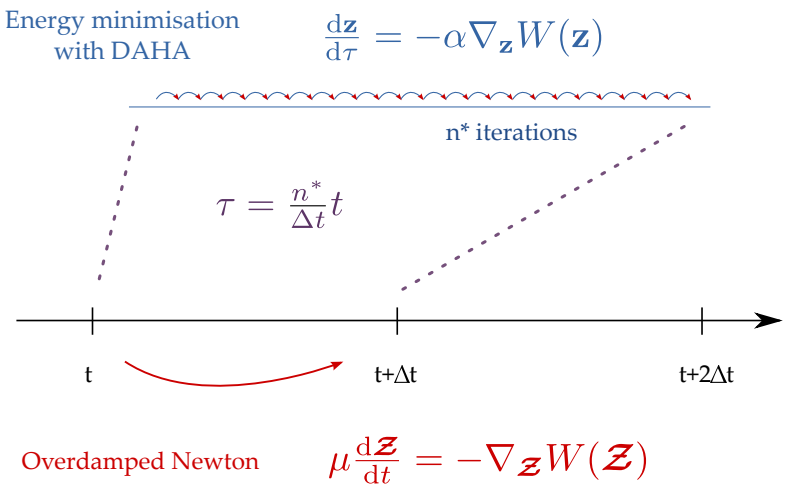

Figure 12. Sketch of the derivation: We lift us the internal dynamics of the DAHA method as the new equation for the FO-PSE model.

If we now assume that the number of iterations in the DAHA method is always similar to $n^* = 7500$, then we obtain

$$\mu = \frac{\Delta t}{n^*\alpha} = \frac{0.1}{7500 \cdot 10^{-4}} = 0.1333. \tag{3.32}$$

Here, the choice of n^* is the median obtained from Figure 11. We will later see that this choice is almost optimal.

3.2. The first-order PSE model

The previous section showed that than the transition $\boldsymbol{\mathcal{Z}}^k$ and $\boldsymbol{\mathcal{Z}}^{k+1}$ uis close to the dynamics of (3.31). The derivation was without taking constraints into account, we therefore have to reintroduce the constraints back into the model. Here, we use directly the formalism of differential inclusions from Chapter 1. This yields to following overdamped Newton equation as a candidate for our new first-order PSE model

$$\mu\dot{\boldsymbol{\mathcal{Z}}} \in -\nabla_{\boldsymbol{\mathcal{Z}}}W(\boldsymbol{\mathcal{Z}}) - N(S, \boldsymbol{\mathcal{Z}}).$$

Since the set S is uniformly prox-regular by Proposition 1.22, we obtain from Theorem 1.31 and Lemma 1.32 the well-posed of this equation.

In addition, we could add noise to this equation, which yields a *stochastic differential inclusion*

$$\mu\,\mathrm{d}\boldsymbol{\mathcal{Z}} \in -\nabla_{\boldsymbol{\mathcal{Z}}}W(\boldsymbol{\mathcal{Z}})\mathrm{d}t - N(S, \boldsymbol{\mathcal{Z}})\mathrm{d}t + \sqrt{2D}\mathrm{d}\boldsymbol{W}_{\boldsymbol{\mathcal{X}}} \tag{3.33}$$

where D is the diffusion coefficient and $\boldsymbol{W}_{\boldsymbol{\mathcal{X}}}$ denotes a Brownian motion with respect to the $\boldsymbol{\mathcal{X}}$ variable in $\boldsymbol{\mathcal{Z}} = (\boldsymbol{\mathcal{A}}, \boldsymbol{\mathcal{B}}, \boldsymbol{\mathcal{X}})$.

We define the FO-PSE model as (3.33) together the discontinuous cell events as in Model 3.1.

3.3. Application of position-based dynamics

We use the PBD method from Chapter 2 for the numerical discretisation of (3.33). The PBD method is applicable, since all inequality constraints are unilateral or bilateral constraints between either the nuclei positions (non-overlap of hard spheres (C1)) or conditions for the basal points ((C2) to (C4)). All these constraints have in common, that it is very easy to explicity compute the projection for each individual constraint.

Let us denote the feasiable states for each individual constraint as S_j, e.g.

$$S_j \coloneqq \{\boldsymbol{\mathcal{Z}} \mid g_j(\boldsymbol{\mathcal{Z}}) \geq 0\} \quad \text{for } 1 \leq j \leq M.$$

Then we have

$$S = \bigcap_{j=1}^{M} S_j$$

which is the key assumption for the application of PBD.

In the following, we will use the notation

$$\Phi_{\Delta t}^{\mathrm{PBD}}(\boldsymbol{\mathcal{Z}}) = P_{S_1} \circ \cdots \circ \mathrm{P}_{S_M}\left(\boldsymbol{\mathcal{Z}} - \frac{\Delta t}{\mu}\nabla_{\boldsymbol{\mathcal{Z}}} W(\boldsymbol{\mathcal{Z}})\right)$$

to denote one step of the PBD method. To improve the runtime, it is useful to perform the update of parameters and cell events not in every time-step of the PBD method. Therefore, we define the numerical parameter $n^{\mathrm{sub-step}} = 20$ which is the number of uninterrupted PBD steps before updating parameters and cell events. We write

$$\Phi^{\mathrm{PBD}}(\boldsymbol{\mathcal{Z}}) = \left(\Phi_{\Delta t/n^{\mathrm{sub-steps}}}^{\mathrm{PBD}}\right)^{n^{\mathrm{sub-steps}}}(\boldsymbol{\mathcal{Z}}). \tag{3.34}$$

This yields the following implementation of the FO-PSE model.

Method 3.7 (Numerical implementation of the FO-PSE model with PBD)**.** We consider the same initial setup as in Model 3.1. Let $\Delta t > 0$ be the discrete time increment. Given the state of the system at time $t_k = k\Delta t$, as $(\boldsymbol{\mathcal{Z}}^k, \boldsymbol{\mathcal{P}}^k)$, we compute the state of the system at the next time step as follows:

- Increase time step $t_{k+1} = t_k + \Delta t$.
- Perform cell division as defined in Section 2.2.5. (This step possibly updates $\boldsymbol{\mathcal{Z}}^k$ and $\boldsymbol{\mathcal{P}}^k$ and increases their dimensions if new cells are born.)
- Update dynamic cell parameters $\boldsymbol{\mathcal{P}}^k \mapsto \boldsymbol{\mathcal{P}}^{k+1}$. This step updates the hard radii R_i^{hard} (increase during mitosis), see Section 2.2.3 and it sets the desired rest lengths $\eta_i^{\mathrm{ax}*}, \eta_i^{\mathrm{bx}*}$ according to the cell cycle (see Section 2.2.3).
- Update adaptive rest lengths $\eta_i^{\mathrm{ax}}, \eta_i^{\mathrm{bx}}, \eta_i^{\mathrm{aa}}$ (see Sections 2.2.2 and 2.2.4).

parameter	value	description
μ	$0.15\,\mathrm{h}^{-1}$	Damping coefficient
$n^{\mathrm{sub-steps}}$	20	Substeps of the PBD method

Table 5. New parameters for the FO-PSE model. With this choice of the damping coefficient, the simulations match with [Fer+19].

- Add noise to the nuclei positions

$$\tilde{\boldsymbol{X}}_i^{k+1} - \boldsymbol{X}_i^k \sim \mathcal{N}_2(0, 2D\Delta t), \tag{3.35}$$

  where $\mathcal{N}_2(0, 2D\Delta t)$ denotes the 2 dimensional normal distribution with diagonal covariance matrix.

- Apply the time stepping of the PBD method (3.34) with $n^{\mathrm{sub-steps}}$ many substeps:

$$\boldsymbol{\mathcal{Z}}^{k+1} = \Phi^{\mathrm{PBD}}(\tilde{\boldsymbol{\mathcal{Z}}}^k)$$

  where $\tilde{\boldsymbol{\mathcal{Z}}}^k := \tilde{\boldsymbol{\mathcal{Z}}}^k = (\boldsymbol{\mathcal{A}}^k, \boldsymbol{\mathcal{B}}^k, \tilde{\boldsymbol{\mathcal{X}}}^k)$ is the previous state with noise added to the nuclei positions.

The new simulation approach uses exactly the same parameters as the QSS-PSE model, with only the two additions from Table 5.

3.4. Numerical comparison between OSS-PSE and FO-PSE model

The theoretical derivation depends on assumptions, for example, that the energy terms dominate the system. To ensure that these approximations hold in the indented application, we compare simulations of the OSS-PSE model with the FO-PSE model.

In the following, we compare two simulations

(1) **DAHA with** $\varepsilon = 10^{-6}$: This is the control case which want to reproduce,

(2) **PBD with** $\mu = 0.14$: Theoretical prediction of the matching damping coefficient.

Before looking at the outcome, we want to report the runtime and stability differences:

- **Runtime:** PBD needed $0.08\,\mathrm{s}$ whereas DAHA used $28\,\mathrm{s}$ for the same task. This corresponds to a $300\times$ speed-up. The faster simulation is simply a result of less evaluations of the energy gradient. (We note that runtime improvement is essentially the ratio between $n^* = 7500$ and $n^{\mathrm{sub-steps}} = 20$.)

- **Stability:** In all our experiments, the PBD method did never diverge. The only condition is that Δt and $n^{\mathrm{sub-steps}}$ have reasonable values such that the explicit Euler method converges. For the same conditions, the DAHA method did fail in around every fourth simulation. In many of these situations, it is not clear how to change the numerical parameters to ensure convergence.

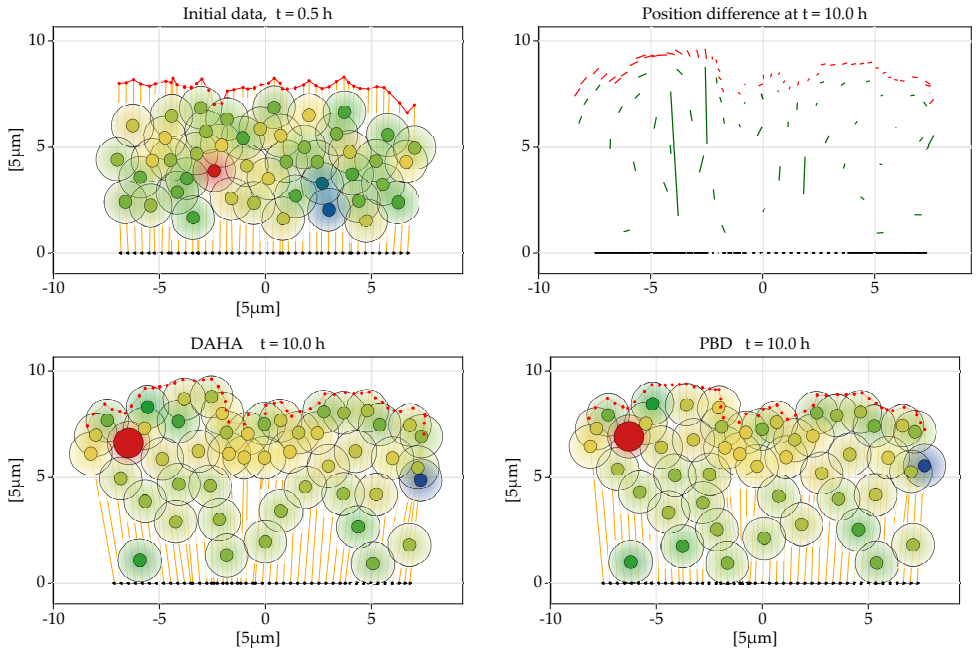

Figure 13. Comparison between the DAHA-PSE model with tolerance parameter $\varepsilon = 10^{-6}$ and PBD-PSE model with damping parameter $\mu = 0.14$ and $n^{\text{supsteps}} = 20$. The top right figure shows the difference between the position of both simulations at time $t = 10\,\text{h}$. For most cells, the nuclei position $\boldsymbol{X}_i$ is almost the same. There are some exceptions, with typically do not impact the overall tissue too much.

Next, we check that the solutions do actually conicide. As Figure 13 shows, both simulations are very similar and only show differences in a few cells which do not impact the overall behaviour of the tissue.

For a quantitative comparison, we measure the relative difference between the nuclei positions at time $t = 10\,\text{h}$ which yields

$$\frac{\|\boldsymbol{X}^{\text{DAHA}}(10\,\text{h}) - \boldsymbol{X}^{\text{PBD}}(10\,\text{h})\|}{\|\boldsymbol{X}^{\text{DAHA}}(10\,\text{h})\|} \approx 0.06 \quad \text{for } \mu = 0.14$$

The difference in the position is a rather strict error measure, since individual small differences (like a cell passing another cell at some time) can have larger long-term effects. This explains why the error is $6\,\%$ even though the tissue itself and most cells are at identical positions in Figure 13.

More importantly, the macroscopic quantities such as tissue height, shape and growth, remain intact which ensures our main goal: to stay consistent with the results from [Fer+19] in the sense that their parameter calibration applies also to the FO-PSE model.

4. Simulation examples

We will not repeat all the findings from [Fer+19], but instead only consider one particular aspect.

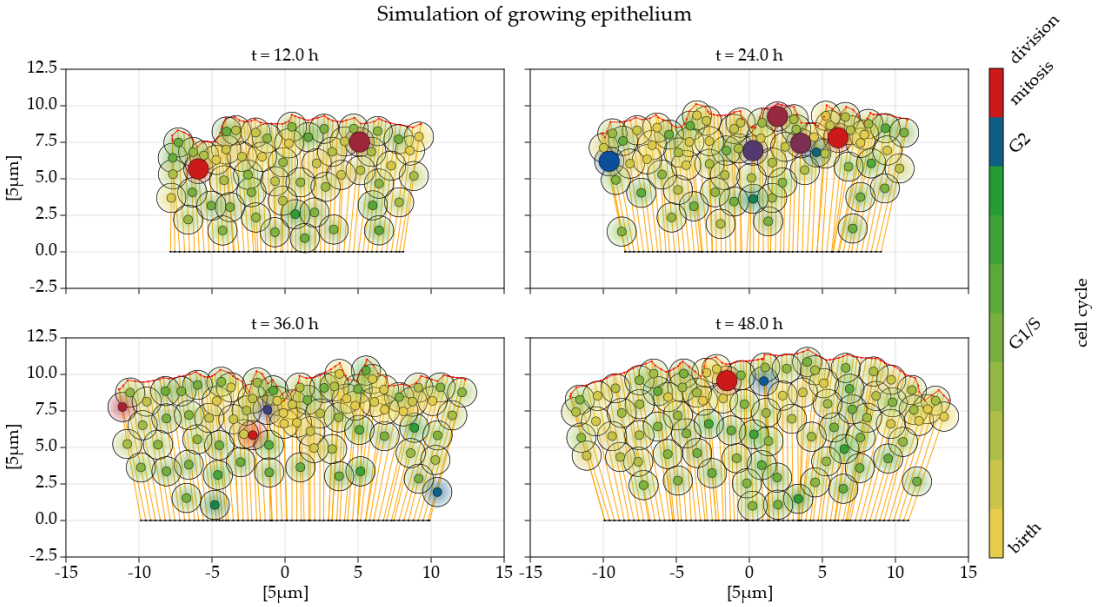

Figure 14. Simulation of growing epithelium with the OSS-PSE model and default parameters. We see the expected behaviour of tissue growth with accumulation of nuclei on the apical side (red line). However, the height increase is less than reported in vivo.

One aspect from the future work section of [Fer+19] was that the growth of the tissue height is a bit too slow in the QSS-PSE model. Matching the experimental data turned out difficult since the required parameters lead to stability issues. In some areas of the neural tube the tissue doubles in height within $48\,\mathrm{h}$. Figure 14 shows a simulation with the QSS-PSE model where the height increase is less than $50\,\%$ of the initial height.

Since the FO-PSE model fixes these instabilities, we can now explore new parameter ranges to see if we can obtain faster growth of tissue height. Among many possible choices to modify the parameters, we restrict ourselves to choosing different values for the damping coefficient μ.

In Figure 15, we show simulations with the FO-PSE model for different damping coefficients. The results show that reduced damping leads to much faster tissue growth while still maintaining a realistic tissue structure. This shows that larger damping coefficients would fit better to the in vivo experimental data. Figure 16 shows how the height growths during the simulation.

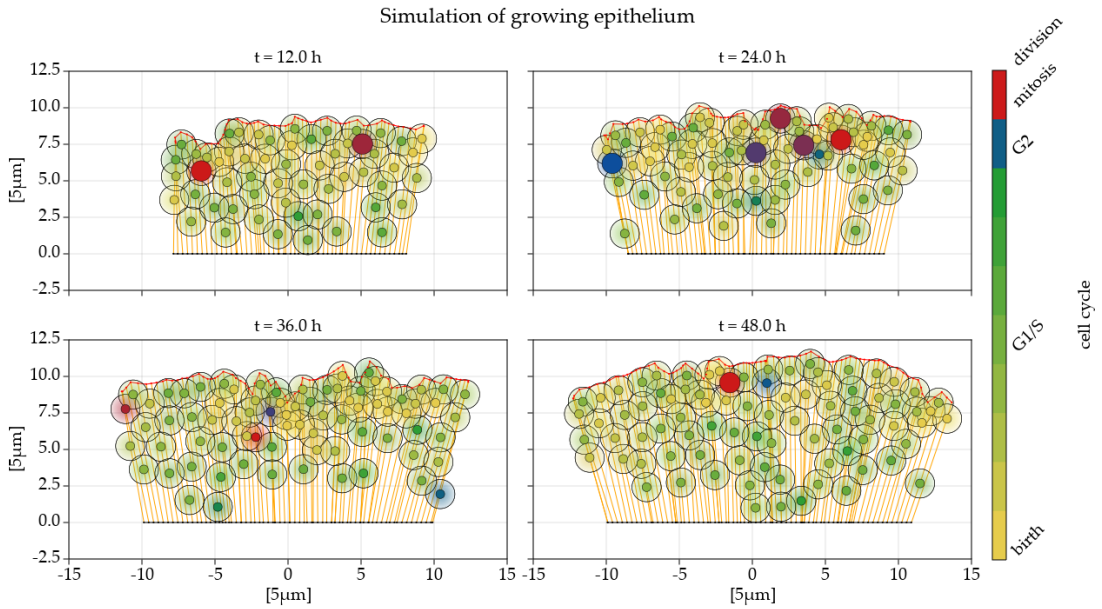

Figure 15. Simulations of the FO-PSE model with different damping coefficients. Values around $\mu = 0.2$ give similar results as the OSS-PSE model. We see that for small damping coefficient the growth of the tissue is much faster, fitting better to the experiments.

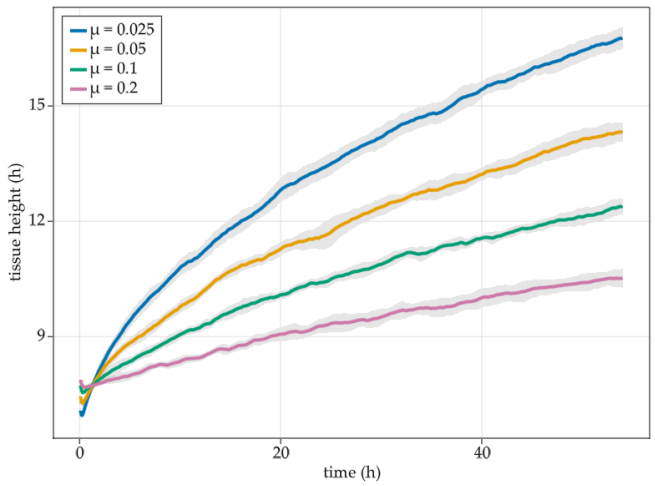

Figure 16. Tissue growth for different values of μ. A realistic increase within $48\,\mathrm{h}$ would be a doubling, that means an increase from 8 to 16, similar to the choice $\mu = 0.025$.

5. Conclusion and further directions

Most of this chapter, in particular the PSE model itself, is taken from [Fer+19]. Our modifications extend that model by providing a faster and more stable numerical implementation with only minor changes to the simulation outcomes.

With the new stability, we can in particular simulate the model with parameters which give more realistic height increase of the tissue, which was one of the remaining open tasks in [Fer+19]. In the following chapter, we will add rules for epithelial-to-mesenchymal transitions to the model, which was also the initial modelling goal.

Other than the EMT modelling, there are further possible extensions one could consider:

- Curved basal layers: as the name suggests, the neural tube is not a straight sheet. Therefore, it could be interesting to model curved basal layers. We did a preliminary implementation of curved basal membranes and the model seems to work with only minor modifications to the parameters.
- 3D modelling: probably the most common and most neglected extension for many models in biomathematics. However, most of the rules are already independent of the dimension. The 'only' remaining task is to find good rules for cell division and construction of apical-apical springs. The difficulty here is that for the 2D model the apical layer is a line with obvious topology. However, for a 3D model the apical layer is a surface and it is less obvious which apical points become neighbours after a cell divides. It could also be that the use of 'points' is not suitable to model the apical surface in 3D.

For both the curved basal layer and the 3D modelling preliminary implementations exist, see for example Figure 17. However, in both cases work remains to make these implementations useful for application to biological questions.

Figure 17. Preliminary implementation of a 3D model. Most rules from [Fer+19] generalise directly to 3D and already the first simulations gave rise to growth of the tissue height. However, the preliminary simulation lack a precise modelling of the apical surface.

Chapter 4

How do epithelial-to-mesenchymal transitions initiate cell migration?

In this chapter, we model so-called *epithelial-to-mesenchymal transitions* (EMT), which are complex cellular processes during which epithelial cells change their properties and transform into mesenchymal cells. Contrary to epithelial cells, these new mesenchymal cells can disassemble from the epithelium to fulfil new functions. In particular, *cells which undergo EMT can start to migrate and invade the basal membrane* which leads to the development of tumours (in the case of cancer) but is also important for morphogenesis in animal embryos where cells have to migrate long distances to develop new organs.

Typical events that take place during the epithelial-to-mesenchymal transition are

- loss of stable cell-cell junctions,
- loss of cell adhesion with the basal membrane,
- changes in cell polarity and
- changes of cytoskeleton dynamics (e.g. leading to migration).

Our primary aim is to understand which aspects of EMT lead to basal extrusion (i.e. cells leaving the epithelial tissue). For this task, we extend the PSE model (Chapter 3) and integrate EMT-specific cell events (as explained in Section 2).

An essential aspect of EMT is that the different behavioural changes that can occur during EMT (EMT events) do not occur all at once. But instead, so-called partial EMT is ubiquitous which means that cells might only gain some mesenchymal traits but not all. This leads to a *spectrum of intermediate cell phenotypes* and *heterogeneity* in observed cell behaviour, as sketched in Figure 1.

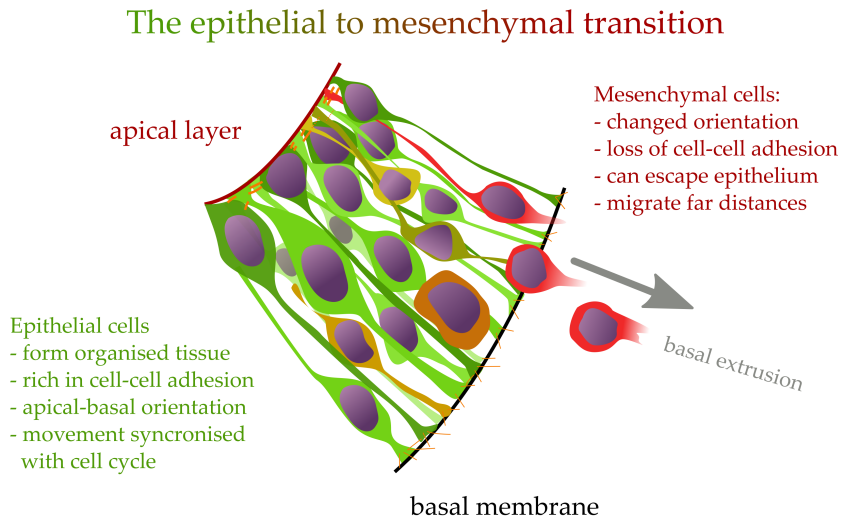

Figure 1. Typical steps of the epithelial-to-mesenchymal transition (EMT). Cells undergo various changes which leads overall to a spectrum of possible intermediate cell types (phenotypes). Our goal is to explain which factors cause basal extrusion. For example, it is not known if the heterogeneity of cell types is mechanically relevant for basal extrusion.

From a biological point-of-view the *heterogeneity* poses a significant challenge. For in vivo experiments, precise control over specific successions of EMT events is technically infeasible. In addition, it is unclear which EMT events are most relevant and whether heterogeneity and the interaction among EMT cells matter. This experimental bottleneck is the initial motivation to apply mathematical modelling.

However, using an in silico EMT model to investigate this heteroegeneity of scenarios is challenging on its own. Since comparing many different EMT scenarios requires some data crunching. Depending on the number of EMT cells and their heterogeneity, the number of simulations needed for statistically reliability increases from a few dozens to more than 10^5 simulations. Such extensive simulation studies are possible thanks to the runtime improvements we discussed in Chapters 2 and 3.

Originally, it was thought that the order of events during EMT and their timing was crucial to explain basal extrusion. In particular, we thought that there are some EMT scenarios which mostly lead to basal extrusion and others which do not. We will see that this statement is only partially true. We will reach the following conlusions among others:

(1) According to the model, cell mobility is very essential for basal extrusion. Lack thereof could even lead to apical extrusion, which occurs only in non-physiological conditions. This could indicate that cells indeed need cell protrusions to escape the epithelium.

(2) Beyond the particular EMT scenario taking place, the position of a cell at the onset of EMT affects the rate of basal extrusion.
(3) Cells that stop internuclear movement (INM) during EMT are more often extruded basally

These three conclusions from the simulations are being tested experimentally: Theveneau's experiments, showing that EMT cells have non-apical mitosis with increased frequency, indicates that EMT cells do indeed stop INM already before EMT.

This chapter has the following structure: First, Section 1 introduces to the biology of EMT in the neural tube of the chick embryo. Then, we extend the PSE model from Chapter 3 with EMT-specific cell events in Section 2. Section 3 explains our approach to analyse the simulation results. Our analysis of the EMT model is presented in Section 4. Finally, we present experimental results corresponding to the hypotheses derived from our modelling in Section 5.

My contribution

This chapter contains the main results of my PhD. I extended the PSE model with EMT specific rules and implemented the model in Julia. The modelling and the analysis of the simulation was done in close collaboration with Dr. Eric Theveneau.

1. Biological background: the neural tube of the chick embryo

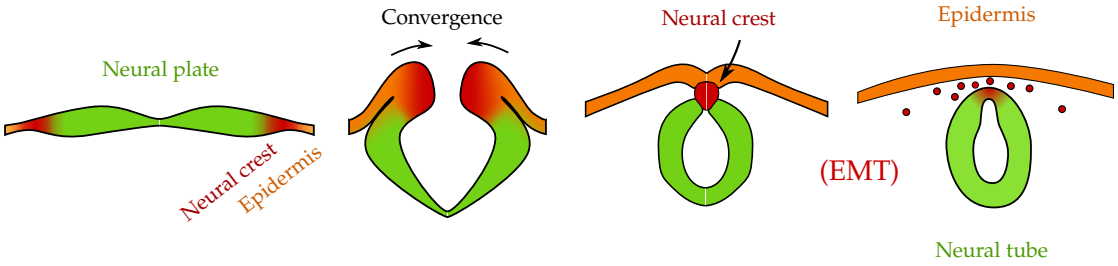

Figure 2. Sketch of the neural tube formation during embryo development. For birds, the neural crest cells start migrating after the neural tube is closed (fourth picture), whereas in mammals the migration starts already prior to neural tube closure [GG00]. In chick embryo the closure happens first in the cephalic (head) region, then in the trunk and last in the caudal (tail) region. The experimental data we show in this thesis will often use this fact to capture the same tissue at different stages of EMT, by slicing different regions of the neural tube.

During the development of chick embryos, EMT takes place after the closure of the neural tube. The closure marks the end of the neural tube formation where the neural plate folds and forms the neural tube, as depicted in Figure 2. Then, beural crest cells, which undergo EMT, migrate long distances across the embryo and form various new tissues like bones, glands, nerves or parts of our neck and head.

Along the neural tube, the way how EMT takes place differs. For example, in the cephalic region (head) many neural crest cells undergo EMT at the same time, leading to a chaotic

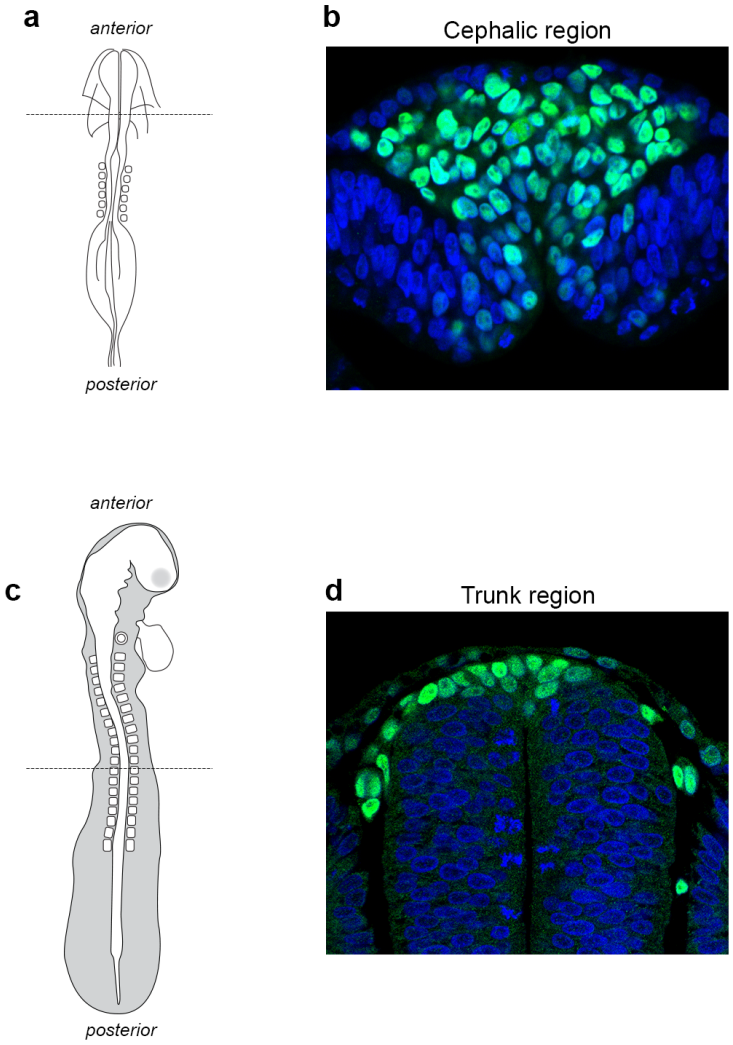

Figure 3. Panels **a & c** show diagrams (dorsal view) of a chicken embryo at 32 hours of development (a) and 48 hours of development (c). In panels **b & d**, we see the corresponding transversal sections of the neural tube at the time of neural crest migration (dorsal is on top). Nuclei have been stained using DAPI (blue) and neural crest cells have been labelled by immunostaining against the Sox9 protein (green).
In the cephalic region, many cells exit the neural tube at the same time. Around 100 cells perform EMT simultaneously at a given anteroposterior level within the cephalic domain. Cells are produced for about 6h before EMT stops. By contrast, in the trunk, around 5 to 10 cells per anteroposterior level perform EMT simultaneously. The neural crest domain keeps producing cells by EMT for 48h at each level in the trunk region. The most lateral green cells are migrating away and have completed EMT several hours ago. *Image source: unpublished, provided by Dr. Eric Theveneau (CNRS).*

disassembly of the epithelium. Whereas in the trunk region much less cells transform simultaneously [TM12; AE09]. Figure 3 shows the migration in both regions. With our

simulations, we will consider both cases. We will look at individual EMT cells (trunk region) and heterogeneous groups of EMT cells (cephalic region).

As highlighted in the introduction, cells show a large degree of heterogeneity in their EMT programs. The amount of heterogeneity is so large that there is no even a precise characterisation of mesenchymal cells [Yan+20]. Different communities use different traits as defining properties since neither molecular markers nor their behaviour is fully conclusive. The role of heterogeneity is also not clear. One example of EMT are cancer cells (carcinoal cells). Here, heterogeneity could be a survial strategy, since it increases the adaptivity and resistance of these cells to external clues and physiological stress [Yan+20].

Heterogeneity can also be measured by identifying different *transcription factors*. These transcription factors control different steps of the transition, but not in an obvious way, e.g. there is not one transcription factor responsible for loss of apical adhesion, but instead many factors combine and give rise to different behaviour. Figure 4 shows a experimental evidence of EMT heterogeneity since it shows the heterogeneity of the transcription factors.

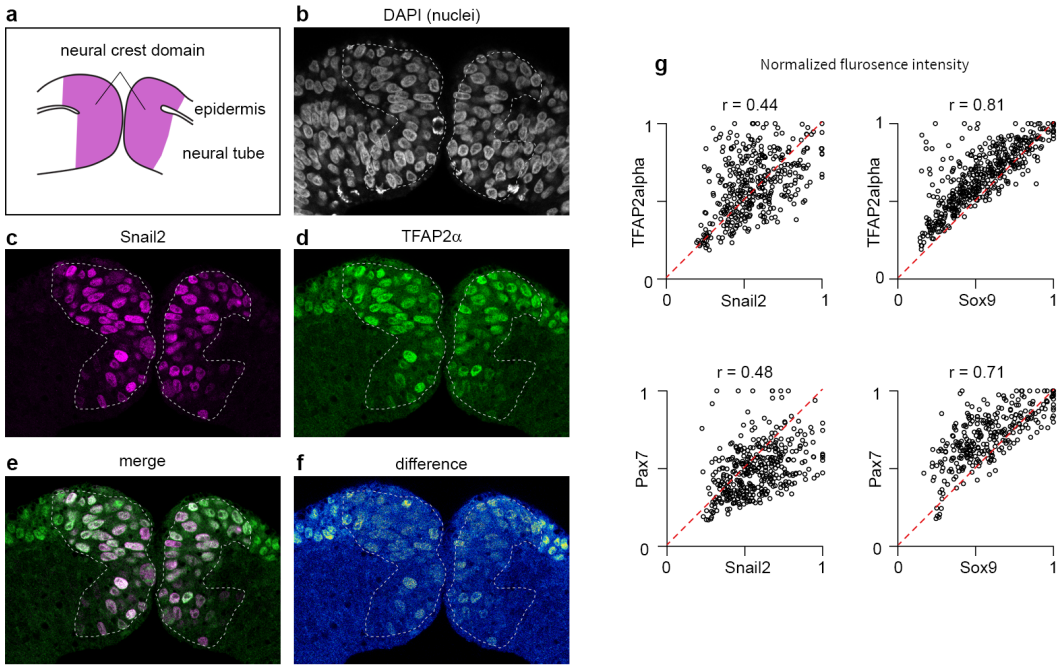

Figure 4. Measurements of different transcription factors (Snaul2, Pax7, Sox9, TFAP2α) which regulate EMT. Figures **b** to **f** show the neural crest domain in an early stage (before neurulation, i.e. before the neural crest domains merge and form the neural tube). As visible in plot **f** the distribution of the transcription factors is not homogeneous. The variation of the transcription factors leads to heterogeneous EMT. In Figure **g** the fluorescence intensity is plotted against each other which demonstrated the heterogeneity. *Image source: unpublished, provided by Dr. Eric Theveneau (CNRS).*

In this chapter, we will investigate in silico the heterogeneity in EMT in the neural tube. In the next section, we will modify the PSE model to introduce neural crest cells, which undergo EMT.

2. Modelling of epithelial-to-mesenchymal transitions

In this section, we describe the mathematical model for EMT. In a nutshell, we model EMT via four possible *EMT events*, which are

- **[A]**: loss of apical adhesion,
- **[B]**: loss of basal adhesion,
- **[S]**: loss of cell straightness (which models loss of polarity) and
- **[P]**: start of active self-propulsion (in the direction of the current cell polarity).

These events are visualised in Figure 1 and described in more detail in this section.

2.1. Description of the model

Our EMT model extends the PSE model from Chapter 3. For a detailed description of the PSE model we refer to Section 2.1. Here, we quickly recall that in the PSE model each cell is described by an apical point $\boldsymbol{A}_i$, a basal point $\boldsymbol{B}_i$ and the position of the nucleus $\boldsymbol{X}_i$. The apical points form an apical layer of linear springs and the basal points form the basal layer. Among other rules, epithelial cells perform interkinetic nuclear movement (INM) which consists of passive downward (apical-basal) movement for most of the cell cycle and a rapid upward (basal-apical) movement shortly before the mitosis phase.

We now introduce a new cell type: the 'EMT cells', which inherit all the rules of epithelial cells but in addition at possibly random times eacg EMT cell can perform one of the four EMT events **[A]**, **[B]**, **[S]** or **[P]**. These are described in detail next:

[A] Loss of apical adhesion. When cells lose cell-cell adhesion on the apical side, then the cell's cytoskeleton will contract and the surrounding epithelial cells create new cell junctions to fill the gap in the apical layer. In our model we implement these steps by removing the apical point from the apical network, setting the desired rest length of the apical-nuclei spring to zero and creating a new linear spring between apical points of the adjacent epithelial cells.

[B] Loss of basal adhesion. Loss of adhesion to the basal membrane is modelled with the same steps as in the previous case: We remove the basal point from the basal layer, set the desired rest length of the basal-nuclei spring to zero and connect the adjacent basal points.

[S] Loss of cell straightness (loss of polarity). Epithelial cells have an apical-basal polarity which can get disoriented during EMT. In our model the polarity is indirectly represented by the apical and the basal points which are at opposite sides of the nucleus due to the bending spring. We model the loss of polarity by decreasing the stiffness of

the bending spring, which has the effect that the apical and basal points might not be located on a straight line.

[P] Protrusions and active motion. The area outside the basal region of the epithelium is called the *extracellular matrix* (ECM), which is full of collagen fibers. Cells can form protrusions to implement a seek-and-grab mechanism of migration where they seek for fibers of the ECM and then attach to pull themself forward. In the model, we utilise the basal point to represent such cell protrusions. If the basal point is already detached from the basal membrane, cells can protrude by moving their basal point in the direction of the basal-nuclei spring and as soon as the basal point is below the basal layer, we set the desired rest length of the basal-nuclei spring to zero.

Stop of interkinetic nuclear movement (INM). In addition, we also consider cases where some EMT cells do not perform interkinetic nuclear movement (INM) from the beginning of the simulation. Since EMT cells aim to exit the tissue basally, the inhibition of INM can lead to cells which are positioned closer to the basal layer, possibly preparing basal extrusion.

Heterogeneity of EMT. The timing of these four EMT events and stop of INM are the source of heterogeneity in EMT, in particular:

- Not all EMT cells undergo all events **[A]**, **[B]**, **[S]**, **[P]** and stop of INM.
- EMT events happen with different sequential order and at different times.
- Epithelial cells can become EMT cells in isolation or as a cluster.

2.2. Mathematical rules to model EMT

In this section, we describe mathematically the rules given in Section 2.1

Let $\mathcal{I}^{\mathrm{EMT}} \subset \mathcal{I} = \{1, \dots, N\}$ denote the indices of EMT cells. All other cells $\mathcal{I} \setminus \mathcal{I}^{\mathrm{EMT}}$ are control cells which do not perform EMT. To simplify things, let us assume that the first N^{EMT} indices refer to EMT cells and the remaining are used for control cells, i.e.

$$\mathcal{I} = \mathcal{I}^{\mathrm{EMT}} \cup \mathcal{I}^{\mathrm{control}} = \{1, \dots, N^{\mathrm{EMT}}\} \cup \{N^{\mathrm{EMT}} + 1, \dots, N\}.$$

Now, let $i \in \mathcal{I}^{\mathrm{EMT}}$ be the index of an EMT cell. For each EMT cell there are four extra parameters $T^{\mathrm{A}}, T^{\mathrm{B}}, T^{\mathrm{S}}, T^{\mathrm{P}} \in \mathbb{R} \cup \{\infty\}$ which define the timings of the corresponding EMT events **[A]**, **[B]**, **[S]** and **[P]**. If $T_i^{\mathrm{A}} = \infty$, this means that event **[A]** does not take place in the ith cell.

2.2.1. Event [A]: Loss of apical adhesion. At time $t = T_i^{\mathrm{A}}$, we remove the apical point $\boldsymbol{A}_i$ from the apical network and connect the neighbours of the ith cell, i.e. we replace the edges (j_1, i) and (i, j_2) with the new edge (j_1, j_2) in $\mathcal{A}$ (which is the set of edges forming the apical layer, see (3.5)). If the cell is at the boundary, we will only remove the existing apical edge.

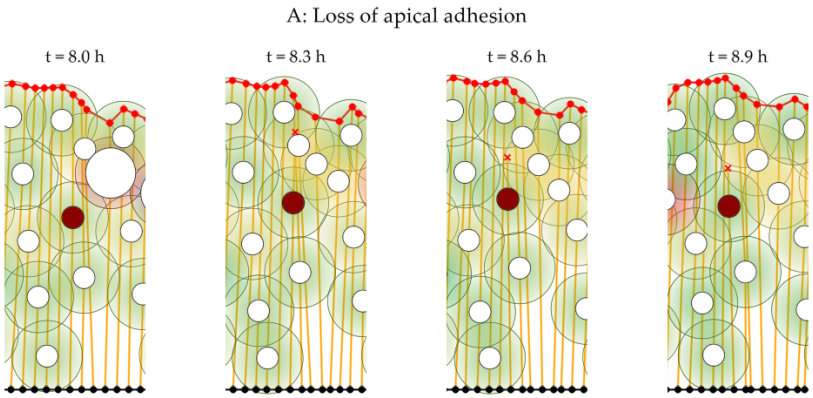

Figure 5. Example for loss of apical adhesion **[A]** (cell in red). The apical point (small red cross) first leaves the apical layer and the contraction of the apical-nuclei spring pulls it towards the nuclei.

Moreover, the desired rest length of the apical-nuclei spring is set to zero, i.e.

$$\eta_i^{\mathrm{ax}*}(t^+) := 0.$$

The desired apical-nuclei rest length will remain unchanged for the rest of the simulation, in particular, the INM-specific cell event (3.2) will not apply anymore for the ith cell.

2.2.2. Event [B]: Loss of basal adhesion. At time $t = T_i^{\mathrm{B}}$, we remove the basal point $\boldsymbol{B}_i$ from the basal layer and connect the neighbours of the ith cell, i.e. we replace the edges (j_1, i) and (i, j_2) with the new edge (j_1, j_2) in $\mathcal{B}$ (see (3.15)). If the cell is at the boundary, we will only remove the existing basal edge.

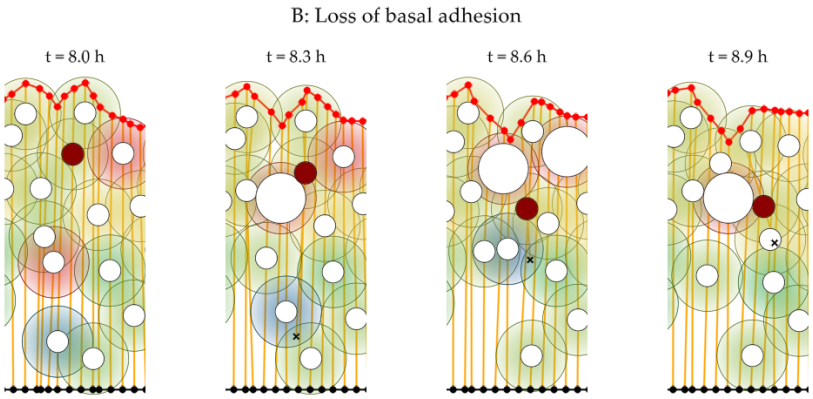

Figure 6. Example for loss of basal adhesion **[B]** (cell in red). The basal point (black cross) detaches from the basal layer and the basal-nuclei spring contracts. Notice how the nucleus is pulled towards the basal point during this contraction.

Moreover, we set the desired rest length of the basal-nuclei spring to zero, i.e.

$$\eta_i^{\mathrm{bx}*}(t^+) := 0.$$

The desired basal-nuclei rest length will remain unchanged for the rest of the simulation, in particular, the INM-specific cell event (3.3) will not apply anymore for the ith cell.

We recall, that the constraints for basal points (C3) and (C4) do only hold for vertices of the basal network. Therefore, after the loss of basal adhesion, the basal point of the ith cell can move freely in $\mathbb{R}^2$.

2.2.3. Event [S]: Loss of straightness. At time $t = T_i^{\mathrm{S}}$ we set the stiffness of the bending spring to zero, e.g.

$$\alpha_i^{\mathrm{axb}}(t^+) := 0.$$

As Figure 7 shows, this increases the ability of the cell to move sideways since the nuclei is not restricted to be along the line that joins the apical and basal sites.

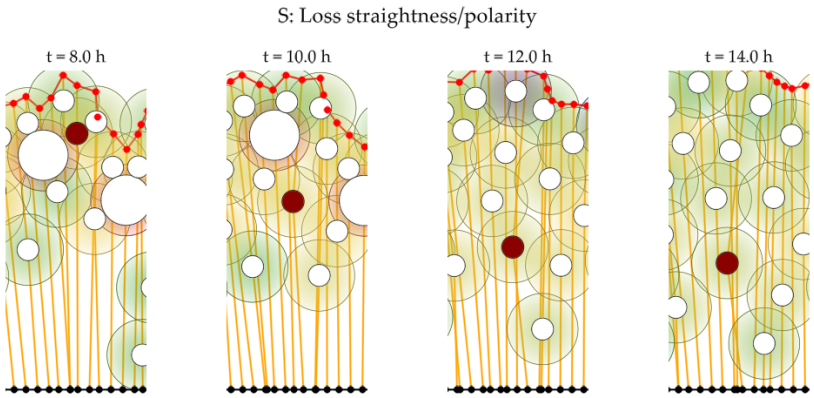

Figure 7. Example for loss of straightness **[S]**. The EMT cell undergoing event **[S]** is in red. Notice how the angle between the apical-nuclei and basal-nuclei springs is no longer straight.

2.2.4. Event [P]: Protrusive activity. At the time $t = T_i^{\mathrm{P}}$ the ith cell will start to self propel. If at this time the basal point is still attached to the basal layer, then the activation of this rule is delayed to the time $t = \max(T^{\mathrm{P}}, T^{\mathrm{B}})$. Therefore, event **[P]** always happens after event **[B]**.

Then, we replace the dynamical rule of the detached basal point $\boldsymbol{B}_i$ (given in (3.33)) with the new law

$$\dot{\boldsymbol{B}}_i = \begin{cases} v^{\mathrm{run}} \frac{\boldsymbol{B}_i - \boldsymbol{X}_i}{\|\boldsymbol{B}_i - \boldsymbol{X}_i\|} & \text{if } y(\boldsymbol{B}_i(t)) > -2R^{\mathrm{soft}} \\ \boldsymbol{0} & \text{else,} \end{cases} \tag{4.1}$$

where $y(\boldsymbol{B}_i(t))$ denotes the y-coordinate of the basal point. This means that the basal point $\boldsymbol{B}_i$ will move in the direction $\boldsymbol{B}_i - \boldsymbol{X}_i$ at speed v^{run}. The motion stops once the basal point $\boldsymbol{B}_i$ reaches a point that has distance $2R^{\text{soft}}$ from the basal layer (i.e. the full cell must have left the tissue).

The choice of stopping the forward movement if the point is below the basal layer at $+2R^{\text{soft}}$ units of distance is only a convenience, as we do not model the dynamics below the basal layer any further.

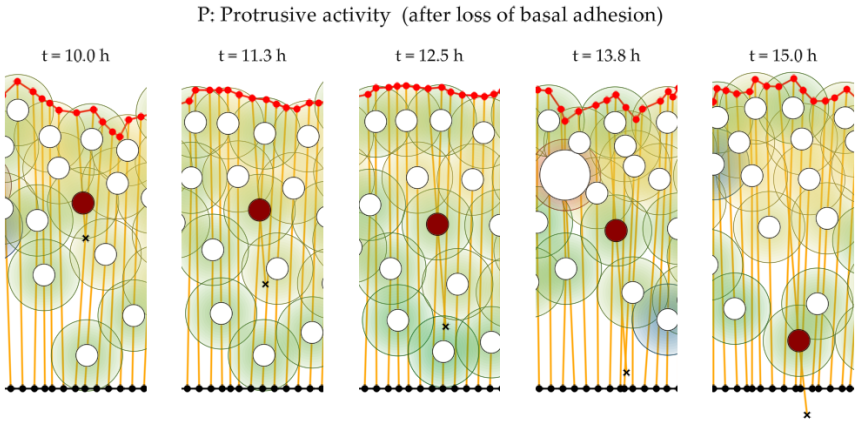

Figure 8. Example of protrusive activities **[P]**. In this case the cell first lost the basal adhesion at $t = 8\,\text{h}$ (see Figure 6). The detached basal point is indicated with a black cross and the EMT cell is in red. We note that **[P]** is the only EMT event which introduces an active force that leads to extrusion.

We recall that the basal-nuclei spring leads to the force

$$\boldsymbol{F}^{\text{basal}-\text{cytos}} = \frac{2\alpha^{\text{bx}}}{R^{\text{soft}} + \eta_i^{\text{bx}}} \left(\|\boldsymbol{B}_i - \boldsymbol{X}_i\| - R^{\text{soft}} - \eta_i^{\text{bx}} \right) \frac{\boldsymbol{B}_i - \boldsymbol{X}_i}{\|\boldsymbol{B}_i - \boldsymbol{X}_i\|}$$

where η_i^{bx} is the rest length of the basal-nuclei spring and $\|\boldsymbol{B}_i - \boldsymbol{X}_i\| - R^{\text{soft}}$ is the current distance between the basal point and the boundary of the nuclei.

As long as the basal point is above the basal layer, this force will be zero since there is nothing the cell can hold onto. But bnce the basal point is below the basal layer it will grab onto the basal membrane and the cytoskeleton will pull the cell. We archive this with the following rule

$$\eta_i^{\text{bx}}(t) := \begin{cases} \|\boldsymbol{X}_i - \boldsymbol{B}_i\| - R^{\text{soft}} & \text{if } y(\boldsymbol{B}_i(t)) > 0 \\ 0 & \text{if } y(\boldsymbol{B}_i(t)) \leq 0. \end{cases}$$

This equation replaces (3.3).

We note, for basal points above the basal layer, we have $\boldsymbol{F}^{\text{basal}-\text{cytos}} = \boldsymbol{0}$, but once $\boldsymbol{B}_i$ is below the basal layer, the cytoskeleton will contract and pull on the nuclei position $\boldsymbol{X}_i$ towards the basal point.

2.2.5. Stop of division. We will not allow EMT cells to further proliferate to simplify statistical evaluations. Therefore, we will use for all EMT cells the cell division rules as in Section 2.2.5 with the additional choice $p^{\mathrm{div-out}} = 100\,\%$. As a result, the EMT cells will effectively reset their cell cycle instead of performing cell division.

2.2.6. Initial configuration. In all simulations presented within this thesis, we will choose the EMT cells to be situated in the middle of the tissue so that these are surrounded by non-EMT cells, i.e. epithelial cells (neural tube cells).

2.3. Timing of EMT events: heterogeneity

To summarize, the four EMT-specific cell events are loss of apical adhesion **[A]**, loss of basal adhesion **[B]**, loss of straightness **[S]** and protrusive activity **[P]**. The timing of these events is determined by the parameters $T_i^{\mathrm{A}}, T_i^{\mathrm{B}}, T_i^{\mathrm{S}}$ and T_i^{P}. We will consider cases in which a particular event will not occur, which we denote as $T_i^{\mathrm{S}} = \infty$.

The Figures 5 to 8 demonstrate all individual EMT events.

The last extension of the model is to add heterogeneity of EMT timings. Considering different EMT timings allows us to study how EMT cells interact, compete or possibly support each other. An example of a simulation with heterogeneous EMT timings is shown in Figure 9.

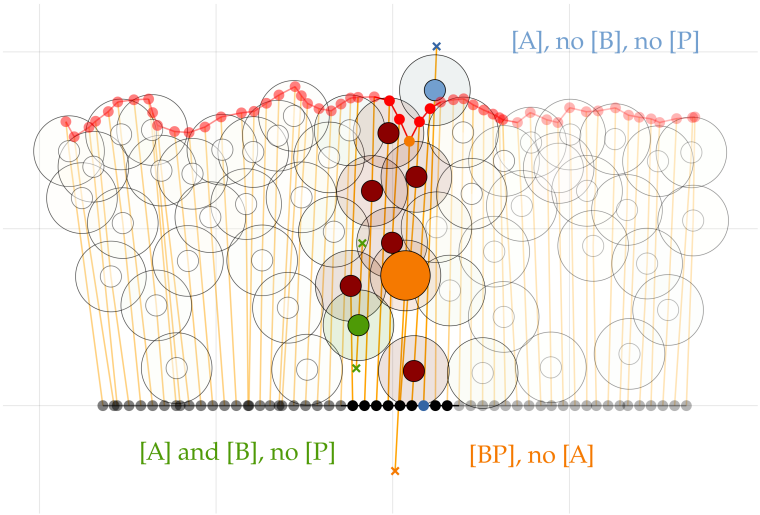

Figure 9. Example for heterogeneous EMT timings: all colourful cells are EMT cells, but at this simulation snapshot, cells undergo different EMT events.

2.3.1. Implementation of heterogeneous EMT timings. To model the heterogeneity, we pick independent uniformly randomly distributed timings for EMT. To allow the possibility of skipping events, we define the distribution

$$T \sim \mathcal{U}^{70\,\%}(T^{\min}, T^{\max}),$$

which assigns the value $T = \infty$ in $30\,\%$ of the cases and otherwise picks a uniformly random value from the interval $T \sim \mathcal{U}(T^{\min}, T^{\max})$, e.g.

$$\mathbb{P}[T = \infty] = 0.3 \quad \text{and} \quad \mathbb{P}[T \in (a, b)] = \frac{0.7(b-a)}{T^{\max} - T^{\min}}$$

for $T^{\min} \leq a \leq b \leq T^{\max}$.

We restrict ourselves to the case that N^{EMT} is constant over time, which means that all EMT cells only reset the cell cycle (Section 2.2.5) instead of dividing with possibly two daughters.

To model *heterogeneous EMT* we select i.i.d. random parameters for all four EMT timings. For example

$$T_i^{\mathrm{A}}, T_i^{\mathrm{B}}, T_i^{\mathrm{S}}, T_i^{\mathrm{P}} \sim \mathcal{U}^{70\,\%}(T^{\min}, T^{\max}) \quad \text{for } i \in \mathcal{I}^{\mathrm{EMT}}. \tag{4.2}$$

We note that the protrusive activity is only active after the loss of basal adhesion, which effectively implies $T_i^{\mathrm{B}} \leq T_i^{\mathrm{P}}$. In situations where this is relevant, we will ensure that this doesn't lead to unwanted statistical dependence.

The particular choice of $70\,\%$ ensures that the number of one-step, two-step and three-step EMT events is roughly proportional to the number of possible combinations of EMT events. Due to lack of data, we could not determine this parameter more accurately.

All simulations in this thesis will use $T^{\min} = 6\,\mathrm{h}$ and $T^{\max} = 24\,\mathrm{h}$.

For notational convenience, we might collect all these EMT timings into one vector $\boldsymbol{\mathcal{T}} = (\boldsymbol{T}_1, \ldots, \boldsymbol{T}_{N^{\mathrm{EMT}}}) \in ((\mathbb{R} \cup \{\infty\})^4)^{N^{\mathrm{EMT}}}$ such that

$$\boldsymbol{T}_i = (T_i^{\mathrm{A}}, T_i^{\mathrm{B}}, T_i^{\mathrm{S}}, T_i^{\mathrm{P}}) \quad \text{for } i \in \mathcal{I}^{\mathrm{EMT}}.$$

In addition, we might also vary which cells perform interkinetic nuclear migration (INM). Here we will decide for each EMT cell if INM is active or not. In the simulation results presented in Section 4.5 we used $50\,\%$ probability of active INM for each cell.

3. Methods to analyse the simulation

Before we will present the results of our simulations, we will collect the biological questions and show which quantities we can compute with the model to answer these questions.

3.1. Translation of biological questions in terms of the EMT model

Abstractly speaking, we are interested in how the rate of apical and basal extrusion depends on the parameters which control the behaviour of EMT cells. In particular, which *EMT scenarios*, i.e., which sequences of events and their timings lead more frequently to cell extrusion from the tissue.

To analyse the 'efficiency' of EMT scenarios leading to basal extrusion, we will consider three metrics, which are:

- **Ratio of basal extrusion** ($r^{\mathrm{basal-extr}}$), which is the fraction of EMT cells for which the nuclei center is below the basal layer.
- We measure the **ratio of basal positioning** ($r^{\mathrm{basal-pos}}$), i.e., is the ratio of cells with nuclei below the lowest epithelial (non-EMT) cell's nuclei.
- Finally, the **ratio of apical extrusion** ($r^{\mathrm{apical-extr}}$) is the fraction of cells above the apical surface.

We will provide precise mathematical definitions and how to compute them later in this section.

The ratio of basal extrusion is the key outcome we are interested in, and the most effective EMT scenario would be the one with the highest rate of basal extrusion. Since we do not model the basal membrane itself, we introduced basal positioning as an alternative measure which gives information on the relative position of the EMT cells compared to the remaining tissue.

On the other hand, the ratio of apical extrusion should be as low as possible since apical extrusion does not occur in physiological situations. We will discuss this aspect in more detail in the result section Section 5.

In the following list, we reformulate the biological questions we are interested to investigate by expressing them in relation to the model parameters.

- **(Q1) Group efficiency:** Are individual EMT cells more effective compared to groups of EMT cells? We note that both settings occur in the neural tube, e.g. isolated EMT in the trunk region and collective EMT in the cephalic region.
  - With our simulations, we compare individual cells ($N^{\mathrm{EMT}} = 1$) and group of EMT cells (with the choice $N^{\mathrm{EMT}} = 10$).
- **(Q2) Selection of EMT events:** Is basal extrusion possible without the implementation of all EMT events? Which EMT events have to occur for basal extrusion to happen?
  - We represent inactive EMT events by an infinite starting time. The number of possible combinations is quite large. With four EMT events (**[A]**, **[B]**, **[S]** and **[P]**) and the restriction that **[P]** occurs after **[B]**, we get $2^3 + 2^2 = 12$ possible selections of active EMT events.
- **(Q3) Timing of onset of EMT:** Are early EMT events more efficient?
  - The timing of onset of EMT in the model is the minimum of T^{A},T^{B},T^{S} and T^{P}.
- **(Q4) Order of EMT events:** Are there specific sequential orders of EMT events which lead to more basal extrusion?

  - There are 29 possible orderings of the EMT events, for example **[AB]**, **[BA]**, **[AS]**, **[SA]**, ... [1]

- **(Q5) Group efficiency of heterogeneous EMT:** Is it an advantage if a group of EMT cells has all the same timings, or is a mixture of timings better?
  - To model heterogeneous EMT, we will use randomised timings. We compare this to groups of EMT cells with homogeneous EMT timings, i.e. where all cells perform the EMT events simultaneously.
- **(Q6) Effect of interkinetic nuclear movement (INM):** Are EMT cells without INM more effective than EMT cells with INM?
  - To deactivate INM for EMT cells, we do not apply the cell events from Chapter 3, Section 2.2.3 for these cells. (However, the epithelial cells will still perform INM.)

During the analysis of the simulation results, it became apparent that not only the EMT events themself but also the environment of the cells which undergo EMT is essential. The environment of an EMT cell consists of the host tissue, the current location of the cell within the tissue and the location of the cell relative to other EMT cells. To capture also these contributions, we will consider the following factors and their effect on basal extrusion:

- **(Q7) Distance to basal layer at onset of EMT:** Does the position of an EMT cell at the start of EMT events impact the outcome? For example, are cells closer to the basal layer more likely to escape the tissue successfully?
- **(Q8) Amount of other EMT cells with protrusive activity [P]:** We will see that protrusive activity is very effective in ensuring the basal exit of EMT cells. This raises the question of how other EMT cells are affected by the presence of many EMT cells with protrusive activity.

In summary, we have eight questions which we want to explore with our mathematical model. In the next section, we will describe how we organise the simulations to draw conclusions from the model.

3.2. Simulation approach

The key challenge in analysing the simulation results is the vast number of possible input parameters. Large parameter spaces are often mainly a runtime concern as parameter optimisation takes longer. However, we are not just interested in finding the most effective EMT events. Instead, our goal is to gain a global understanding of the mechanics

[1] We have to consider P has only an effect when occurring after B. Plain counting yields:
3× one-step EMT: A, B, S.
7× two-step EMT: AB, AS, BA, BS, BP, SA, SB.
10× three-step EMT: ABS, ABP, ASB, BAS, BAP, BSA, BSP, BPA, BPS, SAB, SBA, SBP.
9× four-step EMT: ABSP, ABPS, ASBP, BASP, BAPS, BSAP, BSPA, BPAS, BPSA.

of the model. In other words, we want to find the key factors which determine the outcome rather than finding just one optimal value for all parameters.

To identify the key factors leading to cell extrusion, we will essentially try to compute approximatively the correspondance between

'EMT parameters' $\rightarrow$ 'expected number of basally extruded cells'.

For homogeneous EMT simulations, the amount of parameters is small enough that we can just run sufficiently many simulations and compare the outputs manually.

This changes for heterogeneous EMT, where the number of EMT parameters is too large for a one-to-one comparison. Therefore we used ensemble simulations and some statistics to compute from the output of thousands of simulations what the expected amount of basal extrusion is for given EMT scenarios.

For this task, we use the following steps:

- **Step 1 (Ensemble simulation):** Simulate the tissue with randomised EMT parameters n^{rep} times. For each simulation, we individually store information about the EMT outcome for each EMT cell. This yields a dataset of samples which associate EMT parameters and their outcome (per cell).
- **Step 2 (EMT categories):** Partition the space of EMT parameters into discrete categories. One category could be, for example 'all EMT cells with INM, loss of apical adhesion between $6\,\mathrm{h}$ and $9\,\mathrm{h}$ and no other EMT events'. Our aim is then to compare these different *EMT categories*.
- **Step 3 (Compute extrusion ratios):** With the categorised dataset from step 2, we can compute how many cells did escape basally for each category. Dividing this number by the total number of cells per category gives the **ratio of basal extrusion per EMT category**. These ratios provide a convenient parameter to rank the individual EMT categories. We also compute the ratio of apical extrusion in the same way.

These three steps are our primary approach to getting a global picture of the model and identifying the key factors leading to basal extrusion. We can focus on different aspects of the model by choosing different categorisations (e.g. more sparse or detailed ones).

The steps outlined essentially sample the conditional expectation of basal extrusion for given EMT timings. We will define the precise mathematical definition of the extrusion ratios in Section 3.3.3.

3.3. Extrusion metrics and analysis of heterogeneity

Notation. We recall that every single simulation gives us an approximation of $\boldsymbol{\mathcal{Z}}(t,\omega) = (\boldsymbol{\mathcal{X}}(t,\omega), \boldsymbol{\mathcal{A}}(t,\omega), \boldsymbol{\mathcal{B}}(t,\omega))$ which are samples of the random trajectories solving (3.33). To make explicit that we draw particular samples of these random trajectories, we keep the

variable ω in the notation. Otherwise we will neglect ω and write $\boldsymbol{\mathcal{Z}}(t)$, which we then consider as random variables.

We also want to refer to y coordinates conveniently. Since indices already serve multiple roles, we will use the projection maps instead, i.e. we recall the definition

$$y : \mathbb{R}^2 \to \mathbb{R} : (a, b) \mapsto b.$$

With this notation, $y(\boldsymbol{X}_i)$ is the y coordinate of the ith nuclei center.

The last notation we need is that of a line connecting two points $\boldsymbol{a}, \boldsymbol{b} \in \mathbb{R}^2$, which we denote as

$$\overline{\boldsymbol{a}\,\boldsymbol{b}} \coloneqq \{\lambda \boldsymbol{a} + (1-\lambda)\boldsymbol{b} \mid \lambda \in [0,1]\}.$$

3.3.1. Computing the number of apical and basal extrusions. The three most important quantities for our analysis of EMT are the numbers of apically extruded cells, basally extruded cells and the number of EMT cells below the epithelial cells.

These quantities are related to their biological counterpart, and it is natural to introduce the *apical-basal scale (AB scale)* which is also used in experimental data. The apical-basal scale is zero at the basal layer and one at the apical layer. It allows us to compare the relative positions of cell nuclei independent of the current development stage. In the EMT model, not all cells have their apical point on the apical layer. To define the AB scale, we will therefore use the projection of the nuclei onto the apical layer as a reference point.

For a fixed time $t \in [0, T]$ we define the apical layer $L_{\boldsymbol{\mathcal{A}}(t)}$ as the path of lines which passes through all points $\boldsymbol{A}_i(t)$, i.e.

$$L_{\boldsymbol{\mathcal{A}}(t)} \coloneqq \bigcup_{(i,j)\in\mathcal{A}(t)} \overline{\boldsymbol{A}_i(t)\,\boldsymbol{A}_j(t)}$$

where $\mathcal{A}(t)$ are the edges of the current apical network. For each nuclei center $\boldsymbol{X}_i$ we can compute the closest point on the apical layer as $\boldsymbol{A}_i^{\mathrm{ref}}(t) \coloneqq \mathrm{P}_{L_{\boldsymbol{\mathcal{A}}(t)}}(\boldsymbol{X}_i)$ where P denotes the projection operator onto $L_{\boldsymbol{\mathcal{A}}(t)}$. Since the basal layer is fixed at the x-axis, we can define the *position of a cell on the AB scale* as

$$y^{\mathrm{AB}}(\boldsymbol{X}_i(t)) \coloneqq \frac{y(\boldsymbol{X}_i(t))}{y(\boldsymbol{A}_i^{\mathrm{ref}}(t))}.$$

For later use, we define the following indicator functions:

(4.3)

$$\delta_i^{\mathrm{basal-extr}}(t) \coloneqq \begin{cases} 1 & \text{if } y^{\mathrm{AB}}(\boldsymbol{X}_i(t))) < 0, \\ 0 & \text{else} \end{cases}, \quad \delta_i^{\mathrm{apical-extr}}(t) \coloneqq \begin{cases} 1 & \text{if } y^{\mathrm{AB}}(\boldsymbol{X}_i(t))) > 1, \\ 0 & \text{else.} \end{cases}$$

These indicator functions tell if the ith cell is below or above the tissue respectively.

The identicator function for EMT cells to be below the epithelial cells is:

$$\delta_i^{\text{basal}-\text{pos}}(t) := \begin{cases} 1 & \text{if } y^{\text{AB}}(\boldsymbol{X}_i(t))) \leq \min_{j \in \mathcal{I}^{\text{control}}} y^{\text{AB}}(\boldsymbol{X}_j(t)) \\ 0 & \text{else.} \end{cases}$$

We define the following values, which count how many cells are above, between and below the apical or basal layer:

$$N^{\text{basal}-\text{extr}}(t) := \sum_{i \in \mathcal{I}^{\text{EMT}}} \delta_i^{\text{basal}-\text{extr}}(t), \tag{4.4}$$

$$N^{\text{apical}-\text{extr}}(t) := \sum_{i \in \mathcal{I}^{\text{EMT}}} \delta_i^{\text{apical}-\text{extr}}(t), \tag{4.5}$$

$$N^{\text{basal}-\text{pos}}(t) := \sum_{i \in \mathcal{I}^{\text{EMT}}} \delta_i^{\text{basal}-\text{pos}}(t). \tag{4.6}$$

Since each simulation is subject to noise and random event times, all these numbers are random variables.

Overall, we are interested in the average behaviour of EMT cells, for example, by computing the *ratio of extruded cells*

$$r^*(t) := \frac{1}{N^{\text{EMT}}} \mathbb{E}\left[N^*(t)\right]$$

where $*$ is a placeholder for 'basal-extr', 'apical-extr' or 'basal-pos'.

Given n^{rep} many simulations we approximate R^* by the sample mean

$$r^*(t) \approx \frac{1}{n^{\text{rep}} N^{\text{EMT}}} \sum_{\ell=1}^{n^{\text{rep}}} N^*(t, \omega_\ell), \tag{4.7}$$

where $\omega_\ell \in \Omega$ denotes the different outcomes for $1 \leq \ell \leq n^{\text{rep}}$ and $*$ is again a placeholder for 'basal-extr', 'apical-extr' or 'basal-pos'.

3.3.2. Basal positioning at the onset of EMT. For an EMT cell with index $i \in \mathcal{I}^{\text{EMT}}$ we define the basal positioning at the onset of EMT as

$$h_i^{\text{EMT}} := y^{\text{AB}}(\boldsymbol{X}_i(T_i^{\text{EMT}})), \tag{4.8}$$

where T_i^{EMT} is the minimum of T_i^{A}, T_i^{B} and T_i^{S}.

3.3.3. Estimation of extrusion ratios for heterogeneous EMT. As described in Section 3.2, we want to evaluate how efficient an individual EMT cell is when surrounded by other EMT cells with heterogeneous timings. This question arises in **Q2, Q3, Q4** and **Q8**. To obtain a quantity which allows us to compare various EMT timings in the heterogeneous case, we will compute conditional expectations for the number of extrusions of a particular cell given its EMT timings. This section provides the mathematical details behind the steps outlined in Section 3.2.

In the following, we continue with the setup from Section 2.3.1 where all EMT timings are i.i.d. random variables as defined in (4.2).

The setup is slightly technical since there are now two sources of randomness:

- **Noise in the simulation:** The initial positions are random, and there is additive noise on the nuclei positions (3.33).
- **Random EMT parameters:** Due to heterogeneity, the EMT timings $\boldsymbol{\mathcal{T}}$ are also random.

We will first discretise the continuous parameter space for timings to analyse how the EMT timings influence extrusion. That means we will consider a partition of the space of possible values for $\boldsymbol{T}_i$ into $n^{\mathrm{D}} + 1$ many subsets

$$D_1, \dots, D_{n^{\mathrm{D}}} \subseteq (\mathbb{R}^4 \cup \{\infty\})^{4N^{\mathrm{EMT}}}.$$

We call these sets *EMT categories* since they partition the space of EMT timings.

To compare if one EMT category is more efficient than another, we will compute the following conditional expectations

$$\mathbb{E}[\delta_i^*(t) \mid \mathcal{T}_i \in D_k] \coloneqq \frac{\mathbb{P}[\delta_i^*(t) \text{ and } \mathcal{T}_i \in D_k]}{\mathbb{P}[\mathcal{T}_i \in D_k]} \tag{4.9}$$

where $*$ is a placeholder for 'apical-extr', 'basal-extr' and 'basal-pos' (see Section 3.3.1). These values predict for the ith cell how much basal extrusion one can expect in average if the cell's EMT timings are in the kth EMT category.

Since there might be a difference depending on the location of a cell within the group of EMT cells, we define the *ratio of basal extrusion for the EMT category* D_k as the average

$$r^*(D_k) \coloneqq \frac{1}{N^{\mathrm{EMT}}} \sum_{i \in \mathcal{I}^{\mathrm{EMT}}} \mathbb{E}\left[\delta_i^*(t) \mid \mathcal{T}_i \in D_k\right], \tag{4.10}$$

where * is again a place-holder for 'basal-extr', 'basal-pos' and 'apical-extr'.

This approach to sample these conditional expectations is an inverse transform sampling for the conditional probabilities. There are more sophisticated statistical methods for this kind of problem, for example, accept-rejection algorithms used in Monte-Carlo methods, see [MNR12]. However, these methods do not fit the way we obtain the data.

To obtain an estimation for the conditional expectation, we notice that we can rewrite (4.9) as

$$\mathbb{E}[\delta_i^*(t) \mid \mathcal{T}_i \in D_k] = \frac{\mathbb{E}\left[\delta_i^*(t) \mathbb{1}_{D_k}(\boldsymbol{T}_i)\right]}{\mathbb{E}\left[\mathbb{1}_{D_k}(\boldsymbol{T}_i)\right]}, \tag{4.11}$$

where $\mathbb{1}_{D_k}$ is the indicator function which is 1 at D_k and zero elsewhere.

This motivates the estimation

$$\mathbb{E}\left[\delta_i^*(t) \mid \mathcal{T}_i \in D_k\right] \approx \frac{\sum_{\ell=1}^{n^{\mathrm{rep}}} \delta_i^*(t,\omega_\ell)\mathbb{1}_{D_k}(\boldsymbol{T}_i(\omega_\ell))}{\sum_{\ell=1}^{n^{\mathrm{rep}}} \mathbb{1}_{D_k}(\boldsymbol{T}_i(\omega_\ell))}, \tag{4.12}$$

where $\omega_\ell \in \Omega$ represent N^{rep} many outcomes.

For the statistical accuracy of (4.12) it is relevant that the samples cover all EMT categories equally. One way to ensure that is to pick partitions such that $\mathbb{P}\left[D_1\right] \approx \mathbb{P}\left[D_2\right] \approx \cdots \approx \mathbb{P}\left[D_{n^{\mathrm{D}}}\right] \approx \frac{1}{n^{\mathrm{D}}}$, then, we get that the average number of samples per EMT category is

$$\mathbb{E}\left[\sum_{\ell=1}^{n^{\mathrm{rep}}} \mathbb{1}_{D_k}(\boldsymbol{T}_i(\omega_\ell))\right] = \sum_{\ell=1}^{n^{\mathrm{rep}}} \mathbb{P}\left[\boldsymbol{T}_i(\omega_\ell) \in D_k\right] \approx \frac{n^{\mathrm{rep}}}{n^{\mathrm{D}}}.$$

That means, on average, we have $\frac{n^{\mathrm{rep}}}{n^{\mathrm{D}}}$ samples for each EMT category.

In our application, we typically had numbers of $n^{\mathrm{D}} \in [10, 500]$ and therefore, we used $n^{\mathrm{rep}} \in [10^4, 5 \cdot 10^5]$ to ensure that we have around 10^3 simulations to rate each EMT category.

Remark 4.1 (Easy interpretation)**.** The precise mathematical framework might obliviate that (4.12) is a very intuitive value which can also be motivated without much math.

Essentially, we compute

$A \coloneqq$ Number of basally extruded cells with EMT timings of category k,

$B \coloneqq$ Number of cells with EMT timings of category k

which then gives

$$\text{Expected ratio of basally extruded cells in category } k = \frac{A}{B}.$$

3.3.4. Relation between basal extrusion and basal positioning at the onset of EMT. Finally, we will also compute conditional expectations in a more general setup to estimate for example, how the basal positioning at the onset of EMT h_i^{EMT} (4.8) might influence the extrusion rates.

The situation is completely analogous to (4.12): We will use the partition

$$(0, 1/n^{\mathrm{D}}] \cup (1/n^{\mathrm{D}}, 2/n^{\mathrm{D}}] \cup \cdots \cup (n^{\mathrm{D}}-1/n^{\mathrm{D}}, 1] =: \bigcup_{k=1}^{n^{\mathrm{D}}} D_k = [0,1]$$

and we compute the expectation of basal extrusion under the condition that $h_i^{\mathrm{EMT}} \in D_k$ with the same sampling approach as before

$$\mathbb{E}\left[\delta_i^{\mathrm{basal-extr}}(t^{\mathrm{end}}) \mid h_i^{\mathrm{EMT}} \in D_k\right] \approx \frac{\sum_{\ell=1}^{n^{\mathrm{rep}}} \delta_i^*(t,\omega_\ell)\mathbb{1}_{D_k}(h_i^{\mathrm{EMT}}(\omega_\ell))}{\sum_{\ell=1}^{n^{\mathrm{rep}}} \mathbb{1}_{D_k}(h_i^{\mathrm{EMT}}(\omega_\ell))}$$

for n^{rep} many outcomes $\omega_\ell \in \Omega$.

4. Modelling results

This section presents our simulation results. Please note that the conclusions drawn are qualitative rather than quantitative predictions. Intentionally, we did not fite the model to real data. Instead, we use it as a framework to explore a variety of scenarios. This exploration leads to various biological hypotheses, which we will discuss in Section 5.

Specifically, the model will be used to investigate the questions posed in Section 3.1, which we recall next:

- **(Q1) Group efficiency:** Are groups of EMT cells (such as in the cephalic region) extruded more frequently than isolated EMT cells (as in the trunk region)?
- **(Q2) Selection of EMT events:** Is basal extrusion possible without of all possible EMT events? Or, more generally, Which EMT events have to occur for basal extrusion?
- **(Q3) Timing of onset of EMT:** Are early EMT events more efficient in producing cell extrusion?
- **(Q4) Order of EMT events:** Are there specific sequential orders of EMT events which lead to more basal extrusion?
- **(Q5) Group efficiency of heterogeneous EMT:** Is it an advantage if a group of EMT cells has all the same timings or is a mixture of timings better?
- **(Q6) Effect of interkinetic nuclear movement (INM):** Are EMT cells without INM extruded more frequently than EMT cells with INM?
- **(Q7) Basal positioning at the onset of EMT:** Does the position of an EMT cell at the start of EMT events impact its rate of extrusion?
- **(Q8) Competition:** Do other EMT cells with very effective EMT programs decrease the efficiency of non-effective EMT programs?

Notation. We recall that we use **[A]**, **[B]**, **[S]** and **[P]** to refer to the EMT events *loss of apical adhesion*, *loss of basal adhesion*, *loss of straightness* and *protrusive activity*, respectively.

We combine these notations to refer to a specific order of events. For example, the EMT events **[AB]** are all possible timings with $T^{\mathrm{A}} \leq T^{\mathrm{B}}$ and $T^{\mathrm{S}} = T^{\mathrm{P}} = \infty$.

Strategy. Our point-of-departure is the simplest EMT scenario, and we will increase the complexity step-by-step: First, we will consider an individual EMT cell that only performs one EMT event (Sections 4.1 and 4.2), then we increase the complexity and consider multiple EMT events (Section 4.3). The next step is to compare individual EMT cells with homogeneous groups (i.e. groups of cells performaing the same EMT scenario) in Section 4.4. Finally, Section 4.5 will look at heterogeneous EMT timings. The summary of results is given in Section 4.7.

4.1. Isolated cell and single EMT event

In our most elemental setup, we will compare how the different EMT timings impact the extrusion rate for a single, isolated EMT cell. Isolated cells might occur in the trunk region of the neural tube, as shown in Figure 3.

In Figure 10, we plot the results of $n^{\mathrm{rep}} = 400$ simulations for the EMT events **[A]**, **[B]**, **[S]** and **[BP]**. For active protrusions, cells need to detach from the basal layer first, that is why we include **[BP]** here already. We sample the extrusion rates according to (4.7). All simulations use the default parameters from Tables 1 to 3 (from Chapter 3) with the modifications from Table 1.

	N^{EMT}	INM	T^{P}	T^{A}	T^{B}	T^{S}
[A]	1	100 %	∞	12 h	∞	∞
[B]	1	100 %	∞	∞	12 h	∞
[S]	1	100 %	∞	∞	∞	12 h
[BP]	1	100 %	24 h	∞	12 h	∞

Table 1. EMT-specific parameters for the simulations in Figure 10 (individual cells and single-step EMT). Here, the timing is fixed (not random).

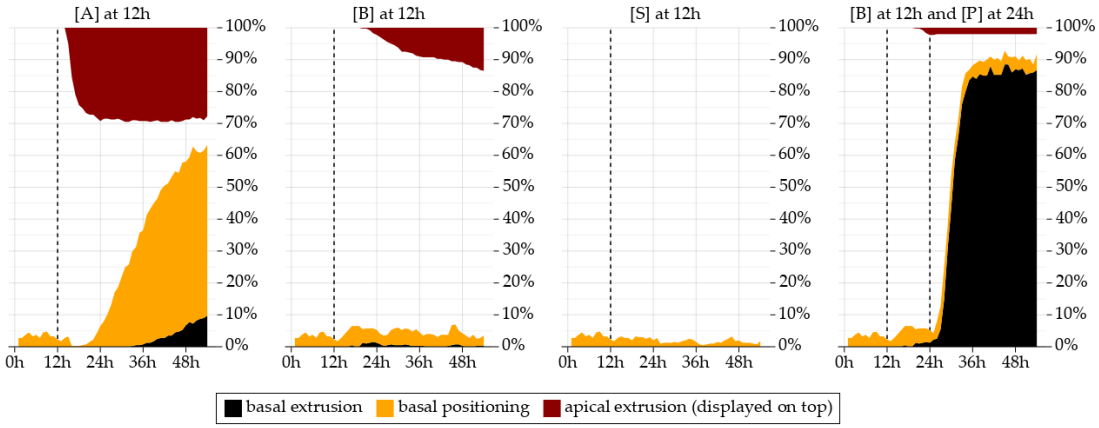

Figure 10. Average extrusion ratio from $n^{\mathrm{rep}} = 400$ simulations. The yellow color shows the ratio of EMT cells below all epithelial cells, i.e. cells in basal positioning. In the first three plots, only one EMT event is active. After *loss of apical adhesion* ***[A]***, cells will leave the center of the tissue and possibly escape apically (30 %) or basally (10 %). For *loss of basal adhesion* ***[B]*** and *loss of straightness* ***[S]***, cells remain mostly between the control cells. With *protrusive activity* ***[P]*** (fourth graph), cells will almost always exit basally.

We see in Figure 10 that the individual EMT events lead to very different results. In the following, we observe that

(1) **[P]** almost guaranties basal extrusion

(2) **[A]** drives cells out of the tissue, mostly basally.

(3) Apical extrusion can also happen.

We give more details on these observations next.

4.1.1. Observation: [P] almost guaranties basal extrusion. Protrusive activities **[P]** are the only EMT event which introduces an *active force* pulling cells towards the basal layer. This makes **[P]** extremely effective compared to all other EMT events.

We could stop here and conclude that **[P]** is the critical factor leading to basal extrusion. However, it is not known if cells escape the epithelium via self-protrusions. Therefore, we will not ignore the other EMT events right away and instead we will try to find other mechanisms that could lead to basal extrusion.

In the following, we will differentiate between *active extrusion* and *passive extrusion*. With our model, *active extrusion* only occurs with **[P]**, and all other cases are passive since they do not lead to forces which pull the cell basally.

We also note that with the EMT event **[BP]**, a small number of cells exit apically. We recall that cells perform the seek-and-grab mechanism in the direction of $\boldsymbol{B}_i - \boldsymbol{X}_i$, which represents the cell polarity. Since cells with EMT events **[BP]** will first lose basal adhesion, the polarity of cells can point apically, in which case these cells may never be able to grab onto the basal matrix to pull.

4.1.2. Observation: [A] drives cells out of the tissue, mostly basally. Most surprising are probably the high rates of extrusion caused by **[A]**. At the end of the simulations, there is only a $10\,\%$ likelihood that an EMT cell is neither apically extruded nor below all epithelial cells at the end of the simulation. In Figure 11, we see two typical simulations of the **[A]** scenario where cells are pushed away from the tissue center.

While there is more apical extrusion than basal extrusion, it is interesting that in $60\,\%$ of the cases, the loss of *apical* adhesion pushes cells *basally*. It is because of *interkinetic nuclear movement* (INM): INM leads to a passive apical-basal movement of all cells which are not close to mitosis. Normally the rapid basal-apical movement before mitosis brings cells back to the apical layer, but cells without apical adhesion do not perform the rapid basal-apical movement. Therefore these cells only experience the passive apical-basal movement.

We see that **[A]**, in combination with INM, leads to cells which move passively towards the basal side and might fail to reach the apical layer at mitosis. This leads to a slow but overall basally directed trend after **[A]**.

4.1.3. Observation: Apical extrusion can happen as well. Our simulations show that the EMT scenarios **[A]** and **[B]** also lead to apical extrusion. Apical extrusion does normally not occur in experiments. However, in vivo studies show that apical extrusion can happen under altered conditions. After apical extrusion, cells are in the lumen, where they die rather quickly and get flushed out of the body [NT98, Fig. 5c].

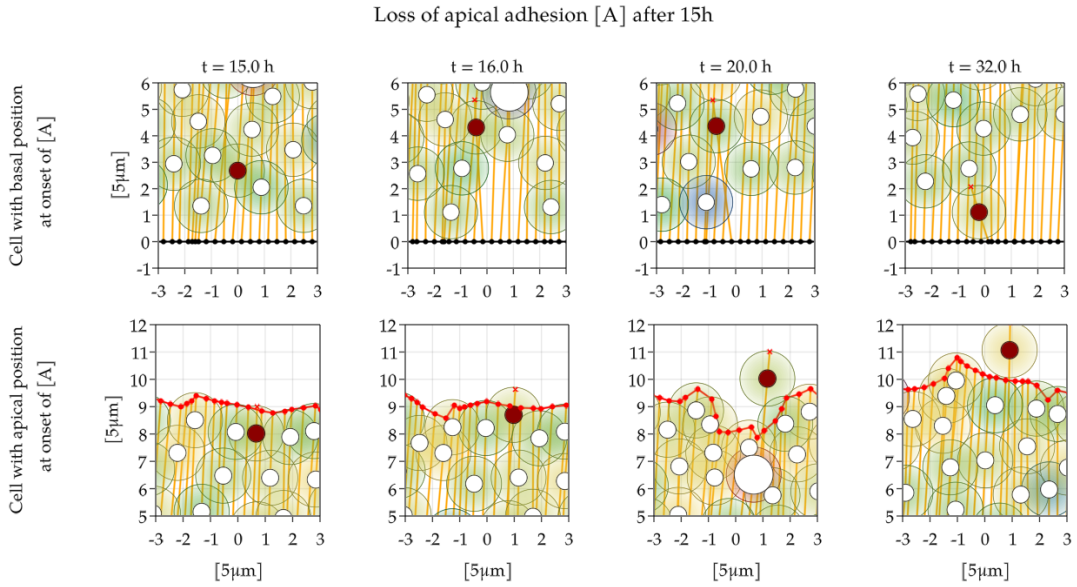

Figure 11. Examples for the EMT event **[A]**. Here, the top and bottom row show cells which perform **[A]** after 15 h. **Top:** The EMT cell (in red) is located basally at the onset of EMT at time $t = 16\,\mathrm{h}$. The nucleous moves apically, since the apical-nuclei spring contracts after **[A]** which pulls the nuclei towards the apical point, see Section 4.3.2. However, by the end of the simulations at $t = 32\,\mathrm{h}$ the cell has moved towards the basal side due to the pushing of the other cells. **Bottom:** Here, the EMT is part of the top layer of the tissue. Once **[A]** is active, the cell can escape apically when pushed by the other cells.

The occurance of apical extrusion in the model is interesting, because the discrepancy with experimental data under physiological conditions raises biological questions. It could indicate that cells need protrusive activities to avoid apical extrusion, or that there is another strategy cells emply which we have not considered in the model. We will discuss the relation with experimental results in Section 5.1.

4.2. Isolated cell with single EMT event and without INM

We already saw in Section 4.1.2 that INM interacts with the different EMT events. In the next simulations, we will use the same setup as in Section 4.1 with the only change that the EMT cell does not perform INM.

The changes are quite substantial as we see in Figure 12. In particular, we can observe that

(1) Stopped INM leads to more basal and less apical extrusion.

(2) **[S]** is mostly irrelevant.

	N^{EMT}	INM	T^{P}	T^{A}	T^{B}	T^{S}
[A] no INM	1	0 %	∞	12 h	∞	∞
[B] no INM	1	0 %	∞	∞	12 h	∞
[S] no INM	1	0 %	∞	∞	∞	12 h
'no EMT & no INM'	1	0 %	∞	∞	∞	∞

Table 2. EMT-specific parameters for the simulations in Figure 12 without INM. Notice that only the EMT cell stops INM. Nonetheless, all other epithelial cells will perform INM.

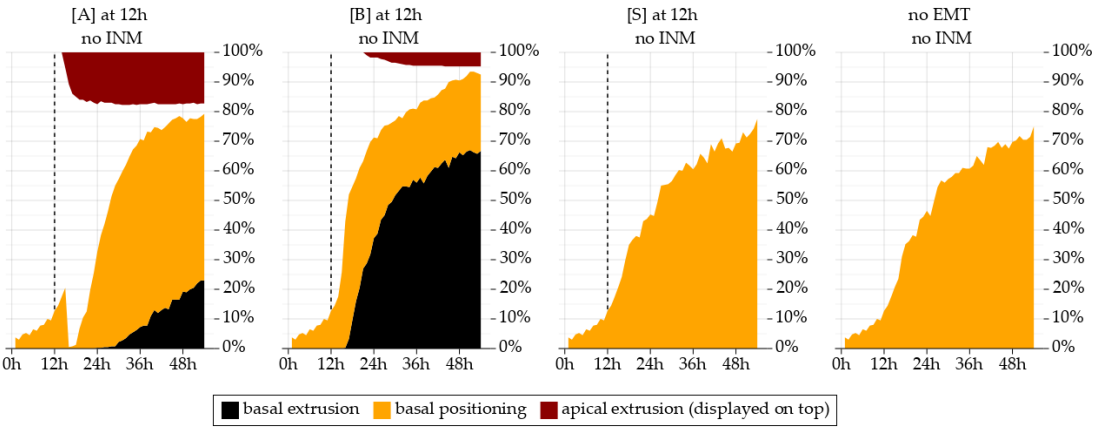

Figure 12. If the isolated EMT does not perform INM, the affect of the EMT events changes. Suddenly, **[B]** leads to much more basal extrusion compared to **[A]**. In the simulations with INM it was the other way around. The third and fourth graphs show that the basal positioning increases even for EMT cells which only stop INM but do not perform any event or only perform **[S]**. (**[P]** is not displayed, but the situation is similar to Figure 10.)

We detail these observations next.

4.2.1. Observation: Stopped INM leads to more basal and less apical extrusion. In Figure 13, we compare the extrusion rates with and without INM from Figures 10 and 12. We notice that the ratio of basal extrusion increased for **[A]** and **[B]**. For **[A]** it went from 10 % to 20 % and for **[B]** it jumped from 0 % to 70 %.

This highlights the relevance of INM for the extrusion rates. Which is a trend we will also observe for groups of EMT cells: *The epithelial cells with INM create a slow basally directed stream which causes cells without INM to drift and stay on the basal side*. If a cell in a basal position loses its basal adhesion **[B]**, then chances are high that it will exit basally.

4.2.2. Observation: [S] is mostly irrelevant. One takeaway from Figure 12 is that cells which lose straightness **[S]** still behave essentially like epithelial cells (control cells) in

the model. To simplify the further plots and limit the number of possible combinations of EMT events, we will ignore **[S]** from now on.

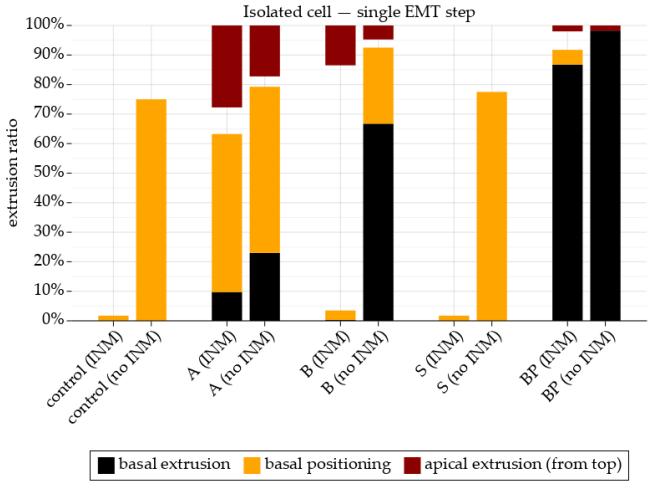

Figure 13. Summary of extrusion ratios at the end of simulations with *an isolated cell and single EMT event*. The most impactful factor is clearly **[P]**, leading to active basal extrusion. Among the passive basal extrusion, scenarios without INM lead to more basal extrusion than their counterparts with INM. This is most prominent for **[B]**, which is much more efficient without INM.

4.3. Isolated cell and multiple EMT events

Next, we study if combinations and timings of EMT events impact the number of extruded cells. From the previous observation, we can already draw that **[P]** will dominate each other event (which is also confirmed later in Figure 15) and **[S]** is irrelevant. This allows us to focus only on different timings for **[A]** and **[B]**.

	N^{EMT}	INM	T^{P}	T^{A}	T^{B}	T^{S}
[A⧗B]	1	100 %	∞	6 h	24 h	∞
[AB]	1	100 %	∞	15 h	15 h	∞
[B⧗A]	1	100 %	∞	24 h	6 h	∞

Table 3. EMT timings for Figure 14. The ⧗ symbol denotes that there is a larger delay between events. For example, for the EMT scenario **[A⧗B]** there is an 18 h delay between **[A]** and **[B]**, whereas for **[AB]** both EMT events happen simultaneously.

In Figure 14, we consider isolated cells with the EMT timings as in Table 3. Since we want to look at the impact of relative timings between events, we also compare the basal positioning of EMT cells close to the start of **[A]**. As we comment in the following sections, we can conclude that the timing of EMT events does not seem to have an impact on basal extrusion.

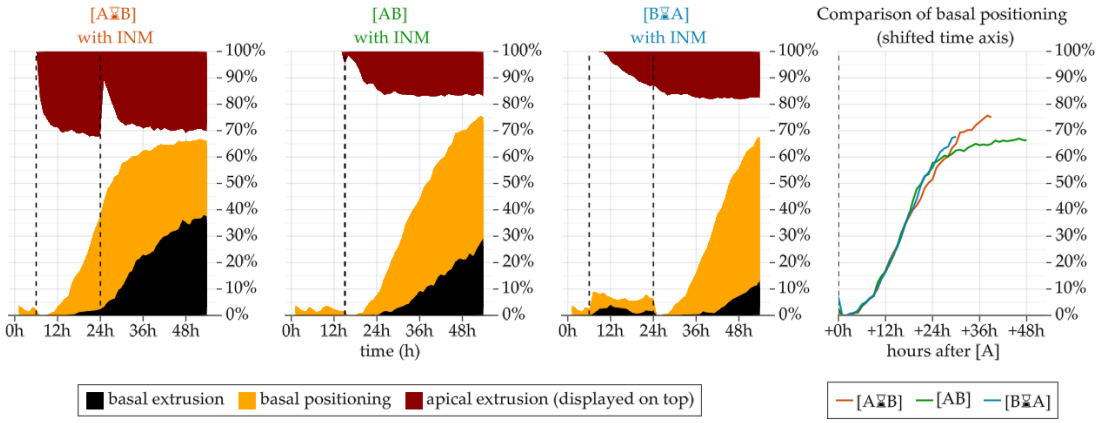

Figure 14. Comparison of different timings for **[A]** and **[B]**. **Left figures:** There are two differences between the extrusion rates. In **[A⧗B]**, the amount of apical extrusion increases rapidly in the beginning, hinting that the absolute timing of **[A]** does have an impact. However, at the onset of **[B]** some cells are pulled back into the tissue. This occurs in the model since the basal-nuclei spring contracts at **[B]**, which leads also to a force which also $\boldsymbol{X}_i$ towards $\boldsymbol{B}_i$. The reverse effect is visible in **[B⧗A]** where cells move apically at **[A]**. **Right:** The curves of basal positioning relative to the onset of **[A]** are almost identical. This is one of many cases where the relative timings between EMT events are less important than the absolute timings.

4.3.1. Observation: The relative EMT timings are not very important. The comparison in Figure 14 shows that in the model, the basal positioning depends on the time passed since **[A]** started. We will reiterate this aspect when we look at homogeneous EMT cells, but in general we did not observe that the relative timings between EMT events completely change the outcome. It seems rather more a give-and-take between the characteristics of the individual EMT events.

We will see another similar result for heterogeneous EMT in Section 4.5.3

4.3.2. Notes on the pull-in effect. We observe in Figure 14 the pull-in effect of the cell nucleus. This happens because cells contract their free apical-nuclei or basal-nuclei springs after **[A]** or **[B]**. This is a two-sided effect that not only pulls the apical or basal point towards the nucleus but it also pulls the nucleus itself which can lead to a movement back into the tissue.

Biologically, even though not tested experimentally, this effect could be due to a combination of high cell-cell adhesion forces and contraction forces of the cytoskeleton of the EMT cell.

4.4. Groups of EMT cells: homogeneous EMT

So far, the EMT cells were always isolated and had to cope with the remaining tissue alone. This raises the question of whether a group of EMT cells is more effective since multiple cells could potentially create a basally directed movement. Before we cover

the more realistic case of heterogeneous EMT, we first consider homogeneous EMT to differentiate between effects caused by the number of EMT cells and effects resulting from EMT heterogeneity.

	N^{EMT}	INM	T^{P}	T^{A}	T^{B}	T^{S}
ABP	1 or 10	yes/no	18 h	6 h	12 h	∞
BAP	–	–	18 h	12 h	6 h	∞
BP⧗	–	–	6 h	∞	6 h	∞
B⧗P	–	–	18 h	∞	6 h	∞
A⧗B	–	–	∞	6 h	18 h	∞
B⧗A	–	–	∞	18 h	6 h	∞
A⧗	–	–	∞	6 h	∞	∞
⧗A	–	–	∞	18 h	∞	∞
B⧗	–	–	∞	6 h	∞	∞
⧗B	–	–	∞	∞	18 h	∞
$\emptyset$	–	–	∞	∞	∞	∞

Table 4. Parameters for EMT cells in Figure 15. For each choice, we ran $n^{\mathrm{rep}} = 100$ simulations. Different timings for **[S]** were also tried but led to no significant changes.

In Figure 15, we compare the basal extrusion ratios between individual cells and a homogeneous group with $N^{\mathrm{EMT}} = 10$ cells. The parameters are listed in Table 4. We compare two variations at the same time:

- the difference between individual cells and homogeneous groups and
- the impact of interkinetic movement (INM).

Moreover, we plot the outcome of combinations between **[A]**, **[B]** and **[P]**, possibly with delays between the EMT events.

One observation which repeats itself is the high basal extrusion ratio of EMT cells without INM. As discussed in Section 4.2.1, the extrusion ratios increase drastically, especially if **[B]** is part of the EMT program.

4.4.1. Observation: Collective effects in homogeneous groups do not help to produce basal extrusion. Opposite to our initial expectations, the basal extrusion for homogeneous EMT drops compared to individual EMT scenarios. In many situations, the difference is up to $-10\,\%$ (for example **[B⧗]** without INM) whereas in other cases, it remains on the same level (e.g. **[⧗A]**).

It is difficult to pinpoint the exact reason, but it seems that groups do introduce not only synergy effects but also competition among cells. If other EMT cells occupy the path towards the basal side, then *passive extrusion* is ineffective. See Figure 16 for an example.

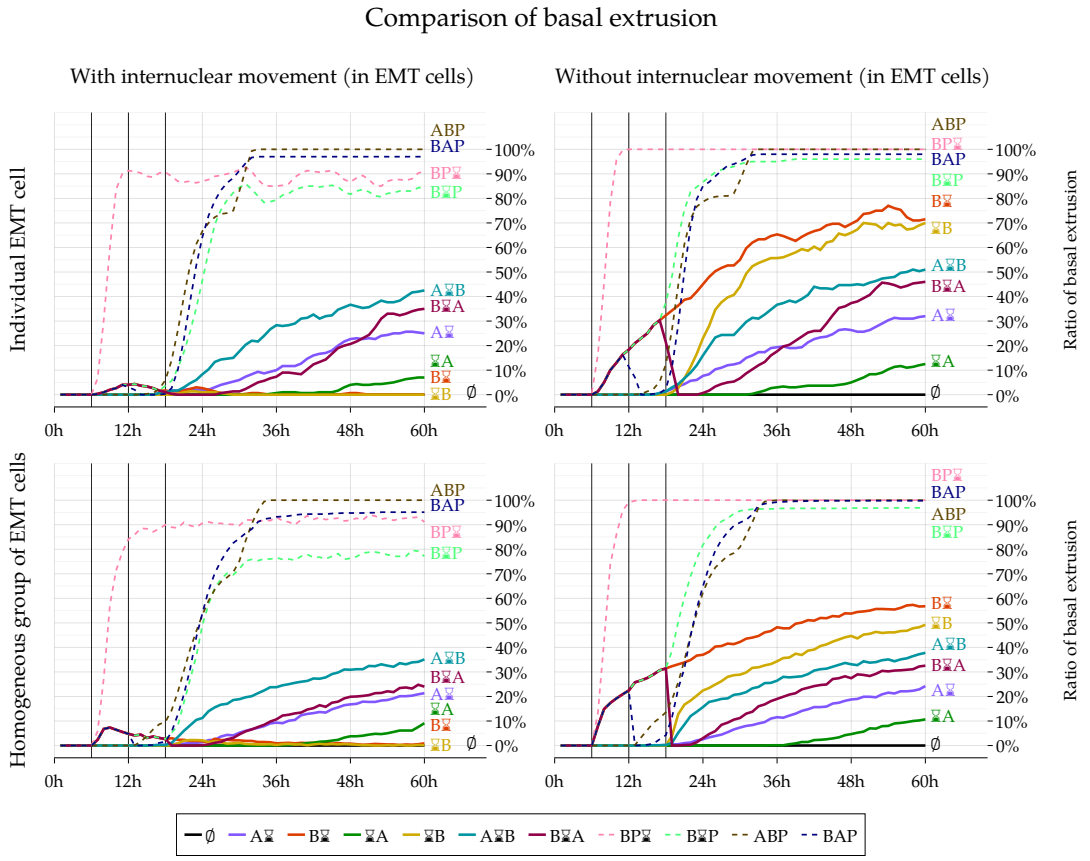

Figure 15. Comparison of basal extrusion ratios between simulations **with and without INM** and **with individual or homogeneous EMT**: The ⧗ symbol denotes 12 h delay before or after an event. It is clearly visible that the lack of INM increases basal extrusion, in particular for events with the EMT event **[B]**. In contrast, homogeneous groups of cells are less efficient than individual EMT cells.

4.5. Groups of EMT cells: heterogeneous EMT

This setup is comparable to the cephalic region of the neural tube (see Figure 3) where multiple cells undergo EMT with heterogeneous EMT events. From a biological point of view, it is not clear if heterogeneity gives an advantage to increase the rate of basal extrusion. We explore this question next.

To model heterogeneity, we choose randomised EMT timings for a group of EMT cells, as described in Section 2.3.1. Again, we restrict our attention to the EMT events **[A]** and **[B]** since **[P]** leads almost always to basal extrusion. We consider $N^{\mathrm{EMT}} = 10$ cells which perform **[A]**, **[B]** with $70\,\%$ probability and in these cases, the timings are uniformly randomly picked in the interval $[6\,\mathrm{h}, 24\,\mathrm{h}]$. The likelihood of **[P]** is varied as shown in Table 5.

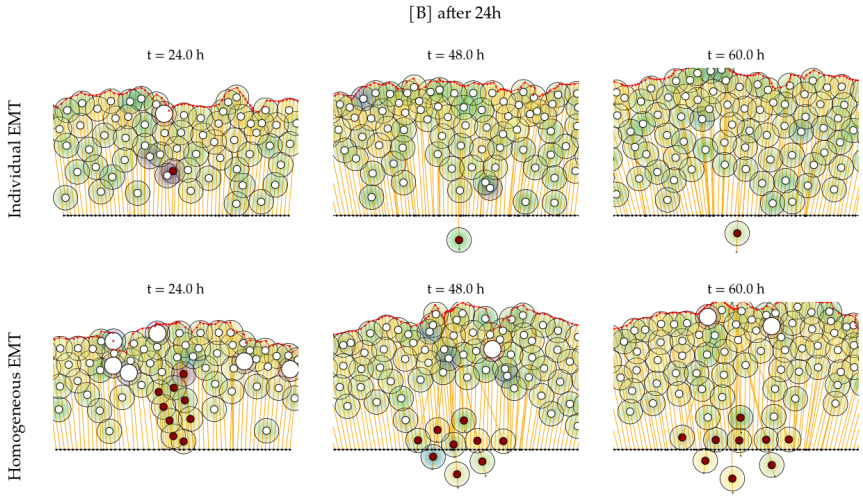

Figure 16. Examples for **[⧗B]** for an individual cell and a group of cells. The basal extrusion rates for individual cells are larger since individual cells have no obstacles, whereas groups of EMT cells might block the way for other EMT cells. This at least slows down the extrusion rates for groups of cells.

	N^{EMT}	INM	T^{P}	T^{A}	T^{B}	T^{S}
'63% **[P]** '	10	50 %	$\mathcal{U}^{90\,\%}(6\,\mathrm{h}, 24\,\mathrm{h})$	$\mathcal{U}^{70\,\%}(6\,\mathrm{h}, 24\,\mathrm{h})$	$\mathcal{U}^{70\,\%}(6\,\mathrm{h}, 24\,\mathrm{h})$	∞
'35% **[P]** '	10	50 %	$\mathcal{U}^{50\,\%}(6\,\mathrm{h}, 24\,\mathrm{h})$	$\mathcal{U}^{70\,\%}(6\,\mathrm{h}, 24\,\mathrm{h})$	$\mathcal{U}^{70\,\%}(6\,\mathrm{h}, 24\,\mathrm{h})$	∞
'6% **[P]** '	10	50 %	$\mathcal{U}^{10\,\%}(6\,\mathrm{h}, 24\,\mathrm{h})$	$\mathcal{U}^{70\,\%}(6\,\mathrm{h}, 24\,\mathrm{h})$	$\mathcal{U}^{70\,\%}(6\,\mathrm{h}, 24\,\mathrm{h})$	∞

Table 5. EMT timings to represent heterogeneous EMT. The notation $\mathcal{U}^{70\,\%}(6\,\mathrm{h}, 24\,\mathrm{h})$ is explained in Section 2.3.1. We recall that **[P]** is only active if also **[B]** happens. For example in the first scenario, protrusion occur effectively in $63\,\% = 90\,\% \cdot 70\,\%$ of the EMT cells. The likelihood of INM is randomised as well, were only $50\,\%$ of all EMT cells in a group exhibit INM. As previously, all epithelial (no-EMT) cells will always perform INM.

There are more sources of randomness in the heterogeneous case, which requires more simulation runs, especially if we only use a subset of the generated data to compute basal extrusion for cells with particular EMT events. For all figures, we used $n^{\mathrm{rep}} = 50000$ simulation runs with 10 EMT cells each, yielding 5×10^6 data points for our analysis.[2]

In Figures 17 to 19, we plot basal extrusion rates for cells with the EMT events **[A]**, **[B]** and **[AB]** comparing their performance in an individual, homogeneous and heterogeneous setup. The three different heterogeneous configurations from Table 5 serve as examples of EMT populations with different competitive advantages. The main observation is that

[2]Here, we see the importance of the numerical efficiency of the PBD method from Chapter 2 and the model change discussed in Chapter 3. The new 300 times faster simulation compared to the original model and method in [Fer+19] allowed us to run 50000 simulations in less than 45 min instead of 10 days.

(1) Heterogeneity with INM decreases the extrusion ratio.

(2) Heterogeneity without INM increases the rate of basal extrusion compared to homogeneous groups.

(3) Timing for heterogeneous EMT cells does not have a big impact.

We discuss this in the following sections.

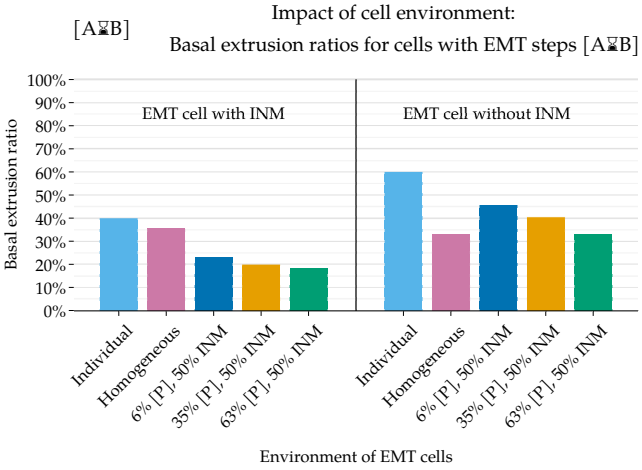

Figure 17. We compare the basal extrusion ratios for cells with the same EMT scenario (here **[A⧗B]**) but for different environments. First, we consider an individual cell, then a cell which is surrounded by other EMT cells with the same EMT scenario and finally, we consider cells which are surrounded by a heterogeneous group of EMT cells. **Left:** EMT cells with INM show lower extrusion rates in the heterogeneous case. **Right:** For EMT cells without INM the situation is different. Here, the heterogeneous scenarios yields extrusion rates which are between the individual and the homogeneous cases.

4.5.1. Observation: heterogeneity with INM decreases the extrusion ratio. As visible in Figures 17 and 18, the simulations show that for EMT cells with INM the frequency of basal extrusion is lowest in the case of heterogeneous EMT. The reason is the increased competition in the heterogeneous case. Since the environment contains cells with protrusive activity and cells without INM, it is unlikely that cells with INM are in a favourable spot for passive push to the basal side. Therefore, the basal extrusion rates are lower than in the homogeneous case or individual case, where cells compete less.

4.5.2. Observation: heterogeneity without INM increases the rate of basal extrusion compared to homogeneous groups. The right plots in Figures 17 to 19 show that EMT cells without INM show higher rates of basal extrusion than they would show in a homogeneous case. That indicates that EMT cells without INM have an advantage compared to the other competing EMT cells.

In all but one of the examples, individual cells are more efficient than cells in a heterogeneous environment. The only exception is in Figure 18 where cells with **[A]** do

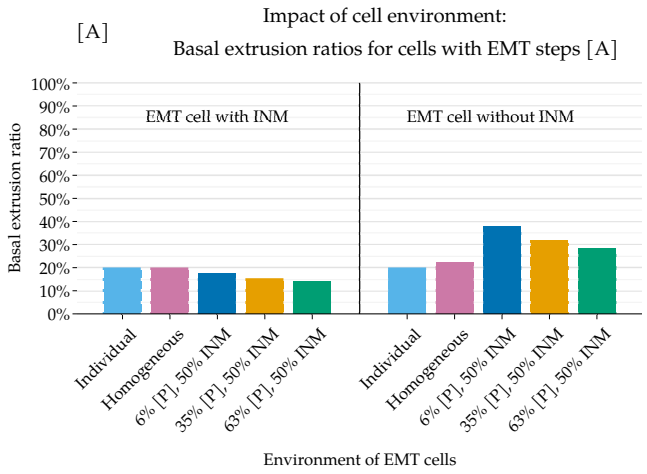

Figure 18. Left: The heterogeneous case is a bit less efficient for EMT cells with INM and **[A]**. **Right:** EMT cells which only lose their apical adhesion **[A]** and do not perform INM benefit from a heterogeneous environment. Here, the presence of cells with more efficient EMT events leads to a passive motion which can also carry cells with only **[A]** to the basal side.

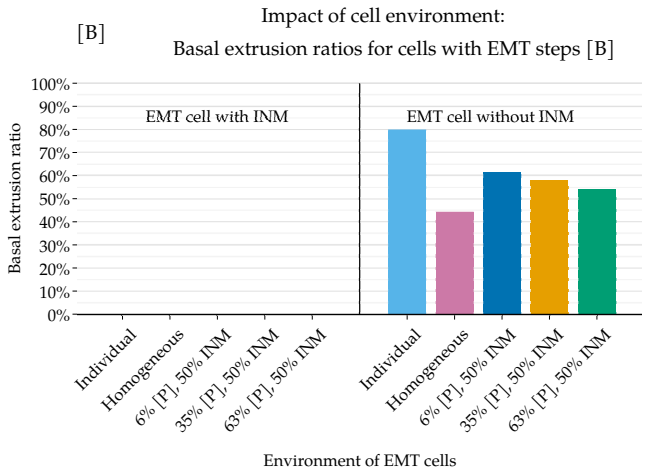

Figure 19. Left: As seen previously, the EMT event **[B]** with INM does not lead to basal extrusion. **Right:** For cells without INM, the extrusion ratios for heterogeneous cases are between the individual and homogeneous values. Also, here, the presence of more protrusive cells in the heterogeneous EMT population decreases the basal extrusion rates for cells without protrusions.

almost double their extrusion ratios in the heterogeneous case. In general, it seems that heterogeneity averages the overall performance of cells without INM, such that efficient EMT events are slightly less effective and inefficient EMT events show increased basal extrusion.

4.5.3. Observation: timing for heterogeneous EMT cells does not have a big impact. Previously, we observed that timing does not play an essential role for the extrusion of individual cells. Also in the heterogeneous case the timings do not have a big impact. We can show this by computing the conditional expectations of basal extrusion ratios as discussed in Section 3.3.3.

In Figure 20, we show the conditional expectations of the basal extrusion rates for EMT cells which perform an EMT event in a particular time interval. The results show that the basal extrusion ratios are independent of the timing of **[B]** and **[P]** and there is a slight dependency on the start of **[A]**. Overall, the model suggests that the timing is only mildly relevant for individual and heterogeneous EMT.

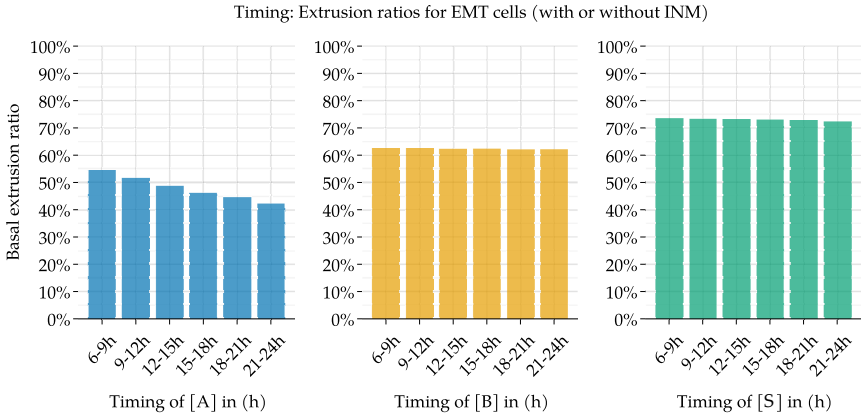

Figure 20. Extrusion ratios for cells which start of **[A]**, **[B]** and **[S]** within a particular time interval. While there is some trend concerning **[A]**, preferring earlier timings. The timing of **[B]** and **[S]** are irrelevant for the extrusion ratios.

Contrary to our expectations, there is no timing and ordering of EMT events which is clearly more efficient than other EMT scenarios with the same EMT events occuring. For this reason, we decided to explore other factors that could have a higher correlation with basal extrusion. In particular, we invesitgated the impact of basal positioning at the onset of EMT, see Section 4.6.

4.6. The effect of basal positioning

We observed that EMT cells without INM are generally more efficient. This raises the question if the lack of INM itself or some other underlying factor is the most relevant here. An obvious candidate is the position of a cell at the onset of EMT. As we have seen, cells do compete with each other for space and starting closer to the basal side could be a favouring factor in this competition.

In the following, we say a cell has basal positioning to refer to cells close to the basal layer.

In Figure 21, we see the conditional expectation of basal extrusion for cells in given intervals of basal positioning (as defined in Section 3.3.4).

The result show quite clearly that basal positioning is for cells without protrusive activities the best predictor of basal extrusion in our model. As Figure 21 shows, EMT cells which are in the most basal 20% of the tissue do exit basally with rates between $70\,\%$ up to $80\,\%$. This is the highest rates we observed among EMT cells without protrusions.

We will discuss this aspect further in Section 5, where we show experimental data supporting this insight from the model.

Comparing Figure 21 and Figure 20, we can conclude that basal positioning has more impact on basal extrusation than the timing of EMT events.

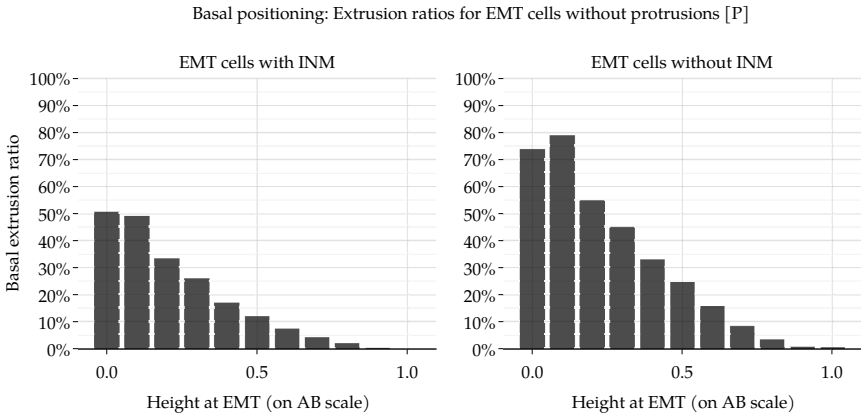

Figure 21. The conditional expectations of basal extrusion for EMT cells depending on the height of the cell within the tissue at the onset of EMT. Here, we only consider EMT scenarios without protrusions. The results show that basal positioning at the onset of EMT is a good predictor for basal extrusion.

Figure 22 shows with a scatter plot how the basal positioning at the onset of EMT correlates with basal extrusion.

4.7. Summary of the simulation results

Returning to our initial questions, we obtained the following results:

(Q1) Group efficiency: *Are groups of EMT cells (such as in the cephalic region) more efficient than isolated EMT cells (as in the trunk region)?*

> **Answer:** No, in most cases, heterogeneous groups are less efficient than individual cells. Only sometimes, heterogeneous environments elevate inefficient EMT events.

(Q2) Selection of EMT events: Is basal extrusion possible without the implementation of all EMT events? Which EMT events have to occur for basal extrusion?

> **Answer:** Yes, without INM all cell events with **[A]**, **[B]** or **[P]** lead to extrusion. If cells continue to perform INM, then only **[P]** or cells with **[A]** or **[B]** and favourable basal positioning get extruded.

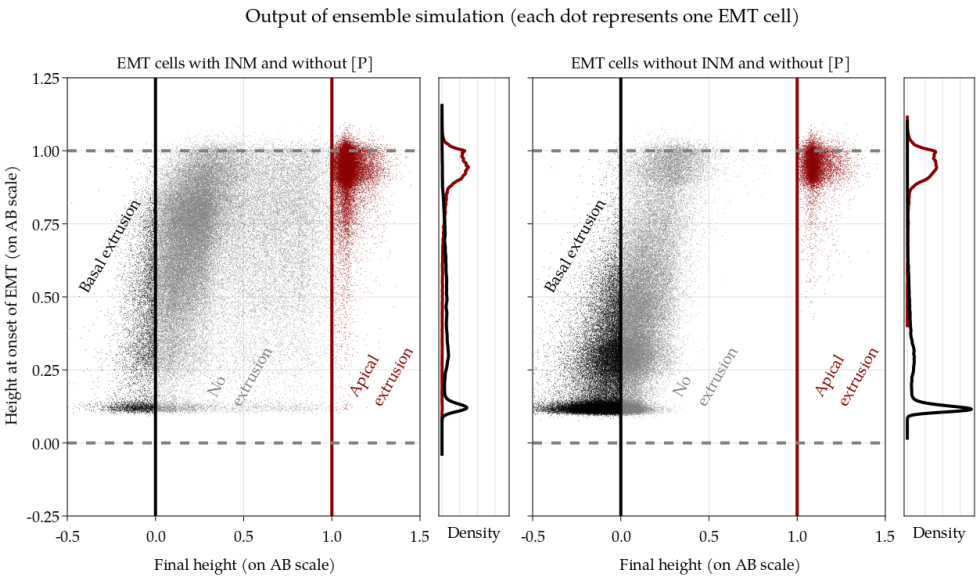

Figure 22. Each dot in these plots represents one EMT cell from the $n^{\text{rep}} = 50000$ simulations of the heterogeneous scenario '35% **[P]** ' from Table 5. The x-axis shows the final position of the cell. Dots left of 0 represent basally extruded cells. Equally, all cells right of 1 are apically extruded. We do not show dots for cells with active protrusions in the plot. **Left:** EMT cells with INM are more likely to be in the center of the tissue, which is visible in comparison by the many gray cells in the center. Most cells in the upper 20 % of the tissue extrude apically. For basal extrusion, the trend is less clear, but there is still a tendency for cells in basal positions to exit basally. **Right:** For cells without INM, the importance of basal positioning is more emphasised. Most cells which extrude basally start EMT from the lower half of the tissue.

(Q3) Timing of onset of EMT: Are early EMT events more efficient?

> **Answer:** Mostly no. Only the early onset of **[A]** shows some increase in extrusion ratios, but overall the timing seems irrelevant.

(Q4) Order of EMT events: Are there specific sequential orders of EMT events which lead to more basal extrusion?

> **Answer:** The order of EMT events, that is, the relative timing between EMT events, can lead to small differences which are better explained by earlier or later absolute timing of one of the EMT events.

(Q5) Group efficiency of heterogeneous EMT: Is it an advantage if a group of EMT cells has all the same timings or is a mixture of timings better?

> **Answer:** Individual EMT cells are more effective than groups of cells. But heterogeneous groups increase the efficiency of basal extrusion for most EMT programs compared to homogeneous groups.

(Q6) Effect of interkinetic nuclear movement (INM): Are EMT cells without INM more effective than EMT cells with INM?

> **Answer:** INM has a major impact on the model, and the lack of INM increases the amount of basal extrusion for EMT programs involving **[B]**.

(Q7) Basal positioning at the onset of EMT: Does the position of an EMT cell at the start of EMT events impact the outcome?

> **Answer:** Very much so. Basal positioning is a favouring factor for basal extrusion, and for cells without **[P]**, basal positioning is more important than the timing and the selection of EMT events (see Figure 21). If cells start EMT when they are close to the basal layers, their likelihood of extrusion is almost $80\,\%$ (according to the model).

(Q8) Competition: Do other EMT cells with very effective EMT programs decrease the efficiency of non-effective EMT programs?

> **Answer:** Yes, a bit. However, basally positioned cells might benefit from the push they obtain from more basally driven cells.

5. Derived biological hypotheses and experimental results

We now want to relate our conclusions from the modelling with experimental data and results from Theveneau's lab.

Using our model, we identified the following factors leading to basal extrusion:

(1) Protrusive activities lead to basal extrusion and prevent apical extrusion, see Figure 10.
(2) The position of nuclei at the onset of EMT is a crucial factor in differentiating between basal and apical extrusion, see Figure 21.

Theveneau's lab used these modelling results to design new experiments that explore the model's claims. In the following sections, we outline the experimental evidence supporting the following hypotheses:

(1) Inhibition of protrusion seems to randomise extrusion outcome (between apical and basal).

(2) Neural crest cells have increased rates of non-apical mitosis before the onset of EMT.

5.1. Inhibition of protrusion seems to randomise extrusion outcome

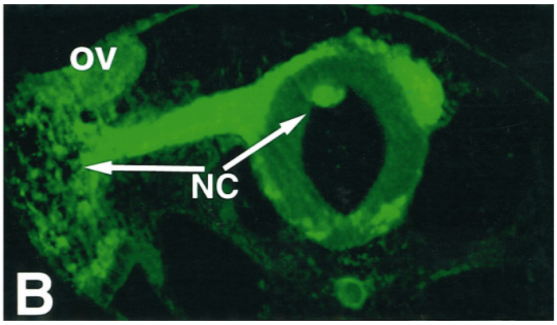

Figure 23. Inhibition of integrin α_4 subunit leads to a reduction of neural crest migration. These in vivo experiments show apical extrusion due to a disrupted migration program. This related to our conclusion from the model, that protrusions are essential for basal extrusion. *Image source: [Kil+98, Figure 8B].*

An important difference between our model and experimental data is in the rate of apical extrusion. Under physiological conditions, the rate of basal extrusion is in practice $100\,\%$, and there are no apical extrusions. The model suggests that such high rates of basal extrusion are only possible with cell protrusions. This leads to the conclusion that cells which undergo EMT will likely use protrusions to escape the tissue. Apical extrusion only occurs in experiments which enforce non-physiological situations [Kil+98; NT98]. The experiments in [Kil+98] show that preventing cells from forming effective protrusions leads indeed to apical extrusion of some cells. This experiment supports our modelling conclusion.

Figure 23 presents experimental results from [Kil+98]. In these experiments, the integrin α_4 subunit was blocked with an function-blocking antibody. Integrins are transmembrane receptors which are important for the regulation of cell-cell and cell-matrix adhesion. Without cell-matrix adhesion, cells cannot migrate since cell protrusions cannot hold onto the fibers of the extracellular matrix. According to [Kil+98], the integrin α_4 subunit may be one of the primary α subunits for neural crest migration (in vivo). Blocking the function of the integrin α_4 subunit reduces the migration of neural crest cells, and in half of the experiments, it successfully prevented any neural crest migration. Under these non-physiological conditions, apical extrusion of neural crest cells occurs, as visible in Figure 23.

Theveneau's lab is currently performing more experiments to detail further the role of protrusions during the onset of EMT.

5.2. Neural crest cells have increased rates of non-apical mitosis before the onset of EMT

To investigate the role of basal positioning, Theveneau's lab collected (in vivo) data about the position of nuclei before the onset of EMT and during EMT. The positions of nuclei usually are tightly regulated by interkinetic nuclear movement (INM), which leads, in most cases, to apical mitosis, i.e. cell divisions on the apical surface of the tissue.

Theveneau's experimental data shows that the nuclei positions of neural crest cells are less tightly regulated, since not all neural crest cells divide apically.

Indeed, already *before* the onset of EMT, neural crest cells have non-apical mitosis with a higher frequency than neural tube cells. (We recall that neural tube cells correspond to the epithelial cells in our model and neural crest cells are the EMT cells, i.e. the cells which perform the epithelial-to-mesenchymal transition.) This could indicate that the basal positioning of cells is a relevant factor and that some cells prepare EMT by inhibition of INM.

Figure 24 shows statistics and examples of non-apical mitosis in the cephalic region (close to the head) of a chicken embryo at 32 hours of development. At this stage, the neural tube is not closed yet (cp Figure 2) which also means that neural crest cells have not started EMT. The results show that around $20\,\%$ of the neural crest cells show non-apical mitosis, whereas only around $5\,\%$ of neural tube cells divide non-apically. We refer to the caption of Figure 24 further details of the experimental setup.

In Figure 25, we see that the rate of non-apical mitosis increases at the onset of EMT and during EMT. We recall that the convergence and closure of the neural tube happen earlier in the cephalic region (head) and later in the trunk region of the neural tube. This allows us to observe different stages of EMT in one chicken embryo at the same time. The presented images show the chicken embryo after 48 hours of development, where EMT has not yet started in some parts of the trunk domain, but is already ongoing in more anterior parts. Compared to Figure 24 the difference in non-apical mitosis between neural tube cells and neural crest cells is less prominent. However, some embryos also

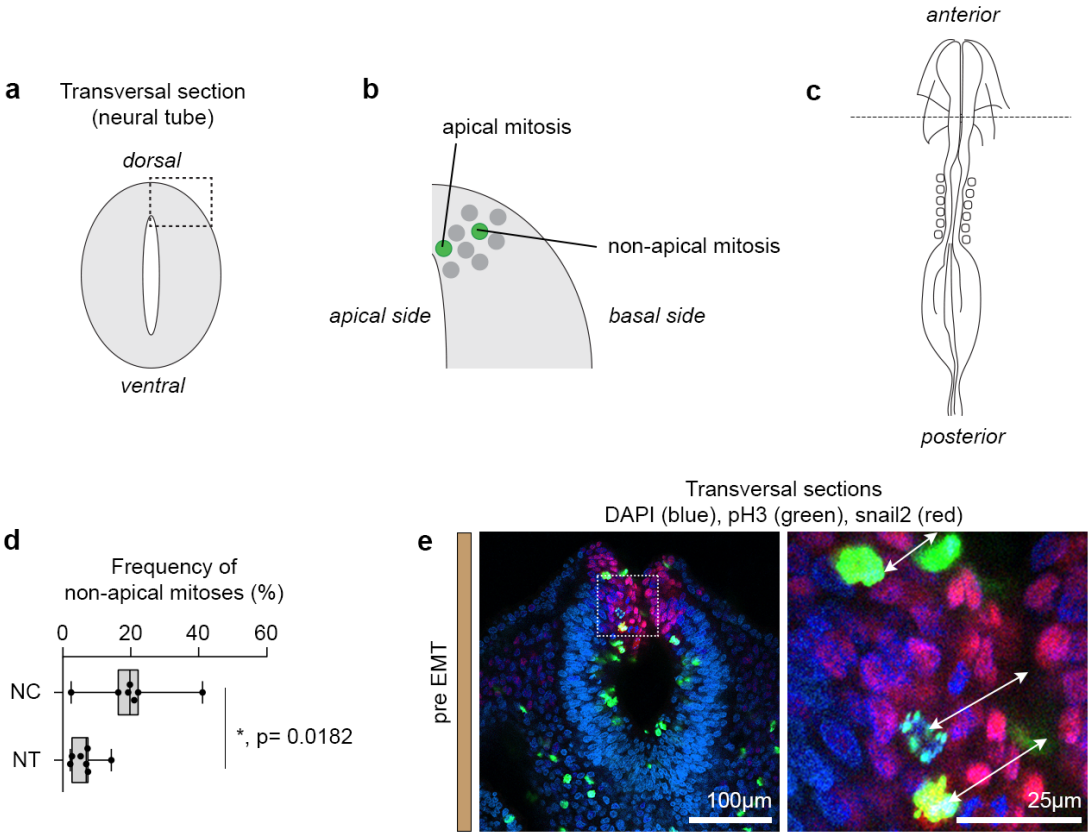

Figure 24. **a-b**, diagrams showing a transversal view of the neural tube (a) and a zoom (b) on the dorsal side showing a few nuclei and what is considered apical or non-apical with respect to the epithelium orientation. **c**, diagram of a chicken embryo at 32 hours of development. The dotted line indicates the level of the images shown in panel e. **d**, percentages of non-apical mitoses in the neural crest region (NC) and the rest of the neural tube (NT). Each dot represents the mean percentage for one embryo. **e**, example of basal mitoses in the region analyzed. **Left panel** shows a low magnification of the neural tube, **right panel** shows a zoom on the dorsal neural tube containing neural crest cells. All nuclei are labelled with DAPI (blue). Neural crest cells are identified by immunostaining against the Snail2 protein (red). Mitoses are detected by immunostaining against the phosphor-Histone H3 (green). Note that numerous non-apical mitoses are detected prior to the onset of EMT. *Image source: unpublished, provided by Dr. Eric Theveneau (CNRS)*

showed increased rates of non-apical mitosis in the neural crest domain, which indicates a lack of tight regulation of INM in the neural crest domain.

Overall, the experiments show around 20 % of neural crest cells do not perform INM already before EMT which could indicate that the position at the onset of EMT is indeed a favouring factor which helps cells to extrude basally.

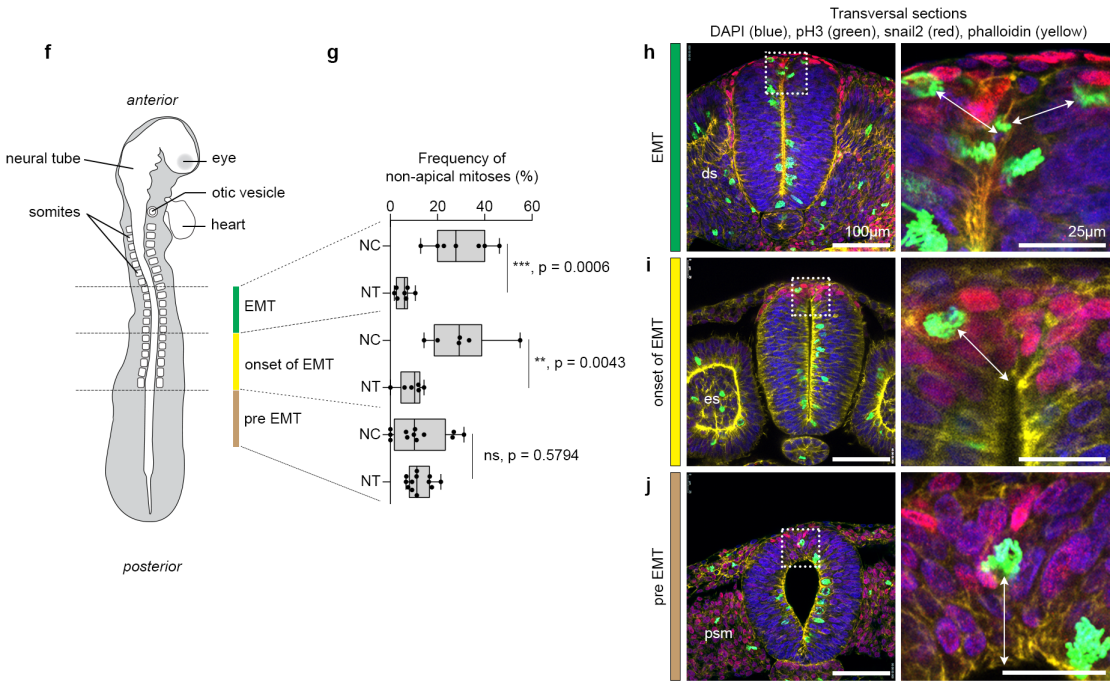

Figure 25. **f**, diagram of a chicken embryo at 48 hours of development. The dotted lines indicate the level of the images shown in panel h. **g**, percentages of non-apical mitoses in the neural crest region (NC) and the rest of the neural tube (NT) at three different anteroposterior levels corresponding to pre-EMT, the onset of EMT and ongoing EMT. Each dot represents the mean percentage for one embryo. **h-i**, example of basal mitoses in the various regions analyzed. Left panel, low magnification of the neural tube, and the right panels show a zoom on the dorsal neural tube containing neural crest cells. All nuclei are labelled with DAPI (blue). Neural crest cells are identified by immunostaining against the Snail2 protein (red). Mitoses are detected by immunostaining against the phosphor-Histone H3 (green). Sections are counterstained with Phalloidin which detects actin filaments that are accumulated on the apical side of the tissue. Note that all neural crest regions in which EMT is implemented display a significantly higher rate of basal mitoses than what is observed in the rest of the neural tube. Interestingly, in most posterior region corresponding to pre-EMT, some embryos display an increase of basal mitoses while other do not. This indicates that basal mitoses progressively become more frequent before the onset of basal extrusion, indicating a lack of tight regulation of interkinetic movements in the neural crest domain compared to the rest of the neuroepithelium. *Image source: unpublished, provided by Dr. Eric Theveneau (CNRS)*

Chapter 5

The mean-field limit for particle systems with uniform full-rank constraints

This chapter contains an article which is currently submitted to the journal *Kinetic and Related Models*. The pre-print is available at [PS22].

My contribution

This article is a follow-up project from my master's thesis, which was supervised by Prof. Bernd Simeon (TU Kaiserslautern).

My main contribution is the proof of Theorem 5.12 which follows classical arguments from [Gol16] with some adaptations which are mainly based on Lemma 5.8.

I am also grateful for the received feedback from the (anonymous) peer-reviews which improved this work in several ways.

1. Introduction

This article is about the question of how to apply the mean-field limit when individual particles are tightly coupled to the dynamics of a macroscopic component. Such a situation arises, for example, in microscopic models for skeletal muscle tissue. In such models, microscopic actin-myosin filaments take the role of 'particles', and the passive muscle tissue acts like a 'macroscopic component', as shown in Figure 1. Indeed, in terms of kinetic theory, the established muscle models are macroscopic approximations of the so called sliding filament theory [Hux57; HS71; HH54]. The most popular macroscopic

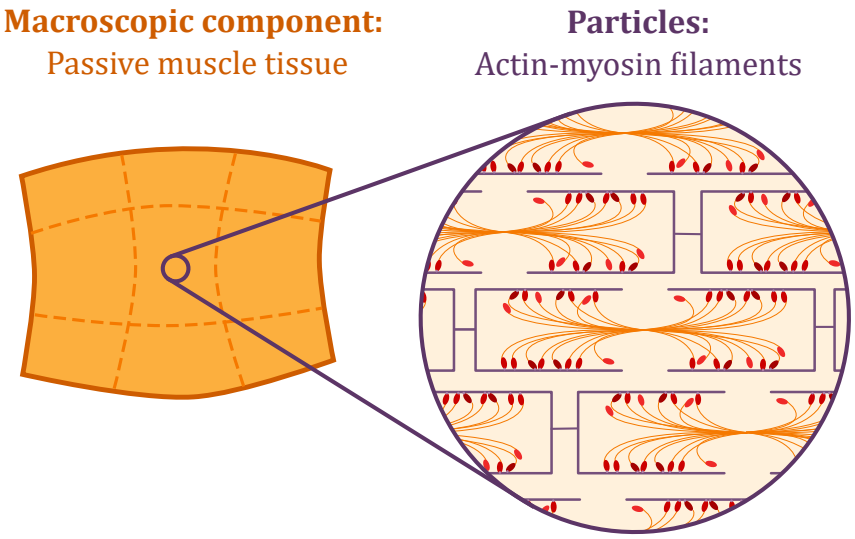

Figure 1. Skeletal muscle tissue contains arrays of aligned actin-myosin filaments. The myosin heads (red) attach to the actin filament (purple). Millions of such actin-myosin filaments repeatedly perform a cycle of 'attaching, pulling and detaching'. The resulting accumulated force leads to muscle contraction. In article, we ignore the repeated cycling. Instead, we focus on the mathematical implication of the coupling to the macroscopic component.

approximation is the distributed moment method [Zah81] which forms the foundation for most numerical simulations of muscle tissue which include fibers, see for example [BR08; GS21; Hei+16].

While sliding filament theory itself is well-established [Her17; How01; MZ91; KS09b; Phi+12], a rigorous application of the mean-field limit to realistic models for muscle tissue is currently out of reach. One challenge is to account for the coupling between the microscopic scale (actin-myosin filaments) and the macroscopic components (passive muscle tissue), see also [SSP09]. Each deformation of the passive muscle tissue deforms, detaches or breaks attached actin-myosin filaments. In terms of mathematical models, this introduces constraints between the passive muscle tissue and the filaments. To tackle this particular challenge, we will consider a simplified model that focuses solely on the coupling between a macroscopic component and particles. The main result of this article is a rigorous proof of the mean-field limit for such coupled particle systems.

From a kinetic theory point-of-view, imposing a general constraint on particle positions is not straightforward. Many fundamental results do not generalise in an obvious way to nonlinear position spaces. For example, the diffusive scaling limit requires that $(t, \boldsymbol{x}) \mapsto (\varepsilon t, \varepsilon^2 \boldsymbol{x})$ is well-defined for $\varepsilon \to 0$. However, if $\boldsymbol{x}$ is subject to constraints, this scaling is ill-posed since $\varepsilon^2 \boldsymbol{x}$ might not satisfy the position constraints. Also, other common

approaches for deriving macroscopic equations (averaging, moment approximations) are not directly compatible with position constraints. Up to our knowledge, there is no canonical way to rigorously derive macroscopic equations when the particles are subject to general constraints. However, the particle model we consider in this article has a specific structure that allows us to derive the mean-field limit and admits macroscopic approximations. We extend the approach from [Gol16, Section 1.4] to such particle systems with constraints. For further references on kinetic theory, we refer to [CIP94; Deg04; Jab14; Spo91].

Major Results at a Glance

Our starting point is a system of differential-algebraic equations (DAE) that describes the motion of particles with positions $\boldsymbol{X}_1, \dots, \boldsymbol{X}_N \in \mathbb{R}^{n_x}$ and a macroscopic component with state $\boldsymbol{y} \in \mathbb{R}^{n_y}$. We impose the algebraic constraints

$$g(\boldsymbol{X}_i, \boldsymbol{y}) = \text{const.} \quad \text{for } 1 \leq i \leq N$$

where $g : \mathbb{R}^{n_x} \times \mathbb{R}^{n_y} \to \mathbb{R}^{n_x}$ is a nonlinear constraint function. These constraints are uniform, in the sense that all particles have to keep the same constraint function constant, and the constant only depends on the initial condition. The DAE system which we study in this article is the constrained Newton equation

$$\begin{cases} m\ddot{\boldsymbol{X}}_i = F_1(\boldsymbol{X}_i) + \dfrac{1}{N}\displaystyle\sum_{k=1}^{N} K(\boldsymbol{X}_k, \boldsymbol{X}_i) - (\partial_{\boldsymbol{X}_i} g(\boldsymbol{X}_i, \boldsymbol{y}))^T \boldsymbol{\lambda}_i & \text{for } 1 \leq i \leq N, \\ \ddot{\boldsymbol{y}} = F_0(\boldsymbol{y}) - \dfrac{1}{N}\displaystyle\sum_{j=1}^{N} (\partial_{\boldsymbol{y}} g(\boldsymbol{X}_j, \boldsymbol{y}))^T \boldsymbol{\lambda}_j, & \\ g(\boldsymbol{X}_i, \boldsymbol{y}) = g(\boldsymbol{X}_i^{\text{init}}, \boldsymbol{y}^{\text{init}}) & \text{for } 1 \leq i \leq N. \end{cases}$$

A key assumption is that the constraint function g is of full rank with respect to $\boldsymbol{X}_i$. Hence, there is a linear map $\Phi(\boldsymbol{X}_i, \boldsymbol{y})$ which translates the velocity of the macroscopic component to the velocities of the particles, i.e. $\dot{\boldsymbol{X}}_i = \Phi(\boldsymbol{X}_i, \boldsymbol{y})[\dot{\boldsymbol{y}}]$. This relation allows the elimination of the Lagrangian multipliers, and we arrive at the following equivalent ODE model

$$\begin{cases} \left(\dfrac{1}{N}\displaystyle\sum_{j=1}^{N} m_{\text{eff}}^{(1)}(\boldsymbol{X}_j, \boldsymbol{y}) \right) \ddot{\boldsymbol{y}} = \dfrac{1}{N}\displaystyle\sum_{j=1}^{N} \left(F_{\text{eff}}^{(1)}(\boldsymbol{X}_j, \boldsymbol{y}, \dot{\boldsymbol{y}}) + \dfrac{1}{N}\displaystyle\sum_{k=1}^{N} K_{\text{eff}}(\boldsymbol{X}_k, \boldsymbol{X}_j) \right), \\ \dot{\boldsymbol{X}}_i = \Phi(\boldsymbol{X}_i, \boldsymbol{y})[\dot{\boldsymbol{y}}] \qquad \text{for } 1 \leq i \leq N \end{cases}$$

where $m_{\text{eff}}^{(1)}$ and $F_{\text{eff}}^{(1)}$ are the effective mass and effective forces of the macroscopic component. The force each particle exerts onto the macroscopic component is included in $m_{\text{eff}}^{(1)}$ and $F_{\text{eff}}^{(1)}$.

With the ODE model, we can mostly follow a standard procedure for proving the mean-field limit. The mean-field PDE is given by

$$\Big(\int m_{\text{eff}}^{(1)}(x,\boldsymbol{y})f(x,t)\,\mathrm{d}x\Big)\,\ddot{\boldsymbol{y}} = \int\left(F_{\text{eff}}^{(1)}(x,\boldsymbol{y},\dot{\boldsymbol{y}}) + \int K_{\text{eff}}(x',x)f(x',t)\,\mathrm{d}x'\right)f(x,t)\,\mathrm{d}x,$$
$$\partial_t f(x,t) = -\mathrm{div}_x\big(f(x,t)\,\Phi(x,\boldsymbol{y})[\dot{\boldsymbol{y}}]\big)$$

where in the mean-field limit the particles $\boldsymbol{X}_i$ converge to i.i.d. random variables with the common law $f(x,t)\,\mathrm{d}x$. A difference to classical mean-field equations is the occurrence of a non-constant *mean-field mass* in addition to the classical mean-field force. Dealing with the mean-field mass is the primary difference compared to standard procedures for proving the mean-field limit.

Our main results are the proof of well-posedness and a stability estimate. Under some assumptions, we show well-posedness of the ODE model and the characteristic flow of the mean-field PDE. The key step is to show that

$$\mu \mapsto \left(\int m_{\text{eff}}^{(1)}(x,\boldsymbol{y})\,\mathrm{d}\mu(x)\right)^{-1}$$

is bounded and Lipschitz continuous with respect to the particle distribution. To show the mean-field limit, we prove a generalisation of Dobrushin's stability estimate [Gol16, Section 1.4], which implies

$$\begin{aligned} W_1(\mu_1^t,\mu_2^t) + \|\boldsymbol{y}_1+\boldsymbol{y}_2\| + \|\dot{\boldsymbol{y}}_1+\dot{\boldsymbol{y}}_2\| \\ \leq Ce^{Lt}\big(W_1(\mu_1^{\text{init}},\mu_2^{\text{init}}) + \|\boldsymbol{y}_1^{\text{init}}-\boldsymbol{y}_2^{\text{init}}\| + \|\boldsymbol{v}_1^{\text{init}}-\boldsymbol{v}_2^{\text{init}}\|\big) \end{aligned}$$

where W_1 is the Monge-Kantorovich distance with exponent 1 (also called Wasserstein distance), $\mu_1^{\text{init}},\mu_2^{\text{init}}$ are two different initial particle distributions and μ_1^t,μ_2^t are weak solutions of the mean-field PDE. The stability estimate implies convergence in the mean-field limit and provides a rate of convergence as well.

This article generalises the results from our previous work [PS20]. Instead of assuming that the constraints and forces are linear, we allow nonlinear constraints and forces. This is motivated by the application to models for muscle tissue [PS20, Section 5.2]. However, the nonlinear constraints introduce two new challenges. First, the position space becomes nonlinear, which prevents many simplifications. Second, the mean-field mass is non-constant in contrast to the linear case. In the context of the Newton equations of the macroscopic component, this implies that we need sufficient bounds for the inverse of the mean-field mass.

We want to point out that even with the extension to nonlinear constraints, the applicability of particle systems with uniform, full-rank constraints remains limited. Practical applications would require further extensions, which are beyond the scope of this article. For example, in the context of muscle tissue models, a necessary extension would be to allow particles to switch between a constrained and an unconstrained state. With such a mechanism, one could model the essential driver for muscle contraction, which is the attachment and detachment of actin-myosin filaments, see [PS20, Section 5.3]. For

the case of unconstrained particles, related mean-field limit results already exist [DN08; Dav84], but these results do not directly apply to constrained particles.

This article is organised as follows: Section 2 defines the discrete particle model as a DAE model and an equivalent ODE model. It shows conservation of energy and well-posedness for the ODE model. Section 3 starts with a formal derivation of the mean-field equations for the ODE model. It continues with showing that the mean-field equations are consistent with the ODE model, preserve energy and are well-posed. As a main result, it proves a stability estimate that implies convergence of the mean-field limit. Appendix 2 contains the proof of the equivalence of the DAE model and the ODE model.

2. The discrete particle model with uniform full-rank constraints

This section describes the discrete particle model with uniform, full-rank constraints. We start with a DAE model and derive an equivalent ODE model for the particle dynamics. Then, we prove conservation of energy and well-posedness for the ODE model.

The derivation of an equivalent ODE model has the following advantage. If we apply the mean-field limit directly to the DAE model, the resulting mean-field equation would be a partial differential-algebraic equation (PDAE). This would be an unnecessary complication. Using the ODE model avoids this issue. By exploiting the particular structure of the DAE, we can eliminate the constraints and their Lagrangian multipliers. The resulting equations will be an equivalent ODE model which yields a PDE in the mean-field limit.

Notation

For vector-valued functions, e.g. $g : \mathbb{R}^{n_x} \times \mathbb{R}^{n_y} \times \mathbb{R}^{n_x}$, we use the shorthand notation $\partial_{\boldsymbol{X}} g(\boldsymbol{X}, \boldsymbol{y}) \coloneqq \frac{\partial}{\partial \boldsymbol{X}} g(\boldsymbol{X}, \boldsymbol{y}) \in \mathbb{R}^{n_x} \times \mathbb{R}^{n_x}$ and $\partial_{\boldsymbol{y}} g(\boldsymbol{X}, \boldsymbol{y}) \coloneqq \frac{\partial}{\partial \boldsymbol{y}} g(\boldsymbol{X}, \boldsymbol{y}) \in \mathbb{R}^{n_y} \times \mathbb{R}^{n_x}$. For scalar functions, e.g. $f : \mathbb{R}^{n_x} \times \mathbb{R}^{n_y} \to \mathbb{R}$, we write $\nabla_{\boldsymbol{y}} f(\boldsymbol{X}, \boldsymbol{y}) \coloneqq \left(\frac{\partial}{\partial \boldsymbol{y}} f(\boldsymbol{X}, \boldsymbol{y}) \right)^T \in \mathbb{R}^{n_y}$ for the gradient with respect to the variable $\boldsymbol{y}$. The differential is denoted by $\mathrm{D} f$ and the second order derivative as $\mathrm{D}^2 f$.

2.1. The DAE model

Let $\boldsymbol{\mathcal{X}}^{(N)} \coloneqq (\boldsymbol{X}_1, \dots, \boldsymbol{X}_N) \in (\mathbb{R}^{n_x})^N$ denote the positions of N identical, non-interacting, microscopic particles and let $\boldsymbol{y} \in \mathbb{R}^{n_y}$ denote the state of a macroscopic component. We denote the internal forces of both systems as

$$F_0(\boldsymbol{y}) \coloneqq -\nabla_{\boldsymbol{y}} \mathcal{W}_0(\boldsymbol{y}) \quad \text{and} \quad F_1(\boldsymbol{X}_i) \coloneqq -\nabla_{\boldsymbol{X}_i} \mathcal{W}_1(\boldsymbol{X}_i) \quad \text{for } 1 \leq i \leq N$$

where $\mathcal{W}_0 \in C^1(\mathbb{R}^{n_y}, \mathbb{R})$ and $\mathcal{W}_1 \in C^1(\mathbb{R}^{n_x}, \mathbb{R})$ are the potential energies of the macroscopic component and the microscopic particles. The pair-wise interaction forces is

$$K(\boldsymbol{X}_j, \boldsymbol{X}_i) = \nabla_{\boldsymbol{X}_i} - \mathcal{V}(\boldsymbol{X}_j - \boldsymbol{X}_i). \tag{5.4}$$

for some potential energy $\mathcal{V} \in C^1(\mathbb{R}^{n_x}, \mathbb{R})$ with $\mathcal{V}(-\boldsymbol{X}) = -\mathcal{V}(\boldsymbol{X})$, $\nabla \mathcal{V}(\boldsymbol{0}) = \boldsymbol{0}$ and $\mathcal{V}(\boldsymbol{0}) = 0$.

The central connection between the particles and the macroscopic component are the constraints

$$g(\boldsymbol{X}_i(t), \boldsymbol{y}(t)) = g(\boldsymbol{X}_i{}^{\text{init}}, \boldsymbol{y}^{\text{init}}) \quad \text{for } 1 \le i \le N \text{ and } t \ge 0$$

where $g \in C^2(\mathbb{R}^{n_x} \times \mathbb{R}^{n_y}, \mathbb{R}^{n_x})$ is the constraint function and $\boldsymbol{X}_i{}^{\text{init}} \in \mathbb{R}^{n_x}, \boldsymbol{y}^{\text{init}} \in \mathbb{R}^{n_y}$ are the initial conditions. We call these constraints uniform since all particles have to remain in the level set of the same constraint function. Moreover, we assume that the constraint function has full-rank, i.e.

$$\partial_{\boldsymbol{X}} g(\boldsymbol{X}, \boldsymbol{y}) \quad \text{is invertible for all } \boldsymbol{X} \in \mathbb{R}^{n_x}, \boldsymbol{y} \in \mathbb{R}^{n_y}. \tag{5.5}$$

This implies that the state of the macroscopic component determines locally the position of all particles.

Now, we can state the discrete particle model as a constrained Newton equation

$$m\ddot{\boldsymbol{X}}_i = F_1(\boldsymbol{X}_i) + \frac{1}{N}\sum_{k=1}^{N} K(\boldsymbol{X}_k, \boldsymbol{X}_i) - (\partial_{\boldsymbol{X}_i} g(\boldsymbol{X}_i, \boldsymbol{y}))^T \boldsymbol{\lambda}_i \qquad \text{for } 1 \le i \le N, \tag{5.6a}$$

$$\ddot{\boldsymbol{y}} = F_0(\boldsymbol{y}) - \frac{1}{N}\sum_{j=1}^{N} (\partial_{\boldsymbol{y}} g(\boldsymbol{X}_j, \boldsymbol{y}))^T \boldsymbol{\lambda}_j, \tag{5.6b}$$

$$g(\boldsymbol{X}_i, \boldsymbol{y}) = g(\boldsymbol{X}_i^{\text{init}}, \boldsymbol{y}^{\text{init}}) \qquad \text{for } 1 \le i \le N \tag{5.6c}$$

with the initial conditions

$$\boldsymbol{X}_i(0) = \boldsymbol{X}_i{}^{\text{init}}, \quad \boldsymbol{y}(0) = \boldsymbol{y}^{\text{init}} \quad \text{and} \quad \dot{\boldsymbol{y}}(0) = \boldsymbol{v}^{\text{init}} \quad \text{for } 1 \le i \le N. \tag{5.7}$$

The equations (5.6a) to (5.6c) form a system of differential-algebraic equations (DAEs). Therefore, we will refer to it as the *DAE model*. The algebraic variables $\boldsymbol{\lambda}_1, \dots, \boldsymbol{\lambda}_N \in \mathbb{R}^{n_x}$ are the Lagrangian multipliers for (5.6c), and their initial value is determined implicitly by the system.

The main objective of this article is to study the limit $N \to \infty$ for this system. The factor $\frac{1}{N}$ in (5.6a) is the typical mean-field scaling of the interaction forces, whereas the factor $\frac{1}{N}$ in (5.6b) stems from a scaling between the action of the macroscopic component and the particle system.

To motivate the scaling factors, we consider the Lagrangian of the system

$$\begin{aligned} L = {} & \frac{1}{2}\|\dot{\boldsymbol{y}}\|^2 - \mathcal{W}_0(\boldsymbol{y}) \\ & + \alpha \sum_{i=1}^{N} \left(\frac{m}{2}\|\dot{\boldsymbol{X}}_i\|^2 - \mathcal{W}_1(\boldsymbol{X}_i) - \frac{1}{2}\beta \sum_{k=1}^{N} \mathcal{V}(\boldsymbol{X}_k - \boldsymbol{X}_i) \right) \\ & - \gamma \sum_{j=1}^{N} g(\boldsymbol{X}_j, \boldsymbol{y})\boldsymbol{\lambda}_j. \end{aligned} \tag{5.8}$$

The choice of the scaling factor $\beta \sim \frac{1}{N}$ is typical for interacting particle systems as it keeps the relative influence of the interaction forces constant.

The factor α controls the energy balance between the macroscopic component and the particles. With the choice $\alpha \sim \frac{1}{N}$ the influence of the particles on the macroscopic component remains of order 1 in the limit. A side effect of this scaling is that the total mass of the particles is constant in the limit.

In contrast to the other two scaling factors, the choice of the factor γ is physically irrelevant, since the Lagrangian multipliers $\lambda_1, \dots, \lambda_N$ are unknowns which would just scale accordinging. However, for the mathematical analysis it is useful to ensure that also $\lambda_1, \dots, \lambda_N$ are of order 1. Therefore, we pick $\gamma \sim \frac{1}{N}$.

The system (5.6a) to (5.6c) consists out of the Euler-Lagrange equations for the choice $\alpha = \beta = \gamma = \frac{1}{N}$.

2.2. The ODE model

The derivation of an equivalent ODE model is elementary but lengthy. Therefore, we just present the results here, whereas the full computations can be found in Appendix 2.

Due to the full-rank constraint, the velocity of the macroscopic component $\dot{\boldsymbol{y}}$ determines the velocity of each particle $\dot{\boldsymbol{X}}_i$, namely

$$g = \text{const.} \Leftrightarrow \frac{\mathrm{d}g}{\mathrm{d}t} = \frac{\partial g}{\partial \boldsymbol{X}_i}\frac{\mathrm{d}\boldsymbol{X}_i}{\mathrm{d}t} + \frac{\partial g}{\partial \boldsymbol{y}}\frac{\mathrm{d}\boldsymbol{y}}{\mathrm{d}t} = 0 \Leftrightarrow \quad \dot{\boldsymbol{X}}_i = \Phi_i[\dot{\boldsymbol{y}}] \tag{5.9}$$

where

$$\Phi_i \coloneqq \Phi(\boldsymbol{X}_i, \boldsymbol{y}) \coloneqq -\left(\partial_{\boldsymbol{X}_j} g(\boldsymbol{X}_i, \boldsymbol{y})\right)^{-1} \partial_{\boldsymbol{y}} g(\boldsymbol{X}_i, \boldsymbol{y}) \in \mathbb{R}^{n_x \times n_y}.$$

Consequentially,

$$\frac{\mathrm{d}g}{\mathrm{d}t} = 0 \Rightarrow \frac{\mathrm{d}^2 g}{\mathrm{d}t^2} = 0 \Leftrightarrow \quad \ddot{\boldsymbol{X}}_i = \Phi_i[\ddot{\boldsymbol{y}}] + \Omega_i[\dot{\boldsymbol{y}}, \dot{\boldsymbol{y}}] \tag{5.10}$$

where

$$\begin{aligned}\Omega_i[\boldsymbol{v}, \boldsymbol{w}] &\coloneqq \Omega(\boldsymbol{X}_i, \boldsymbol{y})[\boldsymbol{v}, \boldsymbol{w}] \\ &\coloneqq \partial_{\boldsymbol{X}_i}\Phi(\boldsymbol{X}_i, \boldsymbol{y})[\boldsymbol{v}, \Phi(\boldsymbol{X}_i, \boldsymbol{y})[\boldsymbol{w}]] + \partial_{\boldsymbol{y}}\Phi(\boldsymbol{X}_i, \boldsymbol{y})[\boldsymbol{v}, \boldsymbol{w}]\end{aligned}$$

for $\boldsymbol{v}, \boldsymbol{w} \in \mathbb{R}^{n_y}$. We remark that taking derivatives of the algebraic equation $g = 0$ is related to the concept of index reduction [HW10, Chap VII].

With the relations (5.9) and (5.10), we can solve (5.6a) for the Lagrangian multipliers and then eliminate both $\boldsymbol{\lambda}_i$ and $\ddot{\boldsymbol{X}}_i$ from the system (5.6a) to (5.6c) to obtain an equivalent ODE model

$$\begin{cases} m_{\text{eff}}^{(N)} \ddot{\boldsymbol{y}} = F_{\text{eff}}^{(N)}, & \text{(5.11a)} \\ \dot{\boldsymbol{X}}_i = \Phi_i[\dot{\boldsymbol{y}}], \quad \text{for } 1 \le i \le N & \text{(5.11b)} \end{cases}$$

with initial condtions

$$\boldsymbol{y}(0) = \boldsymbol{y}^{\text{init}}, \quad \dot{\boldsymbol{y}}(0) = \boldsymbol{v}^{\text{init}} \quad \text{and} \quad \boldsymbol{X}_i(0) = \boldsymbol{X}_i{}^{\text{init}} \quad \text{for } 1 \le i \le N \tag{5.12}$$

where the effective mass and effective force are

$$m_{\text{eff}}^{(N)}(\boldsymbol{\mathcal{X}}^{(N)}, \boldsymbol{y}) = (I_{\mathbb{R}^{n_y}} + \frac{m}{N}\sum_{j=1}^{N} \Phi_j^T \Phi_j), \tag{5.13}$$

$$F_{\text{eff}}^{(N)}(\boldsymbol{\mathcal{X}}^{(N)}, \boldsymbol{y}, \dot{\boldsymbol{y}}) = F_0(\boldsymbol{y}) + \frac{1}{N}\sum_{j=1}^{N} \Phi_j^T \left(F_1(\boldsymbol{X}_j) + \frac{1}{N}\sum_{k=1}^{N} K(\boldsymbol{X}_k, \boldsymbol{X}_j) - m\Omega_j[\dot{\boldsymbol{y}}, \dot{\boldsymbol{y}}] \right). \tag{5.14}$$

The super-index $^{(N)}$ identifies the number of particles. For a detailed derivation of (5.11a) and (5.11b), we refer to Appendix 2.

The system (5.11a) and (5.11b) is a reduced form of the DAE model (5.6a) to (5.6c). In the following, we will call (5.11a) and (5.11b) the *ODE model*. We notice that (5.11a) is in the form of Newton's second law. Therefore, we identify $m_{\text{eff}}^{(N)}$ as the effective mass of the macroscopic component and $F_{\text{eff}}^{(N)}$ as the effective force.

The equations (5.13) and (5.14) fit well into the setting of mean-field theory since both terms are mean values of the individual influence of all particles, i.e.

$$m_{\text{eff}}^{(N)}(\boldsymbol{\mathcal{X}}^{(N)}, \boldsymbol{y}) = \frac{1}{N}\sum_{j=1}^{N} m_{\text{eff}}^{(1)}(\boldsymbol{X}_j, \boldsymbol{y}). \tag{5.15}$$

$$F_{\text{eff}}^{(N)}(\boldsymbol{\mathcal{X}}^{(N)}, \boldsymbol{y}, \dot{\boldsymbol{y}}) = \frac{1}{N}\sum_{j=1}^{N} F_{\text{eff}}^{(1)}(\boldsymbol{X}_j, \boldsymbol{y}, \dot{\boldsymbol{y}}) + \frac{1}{N^2}\sum_{j=1}^{N}\sum_{k=1}^{N} K_{\text{eff}}(\boldsymbol{X}_k, \boldsymbol{X}_j). \tag{5.16}$$

The last equation holds because $K(\boldsymbol{X}, \boldsymbol{X}) = 0$ and with the definition

$$K_{\text{eff}}(\boldsymbol{X}_k, \boldsymbol{X}_j) \coloneqq \Phi^T(\boldsymbol{X}_j, \boldsymbol{y}) K(\boldsymbol{X}_k, \boldsymbol{X}_j). \tag{5.17}$$

We remark that factor $\Phi^T(\boldsymbol{X}_j, \boldsymbol{y})$ implies that K_{eff} might not be anti-symmetric. When K_{eff} is anti-symmetric, the double sum in (5.16) would vanish, meaning that the interaction between particles would cancel.

Every solution of the DAE model (5.6a) to (5.6c) also solves the ODE model (5.11a) and (5.11b), and with solutions of the ODE model we can recover the Lagrangian mutlipliers to construct a solution of the DAE model. The next proposition formalises this equivalence.

Proposition 5.1. *Let $g \in C^2(\mathbb{R}^{n_x} \times \mathbb{R}^{n_y}, \mathbb{R}^{n_x})$ be a constraint function such that*

$$\partial_{\boldsymbol{X}} g(\boldsymbol{X}, \boldsymbol{y}) \text{ is invertible for all } \boldsymbol{X} \in \mathbb{R}^{n_x}, \boldsymbol{y} \in \mathbb{R}^{n_y}. \tag{5.18}$$

If

$$\boldsymbol{y} \in C^2([0,T], \mathbb{R}^{n_y}), \quad \boldsymbol{X}_i \in C^1([0,T], \mathbb{R}^{n_x}) \quad \text{for } 1 \le i \le N$$

Figure 2. Left: simplified model for a straight muscle fiber (orange) with attached cross-bridges (purple) inside. **Right:** model for a muscle tissue element with homogeneous deformation (orange) and attached cross-bridges (purple). The shadow represents a previous state of the system to show how under shear deformation the deformation of springs depends on their rotation. cross-bridges which align with the directions of maximal deformation of the muscle are more extended that cross-bridges which are orthogonal to the maximal axis of deformation.

is a solution of the ODE model (5.11a) and (5.11b), then $\boldsymbol{\lambda}_i : [0,T] \to \mathbb{R}^{n_x}$ *defined by (A.14) is a continuous function and* $(\boldsymbol{y}, \boldsymbol{X}_1, \dots, \boldsymbol{X}_N, \boldsymbol{\lambda}_1, \dots, \boldsymbol{\lambda}_N)$ *is a solution of the DAE model (5.6a) to (5.6c).*

Vice versa, if

$$\boldsymbol{y} \in C^2([0,T], \mathbb{R}^{n_y}), \quad \boldsymbol{X}_i \in C^2([0,T], \mathbb{R}^{n_x}), \quad \boldsymbol{\lambda}_i \in C^0([0,T], \mathbb{R}^{n_x}) \quad \text{for } 1 \leq i \leq N$$

is a solution of the DAE model (5.6a) to (5.6c), then $(\boldsymbol{y}, \boldsymbol{X}_1, \dots, \boldsymbol{X}_N)$ *is a solution of the ODE model (5.11a) and (5.11b).*

The proof is given in Appendix 2.

2.3. Examples and modelling aspects

To motivate the class of systems, we give a few examples related to models for muscle tissue. We start with a general nonlinear model and consider two special cases, where the first serves as an illustrative example and the second relates the nonlinear models to their linear counterparts.

The macroscopic component represents a muscle tissue element in a d dimensional space. Let $F : \mathbb{R}^{n_y} \to \mathbb{R}^{d \times d}$ be a linear map which maps the state $\boldsymbol{y} \in \mathbb{R}^{n_y}$ to the deformation gradient of the muscle tissue element. We assume that the muscle tissue element has a spatially homogeneous deformation gradient.

The particles in this setup represent the so-called cross-bridges inside the muscle tissue. We consider N attached cross-bridges with states $\boldsymbol{X}_1, \dots, \boldsymbol{X}_N \in \mathbb{R}^d$. The vectors

represent the direction of the cross-bridges inside the muscle, i.e. the ith cross-bridges spans between $\boldsymbol{p}$ and $\boldsymbol{p} + \boldsymbol{X}_i$ for some point $\boldsymbol{p} \in \mathbb{R}^d$. Since we consider a homogeneous deformation of the muscle tissue, the position $\boldsymbol{p}$ of the cross-bridge is irrelevant. See Figure 2 for two examples.

The fundamental constraint is

$$F(\boldsymbol{y})^{-1}\boldsymbol{X}_i = F(\boldsymbol{y}^{\text{init}})\boldsymbol{X}_i^{\text{init}} \quad \text{for all } 1 \leq i \leq N. \tag{5.19}$$

These constraints model that the cross-bridges deform exactly proportional to the surrounding muscle tissue element.

Example 5.2 (Straight muscle fiber)**.** We consider the special case $d = n_y = 1$ and $F(y) \coloneqq y$. This represents a straight muscle fiber with N attached cross-bridges.

The constraint simplifies to

$$g(X_i, y) = \frac{X_i}{y}, \tag{5.20}$$

and we can directly compute $\partial_{X_i} g(X_i, y) = \frac{1}{y}$ and $\partial_y g(X_i, y) = -\frac{X_i}{y^2}$ which yields

$$\Phi(X_i, y) = \frac{X_i}{y} \quad \text{and} \quad \Omega(X_i, y) = \frac{X_i}{y^2} + -\frac{X_i}{y^2} = 0. \tag{5.21}$$

The effective mass and force are

$$m_{\text{eff}}^{(N)} = mI_{\mathbb{R}^{n_y}} + \frac{1}{N}\sum_{j=1}^{N} \frac{X_j^2}{y^2} \tag{5.22}$$

$$F_{\text{eff}}^{(N)} = F_0(y) + \frac{1}{N}\sum_{j=1}^{N} \frac{X_j}{y} F_1(X_j). \tag{5.23}$$

Example 5.3 (Linearised constraints)**.** The nonlinear constraint allows the fibers to have an arbitrary length in the initial configuration. However, if we assume that all fibers have roughly the same length, for example $X_i^{\text{init}} \in \mathcal{O}(\frac{y_c}{N})$ where y_c denotes a characteristic length of the muscle, then, linearising the constraint around $X_i \approx X_c = \frac{1}{N}$ and $y \approx y_c$ yields

$$g(X_i, y) \approx \frac{X_i}{y_c} - \frac{y}{N(y_c)^2} \tag{5.24}$$

To remove the dependency on N, we apply the coordinate change $\tilde{X}_i = \frac{y_c}{X_c} X_i = N y_c X_i$ which yields the linearised constraint

$$g_L(\tilde{X}_i, y) = \tilde{X}_i - y = \text{const}. \tag{5.25}$$

We obtain $\Phi(\tilde{X}_i, y) = 1$ and the corresponding effective mass and force terms are

$$m_{\text{eff}}^{(N)} = mI_{\mathbb{R}^{n_y}} + 1 \tag{5.26}$$

$$F_{\text{eff}}^{(N)}(\tilde{X}_1, \dots, \tilde{X}_N, y) = F_0(y) + \frac{1}{N}\sum_{j=1}^{N} F_1(\tilde{X}_i). \tag{5.27}$$

The linear case yields the typical starting point for sliding filament theory. The ODE model (5.11a) and (5.11b) in this case is

$$m\ddot{y} = F_0(y) + \frac{1}{N}\sum_{j=1}^{N} F_1(\tilde{X}_i) \tag{5.28}$$

$$\tilde{X}_i = \dot{y}. \tag{5.29}$$

Here, the mean-field equations are

$$m\ddot{y} = F_0(y) + \int_{\mathbb{R}} F_1(x) f(x,t)\,\mathrm{d}x \tag{5.30}$$

$$\partial_t f(x,t) = -\partial_x(f(x,t)\dot{y}(t)) \tag{5.31}$$

where $f : \mathbb{R} \times [0,T] \to \mathbb{R}$ denotes the cross-bridge distribution. By adding source and sink terms, we obtain models such as in [KS09a].

In general, for any linear map $G \in \mathbb{R}^{n_x \times n_y}$ the linear constraints

$$g(\boldsymbol{X}_i, \boldsymbol{y}) = G\boldsymbol{y} - \boldsymbol{X}_i$$

imply that $\Phi(\boldsymbol{X}_i, \boldsymbol{y}) = G$ is constant and $\Omega(\boldsymbol{X}_i, \boldsymbol{y}) = 0$.

In this provides a major simplification which is not available in the nonlinear case. Namely, we can solve $\dot{\boldsymbol{X}}_i = G\dot{\boldsymbol{y}}$ explicitly via

$$\boldsymbol{X}_i(t) = \boldsymbol{X}_i^{\text{init}} + G(\boldsymbol{y}(t) - \boldsymbol{y}^{\text{init}}).$$

This simplification is not available for general nonlinear constraints and the main contribution of the present article is to generalise the results from the previous work [PS20] to nonlinear constraints.

By adding nonlinear constraints, the dynamics of the particle system can be more complex. For example in [Zah96], the angle of cross-bridges was considered such that the deformation of cross-bridges is larger if they align with the axis of maximal deformation of the muscle. Within the framework proposed in this article, such dynamics require nonlinear constraints.

The next example is inspired by [Zah96] (but not an exact replication). It represents a model where the cross-bridges are embedded in a two-dimensional muscle tissue element with a homogeneous deformation gradient. The key aspect is, that in this setup shear forces lead to non-uniform deformation of the cross-bridges

Example 5.4 (Fully nonlinear constraints)**.** This time we imagine a two-dimensional muscle, modelled as a solid with a spatially homogeneous deformation gradient. Cross-bridges are are attached inside the muscle, initially between a point $\boldsymbol{z} - \frac{1}{2N}\boldsymbol{x}^{\text{init}} \in \mathbb{R}^2$ and $\boldsymbol{z} + \frac{1}{2N}\boldsymbol{x}^{\text{init}} \in \mathbb{R}^2$.

In a simplified manner, we consider that the state of the macroscopic system is described by $\boldsymbol{y} \in \mathbb{R}^3$ where y_1, y_2 denote the stretch and y_3 denotes the shear of the tissue. The corresponding deformation gradient is

$$\boldsymbol{F}(\boldsymbol{y}) \coloneqq \begin{pmatrix} y_1 & y_3 \\ y_3 & y_2 \end{pmatrix}.$$

The condition is that the cross-bridges deform like the muscle tissue element, which leads to the constraint

$$g(\boldsymbol{X}_i, \boldsymbol{y}) = F(\boldsymbol{y})^{-1}\boldsymbol{X}_i = F(\boldsymbol{y}^{\text{init}})^{-1}\boldsymbol{X}_i{}^{\text{init}}. \tag{5.32}$$

This constraint ensures that the cross-bridges deform exactly like the tissue. [1]

We obtain $\Phi_i[\boldsymbol{v}] = F(\boldsymbol{v})F(\boldsymbol{y})^{-1}\boldsymbol{X}_i$ which leads to

$$\dot{\boldsymbol{X}}_i = F(\dot{\boldsymbol{y}})F(\boldsymbol{y})^{-1}\boldsymbol{X}_i \tag{5.33}$$

Given that $g(\boldsymbol{X}_i, \boldsymbol{y})$ is constant, we obtain

$$\dot{\boldsymbol{X}}_i = F(\dot{\boldsymbol{y}})F(\boldsymbol{y}^{\text{init}})^{-1}\boldsymbol{X}_i{}^{\text{init}} \tag{5.34}$$

therefore this term is the current deformation rate translated to the the invariant initial position of the fiber.

This equation corresponds to the starting point of the modeling in [Zah96] which yields in the mean-field limit the PDE

$$\partial_t f(x,t) = -\text{div}_x(f(x)F(\dot{\boldsymbol{y}})F(\boldsymbol{y})^{-1}x) \tag{5.35}$$

$$= -f(x)\text{tr}(F(\dot{\boldsymbol{y}})F(\boldsymbol{y})^{-1}) - \partial_x f(x)F(\dot{\boldsymbol{y}})F(\boldsymbol{y})^{-1}x. \tag{5.36}$$

where tr denotes the trace of a matrix.

2.4. Assumptions

In the following, we will collect sufficient assumptions for well-posedness of the ODE model (5.11a) and (5.11b) and for convergence in the mean-field limit.

For the terms of the ODE model (5.11a) and (5.11b) we assume:

[1] In terms of elasticity theory, this condition states that the cross-bridge configuration is constant in the bodies reference coordinates.

(1) The forces $F_0 : \mathbb{R}^{n_y} \to \mathbb{R}^{n_y}$ and $F_1 : \mathbb{R}^{n_x} \to \mathbb{R}^{n_x}$ are Lipschitz continuous and bounded, i.e. there exists constants $L_0, L_1, M_0, M_1 \geq 0$ such that

$$\|F_0(\boldsymbol{y}) - F_0(\boldsymbol{y}')\| \leq L_0 \|\boldsymbol{y} - \boldsymbol{y}'\|, \tag{A1a}$$

$$\|F_0(\boldsymbol{y})\| \leq M_0, \tag{A1b}$$

$$\|F_1(\boldsymbol{X}) - F_1(\boldsymbol{X}')\| \leq L_1 \|\boldsymbol{X} - \boldsymbol{X}'\|, \tag{A1c}$$

$$\|F_1(\boldsymbol{X})\| \leq M_1. \tag{A1d}$$

for all $\boldsymbol{X}, \boldsymbol{X}' \in \mathbb{R}^{n_x}$, $\boldsymbol{y}, \boldsymbol{y}' \in \mathbb{R}^{n_y}$.

(2) The interaction kernel satisfies

$$K(\boldsymbol{X}, \boldsymbol{X}') = -K(\boldsymbol{X}', \boldsymbol{X}), \tag{A2a}$$

$$\|K(\boldsymbol{X}, \boldsymbol{Z}) - K(\boldsymbol{X}', \boldsymbol{Z})\| \leq L_K \|\boldsymbol{X} - \boldsymbol{X}'\|, \tag{A2b}$$

$$\|K(\boldsymbol{X}, \boldsymbol{Z})\| \leq M_K \tag{A2c}$$

for all $\boldsymbol{X}, \boldsymbol{X}', \boldsymbol{Z} \in \mathbb{R}^{n_x}$.

(3) The constraint

$$g : \mathbb{R}^{n_x} \times \mathbb{R}^{n_y} \to \mathbb{R}^{n_x} \text{ is twice continuously differentiable} \tag{A3a}$$

and

$$\partial_{\boldsymbol{X}} g(\boldsymbol{X}, \boldsymbol{y}) \text{ is invertible} \tag{A3b}$$

for all $\boldsymbol{X} \in \mathbb{R}^{n_x}$ and $\boldsymbol{y} \in \mathbb{R}^{n_y}$.

(4) The map

$$\Phi : \mathbb{R}^{n_x} \times \mathbb{R}^{n_y} \to \mathbb{R}^{n_x \times n_y} : (\boldsymbol{X}, \boldsymbol{y}) \mapsto -\left(\partial_{\boldsymbol{X}} g(\boldsymbol{X}, \boldsymbol{y})\right)^{-1} \partial_{\boldsymbol{y}} g(\boldsymbol{X}, \boldsymbol{y})$$

is Lipschitz continuous and bounded, i.e. there are constants $L_\Phi, M_\Phi \geq 0$ such that

$$\|\Phi(\boldsymbol{X}, \boldsymbol{y}) - \Phi(\boldsymbol{X}', \boldsymbol{y}')\| \leq L_\Phi \left(\|\boldsymbol{X} - \boldsymbol{X}'\| + \|\boldsymbol{y} - \boldsymbol{y}'\|\right) \tag{A4a}$$

$$\|\Phi(\boldsymbol{X}, \boldsymbol{y})\| \leq M_\Phi. \tag{A4b}$$

for all $\boldsymbol{X}, \boldsymbol{X}' \in \mathbb{R}^{n_x}$ and $\boldsymbol{y}, \boldsymbol{y}' \in \mathbb{R}^{n_y}$.

(5) The map

$$\begin{aligned} \Omega : \mathbb{R}^{n_x} \times \mathbb{R}^{n_y} &\to \mathbb{R}^{n_x \times n_y \times n_y} \\ : (\boldsymbol{X}, \boldsymbol{y}) &\mapsto \partial_{\boldsymbol{X}} \Phi(\boldsymbol{X}, \boldsymbol{y}) \cdot \Phi(\boldsymbol{X}, \boldsymbol{y}) + \partial_{\boldsymbol{y}} \Phi(\boldsymbol{X}, \boldsymbol{y}) \end{aligned}$$

is Lipschitz continuous and bounded, i.e. there exist constants $L_\Omega, M_\Omega \geq 0$ such that

$$\|\Omega(\boldsymbol{X}, \boldsymbol{y}) - \Omega(\boldsymbol{X}', \boldsymbol{y}')\| \leq L_\Omega \left(\|\boldsymbol{X} - \boldsymbol{X}'\| + \|\boldsymbol{y} - \boldsymbol{y}'\|\right) \tag{A5a}$$

$$\|\Omega(\boldsymbol{X}, \boldsymbol{y})\| \leq M_\Omega \tag{A5b}$$

for all $\boldsymbol{X}, \boldsymbol{X}' \in \mathbb{R}^{n_x}$ and $\boldsymbol{y}, \boldsymbol{y}' \in \mathbb{R}^{n_y}$.

2.5. Well-posedness of the ODE model

The assumptions (A1a) to (A5b) are chosen such that the ODE model (5.11a) and (5.11b) is globally Lipschitz. To show this, the main task is to prove that $m_{\text{eff}}^{(N)^{-1}} F_{\text{eff}}^{(N)}$ is Lipschitz continuous. We will do this in two steps.

First, we show in Lemma 5.5 that for given initial conditions, there exists an upper bound for the speed of the macroscopic component, i.e.

$$\|\dot{\boldsymbol{y}}(t)\| \leq M_v \quad \text{for all } t \geq 0$$

where $M_v > 0$ is a constant depending only on the initial conditions. Then, we can show that $m_{\text{eff}}^{(N)}$ and $F_{\text{eff}}^{(N)}$ are bounded and Lipschitz continuous.

In the second step, we use that $m_{\text{eff}}^{(N)}$ is also symmetric and uniformly elliptic to show that the product $m_{\text{eff}}^{(N)^{-1}} F_{\text{eff}}^{(N)}$ is Lipschitz continuous as well.

Finally, the Picard-Lindelöf Theorem implies well-posedness of (5.11a) and (5.11b).

Lemma 5.5 (Conservation of energy)**.** *For $T > 0$, let $(\boldsymbol{\mathcal{X}}^{(N)}, \boldsymbol{y})$ be a solution of (5.11a) and (5.11b) with $\boldsymbol{y} \in C^2([0,T], \mathbb{R}^{n_y})$ and $\boldsymbol{\mathcal{X}}^{(N)} \in C^1([0,T], (\mathbb{R}^{n_x})^N)$. Then, the total energy*

$$E = \frac{1}{2}\|\dot{\boldsymbol{y}}\|^2 + \mathcal{W}_0(\boldsymbol{y}) + \frac{1}{N}\sum_{i=1}^{N}\left(\frac{m}{2}\|\dot{\boldsymbol{X}}_i\|^2 + \mathcal{W}_1(\boldsymbol{X}_i) + \frac{1}{2N}\sum_{k=1}^{N}\mathcal{V}(\boldsymbol{X}_k, \boldsymbol{X}_i)\right) \tag{5.37}$$

is a conserved quantity. In particular,

$$\|\dot{\boldsymbol{y}}(t)\|^2 \leq 2E(\boldsymbol{\mathcal{X}}^{\text{init}}, \boldsymbol{y}^{\text{init}}, \boldsymbol{v}^{\text{init}}) \quad \textit{for all } t \in [0,T]. \tag{5.38}$$

Proof. The result follows from classical conservation of energy. (5.6a) to (5.6c) are exactly the Euler-Lagrange equations of the Lagrangian $L = \|\dot{\boldsymbol{y}}\|^2 - E$. With Proposition 5.1, we obtain that conversation of energy also translates to (5.11a) and (5.11b).

□

Later, in the proof of Lemma 5.11, we show the conservation of energy with an elementary computation which could also be applied to prove Lemma 5.5.

Lemma 5.5 justifies the assumption that the velocity $\boldsymbol{v} = \dot{\boldsymbol{y}}$ is bounded, which is useful for the next lemma.

Lemma 5.6. *For any constant $M_v \geq 0$, the maps*

$$(\boldsymbol{X}, \boldsymbol{y}) \mapsto m_{\text{eff}}^{(1)}(\boldsymbol{X}, \boldsymbol{y}) \quad \textit{and} \quad (\boldsymbol{X}, \boldsymbol{y}, \boldsymbol{v}) \mapsto F_{\text{eff}}^{(1)}(\boldsymbol{X}, \boldsymbol{y}, \boldsymbol{v})$$

and

$$(\boldsymbol{\mathcal{X}}^{(N)}, \boldsymbol{y}) \mapsto m_{\text{eff}}^{(N)}(\boldsymbol{\mathcal{X}}^{(N)}, \boldsymbol{y}) \quad \textit{and} \quad (\boldsymbol{\mathcal{X}}^{(N)}, \boldsymbol{y}, \boldsymbol{v}) \mapsto F_{\text{eff}}^{(N)}(\boldsymbol{\mathcal{X}}^{(N)}, \boldsymbol{y}, \boldsymbol{v})$$

are bounded and Lipschitz continuous for all $\boldsymbol{X} \in \mathbb{R}^{n_x}$, $\boldsymbol{\mathcal{X}}^{(N)} \in (\mathbb{R}^{n_x})^N$ and for all $\boldsymbol{y}, \boldsymbol{v} \in \mathbb{R}^{n_y}$ with $\|\boldsymbol{v}\| \leq M_v$.

Proof. In the following, we list which assumptions imply boundedness and Lipschitz continuity for the terms of $m_{\mathrm{mf}}^{(1)}, F_{\mathrm{mf}}^{(1)}$. We recall

$$\begin{aligned} m_{\mathrm{eff}}^{(1)}(\boldsymbol{X}, \boldsymbol{y}) &= I_{\mathbb{R}^{n_y}} + m\Phi(\boldsymbol{X}, \boldsymbol{y})^T \Phi(\boldsymbol{X}, \boldsymbol{y}), \\ F_{\mathrm{eff}}^{(1)}(\boldsymbol{X}, \boldsymbol{y}, \boldsymbol{v}) &= F_0(\boldsymbol{y}) + \Phi(\boldsymbol{X}, \boldsymbol{y})^T F_1(\boldsymbol{X}) + m\Omega(\boldsymbol{X}_i, \boldsymbol{y})[\boldsymbol{v}, \boldsymbol{v}], \\ K_{\mathrm{eff}}(\boldsymbol{X}, \boldsymbol{Z}, \boldsymbol{y}) &= \Phi(\boldsymbol{X}, \boldsymbol{y})^T K(\boldsymbol{Z}, \boldsymbol{X}). \end{aligned}$$

We use the general fact that if h_1, h_2 are both bounded and Lipschitz continuous, then the product $h_1 h_2$ is also bounded and Lipschitz continuous.

- Φ is bounded and Lipschitz by (A4a) and (A4b), therefore, $m\Phi^T\Phi$ is bounded and Lipschitz as well.
- Φ and F_1 are bounded and Lipschitz continuous by (A1c) to (A4b), therefore $\Phi(\boldsymbol{X}, \boldsymbol{y})^T F_1(\boldsymbol{X})$ is bounded and Lipschitz.
- Φ and Ω are bounded and Lipschitz continuous by (A4a) to (A5b), therefore, $m\Omega(\boldsymbol{X}_i, \boldsymbol{y})[\boldsymbol{v}, \boldsymbol{v}]$ is bounded and Lipschitz continuous provided $\|\boldsymbol{v}\| \leq M_v$.
- F_0 and F_1 are bounded and Lipschitz by (A1a) to (A1d).
- Finally, K is bounded and Lipschitz by (A2b) and (A2c).

Together, this shows that $m_{\mathrm{eff}}^{(1)}, F_{\mathrm{eff}}^{(1)}, K_{\mathrm{eff}}$ are Lipschitz.

Therefore, also $m_{\mathrm{eff}}^{(N)} = \frac{1}{N}\sum_{j=1}^N m_{\mathrm{eff}}^{(1)}$ is Lipschitz and bounded.

Moreover, $F_{\mathrm{eff}}^{(N)} = \frac{1}{N}\sum_{j=1}^N \left(F_{\mathrm{eff}}^{(1)} + \frac{1}{N}\sum_{k=1}^N K_{\mathrm{eff}}(\boldsymbol{X}_k, \boldsymbol{X}_j, \boldsymbol{y})\right)$ is also Lipschitz continuous and bounded.

The derivated bounds do not depend on N. □

Next, we show that ${m_{\mathrm{eff}}^{(N)}}^{-1} F_{\mathrm{eff}}^{(N)}$ is bounded and Lipschitz continuous. For this task, we prove a slightly more general lemma, which we can reuse later to show well-posedness of the mean-field PDE. We introduce the following notation. Let (M, d_M) be a complete metric space, $n \in \mathbb{N}$ and $h : M \to \mathbb{R}^n$, then we define

$$\mathrm{Lip}(h) \coloneqq \sup_{\substack{a,b \in M \\ a \neq b}} \frac{\|h(a) - h(b)\|}{d_M(a, b)}.$$

Lemma 5.7. *Let (M, d_M) be a complete metric space and $n \in \mathbb{N}$. Let $m : M \to \mathbb{R}^{n\times n}$ be bounded and Lipschitz continuous. Moreover, let $m(z)$ be symmetric and uniformly elliptic for all $z \in M$, i.e. there exists a positive constant $\delta_m > 0$ such that $v^T m(z) v^T \geq \delta_m \|v\|^2$ for all $z, v \in \mathbb{R}^n$.*

Then, the map

$$M \to \mathbb{R}^n : z \mapsto (m(z))^{-1}$$

is bounded and Lipschitz continuous with Lipschitz constant $\delta_m^{-2}\mathrm{Lip}(m)$.

Proof. For arbitrary $z \in M$, the ellipticity implies that the lowest eigenvalue of $m(z)$ is bounded from below by $\delta_m > 0$. Hence, the inverse $(m(z))^{-1}$ exists, and its norm is bounded by

$$\|(m(z))^{-1}\| \leq \delta_m^{-1}.$$

This shows implies that $x \mapsto m(z)$ is bounded.

Next, we consider the map $\mathrm{Inv} : GL(n) \to GL(n) : A \mapsto A^{-1}$ which has the derivative

$$\mathrm{D}\,\mathrm{Inv}(m)[w] = -m^{-1} w\, m^{-1} \quad \text{for } w \in \mathbb{R}^{n\times n},$$

which implies

$$\mathrm{D}\,\mathrm{Inv}(m(z))\| \leq \delta_m^{-2}.$$

Now, we can show that $z \mapsto \mathrm{Inv}(m(z))$ is Lipschitz. For $z_1, z_2 \in M$, the matrices $m(z_1), m(z_2)$ have only positive eigenvalues. Hence, they are part of the same connected component of $GL(d)$. Therefore, the mean-value theorem is applicable and yields

$$\|\mathrm{Inv}(m(z_1)) - \mathrm{Inv}(m(z_2))\| \leq \delta_m^{-2}\|m(z_1) - m(z_2)\| \leq \delta_m^{-2}\mathrm{Lip}(m) d_M(z_1, z_2).$$

□

Lemma 5.8. *For any constant* $M_v \geq 0$, *the map*

$$(\boldsymbol{\mathcal{X}}^{(N)}, \boldsymbol{y}, \boldsymbol{v}) \mapsto \left(m_{\text{eff}}^{(N)}(\boldsymbol{\mathcal{X}}^{(N)}, \boldsymbol{y})\right)^{-1} F_{\text{eff}}^{(N)}(\boldsymbol{\mathcal{X}}^{(N)}, \boldsymbol{y}, \boldsymbol{v})$$

is Lipschitz continuous for all $\boldsymbol{\mathcal{X}}^{(N)} \in (\mathbb{R}^{n_x})^N$ *and all* $\boldsymbol{y}, \boldsymbol{v} \in \mathbb{R}^{n_y}$ *with* $\|\boldsymbol{v}\| \leq M_v$.

Proof. By Lemma 5.6, we know that $m_{\text{eff}}^{(N)}$ and $F_{\text{eff}}^{(N)}$ are Lipschitz continuous and bounded. To apply Lemma 5.7, it is left to show that $m_{\text{eff}}^{(N)}$ is symmetric and uniformly elliptic. It suffices to show these properties for $m_{\text{eff}}^{(1)}$. Symmetry follows directly from the definition $m_{\text{eff}}^{(1)}(\boldsymbol{X}, \boldsymbol{y}) = I_{\mathbb{R}^{n_y}} + m\Phi(\boldsymbol{X}, \boldsymbol{y})^T\Phi(\boldsymbol{X}, \boldsymbol{y})$, and since $\Phi(\boldsymbol{X}, \boldsymbol{y})^T\Phi(\boldsymbol{X}, \boldsymbol{y})$ is non-negative definite, we can conclude that $\boldsymbol{w}^T m_{\text{eff}}^{(1)} \boldsymbol{w} \geq \|\boldsymbol{w}\|^2$ for all $\boldsymbol{w} \in \mathbb{R}^{n_y}$. Hence, by Lemma 5.7, $(m_{\text{eff}}^{(N)})^{-1} F_{\text{eff}}^{(N)}$ is Lipschitz continuous provided $\|\boldsymbol{v}\| \leq M_v$. □

Theorem 5.9 (Existence and uniqueness of solutions)**.** *For* $T > 0$ *and for initial conditions* $\boldsymbol{\mathcal{X}}^{\text{init}} \in (\mathbb{R}^{n_x})^N, \boldsymbol{y}^{\text{init}}, \boldsymbol{v}^{\text{init}} \in \mathbb{R}^{n_y}$ *the ODE model (5.11a) and (5.11b) has a unique solution* $(\boldsymbol{\mathcal{X}}^{(N)}, \boldsymbol{y})$ *with* $\boldsymbol{\mathcal{X}}^{(N)} \in C^2([0,T], (\mathbb{R}^{n_x})^N)$ *and* $\boldsymbol{y} \in C^2([0,T], \mathbb{R}^{n_y})$.

Proof. First, we rewrite the ODE model (5.11a) and (5.11b) as

$$\begin{cases} \ddot{\boldsymbol{y}} = (m_{\text{eff}}^{(N)}(\boldsymbol{\mathcal{X}}^{(N)}, \boldsymbol{y}))^{-1} F_{\text{eff}}^{(N)}(\boldsymbol{\mathcal{X}}^{(N)}, \boldsymbol{y}, \dot{\boldsymbol{y}}), & \text{(5.39a)} \\ \dot{\boldsymbol{X}}_i = \Phi(\boldsymbol{X}_i, \boldsymbol{y})[\dot{\boldsymbol{y}}] \qquad \text{for } 1 \leq i \leq N. & \text{(5.39b)} \end{cases}$$

We define $M_v \coloneqq 2(E(\boldsymbol{\mathcal{X}}^{\text{init}}, \boldsymbol{y}^{\text{init}}, \boldsymbol{v}^{\text{init}}))^2$ where E is the total energy from (5.37).

The assumptions (A4a) and (A4b) imply that

$$(\boldsymbol{X}, \boldsymbol{y}, \boldsymbol{v}) \mapsto \Phi(\boldsymbol{X}, \boldsymbol{y})[\boldsymbol{v}]$$

is Lipschitz continuous for $\|\boldsymbol{v}\| \leq M_v$ and Lemma 5.8 shows that $(m_{\text{eff}}^{(N)})^{-1} F_{\text{eff}}^{(N)}$ is Lipschitz continuous for $\|\boldsymbol{v}\| \leq M_v$.

Existence and uniqueness of solutions for (5.11a) and (5.11b) follows from the Picard-Lindelöf Theorem and Lemma 5.5.

The trajectory $\boldsymbol{\mathcal{X}}^{(N)}$ is actually twice continuously differentiable, since the right-hand side of (5.39b) is continuously differentiable by assumption (A3a). □

3. The mean-field limit for the ODE model

For an introduction to mean-field limits, we recommend the lecture notes from François Golse [Gol16] or the review [Jab14]. We will adapt the approach from [Gol16, Section 1.4] to prove the mean-field limit for the ODE model (5.11a) and (5.11b). The main difference to [Gol16, Section 1.4] is that our ODE system contains an additional mean-field mass term, which requires additional estimates. First, we formally define a set of equations and then prove that these equations are the ODE model's mean-field limit. Our main result is the stability estimate in Theorem 5.16.

3.1. Formal mean-field limit for the ODE model

We use the following notation from probability theory, see [Gol16]. The space of probability measures over $\mathbb{R}^{n_x}$ is $\mathcal{P}(\mathbb{R}^{n_x})$ and the space of probability measures with finite first moment is

$$\mathcal{P}^1(\mathbb{R}^{n_x}) \coloneqq \left\{ \mu \in \mathcal{P}(\mathbb{R}^{n_x}) \mid \int \|x\| \, \mathrm{d}\mu(x) < \infty \right\}.$$

The push-forward of a measure $\mu \in \mathcal{P}^1(\mathbb{R}^{n_x})$ under a map $\varphi : \mathbb{R}^{n_x} \to \mathbb{R}^{n_x}$ is defined as

$$\varphi \# \mu(A) \coloneqq \mu(\varphi^{-1}(A)) \quad \text{for all } A \in \mathfrak{B}(\mathbb{R}^{n_x})$$

where $\mathfrak{B}(\mathbb{R}^{n_x})$ are the Borel measurable sets in $\mathbb{R}^{n_x}$.

Let $(\mu^t)_{t \in [0,\infty)} \subset \mathcal{P}^1(\mathbb{R}^{n_x})$ be a family of probability measures representing the statistical particle distribution and let $\mu^{\text{init}} \in \mathcal{P}^1(\mathbb{R}^{n_x})$ be an initial particle distribution.

The formal assumption of the mean-field equations is as follows. If we consider independent, random initial conditions $\boldsymbol{X}_1^{\text{init}}, \ldots, \boldsymbol{X}_N^{\text{init}} \sim \mu^{\text{init}}$, then, we can hope that there exists a statistical distribution $\mu^t \in \mathcal{P}^1(\mathbb{R}^{n_x})$ such that $\boldsymbol{X}_1(t), \ldots, \boldsymbol{X}_N(t) \sim \mu^t$ for $t \geq 0$.[2] This will be made precise in Lemma 5.10 and finally with the proof of mean-field convergence. However, for now, we continue with the formal argumentation.

[2] For general interacting particle systems, this property is non-trivial and relates to the concept of propagation of chaos [Jab14]. However, this property is less surprising for the ODE model (5.11a) and (5.11b) since it lacks pairwise interaction between particles.

We define the mean-field characteristic flow

$$(X^t)_{t\in[0,\infty)} \text{ with } X^t : \mathbb{R}^{n_x} \to \mathbb{R}^{n_x}$$

which describes the trajectories of a single 'virtual' particle subject to the mean-field influence of particles distributed according to the particle distribution $(\mu^t)_{t\in[0,\infty)}$. It is governed by the *mean-field characteristics flow equations*

$$\begin{cases} m_{\text{eff}}(\mu^t, \boldsymbol{y})\, \ddot{\boldsymbol{y}} = F_{\text{eff}}(\mu^t, \boldsymbol{y}, \dot{\boldsymbol{y}}), & \text{(5.40a)} \\ \dot{X}^t(x) = \Phi(X^t(x), \boldsymbol{y})[\dot{\boldsymbol{y}}] \quad \text{for all } x \in \mathbb{R}^{n_x}, & \text{(5.40b)} \\ \mu^t = X^t \# \mu^{\text{init}} & \text{(5.40c)} \end{cases}$$

and initial conditions

$$\mu^0 = \mu^{\text{init}}, \quad \boldsymbol{y}(0) = \boldsymbol{y}^{\text{init}}, \quad \dot{\boldsymbol{y}}(0) = \boldsymbol{v}^{\text{init}} \quad \text{and} \quad X^0(x) = x \quad \text{for all } x \in \mathbb{R}^{n_x}$$

with the definitions

$$m_{\text{eff}}(\mu, \boldsymbol{y}) \coloneqq \int_{\mathbb{R}^{n_x}} m_{\text{eff}}^{(1)}(x, \boldsymbol{y})\, \mathrm{d}\mu(x), \tag{5.41a}$$

$$F_{\text{eff}}(\mu, \boldsymbol{y}, \boldsymbol{v}) \coloneqq \int_{\mathbb{R}^{n_x}} \left(F_{\text{eff}}^{(1)}(x, \boldsymbol{y}, \boldsymbol{v}) + \int_{\mathbb{R}^{n_x}} K_{\text{eff}}(x', x)\, \mathrm{d}\mu(x') \right) \mathrm{d}\mu(x). \tag{5.41b}$$

Both integrals are finite, since both integrands are Lipschitz continuous by Lemma 5.6 and $\mu^t \in \mathcal{P}^1(\mathbb{R}^{n_x})$.

An alternative formulation of the mean-field equations is the mean-field PDE. First, we observe that (5.40b) is precisely the characteristic ODE of a transport equation. Therefore, the mean-field PDE is

$$\begin{cases} m_{\text{eff}}(f, \boldsymbol{y})\, \ddot{\boldsymbol{y}} = F_{\text{eff}}(f, \boldsymbol{y}, \dot{\boldsymbol{y}}) & \text{(5.42a)} \\ \partial_t f(x,t) = -\mathrm{div}_x\Big(f(x,t)\, \Phi(x, \boldsymbol{y}(t))[\dot{\boldsymbol{y}}(t)] \Big) & \text{(5.42b)} \end{cases}$$

where $f : \mathbb{R}^{n_x} \times [0,T] \to [0,\infty)$ is the density of the particle position distribution μ^t, i.e. $\mathrm{d}\mu^t(x) = f(\mathrm{d}x, t)$.

3.2. Consistency with the ODE model

We use empirical measures to show the relationship between the ODE model and the mean-field equations. For a particle position vector $\boldsymbol{\mathcal{X}}^{(N)} \in (\mathbb{R}^{n_x})^N$, we define the empirical measure

$$\mu^{\text{emp}}_{\boldsymbol{\mathcal{X}}^{(N)}} \coloneqq \frac{1}{N} \sum_{i=1}^{N} \delta_{\boldsymbol{X}_i} \tag{5.43}$$

where $\delta_{\boldsymbol{X}_i}$ denotes the Dirac measure, which assigns mass 1 to the point $\boldsymbol{X}_i$. The empirical measure is an exact representation of the particle positions $\boldsymbol{\mathcal{X}}^{(N)}$ up to permutations.

By definition of the empirical measure, we obtain the relations

$$m_{\text{eff}}(\mu^{\text{emp}}_{\boldsymbol{\mathcal{X}}^{(N)}}, \boldsymbol{y}) = \frac{1}{N}\sum_{i=1}^{N} m^{(1)}_{\text{eff}}(\boldsymbol{X}_i, \boldsymbol{y}) = m^{(N)}_{\text{eff}}(\boldsymbol{\mathcal{X}}^{(N)}, \boldsymbol{y}) \tag{5.44}$$

and

$$F_{\text{eff}}(\mu^{\text{emp}}_{\boldsymbol{\mathcal{X}}^{(N)}}, \boldsymbol{y}, \boldsymbol{v}) = \frac{1}{N}\sum_{i=1}^{N}\left(F^{(1)}_{\text{eff}}(\boldsymbol{X}_i, \boldsymbol{y}, \boldsymbol{v}) + \frac{1}{N}\sum_{k=1}^{N} K_{\text{eff}}(\boldsymbol{X}_k, \boldsymbol{X}_i)\right) \tag{5.45}$$

$$= F^{(N)}_{\text{eff}}(\boldsymbol{\mathcal{X}}^{(N)}, \boldsymbol{y}, \boldsymbol{v}). \tag{5.46}$$

We see that the mean-field equations extend the ODE model, which is made precise in the following lemma. The idea is similar to [Gol16, Theorem 1.3.1].

Lemma 5.10 (Consisitency with the ODE model)**.** *Given a solution $(\boldsymbol{\mathcal{X}}^{(N)}, \boldsymbol{y})$ of the ODE model (5.11a) and (5.11b) with $\boldsymbol{\mathcal{X}}^{(N)} \in C^1([0,T], (\mathbb{R}^{n_x})^N)$ and $\boldsymbol{y} \in C^2([0,T], \mathbb{R}^{n_y})$, we define the empirical particle density $f^{(N)}$ by*

$$f^{(N)}(\mathrm{d}x, t) \coloneqq \mu^{\text{emp}}_{\boldsymbol{\mathcal{X}}^{(N)}(t)}.$$

Then, $(f^{(N)}, \boldsymbol{y})$ is a weak solution of the mean-field PDE (5.42a) and (5.42b) with initial condition $\mu^{\text{init}} \coloneqq \mu^{\text{emp}}_{\boldsymbol{\mathcal{X}}^{(N)}(0)}$. Moreover, we can construct $X : [0,T] \times \mathbb{R}^{n_x} \to \mathbb{R}^{n_x}$ such that $(X, \boldsymbol{y})$ is a solution of the mean-field characteristic flow equations (5.40a) to (5.40c).

Proof. We will first show how to construct a solution of (5.40a) to (5.40c). Let $X : [0,T] \times \mathbb{R}^{n_x} \to \mathbb{R}^{n_x}$ be the solution of

$$\begin{cases} \dot{X}^t(x) = \Phi(X^t(x), \boldsymbol{y}(t))[\dot{\boldsymbol{y}}(t)], & \text{(5.47a)} \\ X^0(x) = x & \text{(5.47b)} \end{cases}$$

for all $x \in \mathbb{R}^{n_x}$. The right-hand side is Lipschitz continuous in $X^t(x)$ by (A4a) and continuous in t. Therefore, X^t is well-defined by the Picard-Lindelöf Theorem.

The flow X^t is exactly the flow of the ODE (5.11b). If we evaluate X^t at the initial particle positions $\boldsymbol{\mathcal{X}}^{\text{init}}$, we obtain the original particle trajectories, i.e.

$$X^t(\boldsymbol{X}_i{}^{\text{init}}) = \boldsymbol{X}_i(t) \quad \text{for all } t \in [0,T]. \tag{5.48}$$

Now, we define the initial particle measure as $\mu^{\text{init}} \coloneqq \mu^{\text{emp}}_{\boldsymbol{\mathcal{X}}^{(N)}(0)}$ and $\mu^t \coloneqq X^t \# \mu^{\text{init}}$ as solution candidate. Both measures are empirical measures, hence, $\mu^{\text{init}}, \mu^t \in \mathcal{P}^1(\mathbb{R}^{n_x})$ for all $t \in [0,T]$.

By (5.48), we obtain

$$\mu^t = X^t \# \mu^{\text{init}} = X^t \# \mu^{\text{emp}}_{\boldsymbol{\mathcal{X}}^{(N)}(0)} = \mu^{\text{emp}}_{\boldsymbol{\mathcal{X}}^{(N)}(t)}. \tag{5.49}$$

Using (5.45), (5.49) and (5.11a), we compute

$$\begin{aligned} m_{\text{eff}}(\mu^t, \boldsymbol{y})\ddot{\boldsymbol{y}} &= m_{\text{eff}}^{(N)}(\boldsymbol{\mathcal{X}}^{(N)}, \boldsymbol{y})\,\ddot{\boldsymbol{y}} \\ &= F_{\text{eff}}^{(N)}(\boldsymbol{\mathcal{X}}^{(N)}, \boldsymbol{y}, \dot{\boldsymbol{y}}) \\ &= F_{\text{eff}}(\mu^t, \boldsymbol{y}, \dot{\boldsymbol{y}}). \end{aligned}$$

As a result, $(\boldsymbol{y}, X)$ is a solution of (5.40a) to (5.40c) with initial conditions μ^{init}.

To show that $f^{(N)}$ is a weak solution of the mean-field PDE, we consider a test function with compact support $\xi \in C_c^\infty(\mathbb{R}^{n_x}, \mathbb{R})$ and compute

$$\begin{aligned} \frac{\mathrm{d}}{\mathrm{d}t}\langle \xi, f^{(N)}\rangle &= \frac{\mathrm{d}}{\mathrm{d}t}\int \xi(x)\,\mathrm{d}\mu^t(x) \\ &= \frac{\mathrm{d}}{\mathrm{d}t}\int \xi(X^t(x'))\,\mathrm{d}\mu^{\text{init}}(x') \\ &= \int \frac{\mathrm{d}}{\mathrm{d}t}\xi(X^t(x'))\,\mathrm{d}\mu^{\text{init}}(x') \\ &= \int \partial_X \xi(X^t(x'))\,\dot{X}^t(x')\,\mathrm{d}\mu^{\text{init}}(x'). \end{aligned}$$

Using that $\dot{X}^t$ solves (5.47a) yields

$$\begin{aligned} \frac{\mathrm{d}}{\mathrm{d}t}\langle \xi, f^{(N)}\rangle &= \int \partial_X \xi(X^t(x'))\,\Phi(X^t(x'), \boldsymbol{y}(t))[\dot{\boldsymbol{y}}(t)]\,\mathrm{d}\mu^{\text{init}}(x') \\ &= \int \partial_x \xi(x)\,\Phi(x, \boldsymbol{y}(t))[\dot{\boldsymbol{y}}(t)] f^{(N)}(x,t)\,\mathrm{d}x \\ &= -\int \xi(x)\,\mathrm{div}_x\left(\Phi(x, \boldsymbol{y}(t))[\dot{\boldsymbol{y}}(t)] f^{(N)}(x,t)\right)\,\mathrm{d}x \\ &= -\langle \xi\,, \mathrm{div}((\Phi\,\dot{\boldsymbol{y}}) f^{(N)})\rangle. \end{aligned}$$

Hence, $f^{(N)}$ is a weak solution of (5.42b). □

3.3. Existence and uniqueness for the mean-field equations

The existence and uniqueness of solutions for the mean-field characteristics flow equations (5.40a) to (5.40c) follows the same steps as in the discrete case.

As for the ODE model, we prove conservation of energy to justify the restriction to bounded velocities of the macroscopic component.

Lemma 5.11 (Conservation of energy)**.** *Let $(X, \boldsymbol{y}, \dot{\boldsymbol{y}}) \in C^1([0,T], Z)$ be a solution of (5.40a) to (5.40c). Then, the total energy*

(5.50)

$$E = \frac{1}{2}\|\dot{\boldsymbol{y}}\|^2 + \mathcal{W}_0(\boldsymbol{y}) + \int_{\mathbb{R}^{n_x}} \frac{m}{2}\|\Phi(x, \boldsymbol{y})\,\dot{\boldsymbol{y}}\|^2 + \mathcal{W}_1(x) + \frac{1}{2}\int_{\mathbb{R}^{n_x}} \mathcal{V}(x' - x)\,\mathrm{d}\mu^t(x')\,\mathrm{d}\mu^t(x)$$

is conserved.

In principle one could show Lemma 5.11 again as a result of classical conservation of energy for Lagrangian systems, as we did for Lemma 5.5. However, since the equivalence between (5.42a) and (5.42b) and the corresponding Euler-Lagrange equations is not that trivial, we will give instead an elementary proof for the conservation of energy.

Proof. For the following calculations, we use the shorthand notation

$$\Phi_x \coloneqq \Phi(X^t(x), \boldsymbol{y}) \quad \text{and} \quad \Omega_x \coloneqq \Omega(X^t(x), \boldsymbol{y}).$$

First, we take the time derivative of (5.40b), which yields

$$\begin{aligned} \ddot{X}^t(x) &= \Phi(X^t(x), \boldsymbol{y}(t))[\ddot{\boldsymbol{y}}(t)] + \Omega(X^t(x), \boldsymbol{y}(t))[\dot{\boldsymbol{y}}(t), \dot{\boldsymbol{y}}(t)] \\ &= \Phi_x[\ddot{\boldsymbol{y}}] + \Omega_x[\dot{\boldsymbol{y}}, \dot{\boldsymbol{y}}]. \end{aligned} \tag{5.51}$$

We recall that $K(\boldsymbol{X}_k, \boldsymbol{X}_i) = -\nabla_{\boldsymbol{X}_i} \mathcal{V}(\boldsymbol{X}_k - \boldsymbol{X}_i)$. The anti-symmetry of K allows us to compute

$$\begin{aligned} \frac{\mathrm{d}}{\mathrm{d}t} \mathcal{V}(X^t(x') - X^t(x)) &= \dot{X}^t(x') K(X^t(x'), X^t(x)) - \dot{X}^t(x) K(X^t(x'), X^t(x)) \\ &= -\dot{X}^t(x') K(X^t(x), X^t(x')) - \dot{X}^t(x) K(X^t(x'), X^t(x)) \end{aligned} \tag{5.52}$$

where we use $K(X', X) = -K(X, X')$ in the last step.

Integrating (5.52) yields

$$\begin{aligned} A &\coloneqq \frac{1}{2} \int_{\mathbb{R}^{n_x}} \int_{\mathbb{R}^{n_x}} \frac{\mathrm{d}}{\mathrm{d}t} \mathcal{V}(X^t(x') - X^t(x)) \, \mathrm{d}\mu^{\mathrm{init}}(x') \, \mathrm{d}\mu^{\mathrm{init}}(x) \\ &= \frac{1}{2} \int_{\mathbb{R}^{n_x}} \int_{\mathbb{R}^{n_x}} \Big(- \dot{X}^t(x') K(X^t(x), X^t(x')) \\ &\qquad\qquad - \dot{X}^t(x) K(X^t(x'), X^t(x)) \Big) \, \mathrm{d}\mu^{\mathrm{init}}(x') \, \mathrm{d}\mu^{\mathrm{init}}(x) \\ &= \int_{\mathbb{R}^{n_x}} \dot{X}^t(x) \int_{\mathbb{R}^{n_x}} -K(X^t(x'), X^t(x)) \, \mathrm{d}\mu^{\mathrm{init}}(x') \, \mathrm{d}\mu^{\mathrm{init}}(x), \end{aligned} \tag{5.53}$$

where we swap the role of x and x' in one of the integrands to obtain the last equation.

To shorten the following computations, we also define

$$\mathcal{K}(x) \coloneqq \int_{\mathbb{R}^{n_x}} K(X^t(x'), X^t(x)) \, \mathrm{d}\mu^{\mathrm{init}}(x').$$

We now can compute the time derivative of the total energy

$$\begin{aligned}
\dot{E} &= \frac{\mathrm{d}}{\mathrm{d}t}\Bigg(\frac{1}{2}\|\dot{\boldsymbol{y}}\|^2 + \mathcal{W}_0(\boldsymbol{y}) \\
&\qquad + \int_{\mathbb{R}^{n_x}} \frac{m}{2}\|\Phi(\tilde{x},\boldsymbol{y})\,\dot{\boldsymbol{y}}\|^2 + \mathcal{W}_1(\tilde{x}) + \frac{1}{2}\int_{\mathbb{R}^{n_x}} \mathcal{V}(\tilde{x}'-\tilde{x})\,\mathrm{d}\mu^t(\tilde{x}')\,\mathrm{d}\mu^t(\tilde{x}')\Bigg) \\
&= \frac{\mathrm{d}}{\mathrm{d}t}\Bigg(\frac{1}{2}\|\dot{\boldsymbol{y}}\|^2 + \mathcal{W}_0(\boldsymbol{y}) \\
&\qquad + \int_{\mathbb{R}^{n_x}} \frac{m}{2}\|\Phi(X^t(x),\boldsymbol{y})\,\dot{\boldsymbol{y}}\|^2 + \mathcal{W}_1(X^t(x)) \\
&\qquad\quad + \frac{1}{2}\int_{\mathbb{R}^{n_x}} \mathcal{V}(X^t(x')-X^t(x))\,\mathrm{d}\mu^{\mathrm{init}}(x')\,\mathrm{d}\mu^{\mathrm{init}}(x)\Bigg).
\end{aligned}$$

Using (5.51), (5.53) and (5.40a) to (5.40c), we get

$$\begin{aligned}
\dot{E} &= \dot{\boldsymbol{y}}^T(\ddot{\boldsymbol{y}} - F_0(\boldsymbol{y})) + \frac{\mathrm{d}}{\mathrm{d}t}\int_{\mathbb{R}^{n_x}} \frac{m}{2}\|\dot{X}^t(x)\|^2 + \mathcal{W}_1(X^t(x))\,\mathrm{d}\mu^{\mathrm{init}}(x) + A \\
&= \dot{\boldsymbol{y}}^T(\ddot{\boldsymbol{y}} - F_0(\boldsymbol{y})) + \int_{\mathbb{R}^{n_x}} (\dot{X}^t(x))^T(m\ddot{X}^t(x) - F_1(X^t(x) - \mathcal{K}(x))\,\mathrm{d}\mu^{\mathrm{init}}(x) \\
&= \dot{\boldsymbol{y}}^T(\ddot{\boldsymbol{y}} - F_0(\boldsymbol{y})) + \int_{\mathbb{R}^{n_x}} \dot{\boldsymbol{y}}^T\Phi_x^T(m\Phi_x[\ddot{\boldsymbol{y}}] + m\Omega_x[\dot{\boldsymbol{y}},\dot{\boldsymbol{y}}] - F_1(X^t(x) - \mathcal{K}(x))\,\mathrm{d}\mu^{\mathrm{init}}(x) \\
&= \dot{\boldsymbol{y}}^T\Bigg(\Big(1 + m\int_{\mathbb{R}^{n_x}} \Phi_x^T\Phi_x\,\mathrm{d}\mu^{\mathrm{init}}(x)\Big)\ddot{\boldsymbol{y}} \\
&\qquad - (F_0(\boldsymbol{y}) + \int_{\mathbb{R}^{n_x}} \Phi_x^T\big(F_1(X^t(x)) + \mathcal{K}(x) - m\Omega_x[\dot{\boldsymbol{y}},\dot{\boldsymbol{y}}]\big)\,\mathrm{d}\mu^{\mathrm{init}}(x))\Bigg) \\
&= \dot{\boldsymbol{y}}^T(m_{\mathrm{eff}}\ddot{\boldsymbol{y}} - F_{\mathrm{eff}}) \\
&= 0.
\end{aligned}$$

□

To prove a Lipschitz bound for the mean-field characteristic flow equations (5.40a) to (5.40c), we first need to choose a function space for the flow X^t. We pick the function space of continuous and at most linearly growing functions, see [Gol16, Proof of Theorem 1.3.2]. We define

$$Y \coloneqq \{\varphi \mid \varphi \in C(\mathbb{R}^{n_x},\mathbb{R}^{n_x}),\ \sup_{x\in\mathbb{R}^{n_x}} \frac{\|\varphi(x)\|}{1+\|x\|} < \infty\} \tag{5.54}$$

which forms a Banach space with the norm

$$\|\varphi\|_Y \coloneqq \sup_{x\in\mathbb{R}^{n_x}} \frac{\|\varphi(x)\|}{1+\|x\|}.$$

Our goal is to rewrite (5.40a) to (5.40c) as an ODE of the form $\dot{z} = h(z)$. Therefore, we define

$$Z \coloneqq Y \oplus \mathbb{R}^{n_y} \oplus \mathbb{R}^{n_y}. \tag{5.55}$$

The space Z is a Banach space with the norm

$$\|(\varphi, \boldsymbol{y}, \boldsymbol{v})\|_Z = \|\varphi\|_Y + \|\boldsymbol{y}\| + \|\boldsymbol{v}\|.$$

Since conservation of energy implies that the velocity $\dot{\boldsymbol{y}}$ will stay bounded for all times, we can restrict the domain of the right-hand side to the closed subset

$$Z_{M_v} \coloneqq \{z = (\varphi, \boldsymbol{y}, \boldsymbol{v}) \in Z \mid \|\boldsymbol{v}\| \leq M_v\} \subseteq Z \tag{5.56}$$

where $M_v > 0$ is a constant.

With the definition

$$h : Z_{M_v} \to Z : \begin{pmatrix} \varphi \\ \boldsymbol{y} \\ \boldsymbol{v} \end{pmatrix} \mapsto \begin{pmatrix} x \mapsto \Phi(\varphi(x), \boldsymbol{y})[\boldsymbol{v}] \\ \boldsymbol{v} \\ (m_{\text{eff}}(\varphi \# \mu^{\text{init}}, \boldsymbol{y}))^{-1} F_{\text{eff}}(\varphi \# \mu^{\text{init}}, \boldsymbol{y}, \boldsymbol{v}) \end{pmatrix}$$

we can rewrite (5.40a) to (5.40c) as

$$\dot{z} = h(z).$$

Sometimes, we will write $h(\varphi, \boldsymbol{y}, \dot{\boldsymbol{y}}; \mu^{\text{init}})$ to emphasise the dependency on μ^{init}. The first component of the map b is indeed an element of Y, since (A5b) implies $\|\Phi(\varphi(\cdot), \boldsymbol{y})[\boldsymbol{v}]\|_Y \leq M_\Phi M_v$ for all $(\varphi, \boldsymbol{y}, \boldsymbol{v}) \in Z_{M_v}$.

The following theorem essential relies on the fact that h is Lipschitz continuous.

Theorem 5.12 (Existence and uniqueness)**.** *For $\mu^{\text{init}} \in \mathcal{P}^1(\mathbb{R}^{n_x})$ and $\boldsymbol{y}^{\text{init}}, \boldsymbol{v}^{\text{init}} \in \mathbb{R}^{n_y}$, the system (5.40a) to (5.40c) has a unique solution $(\boldsymbol{y}, X) \in C^2([0,T], \mathbb{R}^{n_y}) \times C^1([0,T] \times \mathbb{R}^{n_x}, \mathbb{R}^{n_x})$.*

To proof existence and uniqueness, we will use the following Lemma.

Lemma 5.13. *Let $\phi : \mathbb{R}^d \to \mathbb{R}$ and $\eta : \mathbb{R}^d \times \mathbb{R}^d \to \mathbb{R}$ be Lipschitz continuous, $\varphi, \psi \in Y$ and $\mu \in \mathcal{P}^1(\mathbb{R}^{n_x})$ then the map*

$$Y \to \mathbb{R} : \varphi \mapsto \int_{\mathbb{R}^{n_x}} \phi(\varphi(x)) \,\mathrm{d}\mu(x) \tag{5.57}$$

$$Y \to \mathbb{R} : \varphi \mapsto \int_{\mathbb{R}^{n_x}} \int_{\mathbb{R}^{n_x}} \eta(\varphi(x), \varphi(y)) \,\mathrm{d}\mu(y) \,\mathrm{d}\mu(x) \tag{5.58}$$

are Lipschitz continuous with constants $\mathrm{Lip}(\phi) C_\mu \|\varphi - \psi\|_Y$ and $2\mathrm{Lip}(\eta) C_\mu \|\varphi - \psi\|_Y$ where $C_\mu \coloneqq \int (1 + \|x\|) \,\mathrm{d}\mu(x) < \infty$.

Proof. First we note that

$$\int_{\mathbb{R}^{n_x}} \|\varphi(x) - \psi(x)\| \,\mathrm{d}\mu(x) = \int_{\mathbb{R}^{n_x}} \frac{\|\varphi(x) - \psi(x)\|}{1 + \|x\|} (1 + \|x\|) \,\mathrm{d}\mu(x) \leq C_\mu \|\varphi - \psi\|_Y.$$

Using this, we compute

$$\begin{aligned}&\left|\int_{\mathbb{R}^{n_x}}\int_{\mathbb{R}^{n_x}}\eta(\varphi(x),\varphi(y))\,\mathrm{d}\mu(y)\,\mathrm{d}\mu(x)-\int_{\mathbb{R}^{n_x}}\int_{\mathbb{R}^{n_x}}\eta(\psi(x),\psi(y))\,\mathrm{d}\mu(y)\,\mathrm{d}\mu(x)\right|\\&\quad\le \mathrm{Lip}(\eta)\left(\int_{\mathbb{R}^{n_x}}\|\varphi(x)-\psi(x)\|\,\mathrm{d}\mu(x)+\int_{\mathbb{R}^{n_x}}\|\varphi(y)-\psi(y)\|\,\mathrm{d}\mu(y)\right)\\&\quad\le 2\mathrm{Lip}(\eta)C_\mu\|\varphi-\psi\|_Y.\end{aligned}$$

This shows the claim for the second map. The result follows analogous to the first map. □

Proof of Theorem 5.12. We define $M_v := 2E(\boldsymbol{y},\dot{\boldsymbol{y}},\mu^{\mathrm{init}})$. Then, Lemma 5.11 shows that every solution candidate has to satisfy $\|\dot{\boldsymbol{y}}(t)\|\le M_v$ for all $t\in[0,T]$.

Now we show that the components of the map h are Lipschitz continuous for all $(\varphi,\boldsymbol{y},\boldsymbol{v})\in Z_{M_v}$.

We start with the component $\Phi(\varphi(\cdot),\boldsymbol{y})[\boldsymbol{v}]$. The map $(\varphi,\boldsymbol{y})\mapsto\Phi(\varphi(\cdot),\boldsymbol{y})$ is Lipschitz continuous by assumption (A4a), i.e.

$$\sup_{x\in\mathbb{R}^{n_x}}\frac{\|\Phi(\varphi_1(x),\boldsymbol{y}_1)-\Phi(\varphi_2(x),\boldsymbol{y}_2)\|}{1+\|x\|}\le L_\Phi\left(\sup_{x\in\mathbb{R}^{n_x}}\frac{\|\varphi_1(x)-\varphi_2(x)\|}{1+\|x\|}+\|\boldsymbol{y}_1-\boldsymbol{y}_2\|\right)$$

and assumption (A4b) yields the upper bound

$$\|\Phi(\varphi(\cdot),\boldsymbol{y})\|_X\le M_\Phi.$$

Therefore, $(\varphi,\boldsymbol{y},\boldsymbol{v})\mapsto\Phi(\varphi(\cdot),\boldsymbol{y})[\boldsymbol{v}]$ is Lipschitz for $\|\boldsymbol{v}\|\le M_v$.

By Lemma 5.6, we know that $m_{\mathrm{eff}}^{(1)}$ and $F_{\mathrm{eff}}^{(1)}$ are bounded and Lipschitz. Therefore, Lemma 5.13 implies that

$$(\varphi,\boldsymbol{y},\boldsymbol{v})\mapsto m_{\mathrm{eff}}(\varphi\#\mu^{\mathrm{init}},\boldsymbol{y},\boldsymbol{v})$$

and

$$(\varphi,\boldsymbol{y},\boldsymbol{v})\mapsto F_{\mathrm{eff}}(\varphi\#\mu^{\mathrm{init}},\boldsymbol{y},\boldsymbol{v})$$

are Lipschitz continuous and bounded for $\|\boldsymbol{v}\|\le M_v$.

Moreover, m_{eff} is symmetric and uniformly elliptic since the integration of $m_{\mathrm{eff}}^{(1)}$ preserves these properties as well.

Lemma 5.7 yields that for fixed μ^{init} the map

$$(\varphi,\boldsymbol{y},\boldsymbol{y})\mapsto h(\varphi,\boldsymbol{y},\dot{\boldsymbol{y}};\mu^{\mathrm{init}})$$

is Lipschitz continuous provided $\|\boldsymbol{v}\|\le M_v$.

Hence, the Picard-Lindelöf Theorem and Lemma 5.11 yield existence and uniqueness of solutions.

We remark that the Lipschitz constant depends on M_v and $C_{\mu^{\mathrm{init}}}$. The latter is finite since $\mu^{\mathrm{init}}\in\mathcal{P}^1(\mathbb{R}^{n_x})$. □

3.4. Stability estimate

The mean-field limit asserts that for $N \to \infty$ the behaviour of the ODE model (5.11a) and (5.11b) is well-approximated by the mean-field characteristic flow (5.40a) to (5.40c). Lemma 5.10 implies that solutions of the ODE model correspond to solutions of the mean-field equations (5.40a) to (5.40c) with empirical measures as initial data. Hence, it is sufficient to show that solutions of (5.40a) to (5.40c) depend continuously on the initial particle distribution μ^{init} to show convergence of the mean-field limit.

As a metric between particle distributions, we use the Monge-Kantorovich distance (also called Wasserstein distance). For a detailed study of the Monge-Kantorovich distance, we refer to [Vil09, Chapter 6]. Since we only need the duality formula of the Monge-Kantorovich distance, we use this characterisation as a definition.

Definition 5.14 (Monge-Kantorovich distance [Gol16, Proposition 1.4.2])**.**
For $\nu, \mu \in \mathcal{P}^1(\mathbb{R}^{n_x})$, we define the *Monge-Kantorovich distance (with exponent 1)* as

$$W_1(\nu,\mu) = \sup_{\substack{\phi \in C(\mathbb{R}^{n_x},\mathbb{R}^{n_x}) \\ \operatorname{Lip}(\phi)\leq 1}} \left| \int_{\mathbb{R}^{n_x}} \phi(x)\,\mathrm{d}\nu(x) - \int_{\mathbb{R}^{n_x}} \phi(x)\,\mathrm{d}\mu(x) \right|. \tag{5.59}$$

The Monge-Kantorovich distance is a complete metric on $\mathcal{P}^1(\mathbb{R}^{n_x})$ [Vil09, Lemma 6.14].

Lemma 5.15. *Let $\phi : \mathbb{R}^d \to \mathbb{R}$ be Lipschitz continuous, then*

$$\left| \int_{\mathbb{R}^{n_x}} \phi(x)\,\mathrm{d}\mu_1(x) - \int_{\mathbb{R}^{n_x}} \phi(x)\,\mathrm{d}\mu_2(x) \right| \leq \operatorname{Lip}(\phi) W_1(\mu_1,\mu_2).$$

Proof. This follows directly from the duality formula (5.59). □

With the Monge-Kantorovich distance we can define the main result of this article. The following estimate is a generalisation of Dobrushin's stability estimate [Gol16, Section 3.3].

Theorem 5.16 (Stability estimate)**.**
Suppose that for $i \in \{1,2\}$ the tuples $(\boldsymbol{y}_i(t), \mu_i^t(t)) \in \mathbb{R}^{n_y} \times \mathcal{P}^1(\mathbb{R}^{n_x})$ are solutions of (5.40a) to (5.40c) with initial conditions

$$\boldsymbol{y}_i(0) = \boldsymbol{y}_i^{\text{init}}, \quad \dot{\boldsymbol{y}}_i(0) = \boldsymbol{v}_i^{\text{init}} \quad \textit{and} \quad \mu_i(0) = \mu_i^{\text{init}}.$$

Then,

$$\begin{aligned} &\|\boldsymbol{y}_1(t) - \boldsymbol{y}_2(t)\| + \|\dot{\boldsymbol{y}}_1(t) - \dot{\boldsymbol{y}}_2(t)\| + W_1(\mu_1(t),\mu_2(t)) \\ &\qquad \leq C e^{Lt} \left(\|\boldsymbol{y}_1^{\text{init}} - \boldsymbol{y}_2^{\text{init}}\| + \|\boldsymbol{v}_1^{\text{init}} - \boldsymbol{v}_2^{\text{init}}\| + W_1(\mu_1^{\text{init}},\mu_2^{\text{init}}) \right), \end{aligned} \tag{5.60}$$

for some constants $L, C > 0$ which do only depend on the initial total energy of both states and on the maximal first moment

$$C_\mu \coloneqq \max\left(\int (1 + \|x\|)\,\mathrm{d}\mu_1^{\text{init}}(x), \int (1+\|x\|)\,\mathrm{d}\mu_2^{\text{init}}(x) \right).$$

To prove this stability estimate, we use the following ODE estimate, see also [HNW93, Theorem 10.2].

Lemma 5.17 (The Fundamental Lemma, [Wal70, Chap 1., §7 Theorem VI])**.** *Let A be a closed subset of a Banach space Z and suppose that for $i \in \{1,2\}$ and $h_i : A \to Z$, the functions $z_i : [0,T] \to A$ solve*

$$\begin{cases} \dot{z}_i(t) = h_i(z_i(t)) \quad \text{for } t \geq 0, & \text{(5.61a)} \\ z_i(0) = z_i^{\text{init}}. & \text{(5.61b)} \end{cases}$$

If for some constants $\varrho, \varepsilon, L > 0$ the following bounds hold

(1) $\|z_1^{\text{init}} - z_2^{\text{init}}\| \leq \varrho$,

(2) $\|h_1(z) - h_2(z)\| \leq \varepsilon \quad \text{for all } z \in Z$,

(3) $\|h_1(z) - h_1(z')\| \leq L\|z - z'\| \quad \text{for all } z, z' \in Z$,

then,

$$\|z_1(t) - z_2(t)\| \leq \varrho e^{Lt} + \frac{\varepsilon}{L}\left(e^{Lt} - 1\right). \tag{5.62}$$

Proof of Theorem 5.16. We define

$$h_i(\varphi, \boldsymbol{y}, \boldsymbol{v}) \coloneqq h(\varphi, \boldsymbol{y}, \boldsymbol{v}; \mu_i^{\text{init}}) \quad \text{for } i \in \{1,2\}.$$

For $i \in \{1,2\}$, we consider the ODEs

$$\begin{cases} \dot{z}_i = h_i(z_i) \\ z_i(0) = z_i^{\text{init}} \end{cases}$$

with initial condition

$$z_i^{\text{init}} \coloneqq (x \mapsto x, \boldsymbol{y}_i^{\text{init}}, \boldsymbol{v}_i^{\text{init}}).$$

Next, we check the conditions of Lemma 5.17.
1. We define

$$\varrho \coloneqq \|z_1^{\text{init}} - z_2^{\text{init}}\|_Z = \|\boldsymbol{y}_1^{\text{init}} - \boldsymbol{y}_2^{\text{init}}\| + \|\boldsymbol{v}_1^{\text{init}} - \boldsymbol{v}_2^{\text{init}}\|.$$

2. For arbitrary $(\varphi, \boldsymbol{y}, \boldsymbol{v}) \in Z_{M_v}$, we consider the maps

$$\mathcal{P}^1(\mathbb{R}^{n_x}) \to \mathbb{R}^{n_y} : \mu \mapsto h(\varphi, \boldsymbol{y}, \boldsymbol{v}; \mu).$$

We compute

$$\begin{aligned} &\|h(\varphi, \boldsymbol{y}, \boldsymbol{v}; \mu_1) - h(\varphi, \boldsymbol{y}, \boldsymbol{v}; \mu_2)\|_Z \\ &\quad = \|(m_{\text{eff}}(\mu_1, \boldsymbol{y}))^{-1} F_{\text{eff}}(\mu_1, \boldsymbol{y}, \boldsymbol{v}) - (m_{\text{eff}}(\mu_2, \boldsymbol{y}))^{-1} F_{\text{eff}}(\mu_2, \boldsymbol{y}, \boldsymbol{v})\|. \end{aligned}$$

Lemmas 5.6 and 5.15 show that the maps

$$\mu \mapsto m_{\text{eff}}(\mu, \boldsymbol{y}) \quad \text{and} \quad \mu \mapsto F_{\text{eff}}(\mu, \boldsymbol{y}, \boldsymbol{v})$$

are bounded and Lipschitz continuous. Like in the proof of Theorem 5.12, $m_{\text{eff}}(\mu, \boldsymbol{y})$ is also symmetric and uniformly elliptic for all $\mu \in \mathcal{P}^1(\mathbb{R}^{n_x})$. Therefore, Lemma 5.7 shows that $\mu \mapsto h(\varphi, \boldsymbol{y}, \boldsymbol{v}; \mu)$ is Lipschitz continuous, i.e.

$$\|h_1(\varphi, \boldsymbol{y}, \dot{\boldsymbol{y}}) - h_2(\varphi, \boldsymbol{y}, \dot{\boldsymbol{y}})\| \leq L_\mu \, W_1(\mu_1^{\text{init}}, \mu_2^{\text{init}})$$

and the Lipschitz constant L_μ depends only on M_v and C_μ. We set

$$\varepsilon \coloneqq L_\mu \, W_1(\mu_1^{\text{init}}, \mu_2^{\text{init}}).$$

3. From the proof of Theorem 5.12 we know that $h_1 : Z_{M_v} \to Z$ is Lipschitz continuous. The constant $\operatorname{Lip}(h_1)$ depends only on M_v and C_μ.

Application of Lemma 5.17 yields

$$\begin{aligned} &\|\boldsymbol{y}_1(t) - \boldsymbol{y}_2(t)\| + \|\dot{\boldsymbol{y}}_1(t) - \dot{\boldsymbol{y}}_2(t)\| + \|X_1^t - X_2^t\|_X \\ &\qquad \leq \varrho e^{tL_{f_1}} + \frac{L_\mu W_1(\mu_1^{\text{init}}, \mu_2^{\text{init}})}{\operatorname{Lip}(h_1)} (e^{t\operatorname{Lip}(h_1)} - 1) \end{aligned} \tag{5.64}$$

In comparison with the claim, equation (5.64) does not include $W_1(\mu_1^t, \mu_2^t)$ yet. We derive one more estimate to fix this. For an arbitrary Lipschitz continuous map $\phi : \mathbb{R}^{n_x} \to \mathbb{R}$, we use Lemma 5.13 and Lemma 5.15 to compute

$$\begin{aligned} &\left| \int \phi(x) \, \mathrm{d}\mu_1^t(x) - \int \phi(x) \, \mathrm{d}\mu_2^t(x) \right| \\ &\qquad \leq \left\| \int \phi(X_1^t(x')) \, \mathrm{d}\mu_1^{\text{init}}(x') - \int \phi(X_2^t(x')) \, \mathrm{d}\mu_1^{\text{init}}(x') \right\| \\ &\qquad\quad + \left\| \int \phi(X_2^t(x')) \, \mathrm{d}\mu_1^{\text{init}}(x') - \int \phi(X_2^t(x')) \, \mathrm{d}\mu_2^{\text{init}}(x') \right\| \\ &\qquad \leq \operatorname{Lip}(\phi) C_\mu \|X_1^t - X_2^t\|_X + \operatorname{Lip}(\phi) W_1(\mu_1^{\text{init}}, \mu_2^{\text{init}}). \end{aligned}$$

Taking the supremum over all ϕ with $\operatorname{Lip}(\phi) \leq 1$ yields

$$W_1(\mu_1^t, \mu_2^t) \leq C_\mu \|X_1^t - X_2^t\|_X + W_1(\mu_1^{\text{init}}, \mu_2^{\text{init}}). \tag{5.65}$$

Combining (5.64) and (5.65) yields the claim. □

Remark 5.18. The proof of Theorem 5.16 follows mainly the same idea as the previous work on the linear case [PS20]. Previsouly, the result was shown for linear constraints g and linear force terms.

The main addition is that for nonlinear constraint the term m_{eff} is non-constant and therefore we need Lemma 5.8 to show that the map $\mu \mapsto h(\varphi, \boldsymbol{y}, \boldsymbol{v}, \mu)$ is Lipschitz.

The second addition is that in the linear case the third step in the proof if Theorem 5.16 is easier, since the particle distributation will only be shifted over time, i.e. there is a vector $w(t)$ such that $\mu^{\text{init}}(A) = \mu^t(A - w(t))$.

3.5. Convergence of the mean-field limit

With the stability estimate Theorem 5.16, we can finally show convergence of the mean-field limit.

Corollary 5.19. *We consider $\mu^{\text{init}} \in \mathcal{P}^1(\mathbb{R}^{n_x})$, $\boldsymbol{y}^{\text{init}}, \boldsymbol{v}^{\text{init}} \in \mathbb{R}^{n_y}$ and a sequence of initial particle positions $\left(\boldsymbol{\mathcal{X}}_k^{\text{init}}\right)_{k\in\mathbb{N}}$ such that*

$$W_1(\mu^{\text{emp}}_{\boldsymbol{\mathcal{X}}_k^{\text{init}}}, \mu^{\text{init}}) \to 0 \quad \text{for } k \to \infty. \tag{5.66}$$

Let $(\mu^t, \boldsymbol{y}(t))$ and $(\mu_k^t, \boldsymbol{y}_k(t))$ be solutions for (5.40a) to (5.40c) with initial conditions $(\mu^{\text{init}}, \boldsymbol{y}^{\text{init}}, \boldsymbol{v}^{\text{init}})$ and $(\mu^{\text{emp}}_{\boldsymbol{\mathcal{X}}_k^{\text{init}}}, \boldsymbol{y}^{\text{init}}, \boldsymbol{v}^{\text{init}})$ for $k \in \mathbb{N}$.

Then,

$$\|\boldsymbol{y}(t) - \boldsymbol{y}_k(t)\| + \|\dot{\boldsymbol{y}}(t) - \dot{\boldsymbol{y}}_k(t)\| + W_1(\mu^t, \mu_k^t) \leq Ce^{Lt} W_1(\mu^{\text{init}}, \mu^{\text{emp}}_{\boldsymbol{\mathcal{X}}_k^{\text{init}}}) \to 0.$$

Corollary 5.19 follows directly from the stability estimate Theorem 5.16.

We use Corollary 5.19 as the main mean-field limit result. For the subtleties of convergences of mean-field limits in different topologies, we refer to [Gol16, Section 1.4]. In particular, the existence of suitable initial conditions such that (5.66) holds is shown in [Gol16, Section 1.4.4].

Remark 5.20 (Macroscopic equations)**.** Since the mean-field PDE (5.42a) and (5.42b) is essentially a transport equation, there are several ways to obtain a macroscopic approximation for the particle dynamics. One approach would be to assume that the density $f(x,t)$ has the shape of a normal distribution and then find equations for the first moments by inserting this ansatz into the (5.42a) and (5.42b).

Let us define

$$m(t) = \int f(x,t)\,\mathrm{d}x, \qquad \boldsymbol{\rho}(t) = \int \boldsymbol{x} f(\boldsymbol{x},t)\,\mathrm{d}\boldsymbol{x}, \qquad \sigma(t) = \int \boldsymbol{x} \otimes \boldsymbol{x} f(\boldsymbol{x},t)\,\mathrm{d}\boldsymbol{x} \tag{5.67}$$

Then

$$\dot{m}(t) = 0 \quad \text{conservation of mass} \tag{5.68}$$

$$\dot{\rho}(t) = \tag{5.69}$$

In the context of muscle models, this method is called distributed moment method [Zah81]. The distributed moment method is the foundation for most numerical simulations of muscle tissue which include fibers, see for example [BR08; GS21; Hei+16].

4. Conclusion

We have generalised the results from our previous work [PS20] to the case of nonlinear constraints. In particular, the same stability estimate as in the linear case also holds for nonlinear constraints. Moreover, the proof follows Dobrushin's classical approach, which shows that many properties of unconstrained particle systems generalise well to particle systems with uniform, full-rank constraints.

Nonetheless, our results are still restricted a particular class of particle systems with uniform, full-rank constraints. We see two main directions for further study. First, with view towards possible applications, it would be desirable to extend our results to cases which cover more general constraints. For example, the particles could switch between a constrained case and an unconstrained case, as outlined in [PS20, Section 5.3]. Second, to further explore kinetic theory-related aspects, one could drop the full-rank condition and add interaction forces between the particles. This would lead to systems with similarities to Vlasov equations. In particular, if the constraints are not of full rank, the propagation of chaos becomes non-trivial since the state space of the particles could be both non-linear and dependent on the state of the macroscopic component.

Conclusions

The main goal of this thesis was to propose a model for epithelial tissue that incorporates epithelial-to-mesenchymal transitions. With this model, and in collaboration with experimentalists, we have investigated the role of EMT on producing basal extrusion. The modelling, its implementation and the exploration of the outcome of the simulations have lead to various results that we summarise next.

- As a mathematical foundation, we used the theory of **differential inclusions on uniformly prox-regular sets**. The theory applies to agent-based models with non-overlap constraints (volume exclusion).
- We introduced a **first-order variant of the position based dynamics (PBD)** method, and we showed numerical evidence for the method's convergence.
- We adapted an existing model for growing epithelium and reformulated it as a first-order differential inclusions. The reformulation allowed us to use PBD, which led to runtime and stability improvements.
- **We modelled heterogeneous epithelial-to-mesenchymal transitions**, extending the model for growing epithelium.
- With a detailed simulation study, we investigated which factors lead to basal extrusion.
- The **simulation results lead to two new biological hypotheses** which are now also **supported by in vivo experiments**.
- Independent from the above projects, we showed with elementary methods a new mean-field limit result which might help to use the kinetic approach for new types of systems.

Mathematically, a common theme of this thesis is the investigation of differential equations with constraints (equality and inequality). Constraints typically lead to mathematical or numerical challenges, which we resolve in this thesis with the theory of differential

inclusions and the PBD method. In Chapter 5, we instead eliminate all constraints by derivation of equivalent unconstrained systems.

Further directions

In the following, we will outline some possible further research directions.

Position based dynamics

On the mathematical side, the most interesting next step would be a proof of convergence for the first-order PBD method.

- **Ideas for proving convergence of PBD.** It seems that most steps from the proof of Theorem 1.31 apply similarly if one replaces Moreau's catch-up scheme with the first-order PBD method. The critical difference is that Moreau's catch-up scheme always stays within the feasible set S, whereas the PBD method can lead to slightly infeasible states. This requires additional estimates to ensure that the distance to the feasible set remains bounded and converges to zero.

  For example, if there exists some $\alpha > 0$ such that $\max_j \operatorname{dist}(\boldsymbol{x}, S_j) \geq \alpha \operatorname{dist}(\boldsymbol{x}, S)$ for all $\boldsymbol{x} \in \mathbb{R}^d$, then we may be able to show that there exists an $c \in (0, 1)$ such that

  $$\|\mathrm{P}_S(\boldsymbol{x}) - \mathrm{P}_{S_M} \circ \cdots \circ \mathrm{P}_{S_1}(\boldsymbol{x})\| \leq c\|\mathrm{P}_S(\boldsymbol{x}) - \boldsymbol{x}\|$$

  holds for $\boldsymbol{x} \in \mathbb{R}^d$ for which $\operatorname{dist}(\boldsymbol{x}, S)$ is sufficiently small (see notations as in Section 2.1). Such an estimate is central to showing that the approximation errors of the PBD method do not accumulate too much (in comparison with Moreau's catch-up scheme). If the above estimate holds, it seems possible to show that the PBD is stable and that the PBD approximation converges in the same sense as Moreau's catch-up scheme (see proof of Theorem 1.31).

Establishing the convergence of the PBD method is important since it is a powerful method for simulating agent-based models under constraints since the stability of the PBD method makes it possible to implement complex constraints effortlessly. Moreover, the simplicity of PBD could accelerate many modelling projects, especially for smaller teams, and it is particularly well-suited for quick implementation of ideas.

Simulation of epithelial-to-mesenchymal transitions and mesenchymal cell migration

Regarding our modelling projects, there are multiple future directions to investigate. In the following, we will list some possible directions that either extend the model or fix certain limitations.

- **Mesenchymal cell migration through the extracellular matrix.** The models in this thesis stop as soon as cells leave the epithelium basally. However, the migration past that point is also challenging in different ways. In the basal extracellular matrix, the cells have to migrate through a space filled with a

dense network of fibers. The fibers support the seek-and-grab mechanism for cell migration (i.e. for cell-matrix adhesion), but if the network is too dense, cells must first remove some fibers to pass these obstacles.

There are many models for mesenchymal cell migration [Woo+14; Sch+; McL+12; BE20]. One particular challenge in our context is that the number of cells varies between tiny groups of cells (in the trunk region) and larger clusters (in the cephalic region). Another open question concerns the used mechanism of these cells. While neural crest cells are, in principle, capable of using chemotaxis [The+10]. It is not clear if chemotaxis is the critical mechanism in vivo. For example, in [Baj+19], it is shown that chemotaxis is not used to guide cells but instead a tool for regulating cell adhesion. Here, the overall topology of the environment seems more important for directionality.

- **Improvements of the existing model.** The model for growing epithelium uses many simplifying assumptions, which make the model more generic but also neglect certain aspects of the actual context of EMT. Taking the neural tube as a model mechanism, one could consider modelling not a rectangular patch but a curved tissue or even a closed tube. A more realistic geometry may also influence EMT and basal extrusion.

- **Three-dimensional modelling.** Most aspects of the EMT model generalise directly to three dimensions. However, the apical layer is not an ordered line of springs in three dimensions. Instead, a more complicated topology of apical cell-cell adhesion is necessary. Here, new rules are required to model the apical surface. A preliminary implementation for three dimensions already exists, but more attention to detail is required to make the mathematical model usable.

Acknowledgements

There are countless people who supported me during my PhD and naming everyone is probably impossible.

First and foremost, I was very lucky to be supervised by Sara Merino-Aceituno. Sara is an endless source of positive energy and she supported me during my PhD in all possible ways, for example with quick responses (even when she was probably very busy herself), comprehensive proofreading (elevating my usually crappy abstracts to another level) and many meetings (which usually took longer than we planned). I am also grateful that I had the freedom to spend quite some time to share my love for programming with people around me.

I had the pleasure to be part of Sara growing research group with Claudia, Carmela, Havva and Raphael, who each added new ideas, fun and a bit of craziness.

One of the most interesting aspects of this PhD project was the collaboration with Eric Theveneau, who was brave enough to install my simulations on his computers and who explained me in countless emails how biology works. His care for details and dedication to our project motivated me throughout my PhD.

Since my main PhD project was a continuation of the work started during Marina A. Ferreira's PhD, it was great that I could always seek out to Marina for advice and hints about the existing modelling. Moreover, I am happy about the advice and feedback I got from the whole team, consisting of Pierre Degond, Sara, Marina, Eric and Diane Peurichard.

I would also like to thank my previous supervisor and mentor Bernd Simeon for his ongoing support during the last six years.

Because of the pandemic, almost one half of my PhD was spent in lockdowns, but once the university was populated, mathematics was much more fun again, thanks to many

motivating and inspiring PhD students and researchers in Vienna. The accumulation of many small chats on the university floors really improve happiness, therefore, people like Giancarlo are invaluable for any department. I would also like to thank David, Eric, Jonathan, Pilar, Willi and Vishnupriya for last minute proofreading.

My PhD was funded by the Vienna Science and Technology Fund (WWTF), grant VRG17-014. And in addition, a six week research stay in Toulouse was made possible by an EMBO short term fellowship (8661).

Appendix

1. The Uzawa algorithm

The Uzawa algorithm is a classical approximation for linear saddle point problems and it extends to nonlinear saddle point problems.

We follow [BBF13, Chapter 5] for the presentation of the linear case.

1.1. Linear case

A linear saddle point problem arises from a constrained optimisation problem such as

$$\begin{aligned} &\text{minimise} \quad \boldsymbol{x}^T A\boldsymbol{x} - \boldsymbol{f}^T\boldsymbol{x} \\ &\text{subject to} \quad B\boldsymbol{x} = \boldsymbol{g} \end{aligned}$$

where $A \in \mathbb{R}^{d\times d}$ is symmetric, $B \in \mathbb{R}^{m\times d}$ with $m < d$, $\boldsymbol{f} \in \mathbb{R}^n$ and $\boldsymbol{g} \in \mathbb{R}^m$.

Using the Lagrangian approach this is equivalent to finding a saddle point of

$$\mathcal{L}(\boldsymbol{x}, \boldsymbol{\lambda}) \coloneqq \boldsymbol{x}^T A\boldsymbol{x} + B^T\boldsymbol{\lambda} - \boldsymbol{f}^T\boldsymbol{x}.$$

That is, we seek a solution of

$$\inf_{\boldsymbol{x}\in\mathbb{R}^d} \sup_{\boldsymbol{\lambda}\in\mathbb{R}^m} \mathcal{L}(\boldsymbol{x}, \boldsymbol{\lambda}).$$

We note that $\sup_{\boldsymbol{\lambda}} \mathcal{L}(\boldsymbol{x}, \boldsymbol{\lambda}) = \infty$ if $B\boldsymbol{x} \neq \boldsymbol{g}$, therefore, the result is also a solution of the original problem.

The corresponding first order conditions yield the linear problem

$$\begin{pmatrix} A & B^T \\ B & 0 \end{pmatrix} \begin{pmatrix} \boldsymbol{x} \\ \boldsymbol{\lambda} \end{pmatrix} = \begin{pmatrix} \boldsymbol{f} \\ \boldsymbol{g} \end{pmatrix}. \tag{A.1}$$

The numerical challenge of this problem arises since this linear system is often not symmetric and positive definite.

If A is invertible, one can eliminate $\boldsymbol{x}$. From the first row in (A.1) we obtain

$$\boldsymbol{x} = A^{-1}\boldsymbol{f} - A^{-1}B^T\boldsymbol{\lambda} \tag{A.2}$$

which can be inserted into the second row (A.1)

$$B\boldsymbol{\lambda} = BA^{-1}\boldsymbol{f} - BA^{-1}B^T\boldsymbol{\lambda} = \boldsymbol{g} \quad \Leftrightarrow \quad BA^{-1}B^T\boldsymbol{\lambda} = BA^{-1}\boldsymbol{f} - \boldsymbol{g}. \tag{A.3}$$

In applications, the Schur complement $BA^{-1}B^T$ has typically good properties (such as the 'inf-sup' conditions in the finite element context) which makes this approach attractive.

Assuming that $BA^{-1}B^T$ is symmetric and positive-definite, we can write (A.3) equivalently as

$$\min_{\boldsymbol{\lambda}} F(\boldsymbol{\lambda}) \quad \text{with} \quad F(\boldsymbol{\lambda}) \coloneqq \boldsymbol{\lambda}^T BA^{-1}B^T\boldsymbol{\lambda} - 2\boldsymbol{\lambda}^T(BA^{-1}\boldsymbol{f} - \boldsymbol{g})$$

The gradient of F is given by

Using a gradient method applied to (A.2) and (A.3) yields the *Uzawa algorithm*:

- Pick $\boldsymbol{\lambda}_0$ arbitrary.
- Iterate for $k > 0$ until convergence:
  - Find $\boldsymbol{x}_{k+1}$ solution of
  $$A\boldsymbol{x}_{k+1} = \boldsymbol{f} - B^T\boldsymbol{\lambda}_n$$
  - Compute $\boldsymbol{\lambda}_{k+1}$ with a properly chosen decent step-size α
  $$\begin{aligned}\boldsymbol{\lambda}_{k+1} &= \boldsymbol{\lambda}_k + \alpha(BA^{-1}B^T\boldsymbol{\lambda}_k - BA^{-1}\boldsymbol{f} - \boldsymbol{g}) \\ &= \boldsymbol{\lambda}_k + \alpha(B\boldsymbol{x}_{k+1} - \boldsymbol{g}).\end{aligned}$$

The steps of the Uzawa algorithm approximate the alternating solution of the problems $\inf_{\boldsymbol{x}} \mathcal{L}(\boldsymbol{x}, \boldsymbol{\lambda}_k)$ and $\sup_{\boldsymbol{\lambda}} \mathcal{L}(\boldsymbol{x}_{k+1}, \boldsymbol{\lambda})$.

1.2. Nonlinear Uzawa algorithm

Generalising the linear case, we can consider to solve the saddle point problem

$$\inf_{\boldsymbol{x}\in\mathbb{R}^d} \sup_{\boldsymbol{\lambda}\in\mathbb{R}^m} \mathcal{L}(\boldsymbol{x}, \boldsymbol{\lambda}).$$

for the Lagrangian

$$\mathcal{L}(\boldsymbol{x}, \boldsymbol{\lambda}) \coloneqq W(\boldsymbol{x}) + (\boldsymbol{g}(\boldsymbol{x})^T)\boldsymbol{\lambda}$$

with $W : \mathbb{R}^d \to \mathbb{R}$ and $\boldsymbol{g} : \mathbb{R}^d \to \mathbb{R}^m$ with corresponding Lagrangian multipliers $\boldsymbol{\lambda} \in \mathbb{R}^m$.

Inspired by the linear case, one might approximate the iterated solution of $\inf_{\boldsymbol{x}} \mathcal{L}(\boldsymbol{x}, \boldsymbol{\lambda}_k)$ and $\sup_{\boldsymbol{\lambda}} \mathcal{L}(\boldsymbol{x}_{k+1}, \boldsymbol{\lambda})$ using the gradient method. The difference to the linear case is that

solving the $\inf_{\boldsymbol{x}} \mathcal{L}(\boldsymbol{x}, \boldsymbol{\lambda}_k)$ is not trivial and also uses the gradient decent method instead of an exact solution. We obtain the following method:

- Pick $\boldsymbol{\lambda}_0, \boldsymbol{x}_0$ arbitrary.
- Iterate for $k > 0$ until convergence:
  - Compute $\boldsymbol{x}_{k+1}$ with a properly chosen step-size γ

$$\boldsymbol{x}_{k+1} = \boldsymbol{x}_k - \gamma(\nabla_{\boldsymbol{x}} W(\boldsymbol{x}_k) + (\nabla_{\boldsymbol{x}} g(\boldsymbol{x}_k))^T \boldsymbol{\lambda}_k)$$

  - Compute $\boldsymbol{\lambda}_{k+1}$ with a properly chosen step-size α

$$\boldsymbol{\lambda}_{k+1} = \boldsymbol{\lambda}_k + \alpha \boldsymbol{g}(\boldsymbol{x}_{k+1}).$$

2. Derivation of the ODE model

In this section, we show that solutions of the DAE model (5.6a) to (5.6c) are also solutions of the ODE model (5.11a) and (5.11b). We recall the DAE model

$$\begin{cases} m\ddot{\boldsymbol{X}}_i = F_1(\boldsymbol{X}_i) + \dfrac{1}{N}\displaystyle\sum_{k=1}^{N} K(\boldsymbol{X}_i, \boldsymbol{X}_k) - (\partial_{\boldsymbol{X}_i} g(\boldsymbol{X}_i, \boldsymbol{y}))^T \boldsymbol{\lambda}_i & \text{for } 1 \le i \le N, \quad \text{(A.4a)} \\ \ddot{\boldsymbol{y}} = F_0(\boldsymbol{y}) - \dfrac{1}{N}\displaystyle\sum_{j=1}^{N} (\partial_{\boldsymbol{y}} g(\boldsymbol{X}_j, \boldsymbol{y}))^T \boldsymbol{\lambda}_j, & \quad \text{(A.4b)} \\ g(\boldsymbol{X}_i, \boldsymbol{y}) = g(\boldsymbol{X}_i^{\text{init}}, \boldsymbol{y}^{\text{init}}) & \text{for } 1 \le i \le N \quad \text{(A.4c)} \end{cases}$$

and the ODE model

$$\begin{cases} m_{\text{eff}}^{(N)} \ddot{\boldsymbol{y}} = F_{\text{eff}}^{(N)}, & \text{(A.5a)} \\ \dot{\boldsymbol{X}}_i = \Phi_i[\dot{\boldsymbol{y}}], \quad \text{for } 1 \le i \le N. & \text{(A.5b)} \end{cases}$$

Proof of Proposition 5.1. In the following we assume $\boldsymbol{X}_i \in C^1([0,T], \mathbb{R}^{n_x})$ and $\boldsymbol{y} \in C^2([0,T], \mathbb{R}^{n_y})$ for $1 \le i \le N$. We start with showing '$(A.4c) \Leftrightarrow (A.5b)$'. Thereafter, we prove that if $(\boldsymbol{\mathcal{X}}^{(N)}, \boldsymbol{y})$ satisfy (A.5b), then '$(A.4a)$ and $(A.4b) \Leftrightarrow (A.5a)$'.

1. We show that (A.4c) is equivalent to (A.5b).

$$(A.4c) \Leftrightarrow \frac{\mathrm{d}g(\boldsymbol{X}_i, \boldsymbol{y})}{\mathrm{d}t} = \partial_{\boldsymbol{X}_i} g(\boldsymbol{X}_i, \boldsymbol{y})[\dot{\boldsymbol{X}}_i] + \partial_{\boldsymbol{y}} g(\boldsymbol{X}_i, \boldsymbol{y})[\dot{\boldsymbol{y}}] = 0 \quad \text{(A.6)}$$

$$\Leftrightarrow \dot{\boldsymbol{X}}_i = \underbrace{-\left(\partial_{\boldsymbol{X}_j} g(\boldsymbol{X}_i, \boldsymbol{y})\right)^{-1} \partial_{\boldsymbol{y}} g(\boldsymbol{X}_i, \boldsymbol{y})}_{=\Phi_i}[\dot{\boldsymbol{y}}] \Leftrightarrow (A.5b) \quad \text{(A.7)}$$

2. Under the condition that (A.5b) holds, we show that (A.4a) and (A.4b) are equivalent to (A.5a).

Taking the time derivative of (A.5b) implies

$$\begin{aligned}\ddot{\boldsymbol{X}}_i &= \Phi_i[\ddot{\boldsymbol{y}}] + \dot{\Phi}_i[\dot{\boldsymbol{y}}] \\ &= \Phi(\boldsymbol{X}_i, \boldsymbol{y})[\ddot{\boldsymbol{y}}] + \partial_{\boldsymbol{X}_i}\Phi(\boldsymbol{X}_i, \boldsymbol{y})[\dot{\boldsymbol{y}}, \dot{\boldsymbol{X}}_i] + \partial_{\boldsymbol{y}}\Phi(\boldsymbol{X}_i, \boldsymbol{y})[\dot{\boldsymbol{y}}, \dot{\boldsymbol{y}}] \\ &= \Phi(\boldsymbol{X}_i, \boldsymbol{y})[\ddot{\boldsymbol{y}}] + \partial_{\boldsymbol{X}_i}\Phi(\boldsymbol{X}_i, \boldsymbol{y})[\dot{\boldsymbol{y}}, \Phi(\boldsymbol{X}_i, \boldsymbol{y})[\dot{\boldsymbol{y}}]] + \partial_{\boldsymbol{y}}\Phi(\boldsymbol{X}_i, \boldsymbol{y})[\dot{\boldsymbol{y}}, \dot{\boldsymbol{y}}] \end{aligned} \tag{A.8}$$

where we used (A.5b) again in the last line to remove the dependency on $\dot{\boldsymbol{X}}_i$. As a side-effect we obtain $\boldsymbol{X}_i \in C^2([0,T], \mathbb{R}^{n_x})$.

To shorten (A.8), we define

$$\begin{aligned}\Omega_i[\boldsymbol{v}, \boldsymbol{w}] &\coloneqq \Omega(\boldsymbol{X}_i, \boldsymbol{y})[\boldsymbol{v}, \boldsymbol{w}] \\ &\coloneqq \partial_{\boldsymbol{X}_i}\Phi(\boldsymbol{X}_i, \boldsymbol{y})[\boldsymbol{v}, \Phi(\boldsymbol{X}_i, \boldsymbol{y})[\boldsymbol{w}]] + \partial_{\boldsymbol{y}}\Phi(\boldsymbol{X}_i, \boldsymbol{y})[\boldsymbol{v}, \boldsymbol{w}] \end{aligned} \tag{A.9}$$

for $\boldsymbol{v}, \boldsymbol{w} \in \mathbb{R}^{n_y}$. Then, we can write (A.8) as

$$\ddot{\boldsymbol{X}}_i = \Phi_i[\ddot{\boldsymbol{y}}] + \Omega_i[\dot{\boldsymbol{y}}, \dot{\boldsymbol{y}}]. \tag{A.10}$$

With this preparation we can prove the desired equivalence.

2.a) '$(A.4a)$ and $(A.4b) \Rightarrow (A.5a)$'

We assume that $(\boldsymbol{\mathcal{X}}^{(N)}, \boldsymbol{y})$ are a solution of the DAE model. Then, (A.4a) and (A.10) imply

$$\boldsymbol{\lambda}_i = (\partial_{\boldsymbol{X}_i} g(\boldsymbol{X}_i, \boldsymbol{y}))^{-T} \left(F_1(\boldsymbol{X}_i) + \frac{1}{N}\sum_{k=1}^{N} K(\boldsymbol{X}_i, \boldsymbol{X}_k) - m\ddot{\boldsymbol{X}}_i \right) \tag{A.11}$$

$$= (\partial_{\boldsymbol{X}_i} g(\boldsymbol{X}_i, \boldsymbol{y}))^{-T} \left(F_1(\boldsymbol{X}_i) + \frac{1}{N}\sum_{k=1}^{N} K(\boldsymbol{X}_i, \boldsymbol{X}_k) - m\Phi_i[\ddot{\boldsymbol{y}}] - m\Omega_i[\dot{\boldsymbol{y}}, \dot{\boldsymbol{y}}] \right). \tag{A.12}$$

Inserting (A.12) into (A.4b) gives

$$\ddot{\boldsymbol{y}} = F_0(\boldsymbol{y}) + \frac{1}{N}\sum_{j=1}^{N} \Phi_j^T \left(F_1(\boldsymbol{X}_j) + \frac{1}{N}\sum_{k=1}^{N} K(\boldsymbol{X}_i, \boldsymbol{X}_k) - m(\Phi_j[\ddot{\boldsymbol{y}}] + \Omega_j[\dot{\boldsymbol{y}}, \dot{\boldsymbol{y}}]) \right). \tag{A.13}$$

Collecting the acceleration terms to the left-hand side yields

$$\begin{aligned}&\left(I_{\mathbb{R}^{n_y}} + \frac{m}{N}\sum_{j=1}^{N} \Phi_j^T \Phi_j\right) \ddot{\boldsymbol{y}} \\ &\qquad = F_0(\boldsymbol{y}) + \frac{1}{N}\sum_{j=1}^{N} \Phi_j^T \left(F_1(\boldsymbol{X}_j) + \frac{1}{N}\sum_{k=1}^{N} K(\boldsymbol{X}_i, \boldsymbol{X}_k) - m\Omega_i[\dot{\boldsymbol{y}}, \dot{\boldsymbol{y}}] \right)\end{aligned}$$

which is equivalent to (A.5a).

2.b) '$(A.4a)$ and $(A.4b) \Leftarrow (A.5a)$' We assume now that $(\boldsymbol{\mathcal{X}}^{(N)}, \boldsymbol{y})$ solves the ODE model.

To find a solution of the DAE model, we define

$$\boldsymbol{\lambda}_i \coloneqq (\partial_{\boldsymbol{X}_i} g(\boldsymbol{X}_i, \boldsymbol{y}))^{-T} (F_1(\boldsymbol{X}_i) + \frac{1}{N} \sum_{k=1}^{N} K(\boldsymbol{X}_i, \boldsymbol{X}_k) - m\Phi_i[\ddot{\boldsymbol{y}}] - m\Omega_i[\dot{\boldsymbol{y}}, \dot{\boldsymbol{y}}]) \tag{A.14}$$

which is exactly (A.12). The assumptions $g \in C^2$, $\partial_{\boldsymbol{X}_i} g(\boldsymbol{X}_i, \boldsymbol{y})$ invertible and $\boldsymbol{y} \in C^2$ imply $\boldsymbol{\lambda}_i \in C^0([0,T], \mathbb{R}^{n_x})$.

Inserting (A.10) into (A.14) yields (A.11) which is equivalent to (A.4a).

And as a final step, inserting (A.14) into (A.5a) yields (A.4b). □

Bibliography

[AB08] Vincent Acary and Bernard Brogliato. *Numerical Methods for Nonsmooth Dynamical Systems: Applications in Mechanics and Electronics*. eng. Vol. 35. Lecture Notes in Applied and Computational Mechanics. Springer Verlag, 2008. ISBN: 9783540753919.

[AE09] Jon D. Ahlstrom and Carol A. Erickson. 'The neural crest epithelial-mesenchymal transition in 4D: a 'tail' of multiple non-obligatory cellular mechanisms'. In: *Development* 136.11 (June 2009), pp. 1801–1812. ISSN: 0950-1991. DOI: 10.1242/dev.034785.

[AHU58] Kenneth J. Arrow, Leonid Hurwicz and Hirofumi Uzawa. *Studies in linear and non-linear programming*. English. Published: Stanford Mathematical Studies in the Social Sciences. 2. Stanford, CA: Stanford University Press. 229 p. (1958). 1958.

[ANT17] Samir Adly, Florent Nacry and Lionel Thibault. 'Discontinuous sweeping process with prox-regular sets'. en. In: *ESAIM: Control, Optimisation and Calculus of Variations* 23.4 (Oct. 2017), pp. 1293–1329. ISSN: 1292-8119, 1262-3377. DOI: 10.1051/cocv/2016053.

[App+14] C. Appert-Rolland et al. 'Pedestrian Flows: From Individuals to Crowds'. en. In: *Transportation Research Procedia*. The Conference on Pedestrian and Evacuation Dynamics 2014 (PED 2014), 22-24 October 2014, Delft, The Netherlands 2 (Jan. 2014), pp. 468–476. ISSN: 2352-1465. DOI: 10.1016/j.trpro.2014.09.062.

[Baj+19] Fernanda Bajanca et al. 'In vivo topology converts competition for cell-matrix adhesion into directional migration'. en. In: *Nature Communications* 10.1 (Apr. 2019), p. 1518. ISSN: 2041-1723. DOI: 10.1038/s41467-019-09548-5.

[BBF13] Daniele Boffi, Franco Brezzi and Michel Fortin. *Mixed finite element methods and applications*. English. Vol. 44. Springer Ser. Comput. Math. Berlin: Springer, 2013. ISBN: 9783642365188 9783642365195. DOI: 10.1007/978-3-642-36519-5.

[BCD18] Rafael Bailo, José A. Carrillo and Pierre Degond. 'Pedestrian Models Based on Rational Behaviour'. en. In: ed. by Livio Gibelli and Nicola Bellomo. Modeling and Simulation in Science, Engineering and Technology. Cham: Springer International Publishing, 2018, pp. 259–292. ISBN: 9783030051297. DOI: 10.1007/978-3-030-05129-7_9.

[BE20] Andreas Buttenschön and Leah Edelstein-Keshet. 'Bridging from single to collective cell migration: A review of models and links to experiments'. en. In: *PLOS Computational Biology* 16.12 (Dec. 2020), e1008411. ISSN: 1553-7358. DOI: 10.1371/journal.pcbi.1008411.

[BMM17] Jan Bender, Matthias Müller and Miles Macklin. 'A Survey on Position Based Dynamics'. en. In: (2017). ISSN: 1017-4656. DOI: 10.2312/egt.20171034.

[BP12] Viorel Barbu and Teodor Precupanu. *Convexity and optimization in Banach spaces*. English. 4th updated and revised ed. Springer Monogr. Math. Dordrecht: Springer, 2012. ISBN: 9789400722460 9789400722477. DOI: 10.1007/978-94-007-2247-7.

[BR08] Markus Böl and Stefanie Reese. 'Micromechanical modelling of skeletal muscles based on the finite element method'. In: *Computer Methods in Biomechanics and Biomedical Engineering* 11.5 (Oct. 2008), pp. 489–504. ISSN: 1025-5842. DOI: 10.1080/10255840701771750.

[Bre11] Haim Brezis. *Functional analysis, Sobolev spaces and partial differential equations*. English. Universitext. New York, NY: Springer, 2011. ISBN: 9780387709130 9780387709147. DOI: 10.1007/978-0-387-70914-7.

[Bro+06] B. Brogliato et al. 'On the equivalence between complementarity systems, projected systems and differential inclusions'. en. In: *Systems & Control Letters* 55.1 (Jan. 2006), pp. 45–51. ISSN: 0167-6911. DOI: 10.1016/j.sysconle.2005.04.015.

[BT20] Bernard Brogliato and Aneel Tanwani. 'Dynamical Systems Coupled with Monotone Set-Valued Operators: Formalisms, Applications, Well-Posedness, and Stability'. In: *SIAM Review* 62.1 (Jan. 2020), pp. 3–129. ISSN: 0036-1445. DOI: 10.1137/18M1234795.

[BV10] Frédéric Bernicot and Juliette Venel. 'Differential inclusions with proximal normal cones in Banach spaces'. English. In: *Journal of Convex Analysis* 17.2 (2010), pp. 451–484. ISSN: 0944-6532.

[BV11] Frédéric Bernicot and Juliette Venel. 'Stochastic perturbation of sweeping process and a convergence result for an associated numerical scheme'. en. In: *Journal of Differential Equations* 251.4 (Aug. 2011), pp. 1195–1224. ISSN: 0022-0396. DOI: 10.1016/j.jde.2011.03.010.

[BV12] Frédéric Bernicot and Juliette Venel. 'Existence of solutions for second-order differential inclusions involving proximal normal cones'. en. In: *Journal de Mathématiques Pures et Appliquées* 98.3 (Sept. 2012), pp. 257–294. ISSN: 0021-7824. DOI: 10.1016/j.matpur.2012.05.001.

[BV13] Frédéric Bernicot and Juliette Venel. 'Convergence order of a numerical scheme for sweeping process'. English. In: *SIAM Journal on Control and Optimization* 51.4 (2013), pp. 3075–3092. ISSN: 0363-0129. DOI: 10.1137/120882044.

[CIP94] Carlo Cercignani, Reinhard Illner and Mario Pulvirenti. *The mathematical theory of dilute gases*. Vol. 106. Applied Mathematical Sciences. Springer-Verlag, New York, 1994. ISBN: 9780387942940. DOI: 10.1007/978-1-4419-8524-8.

[Cla13] Francis Clarke. *Functional analysis, calculus of variations and optimal control*. English. Vol. 264. Grad. Texts Math. London: Springer, 2013. ISBN: 9781447148197 9781447148203. DOI: 10.1007/978-1-4471-4820-3.

[Cle16] Fabrizio Cleri. *The Physics of Living Systems*. Springer International Publishing, 2016. DOI: 10.1007/978-3-319-30647-6.

[Dav84] M. H. A. Davis. 'Piecewise-deterministic Markov processes: a general class of nondiffusion stochastic models'. In: *Journal of the Royal Statistical Society. Series B. Methodological* 46.3 (1984), pp. 353–388. ISSN: 0035-9246.

[Deg04] Pierre Degond. 'Macroscopic limits of the Boltzmann equation: a review'. In: *Modeling and computational methods for kinetic equations*. Model. Simul. Sci. Eng. Technol. Birkhäuser Boston, Boston, MA, 2004, pp. 3–57.

[DFM17] Pierre Degond, Marina A. Ferreira and Sebastien Motsch. 'Damped Arrow–Hurwicz algorithm for sphere packing'. en. In: *Journal of Computational Physics* 332 (Mar. 2017), pp. 47–65. ISSN: 0021-9991. DOI: 10.1016/j.jcp.2016.11.047.

[DN08] R. W. R. Darling and J. R. Norris. 'Differential equation approximations for Markov chains'. In: *Probability Surveys* 5 (2008), pp. 37–79. DOI: 10.1214/07-PS121.

[DR15] Peter Deuflhard and Susanna Röblitz. *A guide to numerical modelling in systems biology*. English. Vol. 12. Texts Comput. Sci. Eng. Cham: Springer, 2015. ISBN: 9783319200583 9783319200590. DOI: 10.1007/978-3-319-20059-0.

[ET05] J. F. Edmond and L. Thibault. 'Relaxation of an optimal control problem involving a perturbed sweeping process'. English. In: *Mathematical Programming. Series A. Series B* 104.2-3 (B) (2005), pp. 347–373. ISSN: 0025-5610. DOI: 10.1007/s10107-005-0619-y.

[ET06] Jean Fenel Edmond and Lionel Thibault. 'BV solutions of nonconvex sweeping process differential inclusion with perturbation'. en. In: *Journal of Differential Equations* 226.1 (July 2006), pp. 135–179. ISSN: 0022-0396. DOI: 10.1016/j.jde.2005.12.005.

[Fer+19] Marina A. Ferreira et al. 'Interkinetic nuclear movements promote apical expansion in pseudostratified epithelia at the expense of apicobasal elongation'. en. In: *PLOS Computational Biology* 15.12 (Dec. 2019), e1007171. ISSN: 1553-7358. DOI: 10.1371/journal.pcbi.1007171.

[Fil88] A. F. Filippov. *Differential equations with discontinuous right-hand sides. Ed. by F. M. Arscott. Transl. from the Russian*. English. Ed. by F. M. Arscott. Vol. 18. Math. Appl., Sov. Ser. Dordrecht etc.: Kluwer Academic Publishers, 1988. ISBN: 9789027726995.

[FO22] Alexander G. Fletcher and James M. Osborne. 'Seven challenges in the multiscale modeling of multicellular tissues'. en. In: *WIREs Mechanisms of Disease* 14.1 (2022), e1527. ISSN: 2692-9368. DOI: 10.1002/wsbm.1527.

[FP15] Marco Fratarcangeli and Fabio Pellacini. 'Scalable Partitioning for Parallel Position Based Dynamics'. In: *Computer Graphics Forum* (2015). DOI: 10.1111/cgf.12570.

[GG00] Scott F. Gilbert and Scott F. Gilbert. *Developmental Biology*. 6th. Sinauer Associates, 2000. ISBN: 9780878932436.

[GKZ07] Michael Griebel, Stephan Knapek and Gerhard Zumbusch. *Numerical simulation in molecular dynamics. Numerics, algorithms, parallelization, applications*. English. Vol. 5. Texts Comput. Sci. Eng. Berlin: Springer, 2007. ISBN: 9783540680949.

[Gol16] François Golse. 'On the dynamics of large particle systems in the mean field limit'. In: *Macroscopic and large scale phenomena: coarse graining, mean field limits and ergodicity*. Vol. 3. Lect. Notes Appl. Math. Mech. Springer, [Cham], 2016, pp. 1–144. DOI: 10.1007/978-3-319-26883-5_1.

[GS21] M. H. Gfrerer and B. Simeon. 'Fiber-based modeling and simulation of skeletal muscles'. en. In: *Multibody System Dynamics* 52.1 (May 2021), pp. 1–30. ISSN: 1573-272X. DOI: 10.1007/s11044-021-09781-1.

[Hei+16] Thomas Heidlauf et al. 'A multi-scale continuum model of skeletal muscle mechanics predicting force enhancement based on actin–titin interaction'. en. In: *Biomechanics and Modeling in Mechanobiology* 15.6 (Dec. 2016), pp. 1423–1437. ISSN: 1617-7940. DOI: 10.1007/s10237-016-0772-7.

[Her17] Walter Herzog. 'Skeletal muscle mechanics: questions, problems and possible solutions'. In: *Journal of NeuroEngineering and Rehabilitation* 14.1 (Sept. 2017), p. 98. ISSN: 1743-0003. DOI: 10.1186/s12984-017-0310-6.

[HH54] Hugh Huxley and Jean Hanson. 'Changes in the Cross-Striations of Muscle during Contraction and Stretch and their Structural Interpretation'. en. In:

Nature 173.4412 (May 1954), pp. 973–976. ISSN: 1476-4687. DOI: 10.1038/173973a0.

[HL93] Jean-Baptiste Hiriart-Urruty and Claude Lemaréchal. *Convex analysis and minimization algorithms. Part 1: Fundamentals*. English. Vol. 305. Grundlehren Math. Wiss. Berlin: Springer-Verlag, 1993. ISBN: 9783540568506.

[HLW10] Ernst Hairer, Christian Lubich and Gerhard Wanner. *Geometric numerical integration. Structure-preserving algorithms for ordinary differential equations*. English. Reprint of the second 2006 ed. Vol. 31. Springer Ser. Comput. Math. Berlin: Springer, 2010. ISBN: 9783642051579 9783540306665. DOI: 10.1007/3-540-30666-8.

[HNW93] E. Hairer, S. P. Nørsett and G. Wanner. *Solving ordinary differential equations. I*. Second. Vol. 8. Springer Series in Computational Mathematics. Nonstiff problems. Springer-Verlag, Berlin, 1993, pp. xvi+528. ISBN: 3-540-56670-8. DOI: 10.1007/978-3-540-78862-1.

[How01] Jonathon Howard. *Mechanics of Motor Proteins and the Cytoskeleton*. eng. Nachdr. Sunderland, Mass: Sinauer, 2001. ISBN: 978-0-87893-333-4 978-0-87893-334-1.

[HS71] A. F. Huxley and R. M. Simmons. 'Proposed Mechanism of Force Generation in Striated Muscle'. en. In: *Nature* 233.5321 (Oct. 1971), pp. 533–538. ISSN: 1476-4687. DOI: 10.1038/233533a0.

[Hux57] A. F. Huxley. 'Muscle Structure and Theories of Contraction'. en. In: *Progress in Biophysics and Biophysical Chemistry* 7 (Jan. 1957), pp. 255–318. ISSN: 0096-4174. DOI: 10.1016/S0096-4174(18)30128-8.

[HW10] E. Hairer and G. Wanner. *Solving ordinary differential equations. II*. Second revised. Vol. 14. Springer Series in Computational Mathematics. Stiff and differential-algebraic problems. Springer-Verlag, Berlin, 2010, pp. xvi+614. ISBN: 978-3-642-05220-0. DOI: 10.1007/978-3-642-05221-7.

[Jab14] Pierre-Emmanuel Jabin. 'A review of the mean field limits for Vlasov equations'. In: *Kinetic and Related Models* 7.4 (2014), pp. 661–711. ISSN: 1937-5093. DOI: 10.3934/krm.2014.7.661.

[Kil+98] S. H. Kil et al. 'The alpha4 subunit of integrin is important for neural crest cell migration'. eng. In: *Developmental Biology* 202.1 (Oct. 1998), pp. 29–42. ISSN: 0012-1606. DOI: 10.1006/dbio.1998.8985.

[KS09a] James Keener and James Sneyd. *Mathematical physiology. Vol. I: Cellular physiology*. Second. Vol. 8. Interdisciplinary Applied Mathematics. Springer, New York, 2009. ISBN: 9780387758466. DOI: 10.1007/978-0-387-79388-7.

[KS09b] James Keener and James Sneyd. *Mathematical physiology. Vol. II: Systems physiology*. Second. Vol. 8. Interdisciplinary Applied Mathematics. Springer, New York, 2009. ISBN: 9780387793870. DOI: 10.1007/978-0-387-79388-7_1.

[KS22] Jan Kleinert and Bernd Simeon. 'Differential-Algebraic Equations and Beyond: From Smooth to Nonsmooth Constrained Dynamical Systems'. en. In: ed. by Michael Günther and Wil Schilders. Cham: Springer International Publishing, 2022, pp. 73–132. ISBN: 9783030961732. DOI: 10.1007/978-3-030-96173-2_4.

[LLM09] A. S. Lewis, D. R. Luke and J. Malick. 'Local linear convergence for alternating and averaged nonconvex projections'. English. In: *Foundations of Computational Mathematics* 9.4 (2009), pp. 485–513. ISSN: 1615-3375. DOI: 10.1007/s10208-008-9036-y.

[LN04] Remco I. Leine and Henk Nijmeijer. *Dynamics and bifurcations of non-smooth mechanical systems*. English. Vol. 18. Lect. Notes Appl. Comput. Mech. Berlin: Springer, 2004. ISBN: 9783540219873.

[Lou03] R. Lougee-Heimer. 'The Common Optimization INterface for Operations Research: Promoting open-source software in the operations research community'. In: *IBM Journal of Research and Development* 47.1 (Jan. 2003), pp. 57–66. ISSN: 0018-8646. DOI: 10.1147/rd.471.0057.

[Mac+19] Miles Macklin et al. 'Small steps in physics simulation'. In: *Proceedings of the 18th annual ACM SIGGRAPH/Eurographics Symposium on Computer Animation*. SCA '19. New York, NY, USA: Association for Computing Machinery, July 2019, pp. 1–7. ISBN: 9781450366779. DOI: 10.1145/3309486.3340247.

[McL+12] Rebecca McLennan et al. 'Multiscale mechanisms of cell migration during development: theory and experiment'. In: *Development* 139.16 (Aug. 2012), pp. 2935–2944. ISSN: 0950-1991. DOI: 10.1242/dev.081471.

[MKT18] N. K. Mahato, A. Klar and S. Tiwari. 'Particle methods for multi-group pedestrian flow'. en. In: *Applied Mathematical Modelling* 53 (Jan. 2018), pp. 447–461. ISSN: 0307-904X. DOI: 10.1016/j.apm.2017.08.024.

[MMC16] Miles Macklin, Matthias Müller and Nuttapong Chentanez. 'XPBD: position-based simulation of compliant constrained dynamics'. In: *Proceedings of the 9th International Conference on Motion in Games*. MIG '16. New York, NY, USA: Association for Computing Machinery, Oct. 2016, pp. 49–54. ISBN: 9781450345927. DOI: 10.1145/2994258.2994272.

[MNR12] Thomas Müller-Gronbach, Erich Novak and Klaus Ritter. *Monte Carlo-Algorithmen*. German. Springer-Lehrb. Berlin: Springer, 2012. ISBN: 978354-0891406. DOI: 10.1007/978-3-540-89141-3.

[Mor77] Jean Jacques Moreau. 'Evolution problem associated with a moving convex set in a Hilbert space'. en. In: *Journal of Differential Equations* 26.3 (Dec. 1977), pp. 347–374. ISSN: 0022-0396. DOI: 10.1016/0022-0396(77)90085-7.

[Mor99] J. J. Moreau. 'Numerical aspects of the sweeping process'. en. In: *Computer Methods in Applied Mechanics and Engineering* 177.3 (July 1999), pp. 329–349. ISSN: 0045-7825. DOI: 10.1016/S0045-7825(98)00387-9.

[Mül+06] Matthias Müller et al. *Position Based Dynamics*. en. The Eurographics Association, 2006. ISBN: 9783905673616. DOI: 10.2312/PE/vriphys/vriphys06/071-080.

[MV11] Bertrand Maury and Juliette Venel. 'A discrete contact model for crowd motion'. English. In: *European Series in Applied and Industrial Mathematics (ESAIM): Mathematical Modelling and Numerical Analysis* 45.1 (2011), pp. 145–168. ISSN: 0764-583X. DOI: 10.1051/m2an/2010035.

[MZ91] Shiping Ma and George I. Zahalak. 'A distribution-moment model of energetics in skeletal muscle'. en. In: *Journal of Biomechanics* 24.1 (Jan. 1991), pp. 21–35. ISSN: 0021-9290. DOI: 10.1016/0021-9290(91)90323-F.

[NT98] S. Nakagawa and M. Takeichi. 'Neural crest emigration from the neural tube depends on regulated cadherin expression'. In: *Development* 125.15 (Aug. 1998), pp. 2963–2971. ISSN: 0950-1991. DOI: 10.1242/dev.125.15.2963.

[Phi+12] Rob Phillips et al. *Physical Biology of the Cell*. 2nd ed. Boca Raton: Garland Science, Nov. 2012. ISBN: 9780429168833. DOI: 10.1201/9781134111589.

[PRT00] R. A. Poliquin, R. T. Rockafellar and L. Thibault. 'Local differentiability of distance functions'. English. In: *Transactions of the American Mathematical Society* 352.11 (2000), pp. 5231–5249. ISSN: 0002-9947. DOI: 10.1090/S0002-9947-00-02550-2.

[PS20] Steffen Plunder and Bernd Simeon. 'Coupled Systems of Linear Differential-Algebraic and Kinetic Equations with Application to the Mathematical Modelling of Muscle Tissue'. en. In: *Progress in Differential-Algebraic Equations II*. Ed. by Timo Reis, Sara Grundel and Sebastian Schöps. Differential-Algebraic Equations Forum. Cham: Springer International Publishing, 2020, pp. 357–395. ISBN: 9783030539054. DOI: 10.1007/978-3-030-53905-4_12.

[PS22] Steffen Plunder and Bernd Simeon. *The mean-field limit for particle systems with uniform full-rank constraints*. Tech. rep. arXiv:2203.07249 [math] type: article. arXiv, Mar. 2022. DOI: 10.48550/arXiv.2203.07249.

[RW98] R. Tyrrell Rockafellar and Roger J.-B. Wets. *Variational analysis*. English. Vol. 317. Grundlehren Math. Wiss. Berlin: Springer, 1998. ISBN: 9783540627722. DOI: 10.1007/978-3-642-02431-3.

[Sch+] Linus J. Schumacher et al. 'Multidisciplinary approaches to understanding collective cell migration in developmental biology'. In: *Open Biology* 6.6 (), p. 160056. DOI: 10.1098/rsob.160056.

[Spo91] Herbert Spohn. *Large scale dynamics of interacting particles*. English. Texts and Monographs in Physics. Berlin: Springer-Verlag, 1991. ISBN: 9783540534914. DOI: 10.1007/978-3-642-84371-6.

[SSP09] Bernd Simeon, Radu Serban and Linda R. Petzold. 'A model of macroscale deformation and microvibration in skeletal muscle tissue'. In: *M2AN. Mathematical Modelling and Numerical Analysis* 43.4 (2009), pp. 805–823. ISSN: 0764-583X. DOI: 10.1051/m2an/2009030.

[ST96] D. E. Stewart and J. C. Trinkle. 'An Implicit Time-Stepping Scheme for Rigid Body Dynamics with Inelastic Collisions and Coulomb Friction'. en. In: *International Journal for Numerical Methods in Engineering* 39.15 (1996), pp. 2673–2691. ISSN: 1097-0207. DOI: 10.1002/(SICI)1097-0207(19960815)39:15<2673::AID-NME972>3.0.CO;2-I.

[TBV12] Richard Tonge, Feodor Benevolenski and Andrey Voroshilov. 'Mass splitting for jitter-free parallel rigid body simulation'. In: *ACM Transactions on Graphics* 31.4 (July 2012), 105:1–105:8. ISSN: 0730-0301. DOI: 10.1145/2185520.2185601.

[The+10] Eric Theveneau et al. 'Collective chemotaxis requires contact-dependent cell polarity'. eng. In: *Developmental Cell* 19.1 (July 2010), pp. 39–53. ISSN: 1878-1551. DOI: 10.1016/j.devcel.2010.06.012.

[Thi22] Lionel Thibault. *Unilateral variational analysis in Banach spaces. In 2 parts. Part I: General theory. Part II: Special classes of functions and sets (to appear)*. English. Singapore: World Scientific, 2022. ISBN: 9789811258169. DOI: 10.1142/12797.

[TM12] Eric Theveneau and Roberto Mayor. 'Neural crest delamination and migration: From epithelium-to-mesenchyme transition to collective cell migration'. en. In: *Developmental Biology*. Neural Crest 366.1 (June 2012), pp. 34–54. ISSN: 0012-1606. DOI: 10.1016/j.ydbio.2011.12.041.

[Vaj60] Steven Vajda. 'Studies in Linear and Non-Linear Programming. (Stanford Mathematical Studies in the Social Sciences.) By K. J. Arrow, L. Hurwicz, and H. Uzawa. Pp. 229. 60s. 1958. (Stanford Univ. Press)'. In: *The Mathematical Gazette* 44 (1960), pp. 151–151.

[VCK99] B. L. van de Vrande, D. H. van Campen and A. de Kraker. 'An approximate analysis of dry-friction-induced stick-slip vibrations by a smoothing procedure'. English. In: *Nonlinear Dynamics* 19.2 (1999), pp. 157–169. ISSN: 0924-090X. DOI: 10.1023/A:1008306327781.

[Ven11] Juliette Venel. 'A numerical scheme for a class of sweeping processes'. en. In: *Numerische Mathematik* 118.2 (June 2011), pp. 367–400. ISSN: 0945-3245. DOI: 10.1007/s00211-010-0329-0.

[Vil09] Cédric Villani. *Optimal transport*. Vol. 338. Grundlehren der mathematischen Wissenschaften [Fundamental Principles of Mathematical Sciences]. Springer-Verlag, Berlin, 2009. ISBN: 9783540710493. DOI: 10.1007/978-3-540-71050-9.

[Von49] John Von Neumann. 'On Rings of Operators. Reduction Theory'. In: *Annals of Mathematics* 50.2 (1949), pp. 401–485. ISSN: 0003-486X. DOI: 10.2307/1969463.

[Wal70] Wolfgang Walter. *Differential and integral inequalities*. Ergebnisse der Mathematik und ihrer Grenzgebiete, Band 55. Springer-Verlag, New York-Berlin, 1970. ISBN: 978-3-642-86407-0. DOI: 10.1007/978-3-642-86405-6.

[Wei+17a] Tomer Weiss et al. 'Position-based multi-agent dynamics for real-time crowd simulation'. In: *Proceedings of the ACM SIGGRAPH / Eurographics Symposium on Computer Animation*. SCA '17. New York, NY, USA: Association for Computing Machinery, July 2017, pp. 1–2. ISBN: 9781450350914. DOI: 10.1145/3099564.3108160.

[Wei+17b] Tomer Weiss et al. 'Position-Based Multi-Agent Dynamics for Real-Time Crowd Simulation (MiG paper)'. In: *Proceedings of the Tenth International Conference on Motion in Games* (Nov. 2017). arXiv: 1802.02673, pp. 1–8. DOI: 10.1145/3136457.3136462.

[Woo+14] Mae L. Woods et al. 'Directional Collective Cell Migration Emerges as a Property of Cell Interactions'. en. In: *PLOS ONE* 9.9 (Sept. 2014), e104969. ISSN: 1932-6203. DOI: 10.1371/journal.pone.0104969.

[Wri06] Peter Wriggers. *Computational contact mechanics*. English. 2nd ed. Berlin: Springer, 2006. ISBN: 9783540326083. DOI: 10.1007/978-3-540-32609-0.

[Yan+20] Jing Yang et al. 'Guidelines and definitions for research on epithelial–mesenchymal transition'. en. In: *Nature Reviews Molecular Cell Biology* 21.6 (June 2020), pp. 341–352. ISSN: 1471-0080. DOI: 10.1038/s41580-020-0237-9.

[Zah81] George Ireneus Zahalak. 'A distribution-moment approximation for kinetic theories of muscular contraction'. en. In: *Mathematical Biosciences* 55.1 (July 1981), pp. 89–114. ISSN: 0025-5564. DOI: 10.1016/0025-5564(81)90014-6.

[Zah96] George I. Zahalak. 'Non-axial Muscle Stress and Stiffness'. en. In: *Journal of Theoretical Biology* 182.1 (Sept. 1996), pp. 59–84. ISSN: 0022-5193. DOI: 10.1006/jtbi.1996.0143.

[ZT22] Antoine Zalc and Eric Theveneau. *If Twitter goes down this weekend (and even if it doesn't). Can we all agree the neuralcrest is the only cell type worth studying in Vertebrates???* Twitter: https://mobile.twitter.com/AntoineZalc/status/1594061235993120768. Nov. 2022.